Title
Effects of Air Flow Modifications on Biomass Cookstoves

Author
Lask, Kathleen

Publication Date
2016

Peer reviewed|Thesis/dissertation

Effects of Air Flow Modifications on Biomass Cookstoves

by

Kathleen Margaret Lask

A dissertation submitted in partial satisfaction of the

requirements for the degree of

Doctor of Philosophy

in

Engineering - Applied Science & Technology

and the Designated Emphasis

in

Development Engineering

in the

Graduate Division

of the

University of California, Berkeley

Committee in charge:

Professor Ashok Gadgil, Chair
Doctor Paul Medwell, Co-chair
Professor Jyh-Yuan Chen
Professor David Attwood

Fall 2016

Effects of Air Flow Modifications on Biomass Cookstoves

Abstract

Effects of Air Flow Modifications on Biomass Cookstoves

by

Kathleen Margaret Lask

Doctor of Philosophy in Engineering - Applied Science & Technology
and the Designated Emphasis in
Development Engineering

University of California, Berkeley

Professor Ashok Gadgil, Chair

Doctor Paul Medwell, Co-chair

Worldwide, nearly three billion people cook and heat their homes with solid fuels such as biomass. Many of these biomass stoves are inefficient and heavily polluting. The emissions produced from biomass stoves are estimated to be the largest environmental threat to human health in the world, causing approximately four million premature deaths per year. Beyond the massive impact on human health, the burning of residential biomass fuels also significantly contributes to air pollution and climate change. Due to the undesirable side effects caused by such cooking practices, there is considerable interest in improving the efficiency and reducing the emissions from biomass cookstoves with researchers around the world exploring new designs and improvements, such as air flow modifications. The availability and location of air relative to the fuel in a cookstove is a crucial parameter in combustion efficiency and the resulting pollutant emissions. By controlling and modifying the air flow within the combustion chamber, cookstove designers and researchers hope to improve efficiency and reduce harmful emissions from biomass cooking. However, while the negative effects of biomass burning have spurred much research into designing less polluting cookstoves, there is a continued need for information about the actual impacts of air flow modifications in cookstoves.

This dissertation explores several applications of controlling or modifying the air flow in biomass cookstoves in order to develop a better scientific understanding of the impacts of the modifications on stove performance and emissions. The first application investigates passive modifications in charcoal cookstoves intended for dissemination in Haiti. There is an acute need for fuel-efficient Haitian cookstoves; charcoal is a predominant cooking fuel in Haiti but its use creates significant burdens on both the environment and the Haitian people. The improved charcoal cookstoves intended for distribution in Haiti that were chosen for investigation were designed to reduce convective heat losses to the environment and to direct air toward the cooking pot in the attempt to reduce fuel consumption as compared to the

traditional Haitian stove. It was found that all improved stoves used less fuel on average than the traditional Haitian stove, with the majority also reducing the total undesirable emissions. However, the traditional stove had the fastest time to boil, an important consideration for end users. Therefore, the improved stoves may face adoption issues in the field due to slow cooking speeds and incompatibilities with the cultural cooking style of Haiti even though they reduce fuel consumption as desired.

The second application investigates a passive ignition aid for charcoal stoves, known as a lighting cone, which is intended to decrease the time needed to ignite a charcoal bed by increasing draft through the stove. Traditional charcoal-burning stoves often have shallow and exposed charcoal beds, which ignite slowly and inefficiently due to interference from the wind and a lack of draft through the stove and the fuel bed. A lighting cone is a simple, metal cone designed to increase the exposure of the charcoal bed surface to fresh air and protect it from heat losses due to wind during ignition. A lighting cone is an accessory intended for user convenience that is already utilized by some local populations around the world; however, no scientific results on lighting cone performance exist in the literature. Therefore, the goal of this work was to determine the effectiveness of a lighting cone in decreasing the ignition time of a traditional Haitian charcoal cookstove and evaluate its impact on stove emissions and fuel consumption during the typically inefficient ignition phase. The results of this work found that the lighting cone operated as desired – ignition time was reduced by over 50%. Due to this more efficient, shorter ignition stage, charcoal consumption during ignition was reduced by over 40% and carbon monoxide emissions were reduced by over 50%. Additionally, the number of ultrafine particles emitted, an important metric for human health concerns, was greatly reduced using the lighting cone as compared to the traditional ignition method. This suggests that a lighting cone is a viable and beneficial accessory for aiding ignition in shallow-bed charcoal stoves.

The third application investigates the use of air injection strategies to reduce emissions from biomass cookstoves. Previous studies have found that air injection, which increases turbulent mixing, is a promising technique for reducing soot or black carbon emissions from cookstoves. However, some air injection strategies have produced undesirable emissions and performance results. Therefore, further insight into the application of air injection strategies is required to ensure the modifications produce desired and positive benefits. This dissertation explores three different mixing strategies (referred to as halos in this work), which were chosen to highlight the impact of the air injection angle on the emissions and performance results. The first strategy injected air straight down toward the fuel bed, the second strategy injected air at a downward angle toward the center of the fuel bed, and the third strategy similarly injected air at a downward and inward angle, but added a tangential component to promote swirling flow. Along with the ex-situ measurements commonly utilized in cookstove research, in-situ measurements were recorded using laser diagnostic techniques to gain a deeper understanding of how the three mixing strategies were affecting the flame zone. Comparing the ex-situ and in-situ soot measurements, the results found that all of the halos appeared to operate as desired; soot was produced in the flame, increasing radiative heat transfer to the pot, but was oxidized prior to leaving the combustion zone.

However, the ex-situ results also showed that the stoves with air injection had comparable or worse performance results (e.g. thermal efficiency and fuel consumption) than the same, unmodified improved stove. Therefore, deeper investigation was pursued to identify adverse effects of the air flow modifications, such as flame quenching. Injecting air straight down toward the fuel bed at the flow rates examined was found to create large reductions in soot emissions but also appeared to quench the flame and promote incomplete combustion, leading to poor performance results. The swirling flow halo reduced soot emissions without appearing to quench the flames; however, it still suffered from poor performance results, potentially due to thermal losses. Similar to the downward air injection, injecting air at a downward and inward angle reduced the soot emissions and appeared to locally extinguish the flames to some extent; however, this mixing strategy produced better performance results than the other mixing strategies. In addition to investigating the effects of air injection on stove performance, this research explored the technical feasibility of applying laser diagnostic techniques to high sooting, temporally- and spatially-variable flames such as those in biomass combustion systems. While many challenges and uncertainties arose when applying the laser-based techniques, useful insights into the mixing strategies were deduced from the in-situ measurements and further explorations of applying laser diagnostic techniques to biomass cookstoves are recommended.

When I was 7, I wanted to be a chemist.
Then my parents told me that I'd have to be in school a LONG time to be a chemist,
so I decided not to be a chemist.
I wound up being in school a long time anyway.

This dissertation is dedicated to my parents who have continued to support and encourage me through these many years.

Contents

List of Figures

List of Tables

Acknowledgments

I would like to express my sincerest gratitude to the numerous people without whom this dissertation would not be possible. First, I would like to thank my research advisor, Prof. Ashok Gadgil, for his support and guidance in developing my research and professional skills throughout my PhD. Next, I want to thank Dr. Paul Medwell and Dr. Cris Birzer for responding favorably to a cold call from halfway around the world and guiding me through the tricky world of laser diagnostics. I would also like to thank Prof. Dave Atwood for his encouragement and words of wisdom throughout my years in AS&T. Thank you to Prof. J.-Y. Chen for his insightful comments and questions over the course of this dissertation, and also thank you to Prof. Robert Dibble and Prof. Aldo Migone for shaping and developing my early research years.

Thank you to the National Science Foundation Graduate Research Fellowship Program, the National Defense Science and Engineering Graduate Program, Lawrence Berkeley National Laboratory, and the Soroptimist Founder Region Fellowship for supporting my PhD while allowing me to develop as a scientist. Also, thank you to the National Science Foundation East Asia and Pacific Summer Institute, the National Science Foundation Graduate Research Opportunities Worldwide, and the Development Impact Lab Explore Grant for funding the laser diagnostics research.

Thank you very much to my colleagues in the LBNL cookstove lab for their help, constructive advice, and stimulating discussions, especially Danny Wilson, Julien Caubel, Allen Boltz, and Carl Wang. A special thank you to Sharon Chen for her dedication and assistance without which I could not have completed this research. I am forever indebted to Vi Rapp for being my draft reader, study partner, and sounding board throughout these years. Thank you to my colleagues on the Haiti stoves research for your excellent insights, including Kayje Booker, Jessica Granderson, Taewon Han, Cristina Ceballos, and Nina Yang. I would also like to thank the many stove testers and interns who devoted countless hours to the lab, especially Ryan Liu, Matt Roeschke, and Arjun Kaul. I deeply thank my colleagues at the University of Adelaide, especially Chia Thong, Jingjing Ye, and Michael Evans, for their assistance during the early mornings, late nights, and countless laser realignments in between. Also, I would like to thank my officemates, Rita Kuhn and Alfonso Chinnici, for enduring my mumblings through data analysis and providing keen insights and cheerful conversation. I am eternally grateful to the staffs at Lawrence Berkeley National Laboratory, UC Berkeley, and the University of Adelaide, especially Pascal Symons, Phil Schmidt, Jason Peak, Gordon Long, Mick Franssen, Howdy Goudey, and the late Doug Sullivan for helping turn my designs into reality, and Natasha Nelson, Pat Berumen, Olivia Salazar, Joseph Silveira, Ariana Castro, Catalina Estrada, Morgan Faulkner, and MaryAnne Peters for guiding me through the ins and outs of graduate school.

Last, but definitely not least, I would like to thank my family and friends. To my father and mother, thank you for your love and optimism and for teaching me the value of hard work and perseverance. To my sisters, thank you for your humor and for always being my

cheering section. To my friends, thank you for your advice and enthusiasm and for generally keeping me sane. I am forever grateful for all of the love, guidance, and encouragement.

1 Introduction

For the last 0.5 – 1.5 million years, humans have been using fire to cook food (Gowlett, 2016). Over the millennia, cooking styles and cuisines have diversified and cooking technologies have adapted to suit cultural desires, reduce unwanted emissions, and improve performance and efficiency. Although many cooking technologies now use modern energy sources such as natural gas and electricity, nearly three billion people continue to cook with traditional solid fuels (Bonjour et al., 2013; World Health Organization (WHO), 2014). Traditionally, biomass cooking uses low efficiency, high polluting stoves (Kshirsagar and Kalamkar, 2014; International Energy Agency, 2016; Sutar et al., 2015). Unfortunately, these cookstove emissions cause major health and environmental issues worldwide (World Health Organization (WHO), 2014; Lim et al., 2012; Bond et al., 2013; Bailis et al., 2003).

Researchers are experimenting with new cookstove designs and modifications to try to improve combustion efficiency in biomass stoves and reduce the detrimental effects of cooking. This work focuses on one design area being explored by researchers – modifying the air flow in cookstoves. As described in Section 1.4, the availability and location of air relative to the fuel in a combustion chamber is a crucial parameter in combustion efficiency. By controlling and modifying the air flow within the combustion chamber, designers hope to reduce the harmful emissions from biomass cooking. This work focuses on two specific air flow modifications – a lighting cone for charcoal stoves and a secondary air injection system for a wood-burning stove – in attempt to validate and provide key information for stove designers as they continue stove improvements and adaptations.

1.1 Overview of Biomass Cooking

Biomass fuels include a wide variety of organic substances such as wood, charcoal, dung, and agricultural waste (Yevich and Logan, 2003; Bridgeman et al., 2010). Biomass typically has lower energy densities than fossil fuels due to having high oxygen and moisture contents (Bridgeman et al., 2010). However, biomass fuels are still a desirable and growing source of energy around the world because they are renewable and carbon neutral if collected sustainably and combusted efficiently (Bridgeman et al., 2010; Sagar and Kartha, 2007; Nussbaumer, 2003). It is estimated that biomass combustion supplies approximately 1 – 2 Gtoe of energy per year or about 10% of the world's energy need (Lackner et al., 2013;

Jones et al., 2014; Bridgeman et al., 2010). An estimated 2.5 – 2.8 billion people cook with solid fuels, such as wood and charcoal (Bonjour et al., 2013; World Health Organization (WHO), 2014; International Energy Agency, 2016). For many cooks, biomass fuels are inexpensive, easy to obtain, and familiar, making them a popular fuel choice (Bailis et al., 2003; Shelton, 1983).

However, biomass combustion currently has many negative impacts on human health and the environment. The emissions from cooking and heating with solid fuels are estimated to cause over four million premature deaths per year, making ambient air pollution the largest environmental threat to health in the world (Vos et al., 2015; Lim et al., 2012; World Health Organization (WHO), 2016, 2014; Smith et al., 2014). Additional consequences often not included in those statistics are diseases caused by unhealthy pregnancies, burns, and injuries or violence sustained while collecting fuel (Pope et al., 2010; Šrám et al., 2005; Glinianaia et al., 2004; World Health Organization (WHO), 2006a; Global Alliance for Clean Cookstoves, 2016). Beyond these impacts on human health, biomass combustion produces approximately 30% of the global black carbon emissions and black carbon is second only to carbon dioxide as an anthropogenic climate-forcing pollutant (Bond et al., 2013, 2004a; Hansen and Nazarenko, 2004). Additionally, emissions from biomass cookstoves cause regional climate effects such as precipitation changes and accelerated glacial melting (Menon et al., 2002; Hansen and Nazarenko, 2004; Ramanathan et al., 2001; Ramanathan and Carmichael, 2008; Jacobson, 2001). If biomass is collected unsustainably, it can lead to forest degradation and soil erosion (Chidumayo and Gumbo, 2013; Hosier, 1993; Okello et al., 2001). Charcoal fuel consumption heightens the risk of unsustainable harvesting because additional wood is commonly used as a heat source in charcoal production.

Due to the potential adverse consequences of cooking with biomass and the increasing availability of modern fuels such as natural gas and electricity, the percentage of the population cooking with biomass is decreasing (Bonjour et al., 2013; Lewis and Pattanayak, 2012). However, because the world population is increasing, the number of cooks using biomass is remaining relatively constant and is forecast to remain at approximately 2.6 billion users until 2030, highlighting the importance of addressing the issues created from biomass cooking (Bonjour et al., 2013; International Energy Agency, 2012; Sagar and Kartha, 2007). Cookstove researchers, designers, and distributors around the world are attempting to produce stoves that meet user desires, improve performance, and reduce harmful emissions from cooking. Traditional cooking methods are often either an open fire (such as that described in Section 2.1.2) or a rudimentary enclosed stove made of mud, clay, or metal (such as the one described in Section 2.1.1); such stoves often have poor thermal efficiencies and high levels of pollutant emissions (International Energy Agency, 2016; Kshirsagar and Kalamkar, 2014; Sutar et al., 2015). Many types of biomass stoves exist to suit different cuisines and fuel types as seen in review papers, such as Kshirsagar and Kalamkar (2014), Sutar et al. (2015), Bryden et al. (2006), and the Regional Wood Energy Development Programme in Asia (1993), that discuss the variety of stove designs and parameters. Common methods for improving thermal and combustion efficiencies from traditional cooking methods include modifications such as enclosing the fire to reduce heat losses out of the sides,

keeping hot air near the cooking pot using a pot skirt, raising the fuel off of the ground so air can be entrained from under the fire for better mixing, and increasing the height of the combustion chamber to increase draft through the stove (Bryden et al., 2006; Jetter et al., 2012; Sutar et al., 2015; Kshirsagar and Kalamkar, 2014; Kumar et al., 2013). However, traditional stoves are inexpensive, easy to build or obtain, and well-adapted for the local cooking style, so new stove technologies can have difficulties with adoption and continued use if they do not also meet those criteria (Ruiz-Mercado et al., 2011; Lewis and Pattanayak, 2012; Kshirsagar and Kalamkar, 2014). Also, even with improved designs, many cookstoves are still emitting more pollutants than recommended so researchers are looking deeper into potential improvements for combustion efficiency such as modifying the air flow in the stoves (Sutar et al., 2015; International Energy Agency, 2016; Kshirsagar and Kalamkar, 2014; Rapp et al., 2016; Preble et al., 2014; Jetter et al., 2012; Just et al., 2013; Tryner et al., 2014; Still et al., 2015; MacCarty et al., 2010). Prior to delving deeper into air flow modifications, some background on biomass combustion and pollutant formation is useful.

1.2 Overview of Combustion in Biomass Stoves

The subject of combustion is vast and complex and a plethora of books, journals, and conferences already exist that are dedicated to its various subjects. This section aims to provide a brief overview of the combustion ideas key to this work which are not explained in later chapters.

Biomass fuels are composed primarily of carbon, hydrogen, and oxygen with other minor constituents such as metals and salts. In an idealized situation, a biomass fuel should combust with air to produce carbon dioxide (CO_2), water vapor, and non-reacting constituents, such as nitrogen (Shelton, 1983; McAllister et al., 2011b). When this perfect mixture of fuel and air occurs, it is said to be stoichiometric. In imperfect conditions, the mixture is said to be fuel rich if there is too much fuel in the region and fuel lean if there is too much air (Flagan and Seinfeld, 1988). It is important to note that the global reaction of initial fuel reacting with air to form final products is actually composed of interacting chains of thousands of intermediate elementary reactions (McAllister et al., 2011b). If for some reason a reaction chain is broken and the reaction cannot continue, it is said to be incomplete and the intermediate products are released. Real combustion conditions, especially for solid biomass fuels, are far from ideal and the combustion is often incomplete. Incomplete combustion forms many products besides CO_2 and water that are typically harmful for human health and the environment, as discussed in Section 1.3. Wood and charcoal are the two biomass fuels focused on in this work, so an overview of wood and charcoal combustion is outlined in this section.

1.2.1 Wood Combustion

Wood is a primary source of household energy in many developing countries, as well as being a common source of energy worldwide (Yevich and Logan, 2003; Beauchemin and Tampier, 2008; Sagar and Kartha, 2007). It is a solid hydrocarbon fuel comprised of mostly carbon (50 – 53 %), oxygen (38 – 43 %), and hydrogen (6 – 7 %) with lesser amounts of other constituents such as nitrogen, sulfur, and ash (Shelton, 1983; Williams et al., 2012; Park et al., 2012; Bhattacharya et al., 2002a).

Combustion of wood fuels is a complex process, but it can be thought of as having two main phases: the solid fuel phase and the gaseous fuel phase (which stems from the solid fuel phase). In fact, wood combustion consists of several separate but related stages; the exact terminology and grouping for those stages varies, but several studies have outlined the process (such as Jones et al. (2014), Ohlemiller et al. (1985), Ohlemiller (2002), Lobert and Warnatz (1993), Suri and Horio (2010), and Nussbaumer (2003)) which is summarized here.

Solid Fuel Phase

The solid fuel phase consists of three main stages: drying, devolatilization, and smoldering combustion.

Drying In the drying stage, moisture is driven out of the wood. This stage begins as the temperature of a section of the fuel approaches the boiling point of water ($\sim 80 - 100$°C) (Ohlemiller et al., 1985). Drying is an endothermic process, requiring energy to vaporize the water. Also, the water can conduct the energy applied at the surface throughout the wood, limiting the effectiveness of surface ignition sources at increasing the local temperature to the boiling point. The moisture content of wood is high compared to other solid fuels such as coal, ranging from $\sim 5 - 30$% for dry wood and >50% for fresh, green wood (Nussbaumer, 2003; Flagan and Seinfeld, 1988; Beauchemin and Tampier, 2008; Sagar and Kartha, 2007). Therefore, this stage will noticeably affect the efficiency of the combustion and can be prohibitively energy intensive if the moisture content is too high (Ohlemiller et al., 1985; Bhattacharya et al., 2002b; Vamvuka, 2010).

Devolatilization As the wood dries and the temperature increases, volatile gases and tars begin to release from the wood. The majority of volatiles are released by pyrolysis, although some are released through surface interactions with the surrounding air. Pyrolysis is a temperature-induced cracking of the solid fuel molecules, breaking apart the fuel without requiring oxygen. Pyrolysis only requires a temperature of ~ 200°C to initiate, releasing the majority of volatiles by ~ 350°C; the pyrolysis rate then slows down but continues releasing volatiles until ~ 500°C (Suri and Horio, 2010; Koppmann et al., 2005; Lobert and Warnatz, 1993; Rein, 2009; Williams et al., 2012). The increased temperature typically propagates through the solid fuel much faster than the thin outer layer exposed to oxygen, so pyrolysis tends to dominate in the release of volatiles from the fuel. Devolatilization releases numerous

species of tars and volatile gases, such as methane, acetylene, benzene, and other aromatics, and leaves behind a carbon-enriched char (Park et al., 2012; Fagbemi et al., 2001; Williams et al., 2012; Bajus, 2010).

Char combustion After the volatiles have been released from the solid fuel, further oxidation occurs on the surface of the remaining char. Some studies classify this as smoldering combustion (Ohlemiller, 2002; Rein, 2009; Ohlemiller, 1985), while others divide it into two stages, glowing and smoldering, where glowing combustion occurs concurrently with the flaming combustion and smoldering occurs after there is no longer a visible flame (Lobert and Warnatz, 1993; Andreae and Merlet, 2001). This discussion uses the first definition.

Unlike the original dried wood, the char remains stable to high temperatures in the absence of oxygen (Ohlemiller et al., 1985). Therefore, the rate of oxygen reaching the surface of the char is a crucial parameter for successful combustion at temperatures typical for biomass fires. In fact, the propagation of smoldering combustion is primarily controlled by the rate of oxygen reaching the surface of the fuel (Ohlemiller, 2002, 1985; Rein, 2009). Note, the temperature at the surface is often increased by the radiative feedback from the luminescing soot in the flaming combustion (discussed in the next section) if it is present, which helps drive the surface oxidation reactions and promote complete combustion of the char (Shelton, 1983; Rein, 2009).

Compared to flaming combustion, smoldering combustion operates at low temperatures and propagates slowly. Surface oxidation can occur at temperatures as low as $150-300^{\circ}$ C. If the temperature is low enough that it does not ignite the products of incomplete combustion into flaming combustion, those products are freely released to the atmosphere (Shelton, 1983; Rein, 2009). Therefore, low-temperature smoldering combustion tends to emit a wide range of products of incomplete combustion (Lobert and Warnatz, 1993; Ward and Radke, 1993).

Gas Fuel Phase (Flaming Combustion)

The pyrolysis stage of solid fuel combustion releases several volatile gases and tars. If these products are not exposed to an oxidizer or if the temperature is not high enough to ignite the volatile products, then the volatile gases and tars are emitted to the atmosphere. However, if an oxidizer is available and the temperature is adequate, the pyrolysis gases essentially act like the fuel of a gaseous nonpremixed flame.

In a nonpremixed flame, as the name suggests, the fuel and oxidant are not mixed prior to combustion. An oft-cited, relatable example of a nonpremixed flame is a candle flame, which will be used here to discuss the basic concepts of a nonpremixed flame (Janbozorgi et al., 2010; Tien and Lee, 1982; McAllister et al., 2011d). When examined, the center of a candle flame appears to be hollow; this hollow region is actually comprised of gaseous fuel. This fuel migrates outwards from the fuel-rich core while the air migrates inwards from the ambient environment via convective or diffusive processes (Janbozorgi et al., 2010). Near the gaseous fuel core, soot particles, discussed in Section 1.3.3, begin to form and

grow in the hot, fuel-rich region. At high temperatures, the soot particles give off a yellow-orange luminescence which makes up most of the visible flame. A thin blue flame, given off from species such as OH radicals and carbon monoxide, is often seen at the edge of the yellow-orange luminescence. This narrow region around the edge of the flame is the stoichiometric, highly-reactive combustion zone (Flagan and Seinfeld, 1988; Belcher, 2010; McAllister et al., 2011d). Indeed, graphical concentration profiles show that the fuel and air concentrations decrease as they approach this boundary from their respective sides, while the concentrations of products peak (Tien and Lee, 1982; McAllister et al., 2011d). Typically in ambient conditions for an open flame, there is an abundance of oxygen in the region which is reacting with fuel at the edge of the flame. As the soot and gaseous fuel progress through the flame, more fuel is consumed by a seemingly endless supply of oxygen. The upper region of the flame appears to taper inward as the previously luminescing soot is oxidized until eventually all gaseous fuel is consumed.

The flames from biomass combustion are similar to candle flames but with greater complexity due to the interaction of multiple flames, the uneven supply and composition of the gaseous fuel (i.e. pyrolysis gases and tars), and the temporal and spatial variability of the large, fuel-rich flame cores. Pyrolysis gases from biomass tend to be highly reactive, meaning the chemical time, or the time needed to complete the reaction, is short. In fact, the chemical time is typically much shorter than the rate of diffusion in a nonpremixed flame, so the mixing of fuel and air is often the rate limiting factor in such flames (Flagan and Seinfeld, 1988). Many practical biomass combustion systems operate with excess air to help counteract the inefficiencies in the mixing of fuel and air in the system (Bolhàr-Nordenkampf, 2010). Additional modifications that induce turbulent mixing, such as those discussed in Section 1.4, can be very beneficial for promoting complete combustion.

It is important to note that for a given piece of burning wood, all combustion stages could be occurring simultaneously in different sections of the wood. In addition to the complexities of the multiple stages of combustion, wood fuel is inherently non-homogeneous; it is made of a varying combination of cellulose, hemicellulose, lignin, sap, ash, metals, and salts, which do not exist uniformly throughout the wood and combust at different temperatures (Nussbaumer, 2003; Williams et al., 2012; Beauchemin and Tampier, 2008; Neves et al., 2011). The multiple stages of combustion and the non-homogeneity of the wood lead to an inherently high level of variability in the combustion processes and pollutant emissions.

1.2.2 Charcoal Combustion

The production of charcoal consists of the first two stages of wood combustion; the wood is slowly heated in the absence of oxygen, causing it to pyrolyze and leave behind a carbon-enhanced char (Bridgeman et al., 2010). This char (i.e. charcoal) is approximately 80 – 85% carbon, while wood is approximately 50% carbon (Bridgeman et al., 2010; Shelton, 1983; Lackner et al., 2013). Because the volatile gases have been released during the production

process, charcoal combustion typically does not produce visible flames, instead consisting primarily of smoldering combustion, the final stage of solid wood combustion (Shelton, 1983).

Charcoal is a desired fuel, especially in urban areas (where it is difficult to collect free fuelwood) and in wealthier rural areas (Bailis et al., 2003). Smoldering combustion produces a more consistent, low temperature heat source which can be better for slower cooking cuisines than the highly variable, high temperature flaming combustion. Also, the charcoal production process drives off the majority of the volatiles in the wood (wood contains approximately 85% volatile matter, while charcoal contains only about 30% (Bridgeman et al., 2010)), which are responsible for forming much of the emitted soot. Therefore, charcoal combustion produces little visible smoke and does not rapidly dirty a kitchen like wood fire emissions. Also, the reduced particulate matter is beneficial for the immediate user's health although the charcoal production process introduces undesirable inefficiencies and emissions prior to the fuel use. It is important to note that because charcoal combustion is predominantly non-flaming, any products of incomplete combustion produced (namely carbon monoxide) are emitted to the atmosphere.

1.3 Pollutants and Adverse Effects

Nearly one hundred different compounds have been identified in biomass emissions (Andreae and Merlet, 2001). These emissions create complex and often negative impacts on the environment and human health. The main pollutants explored in this work (carbon dioxide, carbon monoxide, and particulate matter, such as soot) will be focused on in this discussion.

1.3.1 Carbon Dioxide

Emissions of carbon dioxide (CO_2) from cookstoves are both bad and good. Carbon dioxide is the most prominent anthropogenic climate forcing pollutant (U.S. EPA, 2012). It is detrimental because CO_2 in the atmosphere absorbs the earth's thermal-infrared radiation and emits it back to the surface, altering the earth's climate. In addition, CO_2 is a very stable molecule so once it is emitted to the atmosphere, it tends to remain there for a long time (on the order of 100 years) so the effects of individual emissions of CO_2 are long-lasting (McAllister et al., 2011e; Lackner et al., 2013).

While it is desirable to reduce the amount of CO_2 entering the atmosphere due to its radiative forcing potential and long lifespan, CO_2 is a product of complete combustion. It is therefore the best-case scenario from a combustion efficiency view. Also, in theory, because biomass is a carbon-neutral fuel, the complete combustion of biomass should add no net CO_2 to the environment (Lackner et al., 2013). Therefore, although CO_2 is a prominent greenhouse gas emission, it is a more desirable product than the other pollutants discussed in this section, which are indicators of reduced combustion efficiency and typically have a greater impact on the environment.

It is useful to note that CO_2 serves as the reference gas for a unit of measure, known as the global warming potential, that allows for the comparison of the impacts of different atmospheric trace gases. Although the estimated values are not perfect, the global warming potential (GWP) of a pollutant attempts to quantify the cumulative radiative forcing of that pollutant relative to CO_2 so comparisons can be made (Daniel and Solomon, 1998). Because it is the reference gas, the GWP of CO_2 is always equal to 1.

1.3.2 Carbon Monoxide

Carbon monoxide (CO) is a colorless, odorless, and tasteless gas that has an atmospheric lifetime of approximately $1-2$ months (Myhre et al., 2013; Bond et al., 2004b). It is a common pollutant from incomplete combustion, especially smoldering combustion (Ward and Radke, 1993; Koppmann et al., 2005). The oxidation of CO is significantly reduced if the temperature is less than 1100 K due to a lack of OH radicals in the combustion zone (McAllister et al., 2011e; Flagan and Seinfeld, 1988). Therefore, an increase in emitted CO can indicate an increase in the amount of the lower-temperature smoldering combustion versus flaming combustion (Ward and Radke, 1993). Additionally, high amounts of CO emissions can indicate flame quenching (discussed in Section 1.4) because CO will not be oxidized in localized areas of low temperature. Note, because charcoal combustion consists primarily of smoldering combustion, CO is an especially important pollutant to examine in charcoal cookstove emissions (such as those evaluated in Chapters 5 and 6).

Health Issues due to CO

Severe and abrupt health issues can arise with the inhalation of CO. In fact, acute CO poisoning accounts for more than 50% of the fatal poisonings reported in many industrial countries (Omaye, 2002). Carbon monoxide preferentially bonds to the iron in the hemoglobin in blood (forming carboxyhemoglobin) as compared to oxygen (Belcher, 2010; Lackner et al., 2013). Also, the bond of oxygen to the hemoglobin is relatively weak so the oxygen can be easily replenished in the hemoglobin; the CO bond, however, is 200 times stronger than the oxygen bond, making it harder to remove once in the blood stream (McAllister et al., 2011e; Belcher, 2010). Therefore, even low concentrations of CO can have a major impact on blood oxygen levels. A CO concentration of about 0.1% can convert 50% of the body's hemoglobin to carboxyhemoglobin (Tikuisis et al., 1992; McAllister et al., 2011e). Lesser concentrations of about $30-40$% carboxyhemoglobin will lead to impaired cognitive and motor functionality (Alma, 1993; Belcher, 2010). Onset of a comatose state occurs at 60% carboxyhemoglobin and 70% is fatal (Alma, 1993). Fortunately, acute CO poisoning is often easy to reverse if it is quickly caught by leaving the CO-enriched environment and breathing fresh air to restore blood oxygen levels (Belcher, 2010). Beyond the acute effects of CO, studies have found that chronic exposure to even low levels of CO can also have adverse affects on health, especially the cardiovascular system (Schmidt et al., 2012; Omaye, 2002; Reboul et al., 2012).

Environmental Issues due to CO

Although CO itself is a radiative forcing pollutant, the direct impact of atmospheric CO on the environment has been found to be relatively small (Sinha and Toumi, 1996). Instead, CO tends to indirectly cause adverse environmental issues by altering the concentrations of other important gases in the atmosphere, namely ozone, carbon dioxide, and methane. Emissions of CO lead to the production of tropospheric ozone if there is sufficient nitric oxide (NO) available; ozone is a radiative forcing gas which is undesirable in the troposphere (Daniel and Solomon, 1998; Myhre et al., 2013). Similar to the combustion reactions, CO in the atmosphere will react with OH radicals to form CO_2 (Myhre et al., 2013). The influence of CO on the concentrations of tropospheric ozone and CO_2 combined with its own direct radiative forcing potential give it an estimated GWP of approximately 10 for a 20-year span (i.e. an estimated ten-fold greater warming potential than CO_2) which drops to about 3 for a 100-year span (Bond et al., 2004b; Myhre et al., 2013).

While additional CO_2 in the atmosphere is not ideal because it is a climate-forcing pollutant, biomass should be a carbon-neutral fuel if it is harvested sustainably so the CO_2 created by the emitted CO has little net effect on the environment. Instead, the major issue with the conversion of CO to CO_2 in the atmosphere is its consumption of the OH radical. Another gaseous emission from anthropogenic and natural sources is methane. Atmospheric methane has an expected lifespan of 12 years with a GWP equal to $62-84$ for 20 years and $23-28$ for 100 years, which is of greater intensity than both CO_2 and CO (Bond et al., 2004b; Myhre et al., 2013). Similar to CO, methane is commonly reduced in the atmosphere through reactions with OH radicals (Myhre et al., 2013; Daniel and Solomon, 1998). Large amounts of CO in the atmosphere will decrease the available concentration of OH radicals and therefore inhibit methane reduction, allowing longer methane lifetimes in the atmosphere (Myhre et al., 2013; Daniel and Solomon, 1998).

1.3.3 Particulate Matter – Soot

Particulate matter (PM) is composed of any solid aerosol that is emitted from the fire. Biomass combustion produces many carbonaceous aerosols, consisting of black and organic carbons (Bond et al., 2004a; Chen and Bond, 2010). Studies have found that flaming combustion tends to produce black carbon particles, while smoldering combustion tends to produce a wide-variety of organic carbon particles (McMeeking et al., 2009; Andreae and Merlet, 2001; Yokelson et al., 1997; MacCarty et al., 2008; Chen and Bond, 2010). Biomass combustion is responsible for producing an estimated 30% of the global black carbon emissions (Bond et al., 2004a, 2013; Hansen and Nazarenko, 2004). Black carbon, or soot, is a complex particle that strongly absorbs visible light. This light-absorbing quality makes soot aerosols second only to CO_2 as an anthropogenic atmospheric warming pollutant, so it is greatly desired to reduce the black carbon emissions from cookstoves (Bond et al., 2013, 2004a; Hansen and Nazarenko, 2004). Thus, soot is a primary focus of this work on

wood-burning cookstoves and is discussed in greater detail than the other particulate matter emitted from cookstoves.

Soot Formation and Reduction

The formation of soot has been said to be one of the most complex chemical systems in a flame (McAllister et al., 2011e). As mentioned in Section 1.2.1, soot forms in fuel-rich portions of flaming combustion. Soot emissions are therefore more prominent in wood combustion and nearly non-existent in charcoal combustion (which can be seen in the results in Chapters 6 – 8). Bockhorn (1994) presents a thorough overview of soot formation; that work, along with McAllister et al. (2011e), Lackner et al. (2013), and Leipertz and Kiefer (2010), is used as reference for the brief discussion of soot formation and oxidation presented here.

1. Molecular Formation: Acetylene and aromatic rings (such as benzene) join to form polycyclic aromatic hydrocarbon (PAH) sheets (2-D) in hot, fuel-rich regions.
2. Nucleation: The PAH sheets stack to join soot nuclei (3-D) approximately 1 – 2 nm in diameter.
3. Surface Growth: Hydrocarbon gases readily attach to the soot surface, increasing particle size (3 – 100 nm). This is how the bulk of the solid particle material is formed.
4. Coagulation: Hot particles collide and fuse together. Coagulation increases particle size, like surface growth, but reduces the total number of particles. Note, surface growth and coagulation are often occurring at the same time.
5. Agglomeration: Outside of the hot regions of the flame, particles attach to one another, forming branching chains (>100 nm).

Soot can be reduced at any stage in this process by reacting with oxidants. The OH radical is the primary oxidant of soot in fuel-rich flames (Flagan and Seinfeld, 1988; Lackner et al., 2013). It is important to note that other species, such as CO and hydrogen, also react with OH and therefore can create a barrier to soot reduction. It is easiest to oxidize young soot; young soot is unorganized and contains approximately 10% hydrogen, making it very reactive. As soot travels through the flame, it becomes more structured and loses its hydrogen content, making it less reactive and harder to reduce. Reducing soot formation early in the flame while the soot particles are young and reactive might appear prudent. However, the luminescing soot in the flame increases the radiative heat output (Lackner et al., 2013). This increases the temperature in the combustion zone, promoting gaseous reactions; increases the temperature of the char, promoting surface reactions; and increases the heat being added to the cooking pot, improving thermal efficiency. Therefore, although emitted soot is an undesirable pollutant, in-situ soot, or soot within the flame zone, is desirable for thermal and combustion efficiency gains.

Environmental Issues from Particulate Matter

Particles released to the atmosphere have a complex relationship with the earth's hydrological cycle, playing important roles in cloud condensation, ice nucleation, surface albedo, and surface temperature (Ramanathan et al., 2001; Ban-Weiss et al., 2012; Hansen and Nazarenko, 2004). The varying composition of the aerosols emitted creates this complexity, which is one of the largest uncertainties in radiative climate forcing estimates (Chen and Bond, 2010). Black carbon particles are highly-absorbing with an estimated GWP of approximately 2000 on a 20-year timeline (Bond et al., 2013, 2004b; Hansen and Nazarenko, 2004). On the other hand, organic carbons range in color (typically yellows or browns) and are often light-scattering; organic carbon is estimated to have a GWP of approximately -250 for a 20-year timeline, which means it is climate cooling (Bond et al., 2004b; Chen and Bond, 2010). Therefore, the radiative forcing from biomass combustion aerosols is heavily dependent on the ratio of warming black carbon to (generally) cooling organic carbon. While it is estimated that biomass burning produces about $6-8$ times as much organic carbon as black carbon, the exact ratio of black carbon to organic carbon, as well as the composition of the organic carbon, is affected by factors such as wood size and pyrolysis temperature, making the radiative forcing effect of aerosols unique for each combustion event (Chen and Bond, 2010; Bond et al., 2004a; Andreae and Merlet, 2001; Liousse et al., 1996; Just et al., 2013).

Black carbon emissions are a major influence on anthropogenic climate change (Bond et al., 2004a, 2013; Hansen and Nazarenko, 2004; U.S. EPA, 2012). Soot has a short atmospheric lifetime of about a week, so the effects of the emissions tend to be prominent near the source, reducing atmospheric transparency and visibility (Hansen and Nazarenko, 2004; Bond et al., 2004b). In the heavy biomass-burning areas of India and China, models estimate agricultural productivity is decreased by $10-20\%$ due to atmospheric soot (Chameides et al., 1999; Bergin et al., 2001). Black carbon is very stable in the atmosphere, so its primary removal method is through deposition to a surface (Bond et al., 2013; U.S. EPA, 2012). The deposition of black carbon reduces the reflectivity (i.e. albedo) of a surface, although this has little impact on most landscapes, which are relatively dark. The deposition becomes an issue when it affects highly reflective surfaces such as ice and snow, which reduces the cooling effect of those materials and leads to increased melting of snow (Hadley and Kirchstetter, 2012; Bond et al., 2013; U.S. EPA, 2012; Hansen and Nazarenko, 2004). While black carbon has an extremely high GWP for a 20-year timeline, it has a very short aerosol lifetime; if soot emissions were reduced today, impacts should be apparent in a few decades, whereas effects due to reduced CO_2 would take centuries. Soot mitigation has therefore grown as a potential top-priority method to address climate change in the short-term (USAID, 2010; UNEP, 2011; Gustafsson et al., 2009; Shindell et al., 2012; Wallack and Ramanathan, 2009; Ramanathan and Carmichael, 2008; U.S. EPA, 2012). Because biomass combustion produces approximately 30% of the global black carbon emissions, one of the most important opportunities for black carbon reduction stems from residential biomass cookstoves (Bond et al., 2004a; U.S. EPA, 2012).

Health Issues from Particulate Matter

Combustion aerosol particles of concern are commonly divided into three groups based on how deeply they can deposit in the human respiratory system and classified based on their aerodynamic diameter: Coarse (2.5 – 10 μm), Fine (0.1 – 2.5 μm), and Ultrafine (<100 nm). In regulation, these particles are often referred to as PM_{10} (all particles less than 10 μm), $PM_{2.5}$ (all particles less than 2.5 μm), and ultrafine particles (UFP) (all particles less than 100 nm). Multiple review papers, such as Anderson et al. (2012), Englert (2004), Mannucci et al. (2015), Brook et al. (2010), Donaldson and MacNee (1998), Adar et al. (2014), and Valavanidis et al. (2008) discuss the health effects related to particulate matter (PM), of which a summary is discussed here. Fine and ultrafine particles are formed through combustion processes but coarse particles tend to be generated instead by processes such as mechanical grinding. Therefore, fine and ultrafine particles are the focus of this discussion.

Although many atmospheric pollutants are harmful for human health, especially severe effects have been accredited to PM. All particles classified as PM_{10} are considered to be highly toxic. Particles become more dangerous with decreasing size as they may deposit deeper in the respiratory system. Guidelines for ambient PM concentrations outlined by the World Health Organization (WHO) have recommended exposure to no more than 10 $\mu g/m^3$ annually or 25 $\mu g/m^3$ in 24 hours for $PM_{2.5}$, because both short and long term exposure have been found to adversely impact health (World Health Organization (WHO), 2006b). To put the impact of $PM_{2.5}$ into perspective, it has been estimated that a 10 $\mu g/m^3$ increase in short-term $PM_{2.5}$ exposure (24 hour average) increases the relative risk for triggering cardiovascular mortality by approximately 0.4 – 1% and a 10 $\mu g/m^3$ increase in long-term $PM_{2.5}$ exposure increases the risk by about 1.06 – 1.76% (Brook et al., 2010). In fact, some studies have indicated there is no safe threshold for $PM_{2.5}$ even with the recommended guidelines, and no recommended guidelines even exist for safe UFP concentrations.

$PM_{2.5}$ has a pronounced impact on cardiovascular health. Many studies show an increased risk of ischemic heart disease, myocardial infarction, arrhythmia, and heart failure due to $PM_{2.5}$ exposure, as well as cerebrovascular conditions, such as strokes. Unsurprisingly, $PM_{2.5}$ also greatly effects the respiratory system, increasing the likelihood of asthma, chronic obstructive pulmonary disease (COPD), reduced lung function, and lung cancer. However, studies also suggest that decreasing $PM_{2.5}$ exposure will decrease the heightened cardiovascular risks within a relatively short time frame (about a few years). Therefore, reducing $PM_{2.5}$ emissions could have a quick, positive impact on human health. Beyond $PM_{2.5}$, it has tentatively been found that UFPs have an even greater toxicity than fine and coarse particles (Englert, 2004; Brook et al., 2010; MacNee and Donaldson, 2003). Although soot and its precursors (PAHs) are carcinogenic, the toxicity of UFPs appears to be due to the increased surface area per particle rather than composition with even benign particles found to be toxic at ultrafine sizes (McAllister et al., 2011e; Oberdörster et al., 2005; Donaldson et al., 2002; Li et al., 1996). A greater surface area allows UFPs to be more biologically active and have higher deposition efficiencies than large particles, reaching almost 50% efficiency for 20 nm particles (Donaldson and MacNee, 1998; Oberdörster et al., 2005; Peters et al.,

1997). Also due to their small size, UFPs can translocate readily to the cardiovascular, lymphatic, and even central nervous systems, causing a wide variety of serious human health issues that are well summarized by Oberdörster et al. (2005), Chen et al. (2016), Zlotkowska (2016), and Donaldson and MacNee (1998).

1.4 Air Flow Manipulation

Although theoretically only enough air is required to stoichiometrically mix with fuel for complete combustion, in a realistic cookstove system, only part of the entrained air in the combustion chamber will be close enough to interact with the fuel while the rest will pass through undisturbed (Regional Wood Energy Development Programme in Asia, 1993). Therefore, excess air is often desired in biomass combustion systems to increase the probability of producing stoichiometric air and fuel mixtures (Beauchemin and Tampier, 2008; Regional Wood Energy Development Programme in Asia, 1993). However, even with plentiful air supplies in the combustion chamber, the combustion efficiency can be poor because the general availability of air is not the only requirement for complete combustion. It is known from chemical kinetics that reactions require that: 1. The fuel and oxidizer must be mixed on a molecular level; 2. The temperature must be high enough to add the energy necessary to break apart or form molecules; and 3. The first two conditions must occur for a long enough time to allow the reaction to happen (McAllister et al., 2011e; Keating, 2007; Nussbaumer, 2003). If any one of the three conditions is not met, then the combustion ends up being incomplete. This is because the rate of a reaction is dependent on the local temperature and the concentrations of the reactants. If either the temperature or the concentrations are too low, the reaction rate will be slow. The reaction rate is inversely proportional to the chemical time, or the time necessary for the reaction to proceed to completion. However, in a real system, the first two conditions are only met for a finite amount of time, which is known as the residence time. In essence, the chemical time is the amount of time the reaction needs in order to combust completely and the residence time is the amount of time the reaction actually has. If the chemical time is longer than the residence time, the reaction will take too long and will cease prior to completion, emitting products of incomplete combustion. Therefore, these three items (local mixture composition, local temperature, and residence time) are the main factors affecting and driving the completeness of combustion and pollutant emissions. Note, many combustion textbooks and journal articles discuss chemical kinetics in great detail to which the interested reader may refer; the brief summary included in this paragraph referenced McAllister et al. (2011b) unless otherwise noted.

Manipulating the air flow in a stove can impact all three parameters of complete combustion and can therefore be a powerful and beneficial modification for controlling emissions in biomass stoves. However, with a discussion on air manipulation, especially air-induced turbulent mixing, it is important to highlight the potential for local extinction of the flames due to quenching and flame stretch. The reaction rate is highly sensitive to

temperature, which is often maintained by the large amount of heat released from exothermic reactions in the flame (McAllister et al., 2011b; Shelton, 1983). When a flame is close enough to a cool, conducting surface, it begins losing heat to the material and also potentially losing available radicals due to surface reactions (Warnatz et al., 2006). If the flame loses too much heat and the temperature drops below the ignition threshold of the reactions, the sustained combustion processes cease and the flame is quenched (Shelton, 1983; McAllister et al., 2011c). This abrupt end of the combustion processes releases many products of incomplete combustion, such as CO and soot (Lackner et al., 2013). However, sometimes quenching is desirable. A flame arrestor, like that used in Section 8.2, is a common combustion safety device which operates via quenching; the mesh of conductive wires extracts heat and quenches radicals at the surface, extinguishing undesired combustion processes (Lackner et al., 2013). In addition to quenching, local extinction can occur if the local turbulence intensity is too high. Increasing turbulence increases velocity fluctuations in the flames, which in turn produces large velocity gradients or strain rates (Shaw, 1993). Large strain rates can cause local extinction and allow intermediate reactants to leak out of the flame into the environment (Warnatz et al., 2006; Shaw, 1993; McAllister et al., 2011e).

This dissertation focuses on some current applications of air flow modifications in charcoal- and wood-burning stoves and aims to develop a better understanding of the benefits and risks of those modifications to assist stove designers, manufacturers, and distributors in the field. The specific designs evaluated in this work are improved charcoal cookstoves for Haiti, an ignition aid for the traditional Haitian cookstove, and air-induced turbulent mixing strategies in a wood-burning stove.

1.4.1 Modifications for Charcoal Stoves

As mentioned in Section 1.2.1, the reaction rate for smoldering combustion is often limited by the rate of oxygen reaching the surface of the fuel (Ohlemiller, 2002, 1985; Rein, 2009). Charcoal combustion is predominantly smoldering combustion, so similarly, the availability of oxidizers at the surface of the charcoal bed is often the limiting factor for a charcoal stove. Many traditional charcoal stoves have shallow and wide perforated combustion chambers, providing a large area exposed to ambient air (Bentson et al., 2013). Although excess air is desirable to a point, too much exposure to cooler air can increase heat losses to the environment and reduce the temperature of the charcoal bed. Controlling the air flow through a charcoal stove allows a better balance between promoting air entrainment near the surface of the charcoal while reducing unnecessary air and heat losses to the environment. Some modifications, seen in the improved charcoal stoves evaluated in Chapter 5 and other works, include a more enclosed combustion chamber, a door used to partially regulate the amount of entrained air, and a raised grate for the charcoal bed so air can be entrained from underneath and rise through the charcoal bed, promoting interactions at the surface (Bhattacharya et al., 2002a; Kshirsagar and Kalamkar, 2014; MacCarty et al., 2008; Jetter et al., 2012). Chapter 5 explores how stoves with these modifications compare with a traditional open charcoal stove.

Combustion in traditional charcoal stoves especially struggles during the initial ignition stages. The reaction rate for charcoal is limited by the rate of oxygen reaching the surface of the fuel and the shallow combustion chamber of the traditional stove and cold charcoal bed do not produce much draft to supply fresh air to the surface. Therefore, it can be difficult to achieve stoichiometric mixtures at the surface of the charcoal, leading to a slow ignition stage. Also, although charcoal combustion produces less particulate matter than wood stoves, most of the PM that is emitted from a charcoal stove is produced during this initial ignition period (Jetter et al., 2012). Therefore, efficiency gains in this cooking stage can have a big impact on the total amount of PM emitted from the charcoal combustion as well as convenience and time-savings for the end users. The work in Chapter 6 focuses on this ignition stage to see if an air flow modification could help reduce the time needed for ignition and reduce the harmful pollutants emitted. A dominant commercial air flow modification for charcoal ignition is the charcoal chimney starter. Chimney starters work by sheltering the charcoal from the wind and inducing a draft through the charcoal within, maximizing the amount of oxygen reaching the surface of the charcoal while protecting it from heat losses. The lighting cone air flow modification, evaluated in Chapter 6, operates on the same idea, temporarily increasing the draft through the stove to promote greater interaction of air at the surface of the charcoal bed during ignition, but is simpler in design and potentially less expensive than a commercial chimney starter as well as being easy to build locally and readily scalable for the intended stove. More detail may be found in Chapter 6.

1.4.2 Modifications for Wood Stoves

As mentioned in Section 1.3, biomass combustion can emit large amounts of undesirable pollutants. Increased turbulent mixing created by secondary air injection, an emissions reduction method commonly seen in industrial biomass combustion systems, is being explored as a possible option for biomass cookstoves and is the focus of Chapters 7 – 9.

Out of the three parameters for pollutant production (temperature, turbulence, and time), turbulence is often the most difficult to achieve for biomass furnaces and boilers (Nussbaumer, 2003). Many industrial wood combustion systems, such as grate-fired boilers, employ turbulent mixing along with a carefully regulated primary air supply in a two-stage combustion system to reduce emissions and increase combustion efficiency (Yin et al., 2008; Nussbaumer, 2003; Obernberger, 1998; Suri and Horio, 2010). In two-stage combustion, only part of the air necessary for combustion is introduced by the solid wood fuel in the primary combustion zone, so a fuel-rich mixture of volatile gases and unburnt fuel is left (Yin et al., 2008; Bolhàr-Nordenkampf, 2010). As those volatiles continue downstream, additional (secondary) air is introduced in or just prior to a second combustion chamber to form an ideally stoichiometric mixture before a second burnout completes the combustion. This secondary burnout allows the fuel to be combusted in a partially-premixed or premixed flame (unlike the nonpremixed flame of typical wood combustion), so if this method is well executed, the majority of soot and other pollutants should oxidize prior to emission (Flagan and Seinfeld, 1988). It is important, therefore, that the secondary air injection design is

optimized for thorough mixing. Along with the staged combustion, advanced secondary air systems are designed to produce strong recirculation zones and increase turbulence to promote mixing and lengthen residence time in the combustion zone (Yin et al., 2008; Obernberger, 1998). Some suggested design parameters include high injection velocities to increase secondary air penetration, which allows mixing in the center of the fuel-rich flow as well as near the walls; staggered opposing secondary air jets to increase turbulence; and tangential air injection to produce swirling flow, which can recirculate gases through the reaction zone and increase residence time (Suri and Horio, 2010; Flagan and Seinfeld, 1988; Obernberger, 1998; Yin et al., 2008).

Historically, the majority of biomass cookstoves did not have air injection systems; the power for fan-driven injection required either electricity, which would often be expensive or unreliable, if even available, or batteries (Kshirsagar and Kalamkar, 2014; Sutar et al., 2015; Kumar et al., 2013; Raman et al., 2013). To overcome this barrier, many researchers are evaluating the potential of using thermal-electric generators (TEGs) in the stoves to provide power using waste heat from combustion (Gao et al., 2016; O'Shaughnessy et al., 2015; Champier et al., 2011, 2010; Mal et al., 2015; Lertsatitthanakorn, 2007). These developments are opening the door for implementing air flow modifications in residential biomass cookstoves, even those intended for areas with limited power grids.

In unmodified wood combustion, the nonpremixed flames contain large eddies of soot and gaseous fuel. Even if there is excess air surrounding these eddies, there are no oxidants within the eddies to react with the fuel contained there. Instead, combustion reactions only occur on the boundaries of the flame where stoichiometric amounts of fuel and oxygen can be mixed on a molecular level. Increased turbulent mixing in the system can help achieve suitable, local mixture compositions by making flow patterns irregular, chaotic, and fluctuating (Burluka, 2010; Merci et al., 2010; Flagan and Seinfeld, 1988). Turbulent mixing changes the large fuel-rich eddies of nonpremixed flames into smaller eddies, increasing the flame surface area and boundaries where stoichiometric conditions can occur (Lobert and Warnatz, 1993; McAllister et al., 2011a). Like the secondary air jets used in industrial combustion systems, correctly placed air introduction could increase residence time, recirculate gases through the combustion zone, and improve mixing in biomass cookstoves. Indeed, studies of cookstoves with increased turbulence due to air injection have shown the potential for reductions in particulate matter, including side-fed natural draft stoves like those discussed in Section 2.1.2 (MacCarty et al., 2010; Sutar et al., 2015; Jetter et al., 2012; Rapp et al., 2016; Still et al., 2015). However, the air injection can have negative effects such as cooling the combustion zone, decreasing stove performance at low powers, and increasing ultrafine particle emissions (Shelton, 1983; Rapp et al., 2016; Jetter et al., 2012).

The work discussed in Chapters 7 – 9 focuses on two parameters of the air-induced turbulent mixing (injection angle and velocity) using a side-fed, natural draft stove. As seen previously with the industrial boilers, the velocity of the jets is important for thorough mixing through the combustion area; however, high velocities will increase the strain rate of the flames and potentially extinguish them. Additionally, the air injection angle will have a great impact on the efficacy of the air injection at producing desirable turbulent mixing

characteristics, such as recirculation and swirl, while avoiding undesirable traits such as quenching. This work aims to identify optimal values and trends for these parameters to aid in the design of future air-induced turbulent mixing systems in side-fed, natural draft stoves.

1.5 Dissertation Layout

This dissertation consists of 10 chapters discussing four experimental layouts pertaining to biomass cookstoves and air flow manipulations in these systems. Chapters 2 – 4 serve as reference chapters for the experimental results of Chapters 5 – 9. Equipment used for this work is described in Chapter 2, including the biomass stoves, burners, and individual instruments. Chapter 3 presents descriptions of some of the techniques and experimental setups used in the work. Chapter 4 details the more extensive protocols used in this work as well as details of the data analysis including how the metrics for stove evaluation were calculated and the data processing steps for the OH-LIF and LII images collected in Chapter 9.

Chapters 5 and 6 explore Haitian charcoal cookstoves. In Chapter 5, a case-study comparing the traditional Haitian cookstove with proposed improved cookstoves is presented. The performance and emissions of each stove were evaluated to provide information to stove disseminators and designers in Haiti. Experience with the Haitian stoves led to a desire to examine an air flow modification to improve ignition efficiency of charcoal stoves – a lighting cone. Although lighting cones were in use throughout the world prior to this work, no scientific results on their performance existed in the literature. Chapter 6 presents an evaluation of the lighting cone and the impact this air flow modification has on the performance and emissions of a traditional Haitian cookstove during ignition.

Inspired by the impact air flow modifications can have on the performance and emissions of a cookstove, Chapter 7 explores secondary air injection into a wood-burning cookstove. Different turbulence-inducing mixing strategies were assessed to explore the impact of air flow rate and injection angle on performance and emissions in the cookstove. Along with the ex-situ measurements taken in Chapter 7, in-situ measurements were recorded in Chapters 8 and 9 to gain a deeper understanding of how the mixing strategies were affecting the flame zone. Finally, Chapter 10 summarizes the results and proposes future work.

2 Experimental Equipment

A summary of the equipment used for this work is presented in this chapter.

2.1 Stoves and Burners

Several different stoves and burners were utilized throughout the different stages of this work. The choice of burner was dependent on the type of fuel required for the test, cultural needs, or other desired outputs, such as calibration.

2.1.1 Charcoal-Burning Stoves

The work in Chapters 5 and 6 revolved around cooking in Haiti, where the predominant urban fuel is charcoal (Nexant Inc, 2010). Photographs of the charcoal-burning stoves are shown in Fig. 2.1.

Traditional Haitian Stove

Haitians traditionally use simple stoves made locally from scrap sheet metal. These stoves are widely available and typically have a square or circular charcoal chamber. The stove tested in this study has a square chamber (110 × 110 mm) with evenly-distributed holes along the sides and bottom. It is 270 mm high and weighs 2.8 kg. The pot sits directly on the charcoal bed, and the ash falls through to a tray underneath which can be emptied by turning the stove over.

EcoRecho Stove

The EcoRecho is a metal stove with a ceramic liner made in Haiti by D&E Green Enterprises. The pot sits above a hemispherical charcoal chamber on three triangular metal rod supports. It is 220 mm tall, weighs 6.2 kg, and has a diameter of 275 mm. A door on the front of the stove can be operated to control air flow and remove ash.

(a) Traditional Haitian stove

(b) EcoRecho stove

(c) Mirak stove copy

(d) Prakti Rouj stove

Figure 2.1: Photographs of charcoal cookstoves used for Haitian stove comparison tests.

Mirak Stove (copy)

The Mirak stove copy is a locally-made, scrap metal stove copied from the Mirak stove designed by the humanitarian agency CARE. It is widely available in Port-au-Prince. The charcoal chamber is hemispherical, and the pot sits directly on the charcoal bed. The Mirak is 320 mm tall, weighs 2.8 kg, and has a diameter of 305 mm. An opening in the side of the stove allows air flow, but there is no door for air flow control. The charcoal chamber rests on top of the stove body and can be removed to dump out the ashes.

Prakti Rouj Stove

The Prakti Rouj is a ceramic-insulated metal stove with a small circular charcoal chamber (255 mm diameter). It is 205 mm tall and weighs 4.6 kg. The pot sits on raised metal wedges above the charcoal bed and a door on the front of the stove can be adjusted to control air flow. A tray can be removed through the door to empty ash.

2.1.2 Wood-Burning Stoves

Wood is used as a cooking fuel in households worldwide. The common traditional method is an open three-stone fire. An improved, wood-burning stove, the Berkeley-Darfur stove, was used as the base design for the air injection modifications explored in Chapter 7. It was chosen because it includes design elements, such as a metal combustion chamber and raised grate, that are common to stoves in many regions around the world (Jetter and Kariher, 2009; Jetter et al., 2012) and therefore the results could be relevant for a wide range of wood-burning stoves.

Three-Stone Fire (TSF)

A three-stone fire (TSF) is an arrangement of three stones that supports a pot over an open fire (see Fig. 2.2a). It is a commonly-used, traditional cooking style (Jetter and Kariher, 2009; Galitsky et al., 2006). A TSF often has poor thermal efficiency due to large heat losses to the environment and poor combustion efficiency due to inadequate mixing of the air and fuel, but it is no cost, easy to build, and easy to move so is a popular method of cooking.

The TSF used in Chapter 7 was made of three stones (approximately 500 mm wide) spaced such that the bottom of the pot would rest approximately 100 mm above the ground. The fire was tended by feeding wood through the spaces between the stones, attempting to keep all fuel in the center of the circle under the pot.

Berkeley-Darfur Stove (BDS)

The Berkeley-Darfur Stove (BDS) is a wood-burning cookstove developed at LBNL for internally displaced persons in Darfur, Sudan (Amrose et al., 2008). Built to reduce the amount of wood needed for cooking as compared to the TSF, the BDS is an enclosed metal stove that increases thermal efficiency and decreases fuel consumption by using a raised grate under the fuel bed to promote air flow through the combustion chamber and using a low emissivity stainless steel firebox and tapered wind collar to focus heat towards the pot. The design was originally based on a Tara Stove from India and modified to be durable, low cost, and culturally-acceptable (Amrose et al., 2008). It is a proven fuel-efficient, natural-convection stove (Kirchstetter et al., 2010; Jetter et al., 2012; Preble et al., 2014).

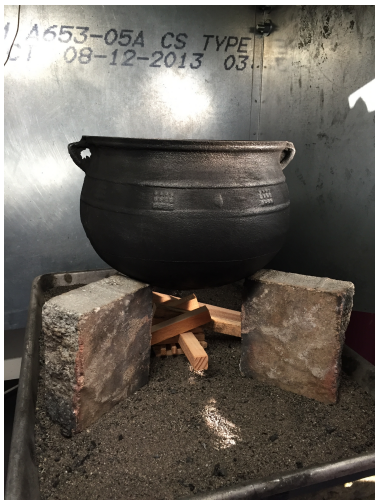

(a) Three-Stone Fire

(b) Berkeley-Darfur Stove

(c) Halo Stove

Figure 2.2: Three wood-burning stoves used for this work: (a) Three-Stone Fire: a traditional cooking method throughout the world; (b) Berkeley-Darfur Stove: an improved cookstove; (c) Halo Stove: a modified version of the BDS which includes secondary air injection.

Halo Stove

The Halo Stove is a modified version of the Berkeley-Darfur Stove. In addition to the main BDS body, the Halo Stove has a copper annulus (i.e. a halo) mounted above the combustion chamber. The purpose of the halo is to inject air into the flames to achieve benefits such as reduced soot emissions. It is bent like a shepherd's crook, such that a nearly complete torus sits above the fire with a tail that mounts through the stove wall and attaches to a compressed air supply (see Fig. 2.2c). A variety of halos were tested in this work, described in Chapter 7. No other alterations were made when modifying the BDS.

2.1.3 Gas Burners

For the laser diagnostic experiments discussed in Chapter 9, three gaseous burners were used, each serving a different purpose.

Proxy Cookstove Burner

The proxy cookstove burner (PCB) is a trident-like pipe burner which was developed as a proxy for the Halo Stove; its development and role are discussed in Chapter 8. The PCB consists of three parallel, horizontal 1/2" stainless steel pipes (21 mm outer diameter and 254 mm length) spaced 19 mm apart; the pipes were mounted to a cross, using elbows as appropriate (as shown in Fig. 2.3). Nine 3.76 mm holes were drilled in each pipe situated such

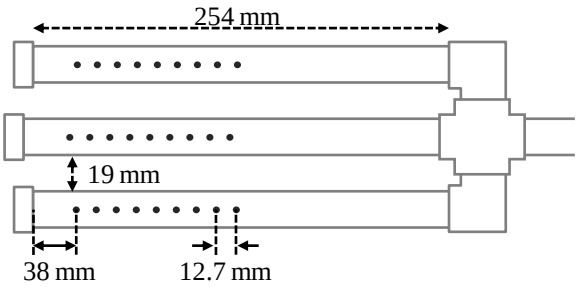

Figure 2.3: Schematic of proxy cookstove burner (PCB). The parallel burner pipes are 21 mm diameter stainless steel with 3.76 mm diameter holes and are mounted to a cross and elbows. Fuel enters the burner from the right of the image and is controlled by a mass flow controller.

that the multiple small flames could interact, similar to a wood fire. Liquefied petroleum gas (LPG) was combusted in nonpremixed flames with the flow of fuel regulated by an Alicat mass flow controller.

Flat-Flame Burner

The flat-flame burner (pictured in Fig. 2.4a) was used for calibrating the laser-induced incandescence experiments conducted in Section 9.3. This type of burner produces a uniform, premixed flame front, making it well-suited for laser measurement calibration (Hartung et al., 2006; Prucker et al., 1994).

The flat-flame burner used in Section 9.3 consists of a 50 mm square face, operating with a premixed ethylene and air mixture (2 L/min of ethylene, 10 L/min of air). To further ensure a stable, uniform flame, a 200 × 200 mm square of 1 mm-thick stainless steel was mounted 35 mm above the flat-flame burner to act as a stabilization plate.

Slot Burner

A slot burner was used as a reference flame for the OH-LIF experiments described in Section 9.3. It is a rectangular burner (pictured in Fig. 2.4b) consisting of three parallel slots with a rectangular chimney above. The middle slot measures 6.5 mm × 26 mm × 120 mm and produces a low velocity (∼3.04 L/min), partially-premixed flame of natural gas and air (mole fractions are approximately 33% natural gas, 14% oxygen, and 53% nitrogen). The two outer slots each measure 11 mm × 26 mm × 120 mm and produce low velocity (∼5.16 L/min) air sheets that are intended to keep the central flame straight, laminar, and uniform. Additionally, a perforated plate is mounted in the chimney to promote a uniform, laminar flame.

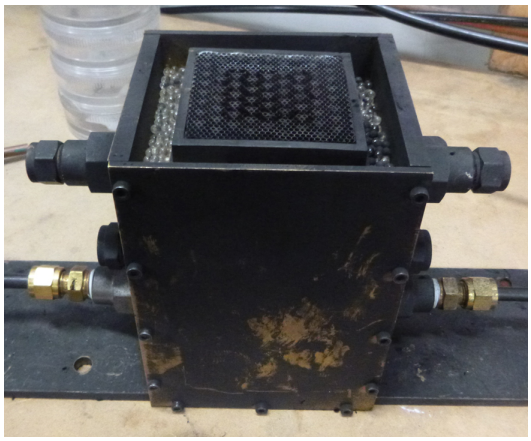

(a) Flat-Flame Burner

(b) Slot Burner

Figure 2.4: Two gaseous calibration burners were used for the laser experiments conducted in Section 9.3. The flat-flame burner (a) was used to calibrate LII and the slot burner (b) was used as a reference flame for OH-LIF.

2.2 Aerosol Instrumentation

For experiments conducted in Chapters 5 – 8, a variety of aerosol equipment was used to measure emissions.

2.2.1 NDIR Gas Analyzer

The gaseous emissions, CO and CO_2, concentrations were measured using a non-dispersive infrared (NDIR) analyzer. In an NDIR analyzer, the gas to be measured passes through a tube containing an infrared lamp, absorbing some of the infrared light at a particular wavelength. A detector in the tube then measures the remaining light and provides a volumetric concentration of the gas in the sample. Each tube is designed for a specific wavelength of light and therefore, a specific gas.

This work used a California Analytical Instruments (CAI) 600-series NDIR gas analyzer to measure the concentrations of CO and CO_2 emitted. An undiluted sample was taken from the exhaust duct, passed through a copper cooling tube and a HEPA filter to reduce the temperature and remove particulates, and then measured by the gas analyzer. All channels of the CAI analyzer were calibrated daily; pure nitrogen was used for a zero gas and the span gases were 5000 ppm CO_2 in N_2 and 350 ppm CO in N_2.

2.2.2 Aethalometer

In an aethalometer, the sample is drawn through a quartz filter, depositing particles; the change in light attenuation ($\lambda = 880$ nm and 370 nm) through the filter is continuously measured to determine the concentration of black carbon in the sample (Hansen et al., 1984; Hansen, 2005).

The aethalometer used in this work was a two wavelength McGee Scientific Rack Mount Aethalometer® (Model AE22). The quartz filter tape was manually advanced between tests to avoid lost data due to the time required for auto-advancing (approximately 30 seconds).

2.2.3 DustTrak Aerosol Monitor

A handheld DustTrak DRX (Model 8534) was used to measure real-time $PM_{2.5}$. A DustTrak uses light scattering to measure the mass concentration of $PM_{2.5}$ in a sample. The instrument is commonly used among cookstove researchers around the world (Leavey et al., 2015; Chowdhury et al., 2012; Masekameni et al., 2015; Preble et al., 2014).

It is important to note, however, that the light scattering is dependent on the properties of the particles, such as shape and refractive index (Arku et al., 2008). As the DustTrak is calibrated with A1 Arizona ultrafine test dust (ISO 12103-1), which is potentially very different from the particulate matter in cookstove emissions, it is helpful to calibrate the DustTrak measurements using an integrated particle mass system, described in Section 3.1.2, to reduce potential measurement error.

2.2.4 Particle Sizers: APS, OPS, and FMPS

Three TSI aerosol particle sizers were used to accurately measure particle size distribution from 5 nm to 20 µm, all at a high temporal resolution of 1 second.

An Aerodynamic Particle Sizer (APS) (Model 3321) was used to detect particles from 0.5 – 20 µm using light-scattering intensity. Another optically-based instrument, an Optical Particle Sizer (OPS) Spectrometer (Model 3330), was used to measure particles from 0.3 – 10 µm. However, optical techniques are ineffective in the smallest desired particle range because the particles are smaller than the light wavelength. Therefore, a Fast Mobility Particle Sizer (FMPS) Spectrometer (Model 3091) was used to detect the smallest particles. An FMPS uses an electrical mobility technique with multiple electrometers to detect particles ranging from 5.6 – 560 nm.

2.3 Lasers

Several different lasers were necessary for this work, specifically for evaluating the gaseous burners. Laser diagnostic techniques allow measurements within the flame zone, unlike aerosol equipment.

2.3.1 Nd:YAG Lasers

A pulsed neodymium-doped yttrium aluminum garnet (Nd:YAG) laser is a solid-state laser where Nd:YAG is the specific crystal used as the lasing medium. Nd:YAGs are one of the most common and reliable scientific lasers and are often used to produce a 1064 nm beam or are frequency-doubled to produce a 532 nm beam (Raffel et al., 2007). The two Nd:YAG lasers used for this work were pulsed in a Q-switch mode, meaning an optical switch depopulates the laser medium at maximum population inversion allowing a higher possible maximum power (Raffel et al., 2007).

Q-Smart

The Quantel Q-smart 850 is a pulsed, single-head Nd:YAG laser. It was used to produce a 1064 nm laser beam at a 10 Hz repetition rate for use in the laser-induced incandescence (LII) experiments described in Section 9.3.

BrilliantB Twins

The Quantel BrilliantB Twins is a Q-switched, double-headed Nd:YAG laser. For this work, the 1064 nm beam was frequency-doubled, generating a 532 nm output, at a 10 Hz repetition rate. The master head was used for experiments in Section 9.3 and both heads were used for experiments in Section 9.2.

2.3.2 Dye Laser

A dye laser uses an organic dye as the lasing medium which allows the laser to be easily tunable to a wide range of wavelengths. The dye laser used in Section 9.3 was a ScanMate 2E manufactured by Lambda-Physik with the master head of the BrilliantB Nd:YAG operating at 532 nm used as its pump source. Rhodamine 6G dye was used to produce a 566.4 nm beam which was then frequency-doubled using a Lambda-Physik FL37.1 crystal to produce an approximately 283 nm laser beam (measured to be 283.2 nm in this work). A four-element Pellin-Broca array separated the 283 nm wavelength from the lasing wavelength before it entered the optical system.

2.4 Particle Seeders

Two particle seeders were designed for the PIV experiments discussed in Section 9.2, which had to overcome the specific challenges of the system, namely low flow rates and an unenclosed system. Seed particles for both seeders were 0.2 μm titanium dioxide (TiO_2).

2.4.1 Cyclone Seeder

A cyclone-type seeder, shown in Fig. 2.5, was developed to seed the air injected through the halo. The design was based off of criteria from Glass and Kennedy (1977) and Kalathoor (2013) as well as several rounds of prototyping to achieve the correct angles and diameters for tubing.

The seeder was constructed from a 50 mm PVC pipe with air-tight but removable end caps for refilling. A 1/4" stainless steel pipe with a 90° bend was used to inject air at a tangential angle along the inner edge of the seeder body. This injected air was intended to entrain seed particles and then form a vortex along the centerline of the seeder body where the flow exited the seeder via a 1/2" stainless steel pipe and continued to the system. The distance between the seeder and halo was minimized to avoid excessive particle loss along the tubing.

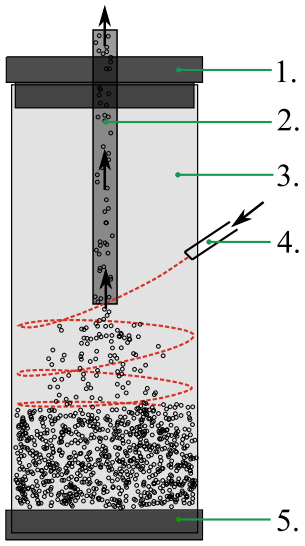

Figure 2.5: Schematic of cyclone particle seeder: 1. Threaded cap (for refilling particles), 2. 1/2" stainless steel pipe, 3. 50 mm PVC pipe, 4. 1/4" stainless steel pipe, 5. End cap. Air enters the system through the 1/4" pipe on the right, entraining particles and forming a vortex which exits through the 1/2" pipe in the center of the seeder.

2.4.2 Sieve Seeder

A sieve-based seeder was designed to seed the experimental area by vibrating the seeder over the measurement zone and introducing particles via gravity. The seeder, shown in Fig. 2.6, was constructed from a 275 mm diameter stainless steel pipe that was 100 mm in length. Stainless steel perforated plate was welded to one side of the pipe to form the bottom of the seeder and a much finer (0.5 – 1 mm) titanium mesh was inserted on top of

Figure 2.6: Picture of the sieve particle seeder without lid and fine mesh insert. The seeder was mounted using L-brackets to identical lever arms. The seeder could then be vibrated above the measurement region to introduce particles.

the perforated plate inside of the pipe to produce the sieve. This fine mesh overlay could easily be cleaned or replaced as needed. In addition to the mesh, flint clay (variable diameter, $d \approx 8$ mm) was added in the seeder to vibrate among the particles and mechanically break up agglomerates. A metal lid was added to prevent particles from exiting upwards. The seeder was mounted on either side to the ends of identical lever arms; three vibrating elements from Aura Interactors were loosely affixed at the other end of the lever arms to shake the sieve and therefore introduce the particles into the system. The shakers were operated by a GW Instek Function Generator which produced an internally-controlled 40.4 Hz square wave amplified by a Response High Power Mosfet Car Amplifier.

2.5 Other Instrumentation

2.5.1 Wood Moisture Meter

A Delmhorst J-2000 wood moisture meter was used for estimating the moisture content of wood used for each test. It can measure a range of moisture contents ($6-40\%$ with 0.1% resolution) via two prong resistance measurements and can be custom-set for the wood species (in this case, Douglas fir).

2.5.2 Gilibrator

A Gilian Gilibrator-2 NIOSH Primary Standard Air Flow Calibrator manufactured by Sensidyne was used to periodically monitor and calibrate the dilution system described in Section 3.1. A gilibrator consists of a wet cell which generates a bubble film. The desired flow to be measured passes through the wet cell, moving the bubble at the same flow rate. An infrared sensor then reads the bubble flow rate, which allows for a very accurate measurement of air flow rate to be taken.

3 Experimental Techniques and Setups

In this chapter, the experimental techniques and setups for this research are presented, primarily as a reference for the results chapters (Chapters 5 – 9).

3.1 Aerosol and Gaseous Emissions Measurements

Aerosol and gaseous emissions are measured ex-situ, outside of the burner or stove; in a laboratory setting, this often consists of sampling emissions from an exhaust duct above the stove or burner to be examined. Two laboratory emissions setups were used in this work to measure aerosol and gaseous emissions from the burners described in Section 2.1.

3.1.1 Original Emissions Setup

The original emissions test system measured gaseous emissions and was used for the comparison of Haitian charcoal stoves described in Chapter 5. It consisted of a stove platform under an exhaust duct which drew emissions upward through an aluminum duct (150 mm diameter) using two blowers, shown in Fig. 3.1. Prior to reaching these blowers, the gases were mixed along a straight stretch of duct with baffles and subsequently sampled for gas analysis.

Carbon monoxide (CO) and carbon dioxide (CO_2) concentrations in the exhaust duct were continuously measured (1 Hz) with the CAI NDIR gas analyzer described in Section 2.2. The CAI analyzer was calibrated daily using span and zero gases. The temperature, pressure, and relative humidity in the duct were measured at 1 Hz frequency to provide a temporally-resolved duct flow rate. In addition to the gaseous emissions, a calibrated analytical balance (5 kg capacity, 0.1 g resolution) manufactured by American Weigh Scales and an Omega HH66R thermocouple reader were used to continuously measure and record the weight of the fuel added to the stove and the temperature of the food or water in the pot (1 Hz).

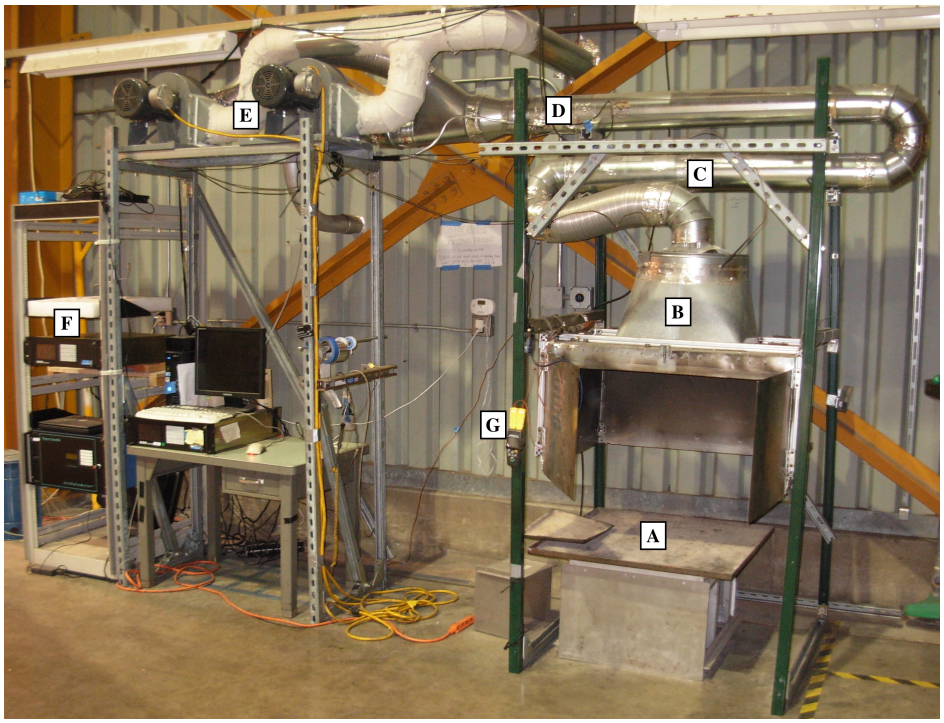

Figure 3.1: The original emissions system used for tests described in Chapter 5. The setup is labeled as: A. Stove platform, B. Exhaust hood, C. Duct work with baffles, D. Sampling port, E. Mechanical blowers, F. CO/CO_2 gas analyzer, and G. Thermocouple reader.

3.1.2 Updated Emissions Setup

The updated emissions system, shown in Fig. 3.2, measured both gaseous and aerosol emissions. It was used for the experiments conducted in Chapters 6 – 8. The stove to be tested sat on a large, high resolution platform scale (64 kg capacity, 0.1 g resolution) manufactured by Sartorius which could continuously record weight loss of the system. A second calibrated analytical balance (5 kg capacity, 0.1 g resolution) manufactured by American Weigh Scales was used for any other necessary weight measurements during testing.

The platform scale was under an extraction hood which drew gases upwards through the duct work using two blowers. Flow was regulated through the exhaust system by a calibrated variable orifice with an iris shutter; pressure was sampled at several points in the duct work to check that the desired volumetric flow rate through the duct (400 m^3/hr) was maintained. The desired rate was chosen to represent 10 air exchanges per hour in an average-sized kitchen (40 m^3), which is within the range outlined by the World Health Organization (World Health Organization (WHO), 2014). A mesh screen with 25 mm square openings was placed at the entrance to the duct work to meet fire code. A straight section of duct was intended to establish well-distributed flow prior to emissions sampling and an APT-8 pressure sensor with a relative humidity sensor measured differential pressure throughout the system and

duct humidity. Ambient, duct, and water (if necessary) temperatures were measured using a thermocouple data logger. As with the original aerosol setup, CO and CO_2 concentrations were measured using the CAI 600-series gas analyzer, calibrated daily for span and offset.

Integrated particle mass system

Concentrations of $PM_{2.5}$ (particles $< 2.5\mu m$) were measured with a gravimetric filter system using quartz and PTFE filters. Beyond providing reliable measurements of total $PM_{2.5}$ mass, the filter measurements provide the basis to develop either wood- or charcoal-specific calibration equations for the real-time $PM_{2.5}$ mass measurements from the DustTrak (described in Section 2.2) (Leipertz and Kiefer, 2010).

In the gravimetric filter system, undiluted particles were drawn from the exhaust duct and passed through a 2.5 μm ultra-sharp cut-off cyclone (BGI instruments). The cyclone separated the sampled emissions such that particles larger than 2.5 μm settled out, so only particles smaller than 2.5 μm ($PM_{2.5}$) continued through the system and deposited on a filter held in a gasket-sealed filter holder. A precision critical orifice was located on the exit of the filter holder to maintain a constant sample flow rate through the filter of 16.7 L/min.

The filter was precisely weighed before and after testing and the difference was taken to be the total mass of $PM_{2.5}$ deposited on the filter; this, along with the ratio of flow rates between the duct and the critical orifice of the integrated particle system, provided the total mass of $PM_{2.5}$ emitted. Prior to weighing, filters were conditioned for at least 24 hours in an environmentally-controlled weighing chamber (Temperature: 70 ± 2°F; Relative humidity: $30 \pm 5\%$). A Sartorius SE-2F analytical microbalance (± 0.1 μg) was used to achieve precise weight measurements. Filters were only handled using clean tweezers to avoid particle and oil deposition.

Time-resolved aerosol system

All particle equipment besides the integrated particle mass system is designed for atmospheric levels of aerosol measurements and therefore, required a diluted sample to analyze the much more polluted cookstove exhaust. The OPS required much higher dilution than the rest of the equipment so it had a separate 1 L/min capillary tube diluter at a 10:1 filtered air to particle-laden air ratio (TSI 332-10). After the OPS, the sample was then combined with a secondary dilution line that supplemented with ultra zero grade air (Praxair AI 0.0UZ) controlled by an Alicat mass flow controller. The amount of flow required through the time-resolved aerosol system was regulated by the individual instrument pumps as well as a critical orifice and pump after the particle instruments, which are relatively constant quantities. Therefore, the secondary dilution line was the primary means of adjusting the dilution ratio for the majority of the aerosol particle instruments.

A PP Systems SBA-5 NDIR gas analyzer measured the CO_2 concentration in the diluted sample and ambient air. The dilution ratio could then be calculated in real-time using the diluted CO_2 sample from the SBA-5 and the undiluted CO_2 measurement from the CAI.

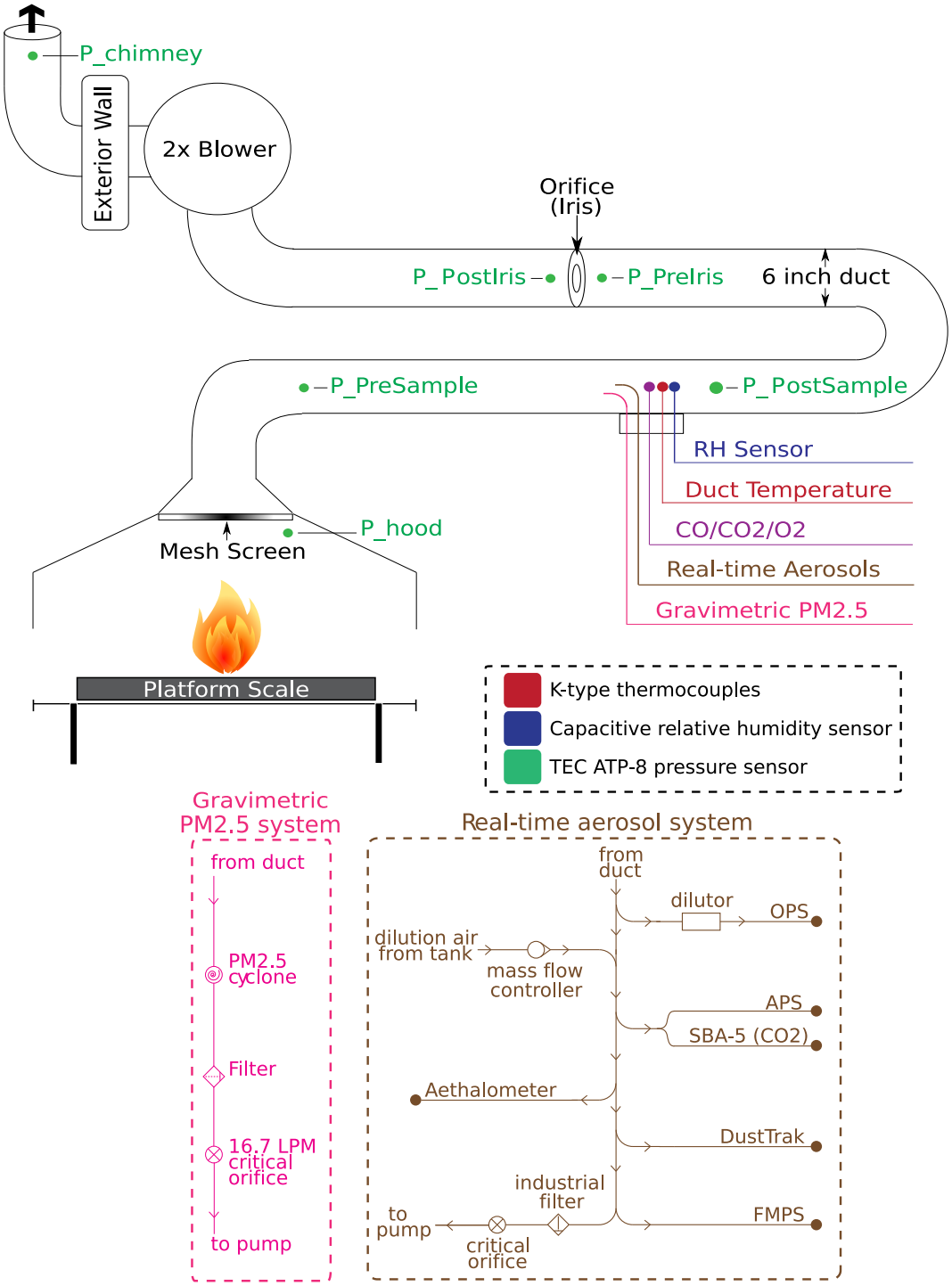

Figure 3.2: The updated emissions system, used in Chapters 6 – 8, measures both gaseous (CO and CO_2) and aerosol emissions ($PM_{2.5}$, BC, and particle size distribution (5.6 nm – 20 μm)).

The SBA-5 calibrated for measurement offset every 20 minutes. In addition, a gilibrator (described in Section 2.5) was routinely used to check the individual instrument pump flows and total system flow to confirm the real-time dilution ratio.

The time-resolved aerosol instruments used in this system were a DustTrak DRX to measure $PM_{2.5}$, a Rack-mount Aethalometer to measure BC, and an Aerodynamic Particle Sizer (APS), Optical Particle Sizer (OPS), and Fast Mobility Particle Sizer Spectrometer (FMPS) to measure particle size distribution (5.6 nm – 20 μm); all of these instruments are described in Section 2.2. However, data from the OPS was only used for wood-burning tests because the refractive index of measured particles must be set externally for the OPS and was chosen to be 1.57 based on previous research using Douglas fir (Hand and Kreidenweis, 2002; Levin et al., 2010).

3.2 Laser Extinction

Laser extinction (LE) is a well-known, adaptable, nonintrusive, and robust technique that is often used as a calibration technique for other methods, such as laser-induced incandescence (Choi et al., 1995; Axelsson et al., 2001; Leipertz et al., 2010b). It is a line-of-sight technique for measuring soot concentration in a flame. It does so by measuring the attenuation of the laser beam, or how much of the laser light is attenuated by particulates in the beam-path, as it passes through the flame. The soot concentration is then calculated from the ratio of transmitted to incident light intensity using the Bouguer-Lambert-Beer law (Choi et al., 1995).

$$\frac{I - I_{background}}{I_o - I_{o,background}} = exp\left(\frac{-K_e f_v L}{\lambda}\right) \tag{3.1}$$

where I is transmitted intensity, I_o is incident intensity, $I_{background}$ and $I_{o,background}$ are the transmitted and incident intensities taken without the flame, K_e is the extinction coefficient, f_v is the soot volume fraction, L is the optical pathlength, and λ is the laser wavelength. It is seen in this equation that the accuracy of LE is limited by the knowledge of the optical properties of the soot particles, which are fuel and laser wavelength dependent (Choi et al., 1995; Williams et al., 2007; Therssen et al., 2007). Note, in all experiments, background (no flame) cases were measured and subtracted from the experimentally found I and I_o in order to remove the ambient background noise of the system.

The simplicity of LE allows for more flexibility in experimentation as only requiring one laser to go through the fire lessens the number of optical entry points necessary. However, because it is a line-of-sight technique, LE only produces total soot concentrations with little spatial resolution so it is necessary to use another technique, such as laser-induced incandescence, to gain high spatial and temporal resolution of in-situ soot.

For the LE experiments conducted in Chapters 8 and 9, a 1064 nm continuous wave laser was used with a frequency-controlled chopper (fixed at 170 Hz in Chapter 8 and 80 Hz in Section 9.3) to provide laser pulses and a measure of background interference. The 1064 nm wavelength laser was chosen to avoid some well documented issues with PAH absorption

created when using a laser in the visible or UV spectrums (Williams et al., 2007; Zerbs et al., 2009). The laser was controlled using a Shanghai Dream Laser Technology control box and the chopper controlled via a Stanford Research Instruments Model SR540 Chopper Controller.

3.2.1 Laser Extinction Experimental Setups

Laser extinction on burning wood (used in Chapter 8)

An LE setup was used to measure soot volume fraction from burning wood in Chapter 8. In this experimental setup, the laser beam was attenuated as it passed through the wood flame (shown in Fig. 3.3) with the attenuated signal I measured by a signal photodiode. Prior to passing through the flame, the laser beam was also partially back reflected to another photodiode using a plano-convex ($f = +500$ mm) lens to acquire a reference signal, I_o. The K_e value for the wood-burning trials was chosen to be 9.0 from the work done by Choi et al. (1995), although this is likely to be an overestimation due to the differences in laser wavelengths between that work and the work in Chapter 8 (laser wavelengths of 633 nm versus 1064 nm, respectively).

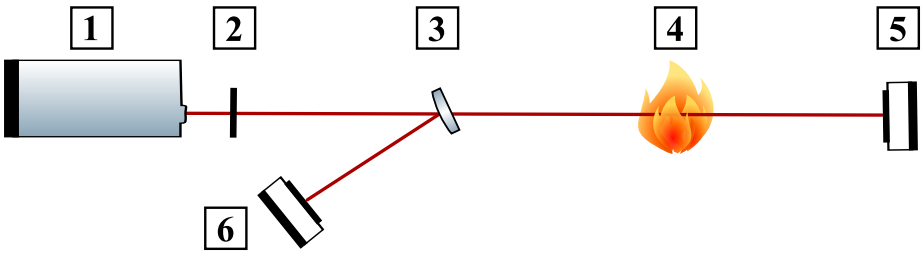

Figure 3.3: Laser extinction schematic for the wood-burning trials in Chapter 8. Labeled instruments: 1. Infrared laser (31 mW); 2. Chopper (170 Hz); 3. Plano-convex lens ($f = +500$ mm); 4. Measurement region; 5. & 6. Photodiodes.

Laser extinction for calibrating laser-induced incandescence (used in Section 9.3)

An LE setup was used to produce the soot volume fractions necessary for calibrating the laser-induced incandescence (LII) experiments (discussed in Sections 4.5 and 9.3); without calibration, LII only produces qualitative results. A premixed ethylene/air flat-flame burner (described in Section 2.1.3) was used as consistent soot source for the measurements, so the K_e value was chosen to be 9.2 for the soot volume fraction calculation, based on the findings of Zhu et al. (2002) and Williams et al. (2007).

In the optical setup shown in Fig. 3.4, a portion of the laser beam was reflected into the first photodiode and served as the incident beam (I_o) for the LE calculations. The other

portion of the beam passed through the burner and was reflected back through the burner on a very shallow angle; this double pass increased the difference in signal between incident and transmitted beams, making it easier to measure. After passing back through the burner, the transmitted beam (I) was measured with the second photodiode. Both photodiodes were angled as much away from the line-of-sight of the burner and had 42 mm sheaths to reduce interference from the flame intensity; in addition, the transmitted photodiode had a neutral density filter to further reduce interference. The measurements were controlled and recorded using National Instruments Signal Express LE software through a National Instruments cDAQ-9171 (4-channel, ±10 V).

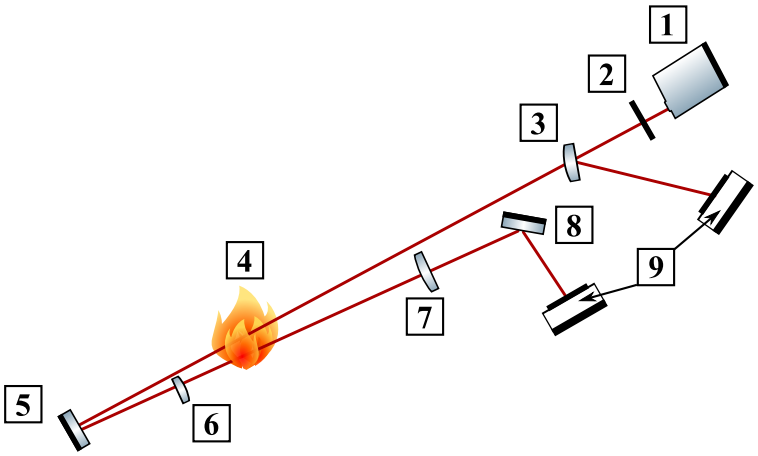

Figure 3.4: Laser extinction schematic for calibrating the LII experiments described in Section 9.3. 1. Infrared laser (31 mW); 2. Chopper (80 Hz); 3. Plano-convex lens (f = + 1000 mm); 4. Measurement region; 5. Plano-convex lens (f = + 500 mm); 6. Front-faced broadband utility mirror; 7. Plano-convex lens (f = + 100 mm); 8. Infrared mirror; 9. Photodiodes.

3.3 Particle Image Velocimetry (PIV)

3.3.1 PIV Background

Particle image velocimetry (PIV) is a non-intrusive, whole field technique used to measure velocity of fluid flows. In this technique, light-scattering tracer particles are added to the flow to be evaluated. Those particles are then illuminated twice in rapid succession at a predefined interval and the light scattered by the particles is recorded in two images. The displacement of the particles between the two images is found and then, using the known time interval, the velocity of those particles may be calculated. The ideal tracer particles therefore are highly reflective and sized to follow the local fluid flow velocities. There are

many thorough reviews of and resources on the history, technique, experimental parameters, and applications of PIV, such as Raffel et al. (2007), Westerweel et al. (2013), Adrian (2005), Grant (1994), Prasad (2000), and Adrian (1996), to which the interested reader should refer for more information.

3.3.2 PIV Imaging Setup

A diagram of the imaging system used for the PIV experiments can be see in Fig. 3.5. The double-headed Nd:YAG laser described in Section 2.3.1 was frequency-doubled to 532 nm and double pulsed at 10 Hz, as is typical for PIV setups (Raffel et al., 2007). From this beam, a laser sheet was formed using an optical telescope and horizontally-mounted cylindrical lens; this laser sheet was 130 mm tall (clipped using beam blocks prior to the burner) to include the entire measurement region from the bottom of the halo to the top of the PCB. Due to the turbulence in the system, it was expected many particles would rapidly move out-of-plane of the laser sheet; the laser sheet was kept relatively thick ($\sim$3 mm) to allow a greater possibility of capturing particle movement. The laser sheet was aligned perpendicularly to the PCB at the centerline of the burner fuel holes, in the same location as the OH-LIF and LII experiments discussed in Section 3.4.

A MegaPlus II (Model ES4020) CCD (2048 $\times$ 2048 pixels) camera manufactured by Princeton Instruments was used for image collection with a 80 – 210 mm Nikon-Tamron TeleMacro lens to capture a measurement region of 166 mm $\times$ 166 mm. A 532 nm interference filter (10 nm bandwidth) was also used with the camera to reduce interference from the flame luminosity by blocking undesired light wavelengths from entering the CCD. Image capture and CCD control were governed using EPIX XCAP 3.0 software.

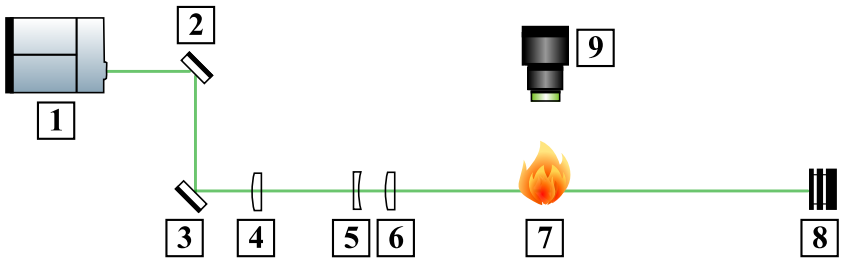

Figure 3.5: Schematic of the PIV optical layout. Labeled instruments: 1. Quantel BrilliantB Twins laser (both heads used); 2. & 3. High energy 532 nm mirrors; 4. Plano-convex spherical lens (f = + 250 mm); 5. Plano-concave spherical lens (f = – 125 mm); 6. Plano-convex cylindrical lens (f = + 25 mm); 7. Measurement region; 8. Beam block; 9. MegaPlus II (Model ES4020) CCD camera with a Nikon-Tamron CF TeleMacro lens (80 – 210 mm) and a 532 nm interference filter.

Timing

The PIV timing system was controlled using a Stanford Research Systems DG535 digital delay generator. The DG535 was triggered by a 10 Hz signal generated by an IDT Timing Hub. Channels A and B of the DG535 controlled the BrilliantB flashlamps so the pulse delay between the two laser heads could be controlled precisely. Channel C triggered the MegaPlus ICCD controller; however, the ICCD required a 2.5 Hz signal trigger instead of the 10 Hz signal used for the lasers so a frequency diverter was installed between the DG535 and the MegaPlus II controller. The internal triggers set using the BrilliantB laser head controllers were found to be satisfactorily accurate when the pulse timing was checked with an oscilloscope so the Q-switches were internally triggered for simplicity.

Seeding System

For the PIV experiment, two different seeders introduced particles into the system: the sieve seeder and the cyclone seeder (both described in Section 2.4). Most PIV systems are enclosed systems with a seeded, recirculated medium (e.g. air or water) so the entire measurement area is always seeded. This experiment, however, was not enclosed due to the high combustion temperatures and obscuring by-products (namely soot); therefore, the sieve seeder was designed to continuously introduce particles into the entire measurement area. The sieve seeder rested approximately 30 mm above the halo in place of the surrogate pot bottom used in other PCB tests (discussed in Section 8.3), and shook particles into the system from above. These introduced particles did have a pre-existing velocity due to gravity; however, it was found to be relatively small compared to the flow rates of the halos so was deemed negligible.

Ideally for PIV measurements, all introduced flows are also seeded so all flow patterns can be captured. To seed the air from the halo, the cyclone seeder was mounted inline with the halo air injection system. The distance along the line between the exit of the cyclone seeder and the entrance of the halo was minimized to reduce particle loss and clumping effects along the tubing. It was also desired to seed the fuel injection from the burner. Although the fuel flow rate was relatively slow (5 L/min), a seeder was designed that could achieve a high output of particles from the seeder. Ultrafine ($d \leq 0.2$ μm) spherical titanium dioxide particles were chosen to seed the experiment but even with these small diameter particles, the fuel flow was not properly seeded; it is assumed that the particles fell out of the flow when passing into the comparatively large diameter pipes of the PCB. Therefore, although desired, it was deemed unfeasible to seed the fuel flow from the PCB.

3.4 Laser-Induced Incandescence (LII) and OH Laser-Induced Fluorescence (OH-LIF)

3.4.1 LII Background

Laser-induced incandescence (LII) has been found to be a powerful measurement technique for soot characterization with high spatial and temporal resolution (Schulz et al., 2006). In LII, soot particles in a flame are rapidly heated with a high-power laser pulse and then the resulting radiative emissions are measured as the particles incandesce (Schulz et al., 2006; Leipertz et al., 2010b). The measured signal intensity has been found to be primarily proportional to the amount of energy absorbed by the soot particles, and therefore, the soot concentration in the measurement region (Leipertz et al., 2010b). Many sources describe LII in greater detail, such as Schulz et al. (2006), Leipertz and Kiefer (2010), Bladh (2007), Zizak (2011), Ben (2015), Santoro and Shaddix (2002), and Desgroux (2013), to which the interested reader can refer for more in-depth information. For this work, LII was used to find the spatial concentration of soot in the flame zone of the proxy cookstove burner for the different cases of secondary air injection studied in Section 9.3.

3.4.2 OH-LIF Background

Laser-induced fluorescence (LIF) is a well-established laser diagnostic tool which operates using an absorption-emission process (Leipertz et al., 2010a). In LIF, a laser is used to excite the desired molecules which then release that excess energy by fluorescing, or spontaneously emitting radiation (Leipertz et al., 2010a). For this work, LIF was used to excite the hydroxyl radicals (OH) in the flame of the proxy cookstove burner for the secondary air injection cases studied in Section 9.3. Because OH concentrations are a suitable indication of the location of the flame front or reaction zone (Leipertz et al., 2010a), this technique was conducted simultaneously with the LII to identify the reaction zones where soot oxidation reactions could be occurring. Like LII, several books and articles exist discussing LIF and OH-LIF in great detail, such as Leipertz et al. (2010a), Smyth and Crosley (2002), Kohse-Höinghaus (1994), and Daily (1997), to which the interested reader can refer for more information about the technique.

3.4.3 OH-LIF and LII Imaging Setups

To potentially achieve the desired results (identifying soot concentrations and reaction zones), the LII and OH-LIF measurements had to be recorded simultaneously, especially since the examined flames are so variable, changing instant to instant. Therefore, the LII and OH-LIF systems had to be well-aligned and well-controlled; this section describes the experimental setup used for those simultaneous measurements.

OH-LIF and LII Optical Layout and Imaging System

Figure 3.6 presents the optical layout for the simultaneous OH-LIF and LII experiments. In the optical arrangement, the OH-LIF and LII beams overlap, forming co-planar laser sheets.

The LII experiments used a Quantel Q-smart 850 (described in Section 2.3.1) to produce a 1064 nm beam. Typically, LII experiments use 1064 nm or 532 nm wavelengths. A 1064 nm wavelength was chosen to reduce issues with interference observed with 532 nm and shorter wavelengths (Schulz et al., 2006); the fluorescence of polycyclic aromatic hydrocarbons (PAHs), common soot precursors, is induced with excitation in the visible and UV spectrums, and is not easily separated from the LII signal, producing high amounts of PAH interference (Schulz et al., 2006; Vander Wal, 1996). Similarly, longer excitation wavelengths like 1064 nm reduce the interference from the generation of electronically-excited C_2 fragments, and wavelengths in the infrared spectrum reduced interference from elastically-scattered light (Schulz et al., 2006).

The output beam was approximately 20 mm $\times$ 8 mm and had a power of 1.62 W. A Princeton Instruments ICCD (576 $\times$ 384 pixel, 16-bit, model ICCD-576-G/1) with a Nikon 50 mm lens (f/1.4) was used to detect the LII signal; it was run with a gate width of 50 ns. The LII camera was mounted perpendicular to the laser sheet, as shown in Fig. 3.6. A 430 nm bandpass filter (10 nm bandwidth) was used for detection; this wavelength was chosen to better differentiate between the LII signal and flame luminosity as well as avoid interference from C_2 swan bands (Schulz et al., 2006; Vander Wal, 1996).

The OH-LIF optical system used a 532 nm beam from the master head of the Quantel BrilliantB Twins, described in Section 2.3.1, to pump a Lambda-Physik ScanMate 2E dye laser (Section 2.3.2) using Rhodamine 6G dye (peak emission at 560 nm). The output of the dye laser was then frequency-doubled using a Lambda-Physik FL37.1 doubling crystal to produce an approximately 283 nm beam; the doubling crystal in the ScanMate was recalibrated daily to ensure the strongest signal in the flame. The lasing and excitation wavelengths were then separated using a four-element Pellin-Broca array. The output beam was approximately 21 mm $\times$ 0.5 mm and had a power of approximately 11 mW. A Princeton Instruments ICCD (1024 $\times$ 1024 pixel, 16-bit, model 7467-0004) was used to detect the OH-LIF signal; it was run with a longer gate width of 100 ns. It is known that the broadband luminescence from soot tends to overwhelm OH fluorescence, often being more than three times greater in intensity (Ciatti, 2010); therefore, a 78 mm ultraviolet lens (f/3.5) and an Andover bandpass filter (310 nm, 10 nm bandwidth) were mounted to the front of the ICCD to reduce interference. The OH-LIF camera was mounted perpendicular to the laser sheet, opposite from the LII camera, as shown in Fig. 3.6. The slot burner, described in Section 2.1.3, was used as a reference flame for the OH-LIF, and was mounted prior to the proxy cookstove burner (PCB) in line with the laser.

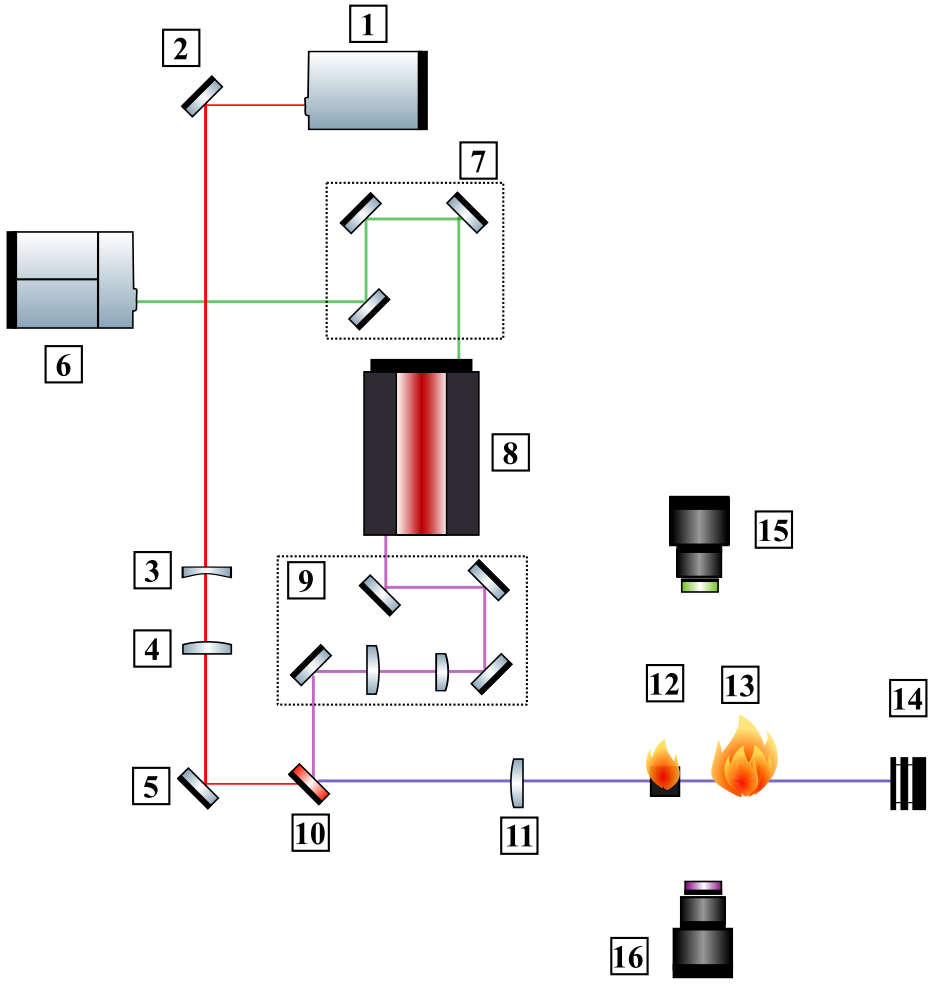

Figure 3.6: Schematic of the OH-LIF and LII optical arrangement. Labeled instruments: 1. Quantel Q-Smart 850 laser; 2. High energy 1064 nm mirror; 3. Plano-concave spherical lens (f = − 125 mm); 4. Plano-convex spherical lens (f = + 250 mm); 5. High energy 1064 nm mirror; 6. Quantel BrilliantB Twins laser (only master head used); 7. High energy 532 nm mirrors; 8. Lambda-Physik ScanMate 2E dye laser (with Rhodamine 6G dye); 9. 4 silvered UV mirrors, plano-convex UVFS lens (f = + 50 mm), and a plano-convex UVFS lens (f = + 200 mm); 10. Dichroic mirror (285/339 nm); 11. UV cylindrical lens (f = + 1000 mm), mounted vertically; 12. Slot burner; 13. Measurement region; 14. Beam block; 15. Princeton Instruments ICCD (576-G/I) with a 50 mm (f/1.4) lens and a 430 nm bandpass filter; 16. Princeton Instruments ICCD (7467-0004) with a 78 mm UV (f/3.5) lens and a 310 nm bandpass filter.

OH-LIF and LII Timing System

The timing system shown in Fig. 3.7 was used to control and synchronize the OH-LIF and LII systems. In order to maintain thermal stabilization, the lasers had to run at 10 Hz, so an IDT Timing Hub was used to generate the primary 10 Hz signal which fed into a Stanford Research Systems DG535 digital delay generator. This DG535 (referred to as DG535-1) controlled the laser flashlamp timings: Output A-1 controlled the BrilliantB flashlamp and therefore the ScanMate dye laser for the OH-LIF; output B-1 controlled the Q-Smart flashlamp for the LII; output C-1 was unused; and output D-1 was the center-point or zero time. This zero time was used to trigger a second DG535 (DG535-2) timing box which controlled the laser Q-switches and cameras. Similar to the DG535-1, the outputs from the DG535-2 controlled the BrilliantB Q-switch (A-2), the Q-smart Q-switch (B-2), and produced an output signal for the camera controllers (D-2). This allowed for precise control over the synchronization of the two laser systems; the flashlamps were advanced relative to the zero time (D-1) and the Q-switches and cameras were delayed. Also, because the two DG535 boxes controlled the flashlamps and Q-switches, the laser power could be easily readjusted by changing the flashlamp/Q-switch delay.

The ICCDs were unable to operate at the 10 Hz frequency used for the lasers. Therefore, a four-input AND gate and a four-way buffer box were used as a go-between for the DG535-2 and camera controllers. The AND gate read in the 10 Hz signal and also read in a "Not Scan" signal from the ICCD controllers. This "Not Scan" signal only turned high when the camera was ready to collect another image, therefore preventing new data to be taken on the CCD while the old image was still being written out. Note, the LII ICCD controller required an external sync input for triggering the ICCD so a PG-200 pulse generator triggered the external sync on the LII camera controller to send a pulse to read the CCD array. To ensure the cameras started recording images at the same time, the 10 Hz trigger to the AND gate was switched off while the camera software began "acquiring images". Image recording would not actually begin, however, until the trigger was switched on, allowing both cameras to began recording simultaneously.

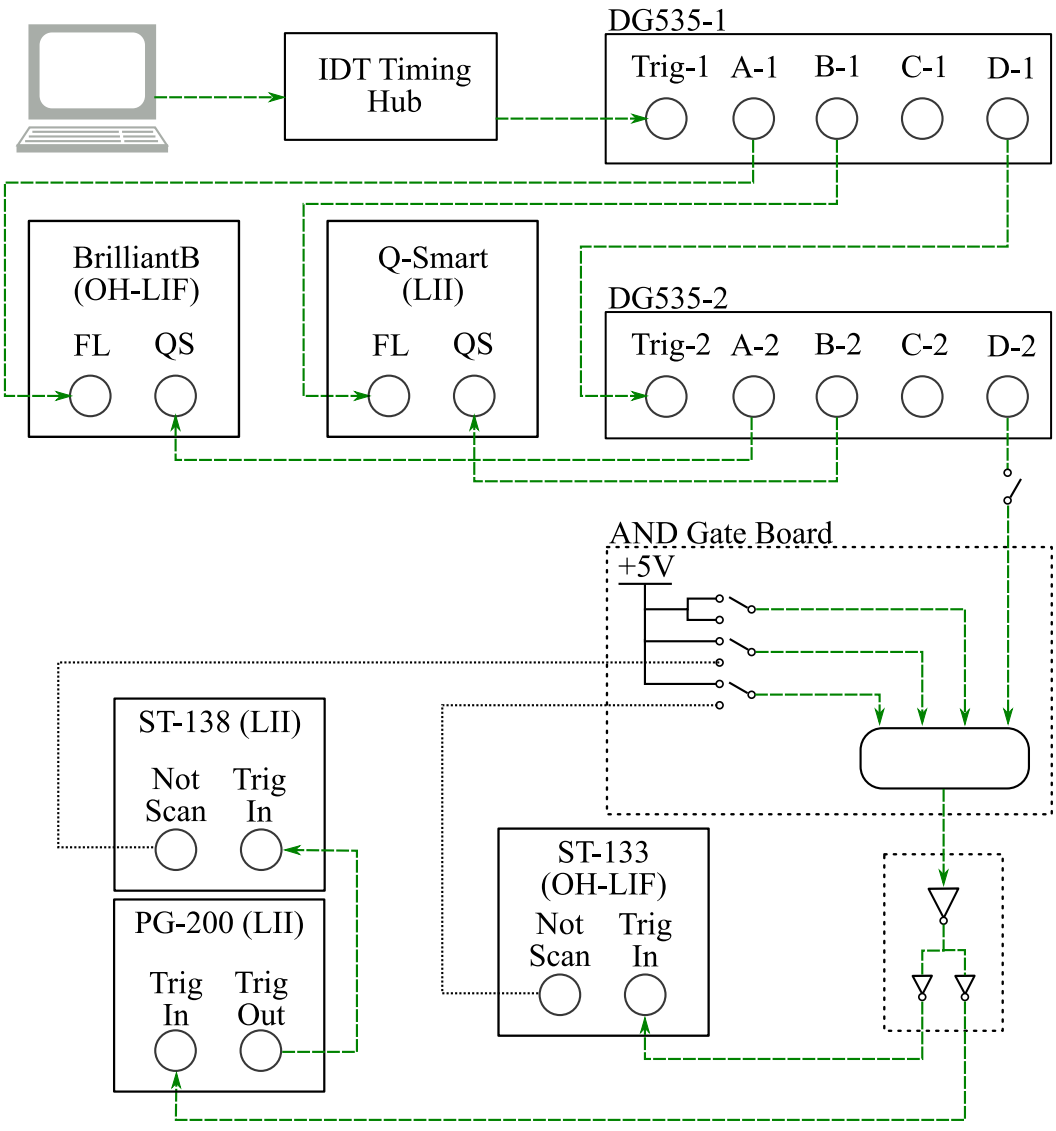

Figure 3.7: Schematic of timing system for OH-LIF and LII measurements.

4 Experimental Protocols and Data Analysis

In this chapter, the more elaborate protocols used for Chapters 5 – 7 are described as well as the metrics used for stove evaluation, primarily as a reference for the results chapters (Chapters 5 – 7). Additionally, the data processing steps for the OH-LIF/LII experiments conducted in Chapter 9 are outlined.

4.1 Water Boiling Test

A Water Boiling Test (WBT), as the name implies, is a standard method for evaluating cookstove performance based on boiling water (Bailis et al., 2007; Global Alliance for Clean Cookstoves, 2013). It is an internationally known and well-defined protocol that can be used to test and compare any cookstove in the field or in the lab. The WBT is especially useful when developing and modifying stove prototypes and selecting prototypes for further field testing. However, the WBT has the disadvantage of being narrowly defined to a specific task, namely boiling water, which may not be relevant to the actual cooking activities conducted in the field so it is not necessarily a good indicator for how a stove will perform in real-world conditions (Global Alliance for Clean Cookstoves, 2013).

The WBT consists of two high-power phases, called cold start and hot start, and one low-power phase, called simmer (see Global Alliance for Clean Cookstoves (2013) for an in-depth description of the protocol). In this work, the WBT was solely used for charcoal stove tests (see Chapter 5), and is described as follows. The same Haitian pot was used for all phases.

1. Cold Start: Using a room temperature stove and a room temperature pot, 2.5 L of room temperature water was brought to a boil (99°C) using a pre-weighed amount of charcoal and a high-resin pine fire starter. Once the water reached a boil, the pot was removed and the remaining charcoal weighed.

2. Hot Start: Immediately following the cold start, the boiled water was replaced with a new 2.5 L of room temperature water; the stove and pot were still hot. Using another pre-weighed amount of charcoal and high-resin pine, the water was brought to a boil.

When the water reached a boil, the burning charcoal embers were quickly weighed and then put back into the stove to act as the fire starter for the next phase.

3. Simmer: Immediately following the hot start, the already boiling water was maintained at a simmer for 45 minutes using a third pre-weighed amount of charcoal and the embers from the previous phase. The desired simmer temperature was 2 – 3°C below the boiling point; if the water temperature fell more than 6°C below the boiling point, the test was considered failed.

Temperature of the water was monitored at 1 Hz resolution using a K-type thermocouple suspended in the water approximately 25 mm from the bottom center of the pot. For stoves with a door to control air supply, the door was kept open for the high power tests (cold and hot start phases) and 50 – 60% open during the low power test (simmer phase).

4.2 Modified Water Boiling Test

For the wood-burning stoves evaluated in Chapter 7, a modified form of the WBT was used as the stoves studied have relatively low thermal mass and therefore should not reveal drastically different results between the cold start and hot start phases. This modified WBT followed the official WBT protocol (Global Alliance for Clean Cookstoves, 2013) but only included the cold start (high power) phase and a 30 minute simmer (low power) phase, described as follows. The same 2.3 kg metal Darfuri pot was used for each phase. The Douglas fir kindling and fuelwood sticks were harvested from the same tree and stored in a dry location for at least one year prior to experiments. As evaluated by ALS Environmental using an automated TGA system, the Douglas fir at 8.35% moisture content comprised of 74.92% volatile matter, 16.69% fixed carbon, and 0.03% ash with a heating value of 7394 BTU/lb. The moisture content of the sticks as measured prior to each test ranged from approximately 7 – 10%.

1. Fire-tending: The fire was started using 15 g of pine wood shavings and 60 g of small Douglas fir sticks (80 mm, × 5 mm, × 5 mm) as kindling. The shavings were arranged in a pile on the grate in the middle of the firebox and the kindling sticks were arranged around the pile in a pyramidal fashion. Larger wood sticks (200 mm, × 20 mm, × 20 mm) were used after the initial kindling. A large stick was added once per minute for the first four minutes. The larger fuelwood was then added and arranged as necessary to maintain a thermal power of approximately 5 kW during the cold start and 3 kW for the simmer; the thermal power estimation is discussed in Section 4.4.

2. Cold Start: Using a room temperature stove and a room temperature standard pot, 2.5 L of room temperature water was brought to a boil (99°C) using the fire-tending technique described above. When the water reached a boil, the burning wood pieces

were quickly weighed and then put back into the stove to act as the fire starter for the next phase.

3. Simmer: Immediately following the cold start, the already boiling water was maintained at a simmer for 30 minutes. The desired simmer temperature was 2 – 3°C below the boiling point; if the water temperature fell more than 6°C below the boiling point, the test was considered failed.

After the simmer, emissions measurements were immediately stopped and the mass of wood remaining was immediately measured prior to extinguishing the fire. The moisture content of the wood used for each phase was found immediately before testing by averaging the moisture content of three sticks per phase, three locations per stick as measured by the moisture meter described in Section 2.5.

4.3 Haitian Controlled Cooking Test

The Haitian Controlled Cooking Test (CCT) was developed for the comparison testing described in Chapter 5. A CCT mirrors specific, culturally-relevant cooking tasks from the intended region of dissemination, standardizing the cooking tasks into a scientifically valid and repeatable protocol (Bailis et al., 2007). The CCT protocol used in this work was developed by LBNL researchers based on notes from Haitian cooks, brief cooking trials conducted in Haiti by an LBNL team, and consultations with Nexant staff, who had conducted cooking field trials in Haiti (Nexant Inc, 2010). The protocol is designed to create a standardized procedure for laboratory testing that closely follows the cooking practices in Haiti for the staple Haitian dish of *diri kole ak pwa* (rice with red beans and vegetables). The CCT protocol is divided into three main cooking tasks: Bean phase, Vegetable phase, and Rice phase.

1. Fire-tending: Approximately 10 – 20 g of high-resin pine was placed in the center of the charcoal bed to act as a fire-starter. The initial amount of charcoal placed in the bed depended on the cookstove because some cookstoves were not designed to accommodate the large initial amounts typically used in the traditional Haitian stove. The initial amounts of charcoal used in each cookstove were 280 g, 450 g, 200 g, and 475 g for the EcoRecho, Mirak, Prakti, and traditional stoves, respectively (these stoves are described in Section 2.1.1). Additional pieces of charcoal were added as needed to maintain a steady fire.

2. Bean phase: The ingredients for the bean phase (500 g beans, 71 g oil, 50 g garlic, 20 g salt, 2500 g water) were brought to a boil in a covered pot and then simmered for 20 minutes. At the end of the 20 minute period, the bean dish was mixed well and checked if fully cooked. A bean was considered fully cooked if the skin of the bean came off easily when squeezed. If any of five randomly selected beans were not fully

cooked, the bean dish was cooked for an additional three minutes, and the beans were checked again. This process was repeated until the beans were considered fully cooked. At that point, the bean dish was strained in order to separate the beans and the water, both of which were kept in separate dishes for later use.

3. Vegetable Phase: To represent cooking vegetables, 500 -– 1100 g of water was heated for 10 minutes. This portion of the test was intended to maintain a steady fire over a fixed burn time with the water acting as a thermal sink, not a test to see how long it took to boil a specific amount of water (unlike the WBT). Simply heating water, instead of heating water with vegetables, is still representative of the vegetable phase because vegetables contain a high percentage of water ($\sim 90\%$ for commonly used Haitian vegetables) so the specific heats of the vegetables ($\sim 3.9 - 4$ kJ/kg K) are similar to that of water (~ 4.2 kJ/kg K) (ASHRAE, 2014). Therefore, water was used as a proxy for vegetables during this phase.

4. Rice Phase: Ingredients for the rice phase consisted of the entirety of the strained cooked beans, 1400 g strained water from cooked bean dish (if the remaining water from the bean dish was less than 1400 g, tap water was added to reach a total of 1400 g), 1100 g tap water, and 1000 g uncooked rice. In a covered pot, the beans and water were brought to a boil. Once the mixture was boiling, the rice was added and again the mixture was covered and brought to a boil. The mixture was then simmered for 20 minutes in the covered pot. At the end of 20 minutes, the rice dish was checked to see if it was fully cooked. The rice was considered fully cooked when no water remained and the rice at the top and bottom of the pan was crisp. If the rice was not fully cooked, it was cooked for an additional 3 minutes and then rechecked. This process was repeated until the rice was fully cooked.

4.4 Important Metrics for Cookstove Evaluation

This section presents the calculations on relevant metrics used in this work's cookstove evaluations.

Time to Boil

The time to boil is the amount of time it takes a specified amount of water to reach the local boiling point. In this work, it was recorded from when the fuel bed was lit until the water reached a predetermined local boiling temperature (99°C).

As the initial temperature of the water varied slightly from test to test, a temperature-correction was applied, shown in Eq. 4.1, as defined in the Water Boiling Test (WBT) 4.3.2 (Global Alliance for Clean Cookstoves, 2013).

$$\Delta t_{corr} = \frac{75 \Delta t}{T_b - T_i} \tag{4.1}$$

where Δt is the measured time to boil and T_b and T_i are the boiling and initial temperatures of the water, respectively. The equation is standardized by assuming a 75°C change in water temperature (25°C – 100°C). Note, in the results chapters, the temperature-corrected time to boil is simply referred to as time to boil.

Time to Light

The time to light is the amount of time necessary for a fuel bed to ignite, defined from when the fuel bed is first lit to the point where the fire will not extinguish if a pot is place on it. The time to light in this work was used in charcoal combustion tests, so was recorded from when the fire-starter was lit until roughly 70% of the charcoal bed was glowing, which occurred at a thermal power of approximately 2.4 kW.

Fuel Consumption

The fuel consumption is the amount of fuel required for an experiment; the fuel consumed as defined in this work is calculated simply as the amount of fuel and char left at the end of a test subtracted from the amount of fuel available at the beginning of the test.

Specific Fuel Consumption

The specific fuel consumption is the amount of fuel required to produce a specific amount of a product (i.e. boiled water or cooked food). The specific fuel consumption is calculated as defined in the Water Boiling Test (WBT) 4.3.2 (Global Alliance for Clean Cookstoves, 2013):

$$SFC = \frac{f_{eq,dry}}{mass\ of\ product} \tag{4.2}$$

where $f_{eq,dry}$ is the amount of dry fuel consumed adjusted to account for the energy required to dry the fuel and the char that is left at the end of the test. It is calculated as:

$$f_{eq,dry} = f_{wet}(1 - MC) - \frac{f_{wet}\, MC\, (4.186(T_w - T_a) + 2257)}{LHV_{fuel}} - \frac{LHV_{char}\, m_{char}}{LHV_{fuel}} \tag{4.3}$$

where f_{wet} is the actual fuel consumed, MC is the moisture content of the fuel, T_w is the temperature of the pot contents, T_a is the ambient temperature, LHV_{fuel} is the lower heating value of the fuel (equal to 18766 kJ/kg for Douglas fir), LHV_{char} is the lower heating value of the char (equal to 29500 kJ/kg), and m_{char} is the mass of char remaining. The moisture contents of the solid fuels for all tests were found using standard oven-drying procedures (ASTM International, 2007), as well as with the Delmhorst moisture meter discussed in Section 2.5.

Thermal Efficiency

Thermal efficiency was calculated as defined in the WBT 4.3.2 protocol (Global Alliance for Clean Cookstoves, 2013):

$$\eta_{th} = \frac{4.186\,\Delta T\,m_{w,i} + 2260\,m_{w,vap}}{f_{eq,dry}\,LHV_{fuel}} \tag{4.4}$$

where η_{th} is the thermal efficiency, ΔT is the change in water temperature, $m_{w,i}$ is the initial mass of water, $m_{w,vap}$ is the amount of water vaporized, $f_{eq,dry}$ is the equivalent dry fuel consumed (defined in the Specific Fuel Consumption section), and LHV_{fuel} is the lower heating value of the fuel.

Thermal Power

In this study, the thermal power as a function of time was estimated using the CO_2 released as a function of time, which was converted to power using the energy content of carbon.

$$P_{th} = gCO_2 \left(\frac{MW_C}{MW_{CO_2}}\right) e_C \tag{4.5}$$

where P_{th} is the thermal power, gCO_2 is the grams of CO_2 per second, MW_C and MW_{CO_2} are the molecular weights of carbon and carbon dioxide, respectively, and e_C is the heat of combustion of carbon (32800 J/g) (Keating, 2007).

CO and CO_2 Emissions

The original CO and CO_2 concentrations were recorded in parts per million (ppm) and then were integrated and converted to g/m^3 with the background room concentrations removed. The volumetric flow rate through the duct was determined empirically by measuring a pressure drop through an orifice and was used to then convert concentrations from g/m^3 to g.

Modified Combustion Efficiency

The modified combustion efficiency (MCE), defined in WBT 4.3.2 (Global Alliance for Clean Cookstoves, 2013) and shown in Eq. 4.6, evaluates the amount of CO_2 released from a fire in comparison to the total gaseous carbon emissions. Typically in cookstove tests, the total gaseous carbon emissions are estimated as the summation of two major carbon-based combustion products, CO and CO_2.

$$MCE = \frac{\Delta CO_2}{\Delta CO + \Delta CO_2} \tag{4.6}$$

where ΔCO_2 is the mean duct CO_2 minus the ambient CO_2 and ΔCO is the average duct CO minus the ambient CO; the ambient CO concentration was assumed to be negligible for all tests in this work.

Black Carbon

The black carbon (BC) results from the aethalometer were adjusted using a calibration fit (shown in Eq. 4.7) developed by Kirchstetter and Novakov (2007) and validated for cookstoves in Kirchstetter et al. (2010). The calibration is necessary to correct for a known sampling artifact caused by a diminishing response to BC as the filter in the aethalometer darkens (Kirchstetter et al., 2010; Kirchstetter and Novakov, 2007).

$$BC_{corrected} = \frac{BC_{initial}}{0.88 exp\left(\frac{-ATN}{100}\right) + 0.12} \tag{4.7}$$

where ATN is the attenuation through the filter.

Total Particle Number Size Distribution

The FMPS, OPS, and APS (see Section 2.2.4) output data in terms of $dN/dlog(D_p)$ where dN is the concentration of particles [number of particles / cm^3 of air / particle size bin] and dlog(D_p) is the logarithmic width of the corresponding particle size bin [nm]; each instrument has a constant logarithmic bin width. This value can be used to find the total particle number size distribution:

$$\frac{dN_t}{dlog(D_p)} = \sum_{t=0}^{t_{test}} \left(\frac{dN}{dlog(D_p)}\right)_t \overline{Q}_{duct}\, \Delta t\, \overline{DR} \tag{4.8}$$

where t_{test} is the length of the test, $(dN/dlog(D_p))_t$ is the particle number concentration as measured by the instrument at time 't', Δt is the sampling interval (equal to 1 second), and $\overline{DR}$ and $\overline{Q}_{duct}$ are the mean dilution ratio and volumetric duct flow rate, respectively.

4.5 Simultaneous OH-LIF and LII Image Processing

There were several steps necessary to process the images taken from the simultaneous LII and OH-LIF tests discussed in Sections 3.4 and 9.3. The image processing steps are outlined in Fig. 4.1 and also are described below.

Flip and Match Images

Because the LII and OH-LIF cameras were facing each other (as shown in Section 3.4), the LII images were flipped left to right so they were in the same orientation as the OH-LIF. The OH-LIF and LII images needed to be matched in order to correct for misalignment

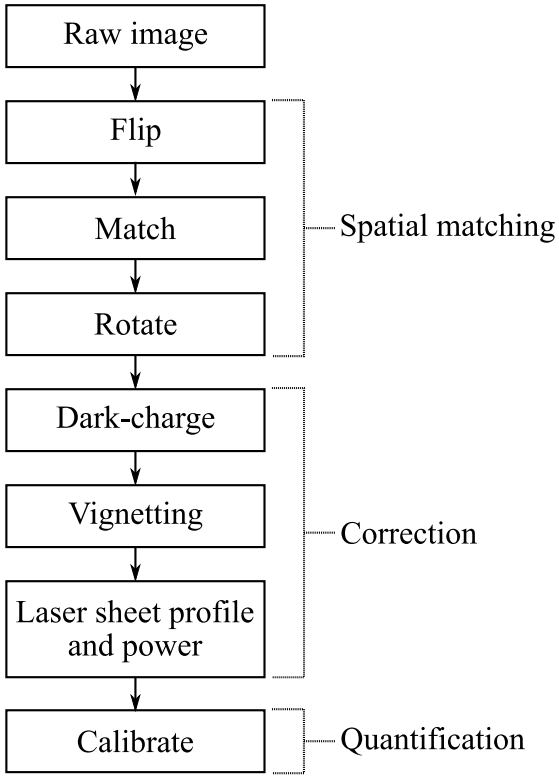

Figure 4.1: Outline of the steps taken for processing the OH-LIF and LII images.

between the OH-LIF and LII cameras. Each camera recorded a transparent lettered grid at the beginning and ending of each experimental day. A unique set of points could be found on both the OH-LIF and LII target grid images, allowing the points on the LII images to be mapped onto the points of the OH-LIF images using a five-point projective transformation algorithm in the MATLAB Image Processing Toolbox (MATLAB® R2012b). The LII images were chosen to be matched to the OH-LIF images because the OH-LIF images had a reference flame (from the slot burner) for image rotation, discussed in the next section.

Rotating Images

Once the images were matched, further manipulation was necessary to correct for any misalignment between the cameras and the laser beams. At the beginning and ending of each experimental day, two non-transparent wires were placed in the path of the laser beams prior to the burners such that their shadows created two easily identified drops in signal intensity in the OH-LIF and LII images. The separation distance between the wires could be compared at two locations along the laser line in an image (the reference flame and the middle flame of the burner for the OH-LIF, and the two outer flames of the burner for the LII) to check laser collimation. If the separation distance was the same but the vertical locations

of the intensity drops along the laser line were different, this meant that the camera was slightly tilted compared to the laser beam so the images needed to be rotated accordingly. The OH-LIF wire images were used for calculating this rotation angle as the reference flame (which was only visible in the OH-LIF images because it produced negligible amounts of soot) allowed the two locations along the laser line to be farther apart and therefore, make the angle easier to calculate. Because the OH-LIF and LII laser beams were co-planar and the LII images were matched to the OH-LIF images, the rotation angle found for the OH-LIF images should be the same for the LII images; therefore, both OH-LIF and LII images were rotated according to the wire images from the OH-LIF camera to correct for rotation of the cameras compared to the laser beams.

Dark Charge and Uniformity Corrections

A major source of noise in CCD cameras is due to thermal noise which generates electron-hole pairs even when the device is in total darkness (Raffel et al., 2007); for this reason, it is referred to as the dark charge. The production rate of electron-hole pairs is constant at a given temperature and exposure (Raffel et al., 2007). Therefore, the dark charge noise was accounted for by subtracting a constant bias calculated from dark charge images taken before and after each experimental day; these dark charge images were taken with external sources of interference, such as lasers or flames, removed.

Another correction is necessary to account for the vignetting effects of the CCD, which produce a radial decrease of light intensity in an image. To correct this effect and produce uniform intensity across an image, uniformity images were taken before and after each experimental day to quantify the vignetting effects so they could be divided out of the experimental images; a white sheet of paper was used as a blank, even surface for the uniformity images.

Background Interference

Extraneous signal due to other sources, such as the flame or the laser, can cause interference with the measured signal. To measure the impact of these sources, background interference caused by the laser (without flame) and the flame (without laser) were measured before and after every experimental day. Both types of interference were found to be less than 2% for LII and less than 10% for OH-LIF. Due to the non-uniform nature of the flames and attenuation in this burner system, however, it was not feasible to remove the background interference from the images so they remain in the final results. Additional interference was found in the OH-LIF images due to the incandescing soot and fluorescing polycyclic aromatic hydrocarbons (PAHs); PAH fluorescence is induced with excitation sources in the visible and UV spectrum, like that used for OH-LIF (Vander Wal, 1996; Schulz et al., 2006). This interference, which is further discussed in Section 9.3.2, was found to be non-negligible but was unable to be removed from the images.

OH-LIF specific corrections

Because the OH-LIF system had a consistent reference flame, corrections could be made to those images for beam profile and power corrections. Nonuniform signal intensities were recorded by the OH-LIF system across the beam sheet height with measured intensity reducing towards the sheet edges. As the slot burner flame itself was uniform throughout the sheet height, it provided a reference so the weaker edges of the beam profiles could be scaled accordingly. Also, as the signal intensity of the reference flame should remain constant, variations in shot-to-shot laser power could be corrected from layer to layer of the measurement images.

LII calibration

Although LII provides a qualitative measurement of soot concentration in the flame, it can be calibrated to provide a quantitative measurement of soot concentration. A calibration constant was found for the LII images each day using laser extinction (described in Section 3.2). Measurements used the uniformly sooting flat-flame burner (described in Section 2.1.3) for both LII and extinction; comparing the two results provides a calibration constant to convert the intensity of the LII images to a quantitative soot concentration so the LII results may be reported in parts per billion (ppb) of soot.

5 Comparison of Haitian Stoves

5.1 Introduction

Most of the ten million people of Haiti use solid fuels, primarily wood and charcoal, for cooking and heating, with the combustion of biomass equaling an estimated 70% of Haiti's annual energy use (Nexant Inc, 2010). Biomass cooking contributes to environmental damages such as deforestation and global climate change (fully discussed in Section 1.3). Charcoal is an especially wood-intensive fuel as wood is typically used not only as the base material for the charcoal but also is burned to produce the heat necessary to convert wood into charcoal. The unsustainable harvesting of wood and production of charcoal over several years has substantially contributed to widespread deforestation in Haiti; in 1923, 60% of Haiti was forested, but by 2009 only 2% of the forests remained (Hubbell et al., 2013; Lim et al., 2012; Highwood and Kinnersley, 2006; Nexant Inc, 2010). Charcoal for cooking also imposes a large economic burden on Haitians with families spending a significant portion of their income on cooking fuel. For example, in Port-au-Prince, a marmite (a local definition of the amount of charcoal needed to cook roughly half a day's worth of food) costs approximately 0.50 USD in the retail market, while the gross national income per capita is only about 760 USD (Booker et al., 2010; United Nations Children's Fund, 2012).

In January 2010, a devastating earthquake rendered approximately 1.5 million Haitians homeless (Yonetani, 2011). Owing to the significant economic burden of procuring cooking fuel felt by the survivors, many organizations, such as USAID, the Women's Refugee Committee, and the World Food Programme, called for the deployment of fuel-efficient cookstoves as an essential part of the relief efforts in Haiti (Nexant Inc, 2010; Women's Refugee Commission, 2010). The distributed stoves were intended to save fuel and reduce health and environmental burdens if possible. Cookstove distributors and non-governmental organizations (NGOs), however, had little to no data on the performance or cultural acceptability of most of the stoves. Because NGOs had neither the time nor the expertise and equipment to conduct experiments to determine the most appropriate stoves, the work discussed in this chapter examined stoves already in or intended for distribution in Haiti at that time to evaluate their performance and emissions characteristics, including cultural acceptability.

5.2 Experimental System

5.2.1 Stoves, Fuel, and Instrumentation

The cookstoves chosen for testing were identified through a field visit by scientists from Lawrence Berkeley National Laboratory (LBNL) to Port-au-Prince (Booker et al., 2010). Typical traditional charcoal cookstoves were purchased in Port-au-Prince and manufacturers of improved cookstoves were contacted to obtain cookstove units for testing. Based upon their timely availability, the four charcoal stoves described in Section 2.1.1 (Traditional Haitian, EcoRecho, Mirak, and Prakti) were included in this work.

Several preliminary tests were conducted with each stove prior to the official evaluations. Using the experience gained from the preliminary tests, each stove was operated in order to maximize combustion efficiency by adjusting airflow if possible. The cooking pots used for testing were common, traditional Haitian pots purchased in Port-au-Prince, as those would be the same pots used by cooks in the field.

Procuring adequate quantities of Haitian charcoal for all testing activities was deemed impractical, so the fuel used for the tests was Grillmark© all-natural lump charcoal. All-natural lump charcoal is produced in a fashion similar to Haitian charcoal, unlike charcoal briquettes which can have additives such as sand, and was broken into pieces similar in size to Haitian charcoal (no larger than 80 mm $\times$ 50 mm $\times$ 25 mm). Charcoal samples, analyzed using standard oven-drying procedures (ASTM International, 2007), were found to have a moisture content of 5.9%. Because some of the cookstoves were not designed to accommodate the large initial amount of charcoal used in the traditional stove, the initial amount of charcoal used in each stove was adjusted for the fuel bed size of that stove so it would be similar to the expected fuel load in the field (Bentson et al., 2013). The initial amounts of charcoal were 280 g, 450 g, 200 g, and 475 g for the EcoRecho, Mirak, Prakti, and traditional, respectively. To ignite each fuel bed, 10 – 20 g of high resin pine was used; additional pieces of charcoal were added to the original fuel bed as needed to maintain a steady, hot fire.

The aerosol test system described in Section 3.1 was used for these tests. All testing was performed in a well-monitored indoor space with initial temperature and humidity data recorded. The CO and CO_2 concentrations were continuously measured (1 Hz) using a CAI gas analyzer (Section 2.2). In addition, the weight of charcoal added to the stove and the temperature of the food or water were continuously measured and recorded.

5.2.2 Experimental Protocols

Two testing protocols were used for these evaluations, a Water Boiling Test (WBT) and a Controlled Cooking Test (CCT); full descriptions of the WBT and CCT may be found in Sections 4.1 and 4.3 respectively. Because each test protocol has limitations in providing high quality laboratory findings and estimations of actual results in the field, both protocols were used for this evaluation.

The WBT has limitations assessing field performance as the protocol is dissimilar to actual Haitian cooking practices. A CCT can provide a more accurate portrayal of cookstove performance in the field. However unlike the WBT, a customized CCT protocol must be developed for each cultural cooking style, making it meaningless to use a CCT protocol to compare stoves developed for different cultures; this is where the WBT results are more useful.

5.3 Results

Results of the comparison of Haitian cookstoves are presented using five metrics relevant to efficient cookstove design and dissemination: time to boil, specific fuel consumption, thermal efficiency, CO emissions, and modified combustion efficiency (see Section 4.4 for full descriptions). From interviews with women in the field, the time to boil was found to be extremely important from the user perspective, as women are unlikely to use a stove that lengthens their usual cooking time. Specific fuel consumption indicates if fuel savings occur, which is important to both the users and environmental agencies. Thermal and modified combustion efficiencies are relevant to stove designers, while the emissions data provides information on the release of pollutants to the environment, important information for funding and public health agencies, governments, and policy makers.

For all metrics, statistical analysis was conducted using the Student's t-distribution to look for statistically significant outcomes. When presenting results for each performance metric, error bars represent 95% confidence intervals calculated using the Student's t-distribution.

5.3.1 Performance Metrics

Time to Boil

As can be seen in Fig. 5.1, for the cold start phase, the traditional stove brought water to boil at least 15 minutes faster than any of the other stoves on average, while the other stoves performed fairly similarly to one another. The amount of time necessary to cook is extremely important to end users per discussions with women and organizations in the field. Therefore, the results indicate a potential barrier to the adoption of these improved cookstoves in the field. For the hot start phase, the traditional stove also had the fastest time to boil; however, the EcoRecho and Prakti were only marginally slower than the traditional.

A trend can be noticed in the average times to boil for the cold and hot start phases due to the differences in the thermal masses of the stoves. During a hot start, the Prakti and EcoRecho stoves, which are insulated and retain heat, are comparable in time to boil with the traditional stove, while during the cold start they take a longer time. The percent difference between the cold and hot start times to boil for each stove and their weight are presented in Table 5.1. For this comparison, weight is held as a proxy for thermal mass;

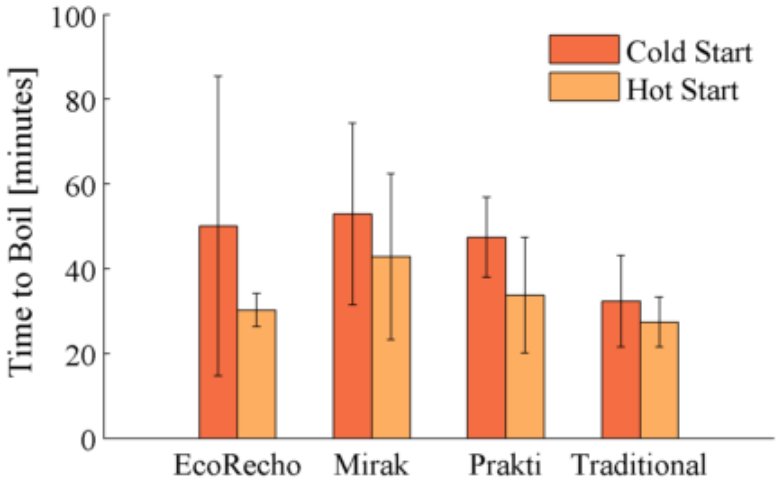

Figure 5.1: The time to boil 2.5 L of water, reported in minutes, for both high power phases of the WBT. For cold starts, the traditional stove was noticeably faster on average than any other stove, but for hot starts, the EcoRecho and Prakti stoves were similar to the traditional one. Error bars represent 95% confidence intervals.

Table 5.1: The weight of each stove (kg) and the percent difference between their cold and hot start times to boil. As the weight increases, so does the percent difference, indicating the importance of even modest differences in thermal mass for stove performance comparisons.

	Weight of stove [kg]	Percent difference [%]
Traditional	2.8	17
Mirak	3.0	21
Prakti	4.6	32
EcoRecho	6.2	50

it overestimates the relative thermal mass for the two lighter, all-metal stoves (traditional and Mirak) and underestimates it for the two heavier stoves made of metal and insulation (Prakti and EcoRecho) so errors due to using the weight as a proxy would only support the resulting trend seen in Table 5.1. It is seen that as the weight of the stove increases, so does the percent difference between the cold and hot start times to boil.

One would expect a large, thermally-massive stove to have a larger difference in times to boil between hot and cold starts than a thermally-light stove. However, none of the stoves in this test are considered particularly thermally-massive, so the trend shown in Table 5.1 suggests thermal mass is an important consideration even for small, thermally-light stoves.

Thermal Efficiency

The average thermal efficiency results for the three improved stoves were better than that of the traditional stove (Table 5.2). The Prakti and EcoRecho were the most efficient and the traditional and Mirak were the least efficient with the Prakti and traditional stoves being significantly different from each other at $p = 0.05$.

Table 5.2: Average thermal efficiencies for the WBTs. All improved stoves had on average a higher thermal efficiency than the traditional one. Error represents a 95% confidence.

	Cold Start Thermal Efficiency [%]	Hot Start Thermal Efficiency [%]
EcoRecho	25.1 ± 2.5	24.6 ± 4.9
Mirak	23.9 ± 1.4	26.9 ± 12.8
Prakti	31.1 ± 3.7	35.3 ± 5.2
Traditional	18.9 ± 1.9	21.7 ± 2.8

Specific Fuel Consumption

All improved stoves reduced fuel use on average compared to the traditional, and in the case of the CCTs, improved stoves reduced fuel by a statistically significant ($p = 0.05$) amount. The results, shown in Fig. 5.2, demonstrate that the stoves dubbed to be "fuel-efficient" actually do save fuel under laboratory settings, both in the strict settings of the WBT and the potentially more realistic settings of the CCT. The results lead to the hope that if cooks in the field have correct training and operate stoves optimally, they will save fuel when cooking, an important consideration for deforested Haiti.

5.3.2 Emissions

Carbon Monoxide Emissions

The total CO in grams emitted from each stove is shown in Fig. 5.3. For the WBT, the Mirak and Prakti stoves emitted less CO than the traditional, on average. For the CCT, the EcoRecho and Prakti stoves both statistically significantly reduced CO emissions compared to the traditional and the Mirak reduced CO on average.

Modified Combustion Efficiency

All stoves had MCEs in a range of 89 – 92% for the WBT and 91.5 – 93% for the CCT (Fig. 5.4). Studies have found these MCE values indicate smoldering to mixed combustion (Ward and Radke, 1993; Urbanski, 2013). For the WBT, the EcoRecho and Prakti appear to have lower combustion efficiencies than the Mirak and traditional. This would indicate the

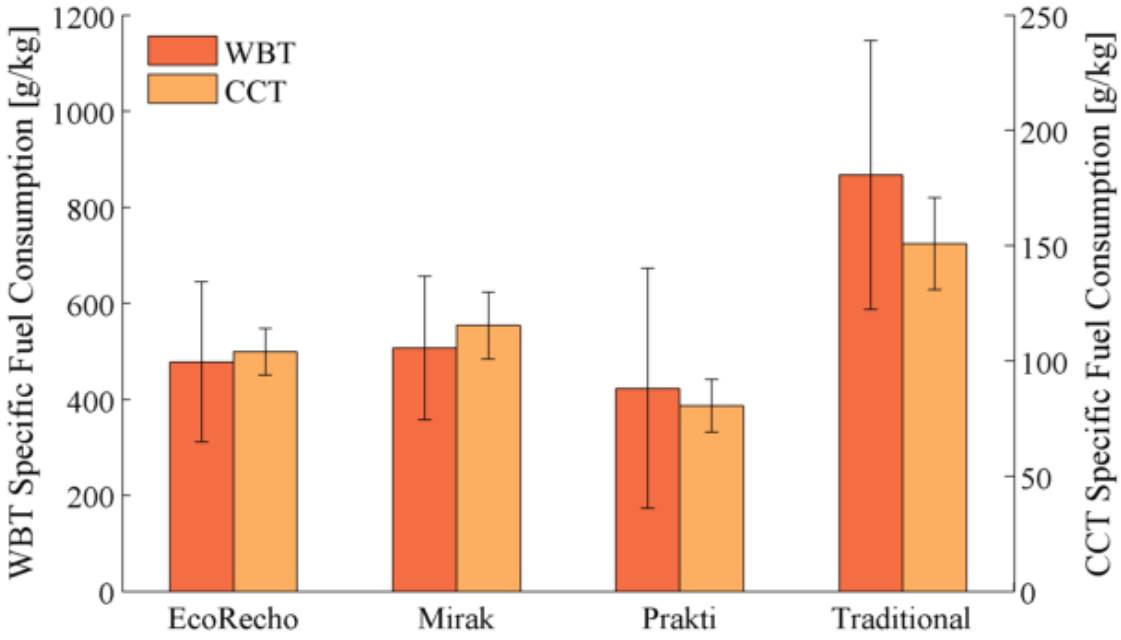

Figure 5.2: Average specific fuel consumption, reported in grams of fuel per kilogram of product, during the WBTs and the CCTs. All improved stoves saved fuel compared to the traditional for both the WBTs (on average) and the CCTs (statistically significantly). Error bars represent 95% confidence intervals.

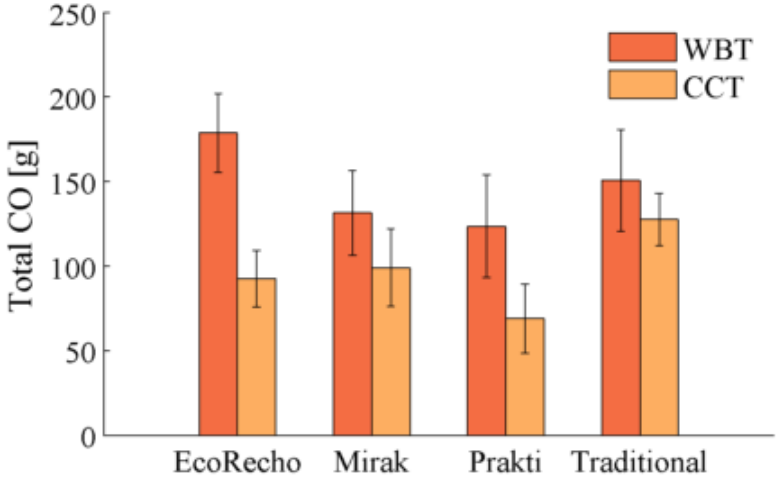

Figure 5.3: The total CO emitted per stove for each test. Note that the Prakti and Mirak stoves have lower emissions than the traditional for the WBT and all three improved stoves have reduced emissions for the CCT. Error bars represent a 95% confidence interval.

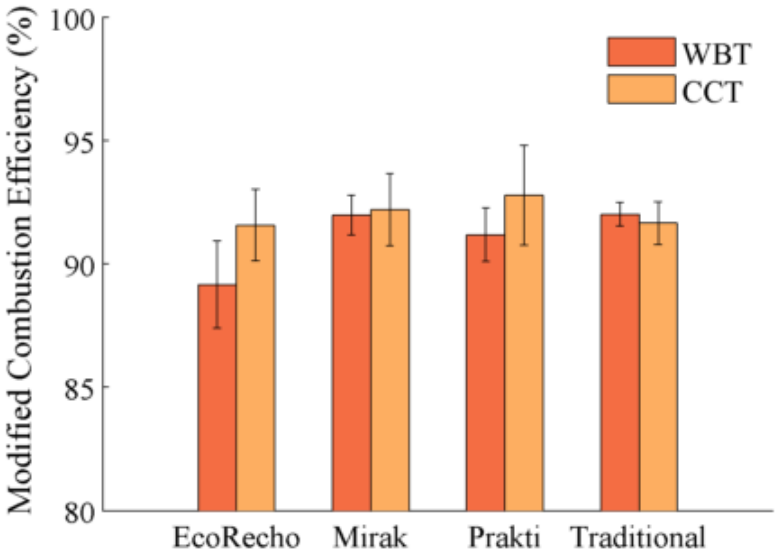

Figure 5.4: The MCEs for both the WBTs and CCTs; error bars represent 95% confidence intervals. Overall, the MCEs are comparable across the stoves, with a deviation between stoves of less than 3.3% for the WBTs and 0.6% for the CCTs. The values range from 89% to 93% indicating smoldering to mixed combustion, which is as expected for charcoal combustion.

EcoRecho and Prakti stoves are burning with a less intense smoldering fire than the others. For the CCT, the standard deviation between the average MCEs of the stoves is less than 0.6%, indicating the efficiencies are comparable.

5.4 Discussion

5.4.1 WBT vs. CCT results

Upon examining the data from the WBTs and CCTs, a few key points emerge. The first is the difference between the stoves' performance per WBT and CCT data, especially for the total CO_2. While the WBT protocol is the universal standard for testing any cookstove in a laboratory setting, the CCT more closely mimics real-world cooking practices and may better indicate true stove performance in the field (Dutt and Ravindranath, 1993; Johnson et al., 2008; Smith et al., 2007). For this reason, variations in stove performance between the WBT and CCT could be quite meaningful as they would indicate the necessity of using multiple protocols for scientific comparisons in the laboratory when estimating field performance. One cause of these variations could be the difference between the magnitude of thermal power, as calculated in Section 4.4, needed to complete a WBT versus a CCT. Example thermal power

cycles for the WBT and CCT in the traditional stove are shown in Fig. 5.5 and Fig. 5.6, respectively, with the different transition events of the tests numbered sequentially.

In Fig. 5.5 prior to '1' , the thermal power increases as the fire spreads in the charcoal bed. When the pot is placed on the fire at '1', thermal power first drops and then increases again until it becomes stable and plateaus until the water boils at '2', ending the cold start portion of the WBT. At this point, the charcoal is emptied between the end of the cold start ('2') and the beginning of the hot start ('3'). The power drops to zero in this interval as the fuel is replaced. A similar rise and plateau in thermal power is seen during the hot start from '4' to '5' as was seen during the cold start from '1' to '2'. The hot start uses slightly less power as the stove is already warm. From '5' to '6', there is a dip in power between the end of the hot start and beginning of the simmer, as the pot is quickly removed for weighing. After the simmer phase begins at '6', the power decreases except when the fire is fed with fresh charcoal at approximately 7100 seconds.

In Fig. 5.6, the rise in thermal power can be seen prior to '1' as the fire lights. At '1', the bean pot was placed on the fire and a large amount of power was required to heat up the pot. By '2', the beans were simmering and the power decreased as the charcoal burns down until the bean phase ends at '3'. Between '3' and '4', the fire is fed and at '4' the vegetable pot is put on. Power increases as charcoal pieces catch on fire, heating up the vegetable pot, which doesn't quite reach simmering before stopping the test at '5'. At '6', the bean pot is placed on the stove again, but heat from the first boiling is still retained so it does not need much power to regain a simmer and then the power decreases. The rice is added at '7' and is quickly brought back to a simmer at '8'. From there, the simmer continues until the end of the test, and the power decreases accordingly.

Although there are some similarities between the two cycles, there are several key differences between them, such as the large amount of energy needed for the hot start ignition in the WBT that does not exist in the CCT. On average over the test duration, a WBT uses approximately 2.3 kW and a CCT uses approximately 1.6 kW, with peak powers of approximately 4.7 kW and 3.0 kW, respectively. The differences between the WBT and CCT in the total amount of thermal energy used as well as fluctuations in the power could result in producing different amounts of emissions and different thermal efficiencies, as well as consuming different amounts of fuel.

5.4.2 Sample Size

The second conclusion drawn from these comparison tests is the need for attention to sample size, which could be a contributing factor to the differences between the WBT and the CCT results. As observed by prior researchers (e.g. Wang et al. (2014)), an appropriately large number of replicate tests must be conducted to obtain useful results with reasonable confidence intervals. Due to the nature of the Student's t-distribution, smaller numbers of replicate tests lead to larger confidence intervals. This is apparent throughout the test data when comparing the amount of error in the WBT and CCT results, as the magnitude of

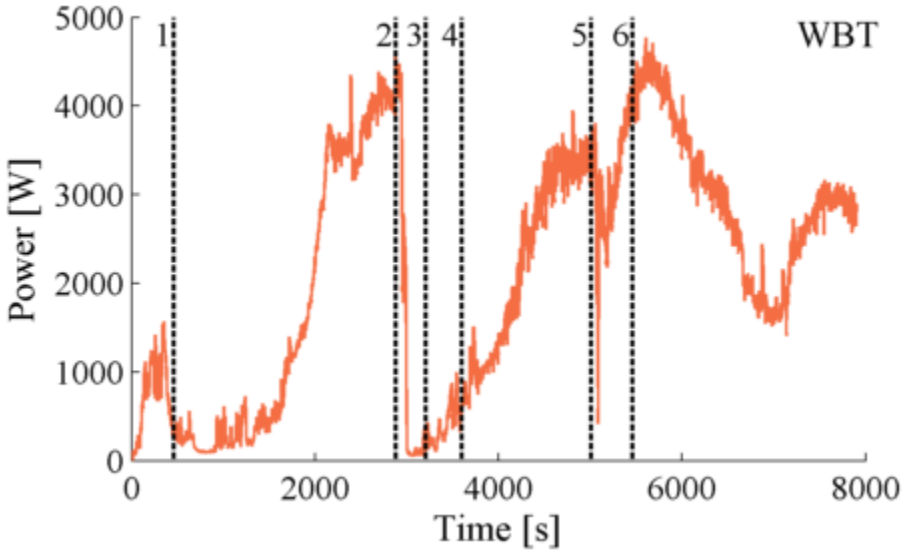

Figure 5.5: Typical power cycle for a WBT of the traditional stove. Vertical numbered lines represent transitions in the test: 1. Pot on for the cold start; 2. End cold start; 3. Begin hot start; 4. Pot on for the hot start; 5. End hot start; 6. Begin simmer.

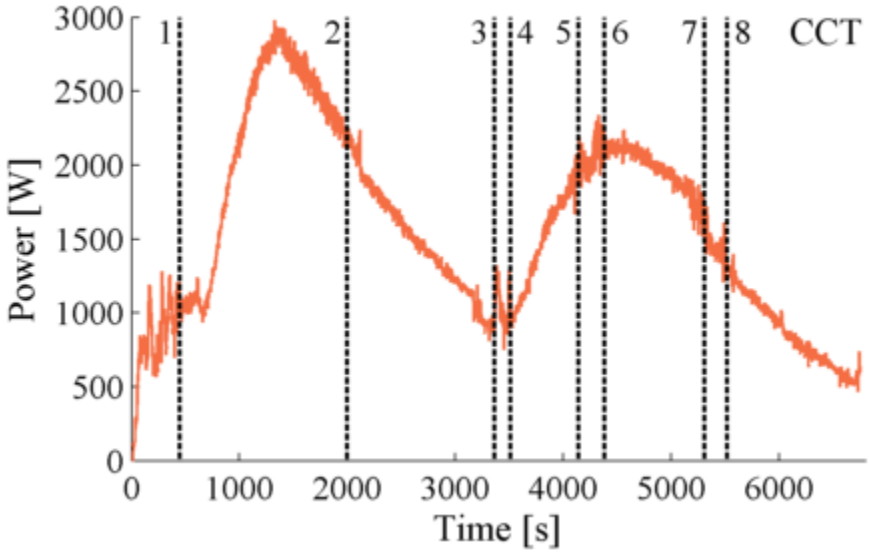

Figure 5.6: Typical power cycle for a CCT of the traditional stove. Vertical numbered lines represent transitions in the test: 1. Bean Pot on; 2. Bean Pot simmering begins; 3. End Bean phase; 4. Vegetable Pot on; 5. Vegetable Pot off; 6. Bean Pot on again; 7. Rice added; 8. Rice and bean mixture simmering begins.

inherent variability was initially underestimated when conducting the WBTs, so the number of replicate tests was increased to obtain tighter confidence intervals for the CCT results.

To illustrate the impact sample size has on error, the specific fuel consumption results for the EcoRecho stove are highlighted. Sample sizes for the average specific fuel consumption of the WBT simmer, WBT cold/hot starts, and the CCT were 3, 4, and 8 respectively. When comparing the amount of error to the average result, the percent errors for these trials are 60%, 30%, and 10% respectively. The data for the other stoves show similar results and trends, emphasizing the need for adequate replicate tests to reduce large statistical error.

5.5 Conclusions

Three improved cookstoves were compared to a traditional Haitian cookstove and the results revealed three key findings. First, all improved stoves saved fuel on average over the traditional Haitian stove, accomplishing the goal of the disseminating entities. However, it is crucial to note that the traditional stove boiled water more than 15 minutes faster than any improved stove during the cold start, which is very important from a users' viewpoint and therefore a potential barrier to user adoption if unaccounted for in improved stove design. Second, the improved stoves reduced the amounts of pollutants emitted overall, owing to their higher thermal efficiencies, despite having similar modified combustion efficiencies to the traditional stove. Third, some results were obscured by sizable statistical errors (i.e., large confidence intervals around mean reported values), revealing the need for a greater number of replicate tests when evaluating cookstoves to avoid inconclusive results.

One interesting observation during the trials was the effect of modest differences in thermal mass for stoves not considered to be thermally massive; even relatively minor differences in mass appear to affect the ratio of times to boil for the cold and hot starts.

This chapter of work provided an understanding of stove users' difficulties lighting the charcoal stoves and the desire for a shorter cooking time. Thus, the next chapter focuses on reducing difficulties and the time necessary to ignite the charcoal bed on the traditional Haitian stove.

6 Lighting Cone: Air flow modification on a Haitian stove

6.1 Introduction

Charcoal beds in traditional stoves can have slow ignition times due to interference from the wind and the initial lack of draft through the stove body and charcoal bed. The combustion rate of charcoal is heavily dependent on the extent to which oxygen can reach its surface and in stoves with relatively shallow and exposed charcoal beds, it is difficult to achieve the draft required to create a self-sustaining flow of oxygen through the charcoal (Shelton, 1983). Since the combustion processes are stifled due to a lack of oxygen, devices that increase the amount of oxygen reaching the surface of the charcoal can greatly speed its ignition, reducing the amount of time needed to begin cooking.

Although devices exist that decrease the amount of time needed for a charcoal bed to be well-lit, such as charcoal chimneys and lighter fluid, these products can be expensive and toxic and are not well-suited for developing economies with low incomes where cooking with charcoal is a daily necessity. A straightforward and inexpensive accessory, known as a lighting cone, is already in use in countries such as China, Zaire, and Mozambique to reduce the lighting time of charcoal stoves. However, little literature exists (Lask and Gadgil, 2015) to confirm if and to what extent the lighting cone performs as desired. Similarly, it is unknown if a lighting cone creates adverse effects, such as increasing carbon monoxide or ultrafine particle emissions. Because such effects would likely go unnoticed by cooks in the field, research was needed to identify any issues harmful for human health or the environment prior to wider spread dissemination of the cones. The work in this chapter aims to evaluate the effectiveness of a lighting cone and its impacts on lighting time, fuel consumption, and emission outputs from the ignition phase of a charcoal-burning fire.

6.2 Experimental System

6.2.1 Lighting Cone

A lighting cone (Fig. 6.1) is a conical tube of sheet metal that is intended to decrease the time needed for ignition by increasing draft through the fuel bed. It is placed on the charcoal bed after the kindling, such as sappy wood or newspaper, has been lit, and is removed once the charcoal is considered lit enough to sustain its combustion even if a pot is placed on the stove. The slightly conical shape allows for improved mechanical stability in placing the cone on the somewhat uneven charcoal bed and reduces the likelihood of wind-driven downdrafts of ambient air entering the top of the cone.

After building and testing several lighting cones, the lighting cone used in this work had a bottom diameter (200 mm) sized to adequately encompass the fuel bed with a top diameter of 100 mm to achieve a slight taper. It was 610 mm tall, which produced adequate draft, and was made from 0.3 mm thick stainless steel sheet metal.

6.2.2 Stove, Fuel, and Instrumentation

The traditional Haitian stove, described in Section 2.1.1, was selected for testing the lighting cone and was chosen for three primary reasons: 1. Most of the 10 million Haitian people cook with charcoal and wood, which totals 70% of Haiti's energy consumption (Nexant Inc, 2010;

Figure 6.1: Lighting cone used for experiments on a traditional Haitian stove.

International Energy Agency, 2004; Van der Plas, 2007); 2. The traditional stove design features a shallow and exposed charcoal bed well-suited for lighting cones; and 3. Prior experience operating the traditional stove as described in Chapter 5.

All testing was performed in the updated emissions setup in the LBNL cookstove lab as described in Section 3.1.2. The fuel used for testing was the same Grillmark© all-natural lump charcoal as used for the Haitian stove comparison testing discussed in Chapter 5.

6.2.3 Protocol and Analysis

Each test was performed by filling the traditional stove with 475 g of charcoal. The charcoal was arranged in a toroidal pile of approximately 200 mm outer diameter and 60 mm inner diameter. High resin pine (total mass of 5 ± 0.2 g) was broken into 3 – 5 thin pieces and arranged in a pyramid-like structure in the center of the charcoal toroid to act as a fire starter. This fuel bed setup is similar to that observed from Haitian cooks using this stove. If the test included a lighting cone, the cone was placed on the charcoal bed immediately after the high resin pine was first lit.

Lighting time was recorded from when the high resin pine was lit until the charcoal bed was considered well-lit. Based on conversations with Haitian cooks, the bed was considered well-lit when at least 70% of the charcoal pieces were observed to be red, which occurred at a thermal power of approximately 2.4 kW. Fuel consumption was continuously recorded on the platform scale as well as weighing the charcoal fuel before and after each test.

Ten baseline (without cone) and eleven lighting cone tests were conducted to achieve reasonable confidence in the results. Statistical significance was determined for all tests by applying the Student's t-test as the sample size was small ($n < 30$) (Taylor, 1997; Spiegel et al., 2008). All error bars on the graphs represent 95% confidence intervals. To calibrate the DustTrak data, a calibration curve was developed by comparing DustTrak and gravimetric filter data (shown in Fig. 6.2). Ideally, the ratio of DustTrak to gravimetric $PM_{2.5}$ measurements would be 1:1 (as discussed in Section 2.2), but the DustTrak was found to overestimate $PM_{2.5}$ resulting in a calibration curve of: $PM_{2.5,filt} = 0.26 PM_{2.5,DT} + 1$.

6.3 Results and Discussion

6.3.1 Time to Light and Specific Fuel Consumption

Using a lighting cone was found to decrease lighting time by over 50% (Fig. 6.3), reducing the time needed from roughly seven minutes to three minutes. Although the burn rate for the lighting cone was found to be slightly greater than the baseline (4.1 ± 0.4 g/min for the baseline and 5.4 ± 0.9 g/min for the lighting cone, where the error is a 95% confidence interval), the significant decrease in lighting time counteracted the effect of a higher burn rate on total fuel consumption. As can be seen in Fig. 6.3, the time necessary to light the cone was short enough that the lighting cone still significantly reduced the fuel consumed

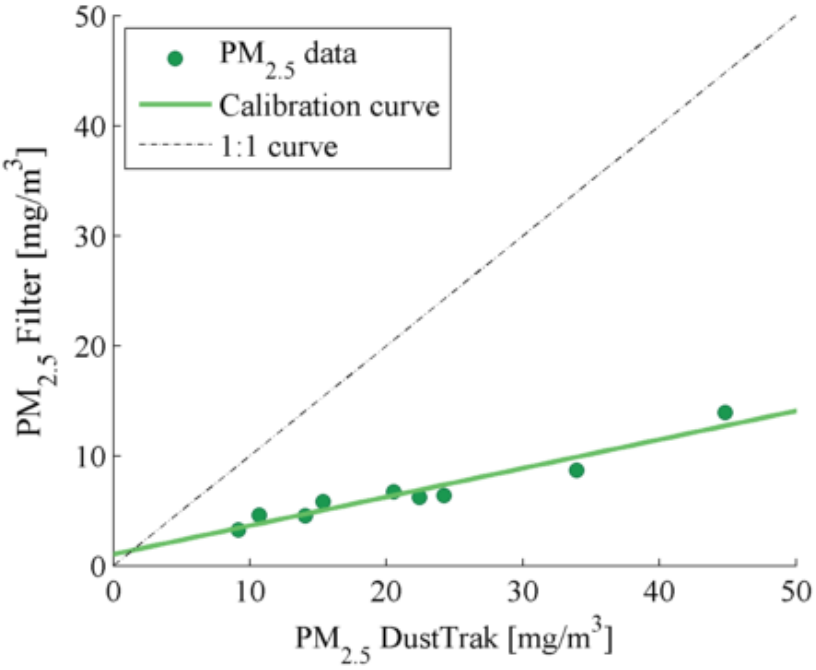

Figure 6.2: $PM_{2.5}$ data from the gravimetric filter and DustTrak allows the development of a calibration curve for correcting the DustTrak data: $PM_{2.5,filt} = 0.26PM_{2.5,DT} + 1$. A 1:1 curve is also shown for reference.

during ignition. These results indicate that the lighting cone works as expected, increasing the draft through the charcoal bed to speed ignition by increasing the burn rate (grams of fuel per second) and promoting higher temperatures in the charcoal bed.

6.3.2 Emissions

Fig. 6.4 shows the total grams of CO, $PM_{2.5}$, and BC emitted from the baseline and lighting cone cases. A far greater amount of CO is emitted than particulates ($PM_{2.5}$ and BC). Charcoal combustion tends to produce a significant amount of CO due to its smoldering combustion conditions and less particulate matter than other fuels such as wood because the volatiles which typically form particles have been driven off in the charcoal production process (Ward and Radke, 1993; Shelton, 1983).

The lighting cone is shown to more than halve the CO emitted during ignition. The modified combustion efficiency was approximately the same for both the baseline and lighting cone cases ($96.1 \pm 0.4\%$ and $96.3 \pm 0.7\%$, respectively), so it is reasonable to assume the reduction in CO is due primarily to the shorter lighting time. The lighting cone did not have a statistically significant ($p = 0.05$) effect on particulate emissions. The particles emitted are likely from the combustion of the high resin pine fire starter since the charcoal contains little

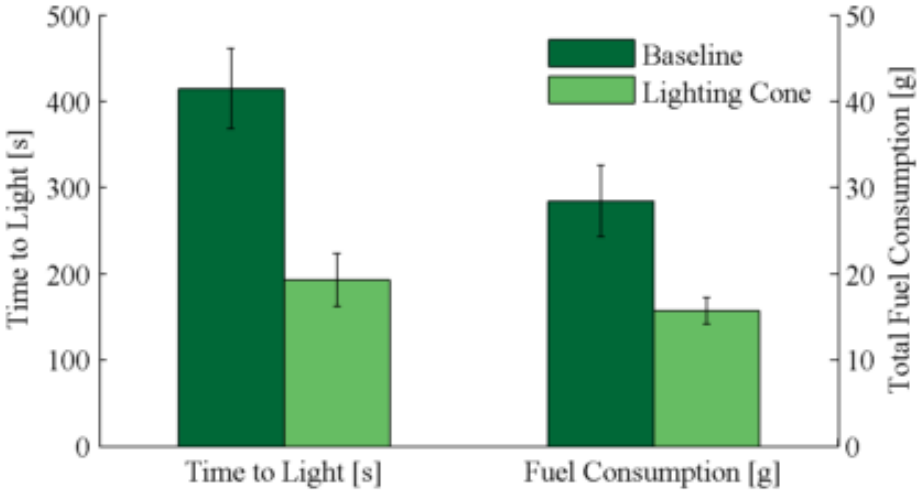

Figure 6.3: Time to light and fuel consumption with and without a lighting cone. The lighting cone decreased lighting time by over 50% and fuel consumption by over 40%. For both time to light and fuel consumption, the differences are significant at $p = 0.05$. Error bars represent 95% confidence intervals.

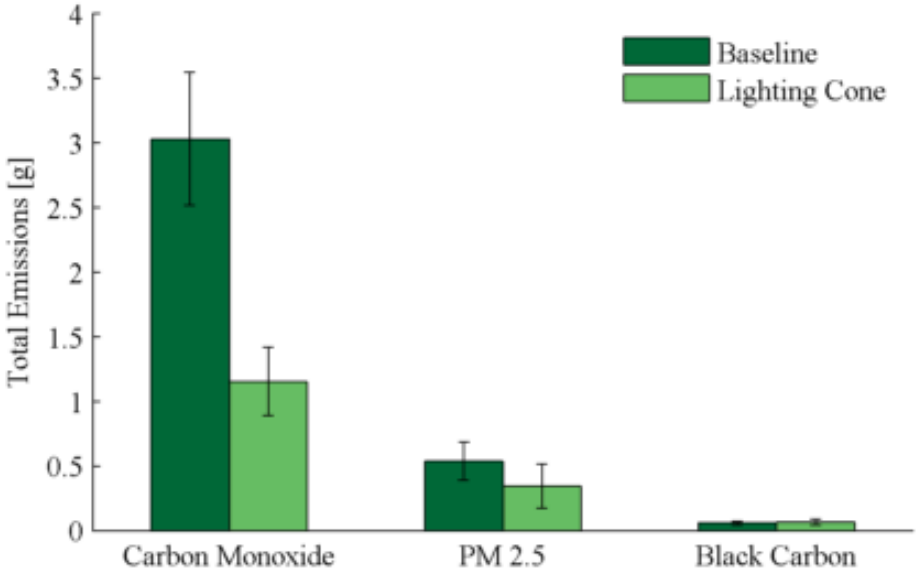

Figure 6.4: Emissions during ignition with and without the lighting cone: CO, $PM_{2.5}$, and BC. It was found the lighting cone decreased emitted CO by over 50% (statistically significant at $p = 0.05$) with relatively small effects on particulate emissions. Error bars represent 95% confidence intervals.

volatiles, so it is unlikely to be able to reduce those emissions dramatically without changing the ignition source.

Particle Size Distribution

Measurements of the size distribution of emitted particles show that most of the particles are quite small (< 1 µm) with a large difference seen between the baseline and cone cases, shown in Fig. 6.5. The lighting cone greatly reduced the number of ultrafine (< 100 nm) particles (UFPs) compared to the baseline. While the particles emitted in combustion are harmful to human health, recent research indicates that UFPs are particularly detrimental (Oberdörster et al., 2005; MacNee and Donaldson, 2003). The reduction of UFPs suggests that in addition to user convenience and comfort, the lighting cone could also be better for human health than traditional lighting practices.

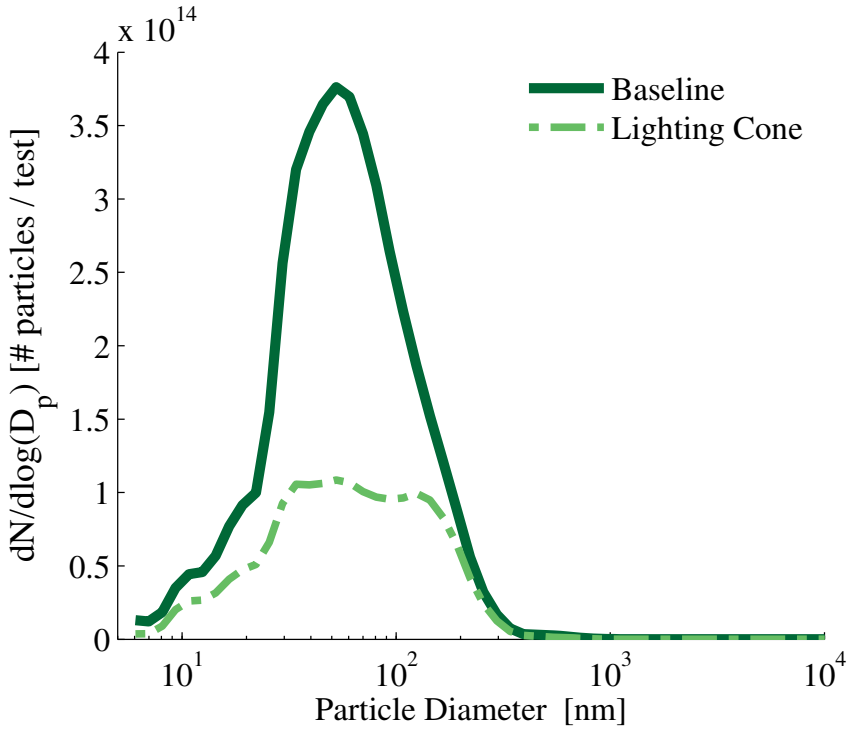

Figure 6.5: Average size distribution of particulates from the baseline and lighting cone. The lighting cone was found to greatly reduce the number of UFPs during ignition compared to the baseline. There were relatively few particles larger than 1 µm released from either the baseline or lighting cone cases.

6.4 Conclusions

A lighting cone is a relatively easy-to-build and inexpensive accessory which has been measured to decrease the lighting time of Haitian charcoal stoves by over 50%. User convenience is a well-known crucial consideration in stove adoption. Therefore, a device that reduces the amount of time and effort needed to light a stove could be beneficial not only for lighting traditional stoves but also as an accompaniment for promoting more efficient stoves, especially if the stove has difficulties with ignition. In addition to shortening lighting time, a lighting cone improves the ignition stage of charcoal stoves for both the environment and human health by reducing the number of UFPs emitted, reducing charcoal consumption by over 40%, and reducing CO emissions by over 50% during ignition.

7 Halo Stove: Air injection in a natural draft wood-burning stove

7.1 Introduction

Compared to charcoal cookstoves, like those discussed in Chapters 5 and 6, the burning of wood in natural draft stoves tends to produce large amounts of black carbon (BC) (Jetter and Kariher, 2009; Jetter et al., 2012). As discussed in Section 1.3, BC emissions from biomass stoves greatly impact the environment as they have a global warming potential equal to ~680 times that of CO_2 and biomass combustion produces approximately 30% of global BC emissions (Bond et al., 2004a, 2013; Hansen and Nazarenko, 2004). Also, BC, as particulate matter, has been shown to be detrimental to human health especially in smaller size ranges (< 10 μm) (Donaldson and MacNee, 1998; Oberdörster et al., 2005; MacNee and Donaldson, 2003; Auffan et al., 2009). Combining the impacts of BC with its short lifetime in the atmosphere (on the order of days), the mitigation of soot from biomass cookstoves is a promising short-term method for addressing global warming (USAID, 2010; UNEP, 2011; Gustafsson et al., 2009; Shindell et al., 2012; Wallack and Ramanathan, 2009; Ramanathan and Carmichael, 2008). Therefore, there is interest in exploring new designs for reducing particulate matter emissions from biomass stoves (Sutar et al., 2015; Tryner et al., 2014; Still et al., 2015), including BC (Kar et al., 2012; Just et al., 2013; Preble et al., 2014; Johnson et al., 2008; MacCarty et al., 2008).

One potentially favorable design option is injecting air into the gas-phase combustion zone to promote turbulence of reacting gases and particles in the flame zone (referred to simply as air injection in this work). In theory (discussed in Sections 1.3 and 1.4), the turbulence generated by the injected air promotes more complete combustion, including soot oxidation, by increasing the mixing of the hot gases with air; also, downward or tangential air injection could recirculate or swirl the air in the combustion chamber, lengthening the residence time of particles in the hot flame region. However, air injection could have negative effects such as increasing the burn rate of the fuel, causing more fuel to be consumed per task; quenching the combustion processes, leading to a greater volume of incomplete combustion products being released; and directing hot gases away from the cooking pot, reducing thermal efficiency and lengthening cooking times. Although MacCarty et al. (2010) and Rapp et al. (2016) found a

natural draft, side-fed stove with secondary air injection to reduce particulate matter, other previous studies including forced draft or secondary air injection in batch-fed stoves have shown that air injection can either greatly reduce or increase the mass of particles emitted (Jetter and Kariher, 2009; Jetter et al., 2012; Sutar et al., 2015; MacCarty et al., 2010; Still et al., 2015). Therefore, stove designers need to carefully consider the parameters chosen for secondary air injection systems, such as injection angle and flow rate, as inappropriate air injection designs could produce undesirable results. However, little discussion exists in the literature examining the differences in air injection design parameters for biomass cookstoves that lead to these large differences between emissions results of stoves with air injection. Research into the effects of different mixing strategies is needed to provide a basis of understanding for designers as they apply secondary air injection systems in cookstoves. The work in this chapter explores different mixing strategies for secondary air injection in a natural-draft rocket stove in order to evaluate the impact on BC emissions as well as other important stove emission and performance metrics. Note, many hypotheses are posed in the Results and Discussion sections based on these ex-situ emissions and performance results; the in-situ measurements conducted in Chapters 8 – 9 are intended to begin evaluating those hypotheses.

7.2 Halo Design and System

The Halo Stove, a new experimental stove discussed in Section 2.1.2, was developed to explore the effects of different mixing strategies in a natural-draft rocket stove. Natural-draft rocket stoves are a popular and oft-studied stove type (Jetter and Kariher, 2009; Jetter et al., 2012; MacCarty et al., 2010; Sutar et al., 2015). The Halo Stove was based on the Berkeley-Darfur Stove (BDS), a fuel-efficient, natural-draft rocket stove described in Section 2.1.2. Because the BDS is well-characterized and has traits of many other wood-burning rocket stoves (Jetter and Kariher, 2009; Preble et al., 2014), it serves a good baseline of comparison and starting point for modification.

Three mixing strategies were chosen to elucidate the causes of positive and negative impacts of injected air as it interacts with the gaseous and solid combustion zones. The first strategy injected air straight down onto the fire, potentially promoting recirculation of particles in the flame zone while heavily interacting with the solid fuel bed. A similar air flow design used in downdraft residential wood stoves has shown that it will promote turbulence and mixing near the fuel, leading to easier ignition and ability to combust fuels with high moisture content (Shelton, 1983); however, the heavy interaction with the fuel bed is intended to highlight effects of the air flow on the solid fuel, either positive or negative. The second strategy injected air at an angle inward toward the flame, potentially lessening interaction with the solid fuel while improving turbulent mixing. The third strategy introduced a tangential component to the angled air injection, creating a swirling effect. Swirling flow is often suggested for other biomass combustion systems, such as grate-fired boilers, to further

increase turbulent mixing and residence time in the flame zone (Yin et al., 2008; Suri and Horio, 2010).

The Halo Stove injects air into the combustion chamber via a copper annulus which is positioned above the combustion chamber like a halo (shown in Fig. 7.1). The halo design was chosen because it allowed for a variety of mixing strategies to be explored while maintaining the design benefits of the BDS as it required only one minor modification to the BDS structure (a hole in the stove body through which to mount a halo); also the minimality of the design avoided potentially adverse effects, such as adding a large thermal sink which could reduce thermal efficiency, and kept all hardware for the air injection system out of the laser beam paths for the desired laser diagnostic experiments (Chapter 9). Halos with different injection angles could be readily manufactured and interchanged in the Halo Stove; four halos were developed to examine the three mixing strategies including two angled-type halos which were developed to further evaluate the impact of different injection angles.

1. 90 Straight (90STR): Holes are set such that air is injected straight down onto the fire (90° from horizontal). The inner diameter of the halo is 102 mm.
2. 45 Angled (45ANG): Holes are set such that air is injected at a 45° angle from the horizontal. The inner diameter of the halo is 140 mm.
3. 30 Angled (30ANG): Holes are set such that air is injected at a 30° angle from the horizontal. The inner diameter of the halo is 140 mm.
4. 30 Swirled (30SWL): Same design as 30ANG, but the holes have been augmented to inject air at a $30-40°$ angle in the horizontal plane (shown in Fig. 7.2), in addition to the 30° angle in the vertical plane, to create a swirling effect. The inner diameter of the halo is 140 mm.

The inner diameter of the 90STR was sized smaller so the injected air would interact with the flame at a similar location to the other halos as opposed to injecting air near the perimeter of the firebox away from the primary combustion zone as it would if the diameters were the same. All halos were constructed using 3/8" copper tubing that was hand-rolled to the desired diameter to form a closed loop with one end bending outward for attachment to the stove (see Fig. 7.1). The halo was then mounted to a tilting, rotary, adjustable-angle, indexing plate on a milling machine to drill 10 holes (3/32") with equidistant spacing at the desired angle for injection. The same modified BDS was used for all trials. Because the halos were mounted above the firebox, the only modification required was a single hole in the outer wall of the BDS. Halos were mounted in the BDS using a through-wall fitting, making them secure but easily interchangeable. Air was injected using a compressed air supply, regulated by an inline rotameter and maintained at room temperature using a copper heat exchanger.

Figure 7.1: Top view of the 90STR halo mounted in the Halo Stove.

(a) 30ANG

(b) 30SWL

Figure 7.2: The holes in the 30SWL halo (b) have been augmented from those of the 30ANG halo (a) to add a $30-40^{\circ}$ angle in the horizontal direction.

7.3 Preliminary Halo Trials

Short preliminary trials of the halos were conducted prior to a full test series for three main purposes: 1. To validate if the halos produced a measurable impact on BC emissions; 2. To judge the uniqueness of results between the mixing strategies (i.e. Are the results different enough between the mixing strategies to warrant pursuing all strategies?); and 3. To establish a suitable air flow rate that highlights the uniqueness of results for further examination in the full test series.

7.3.1 Experimental Setup and Protocol

The experimental setup described in Section 3.1.2 was employed for data collection and the evaluating metrics were calculated as discussed in Section 4.4. As these were preliminary trials, only $1-2$ tests were conducted per case. The $PM_{2.5}$ data presented is from the DustTrak, corrected using the calibration developed in Section 7.4. The stove was initially

loaded and lit with approximately 15 g of pine wood shavings and 60 g of Douglas fir kindling sticks (80 mm × 5 mm × 5 mm). Using Douglas fir fuelwood (200 mm × 20 mm × 20 mm sticks), the fire was then brought to and maintained at a CO_2 output of 3000 ppmv (~5 kW, as calculated in Section 4.4). Once the fire was established, air was injected for 5 minutes at each of four different flow rates (14.2, 28.3, 42.5, and 56.6 L/min). Between each flow rate, no air was injected for 3 minutes so the fire could return to the baseline state.

7.3.2 Results

The emissions results of these preliminary trials reveal large differences between the baseline (no air) and air cases. The baseline measurements presented here are the emissions rates from the cold start phase of the BDS trials discussed in Section 7.4, as the Halo Stove without air injection is equivalent to the BDS.

Black Carbon

The preliminary study found that all four halos reduced BC compared to the baseline at all air flow rates examined, as shown in Fig. 7.3. For the lowest air flow rate (14.2 L/min), as the injection angle decreased so did the BC emitted. The 30SWL reduced BC by over 80% using 14.2 L/min, so the swirl appears to have a positive impact on BC reductions at lower flow rates. At 42.5 L/min and above, all halos decreased BC by at least 90%. This likely indicates the halos are increasing turbulent mixing, providing greater opportunity for soot oxidation or lesser opportunity for soot formation.

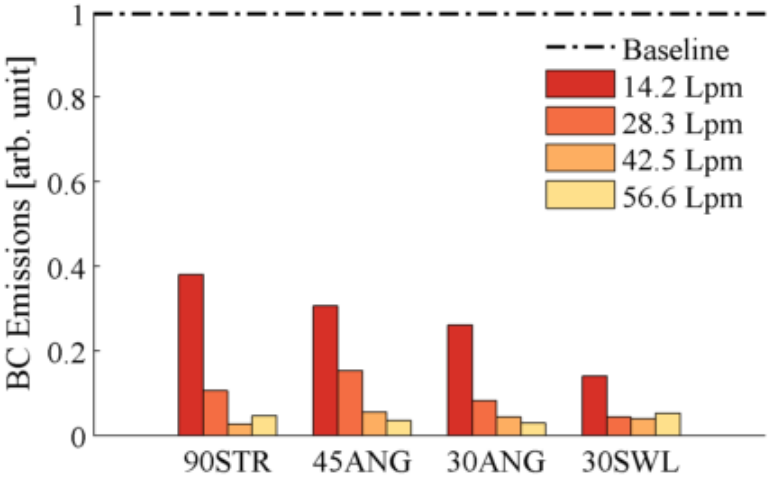

Figure 7.3: Preliminary tests indicate that all halos reduce BC compared to the baseline. Results have been normalized to the maximum value, which was the baseline.

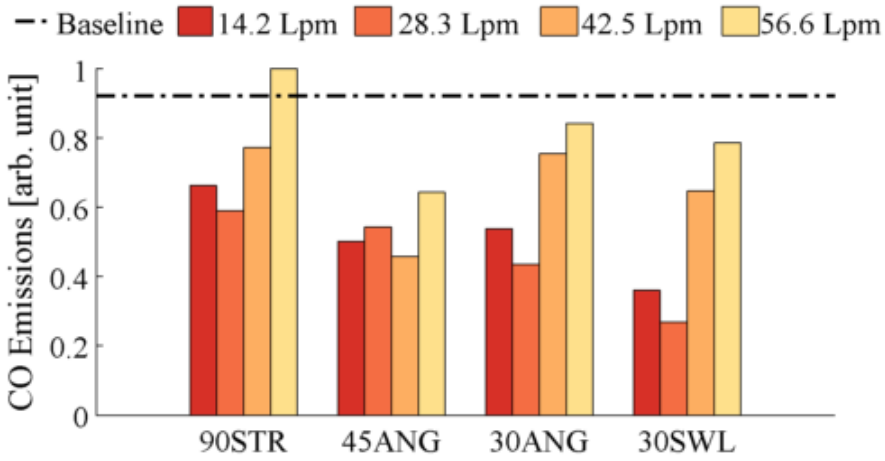

Figure 7.4: The CO emissions results show that CO emissions are greater at higher flow rates, indicating the higher flow rates might be quenching the fire. Results have been normalized to the maximum, which was the 90STR at 56.6 L/min.

Carbon Monoxide

Although air injection appears to decrease BC emissions, especially at higher flow rates, it is important to note the effect on CO emissions, shown in Fig. 7.4. In contrast to BC, the CO emissions reached a minimum at either 28.3 or 42.5 L/min and then increased as the air flow rate increased for all halos. This trend indicates that higher air flow rates might be quenching the combustion or otherwise impeding complete combustion in the gaseous combustion zone. Therefore, although higher flow rates appear to greatly reduce BC emissions for all halos, a balance must be found in the chosen air flow rate in order to maintain reductions while not quenching the fire.

$PM_{2.5}$ and Particle Size Distribution

Similar to the BC results, all halos decreased the total mass of $PM_{2.5}$ emitted compared to the baseline in these preliminary studies (Fig. 7.5) with even the poorest performer still providing a 70% decrease. Again, the 30SWL provided larger reductions than the other halos at the lower flow rates. For the two higher flow rates, the 45ANG, 30ANG, and 30SWL performed relatively equivalently, emitting approximately $5-10\%$ of the baseline. The 90STR, however, did not create such dramatic decreases, providing an approximate 85% reduction.

Insight into the differences in $PM_{2.5}$ may be gained by examining the $PM_{2.5}$ particle size distribution for each halo (Fig. 7.6). Although the halos decreased total $PM_{2.5}$ mass emitted, they did not uniformly reduce the number concentrations across all particle sizes. The halos tended to produce more UFPs (diameter < 100 nm) than the baseline and reduced the number of fine particles (diameter $= 100$ nm $- 2.5$ μm). Because individual fine particles

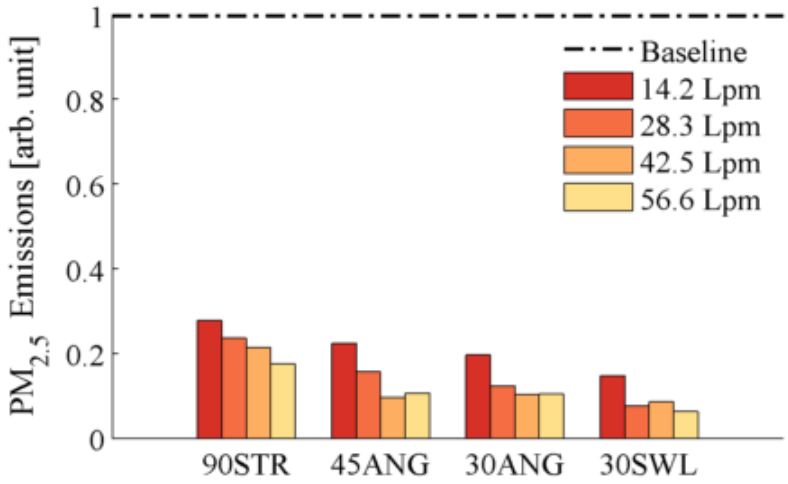

Figure 7.5: All halos at all flow rates reduced $PM_{2.5}$ emissions by over 70% compared to the baseline in the preliminary trials. Results have been normalized to the maximum value, which was the baseline.

have more mass than individual UFPs, a slight change in the number of fine particles can produce significant changes in measured $PM_{2.5}$ mass while large changes in the number of UFPs will have lesser consequences on the mass measurements. It can be seen that the 30SWL, 30ANG, and 45ANG produced more UFPs, even at low flow rates, and reduced the number of fine particles. The 90STR, however, continued to produce larger diameter particles than the other halos (although still fewer than the baseline) at all flow rates, so did not show as dramatic of reductions in $PM_{2.5}$ mass measurements.

It can also be seen in Fig. 7.6 that the particle size distributions across air flow rates vary dramatically. The particle size distributions noticeably change between the lower flow rates until the distributions remain fairly consistent starting at approximately 42.5 L/min and above. All halos show a bimodal distribution at 14.2 L/min, with a smaller diameter mode around 10 nm and a larger diameter mode around 20 nm. This smaller diameter mode is often the nucleation of the volatile particles (Hosseini et al., 2010; Hays et al., 2005). The low flow rate could be cooling the particles with injected air, limiting growth, without providing enough mixing for particles to grow. As the air flow rate increases, however, the size distributions shift to a more unimodal distribution with a peak between $30-50$ nm, indicating the mixing was increasing the surface growth of the particles (Hosseini et al., 2010; Hays et al., 2005).

7.3.3 Discussion

The main goals of the preliminary study outlined at the beginning of this section were well addressed by the results. The preliminary trials revealed that all halos decreased black

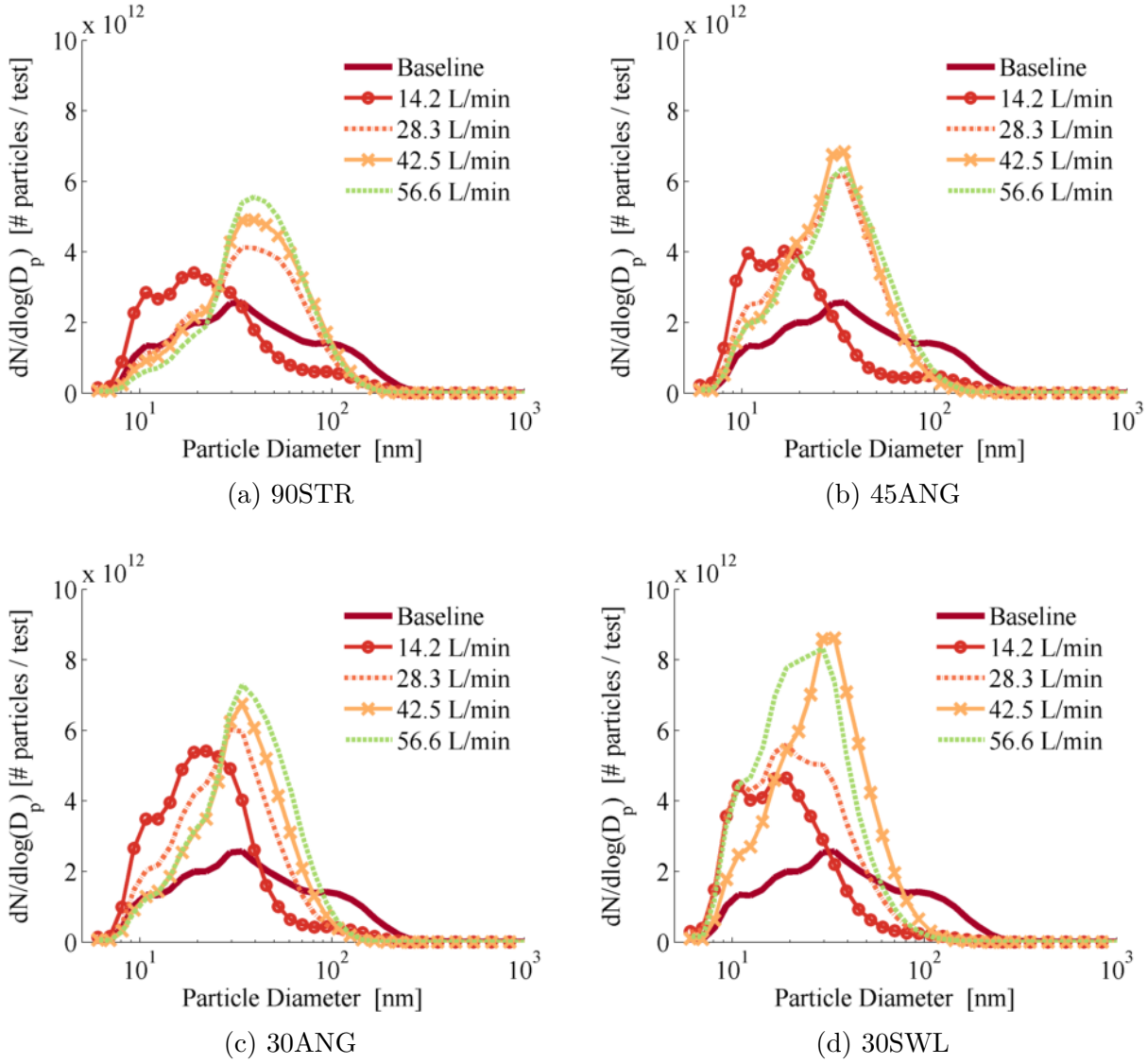

(a) 90STR (b) 45ANG

(c) 30ANG (d) 30SWL

Figure 7.6: The size distributions of emitted particles for the Halo Stove preliminary trials.

carbon emissions as intended although the question still remained if the differences were due to decreased soot formation or increased soot oxidation. Also, different types of halos created noticeably different results in emissions trends so all mixing strategies were chosen to be pursued for further study. An air flow rate between 28.3 – 42.5 L/min was determined to be the most beneficial for reducing emitted particles while avoiding quenching the flame. The study therefore found the necessary variables to conduct an in-depth test series evaluating the impact of the three mixing strategies.

7.4 Comparison Trials of the Halo Stove

The comparison trials for the Halo Stove evaluated the effect of injection angle on high and low power cooking cycles in the stove. Besides examining BC reductions, the chosen metrics for evaluation included emissions, such as CO and particle size distribution, as well as performance characteristics, such as fuel use and thermal efficiency, to provide a well-rounded view of the effects of the different mixing strategies.

7.4.1 Experimental System and Protocol

The same halos (90STR, 45ANG, 30ANG, and 30SWL), stove, fuel, and instrumentation were used for these experiments as were used for the preliminary tests, and the metrics to be evaluated were calculated as discussed in Section 4.4. An unmodified BDS and a three-stone fire (TSF) (described in Section 2.1.2) were chosen as baseline cases for comparison with the Halo Stove. The TSF often serves as the baseline for any wood-burning stove trial, representing what is currently accepted in the field without modification or "improvement". Because the Halo Stove is a modified version of the BDS, comparison with a BDS baseline allows for the effects of the injected air to be isolated from other design improvements of the BDS over the TSF. A modified Water Boiling Test protocol consisting of a cold start (high power) phase and a 30 minute simmer (low power) phase, described in Section 4.2, was used for the halo comparison tests. The same kindling setup, also described in Section 4.2, was used for all stoves with the exception that during the TSF and BDS tests, fuelwood was added as necessary to light the fire (instead of at regular intervals) during start-up because ignition patterns of the TSF and BDS were less consistent than the Halo Stove and required more flexibility. For the Halo Stove tests, the chosen air flow rate was 35.4 L/min as a noticeable transition appeared to occur between 28.3 – 42.5 L/min during preliminary testing. The air injection began two minutes into the high power portion of the test, to reduce the risk of quenching the fire before it was well-established, and continued through the remainder of the test.

As discussed in Section 2.2, ideally when comparing the DustTrak and gravimetric filter data, the ratio would be 1:1 but due to the differences in scattering characteristics between the DustTrak calibration particles and particulate matter from biomass combustion, the DustTrak requires calibration. For this work, the DustTrak was found to overestimate $PM_{2.5}$ compared to the gravimetric filters (shown in Fig. 7.7), resulting in the calibration curve: $PM_{2.5,filt} = 2.67(PM_{2.5,DT})^{0.56}$.

Ten tests were conducted for all halos and baselines, except the 45ANG. During the trials, it became apparent the two angled halos (30ANG and 45ANG) did not provide unique enough results to necessitate completely testing both. To efficiently utilize time, the 45ANG was tested five times instead of ten, while the 30ANG was tested a full ten times so it could both provide results for the angled-type mixing strategy and act as a good basis of comparison for the 30SWL to isolate the effect of the swirl. Statistical significance was determined for

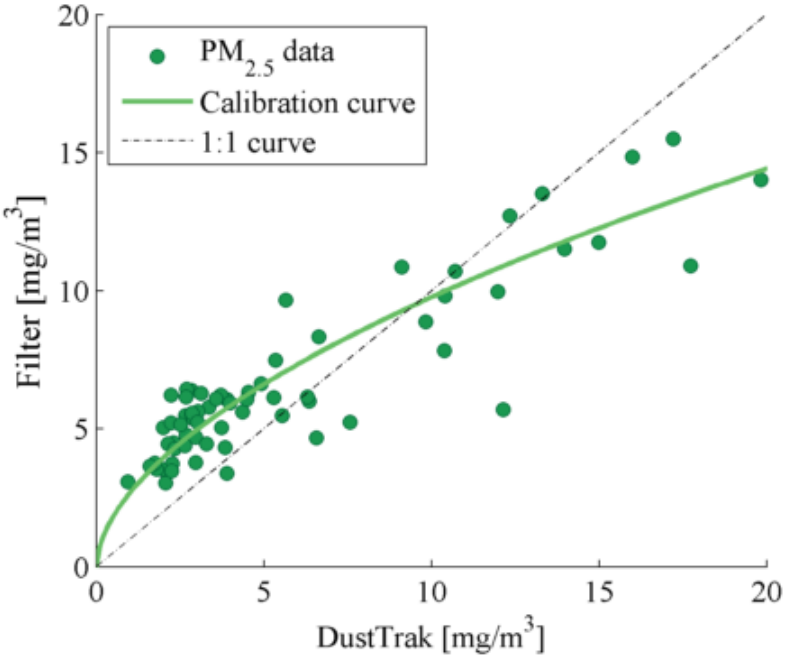

Figure 7.7: Calibration curve for the DustTrak $PM_{2.5}$ data as compared to the gravimetric filter $PM_{2.5}$ data: $PM_{2.5,filt} = 2.67(PM_{2.5,DT})^{0.56}$. A 1:1 curve is also shown for reference.

all tests by applying the Student's t-test as the sample size was small ($n < 30$) (Taylor, 1997; Spiegel et al., 2008). All error bars on the graphs represent 95% confidence intervals.

7.4.2 Results

Black Carbon Emissions

As shown in Fig. 7.8, the halos drastically reduced BC emissions in both the high and low power phases of the test, decreasing BC by over 80%. The halo results without the baselines are shown in Fig. 7.9 so the trends can be better seen between the mixing strategies and injection angles. In the high power phase, as the injection angle moved closer to horizontal, BC emissions were reduced; if swirl was added, it was reduced even further. During the low power phase, the injection angle appears to make less of a difference although BC gradually increased as the injection angle decreased. Adding swirl during the low power phase significantly increased the amount of BC emitted compared to the other halos although the spread of data points reveals greater test-to-test variability.

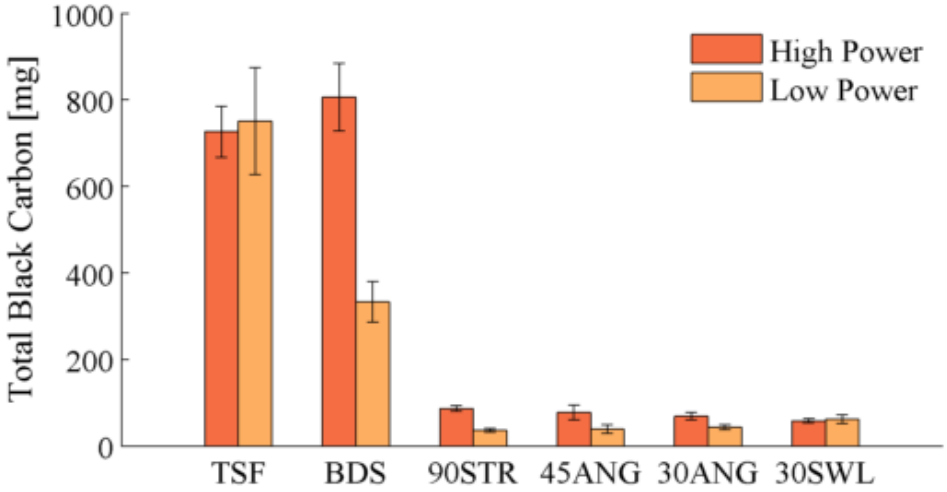

Figure 7.8: The total BC emitted for the halos and baselines.

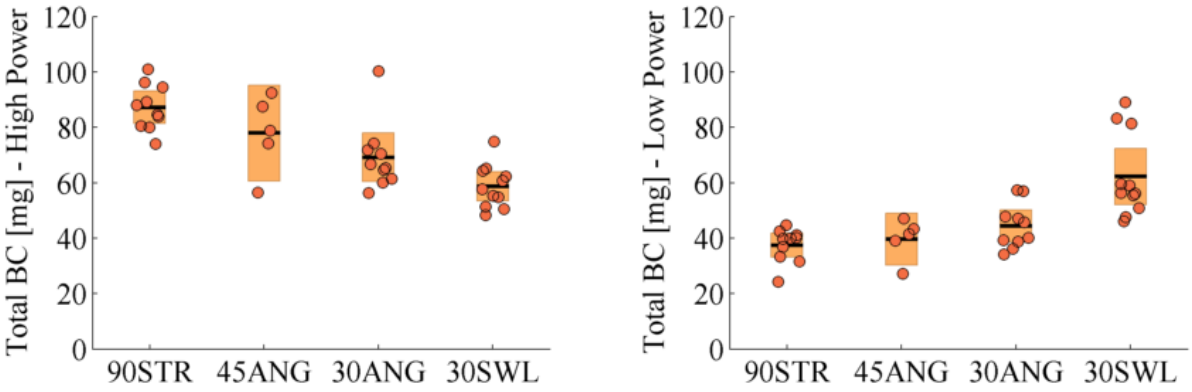

(a) High Power BC data values.

(b) Low Power BC data values.

Figure 7.9: The total BC emitted for the halos. In addition to the individual data points, the black horizontal lines represent the mean and the bar patches show 95% confidence intervals.

Carbon Monoxide and Modified Combustion Efficiency

Carbon monoxide emissions from a wood-burning fire may indicate a high amount of incomplete combustion or quenching especially if the modified combustion efficiency (MCE) is low (Morr et al., 1975). MCE, or the ratio of CO_2 to the total CO and CO_2 emitted, is one metric for identifying the completeness of combustion, where typically smoldering or incomplete combustion produce lower MCE values and flaming or complete combustion produce higher values (Ward and Radke, 1993; Urbanski, 2013). Fig. 7.10 shows the total mass of CO emitted per stove per test phase. All halos reduced CO compared to the TSF for both test phases. However, for the low power phase, all halos increased CO emissions

compared to the BDS. In the high power phase, the 90STR produced significantly more CO than the BDS, the 30SWL produced significantly less, and the 45ANG and 30ANG produced slightly more and slightly less, respectively, on average.

As shown in Fig. 7.11, for the high power phase, the TSF, BDS, and 90STR had the lowest MCEs at roughly 96%. The poorer combustion efficiencies are likely because the TSF and BDS do not benefit from additional mixing due to air injection and the 90STR either encourages less turbulent mixing than the others or it quenches the fire which then releases more products of incomplete combustion. The other halos had higher MCE values for the high power phase, indicating their mixing was encouraging complete combustion and not quenching the flame. The trend changes for the low power phase; the BDS and 30SWL had the highest efficiencies and the 90STR, 30ANG, and 45ANG were similar to the TSF. Because the rate of combustion is less in the low power phase, it is likely both the direct air injection of the 90STR and indirect air injection of the 30ANG and 45ANG had a large enough impact on the fuel bed to quench the low power flame.

$PM_{2.5}$ and Particle Size Distribution

Results for the total $PM_{2.5}$ mass emitted are shown in Fig. 7.12. In the high power phase, the 90STR and TSF emitted similar amounts of $PM_{2.5}$. As the injection angle decreased, the $PM_{2.5}$ emissions were reduced with the 45ANG producing similar results to the BDS and the 30ANG emitting less $PM_{2.5}$ than the BDS. The 30SWL had the largest reduction in $PM_{2.5}$ for the high power phase. These results are well-aligned with the BC and CO results for the high power phase. During the low power phase, all halos emitted less $PM_{2.5}$ than the TSF and emitted more than the BDS; however, the results of the halos are similar to each other.

A noticeable difference exists in the total masses of $PM_{2.5}$ and BC emitted from the stoves because biomass combustion emits many aerosols besides BC (Andreae and Merlet, 2001; Bond et al., 2004a; Yokelson et al., 1997). One possible explanation for the difference in the emitted $PM_{2.5}$ and BC masses could be due to the quenching and smoldering combustion conditions indicated by the CO emissions. Elemental, or black, carbon is often produced by flaming combustion, whereas cooler, smoldering combustion tends to produce a wide-variety of lighter-colored organic particles (Andreae and Merlet, 2001; Yokelson et al., 1997; MacCarty et al., 2008). It has been estimated that biomass burning can produce $6-8$ times as much organic carbon as BC (Chen and Bond, 2010; Bond et al., 2004a; Andreae and Merlet, 2001; Liousse et al., 1996; Just et al., 2013), so the difference between the BC and $PM_{2.5}$ measurements could in part be due to the mass of organic particle emissions, especially if those are large diameter particles. Similarly, it is possible the turbulent mixing promotes conditions which limit soot particle growth or favor soot oxidation, leading to smaller diameter BC particles. To better identify the contributions of BC, further investigation is warranted in another study to examine the ratio of elemental to organic carbon emitted with each mixing strategy.

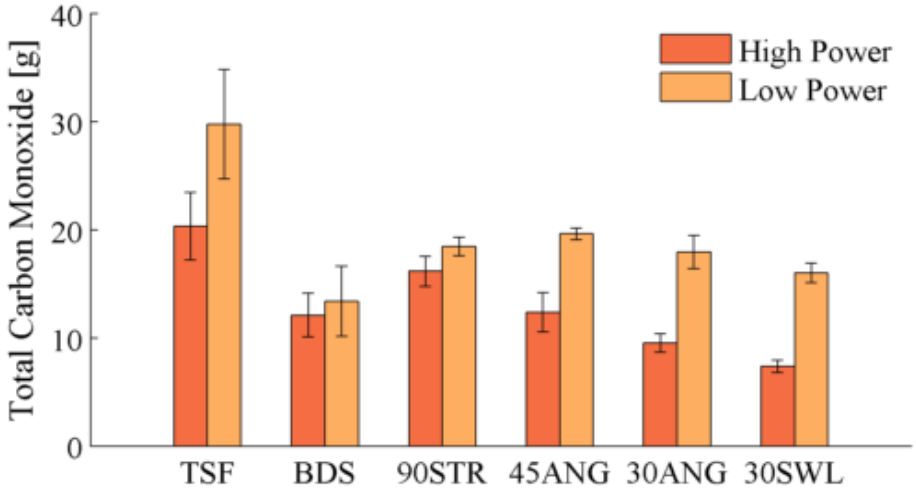

Figure 7.10: The total CO emitted from the different halos and baselines.

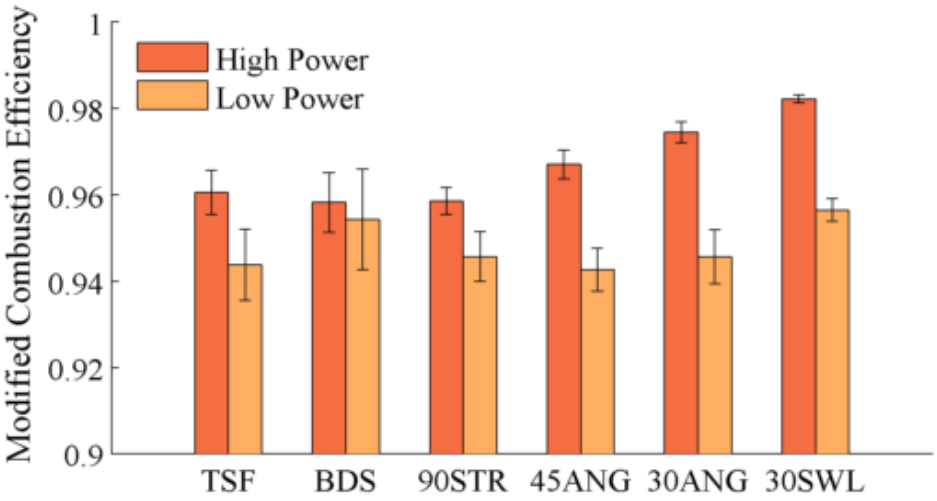

Figure 7.11: The modified combustion efficiency of the different halos and baselines.

The size distributions of emitted particles for the high and low power phases are shown in Fig. 7.13 and Fig. 7.14, respectively. The halos show similar trends in the ultrafine range for the high and low power phases (Figures 7.13a and 7.14a); as the injection angle decreases, the peak of the distribution shifts towards smaller particle diameters, meaning less emitted mass. The TSF also stays consistent in the UFP range; however, the BDS distribution shifts far into small diameter particles for the low power phase. For the larger diameter range shown (500 nm – 10 μm) in Figures 7.13b and 7.14b, the emissions from the Halo Stove are similar to, or less than, those from the BDS and the TSF. Although the mixing strategies examined do emit more UFPs than the stove without mixing (the BDS), they generally

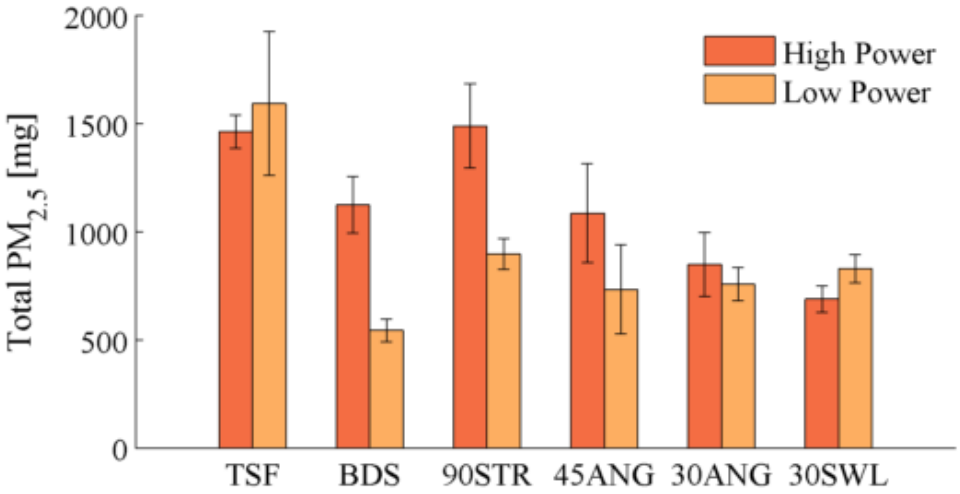

Figure 7.12: The total $PM_{2.5}$ emitted from the different halos and baselines.

emit fewer particles than the traditional baseline (the TSF), an important outcome due to the human health concerns associated with small diameter particles. Also, the preliminary trials revealed that different air flow rates, especially lower flow rates (0 – 28.3 L/min), have dramatically different size distributions up to ~42.5 L/min. Therefore, an optimal flow rate could exist that reduces UFPs compared to the BDS but was unseen in this study because the preliminary trials tested a limited number of flow rates. Future work is needed to assess the impact of different air flow rates on particle size distributions, which are especially important considering the large health risks associated with small diameter particles.

Performance Metrics

The performance metrics evaluated for this trial were time to boil, thermal efficiency, and specific fuel consumption. The results for the time to boil and the thermal efficiency are shown in Fig. 7.15. All halos had similar or slightly longer times to boil relative to the BDS, but all were significantly shorter than the TSF. Similarly, all halos had higher thermal efficiencies than the TSF but slightly lower efficiencies than the BDS. The time to boil and thermal efficiency results indicate that the Halo Stove is benefiting from the design improvements of the BDS, which performs better than the TSF, but the air injection is counteracting some of those improvements, reducing the amount of heat reaching the pot. The specific fuel consumption results (Fig. 7.16) follow the same trend as the time to boil and thermal efficiency results. All halos significantly reduced the fuel necessary for the test compared to the TSF, but required similar or slightly more fuel than the BDS, likely due to the difference in thermal efficiencies. Overall, the performance results show that the mixing strategies improved performance compared to the TSF but did not provide performance gains compared to the BDS.

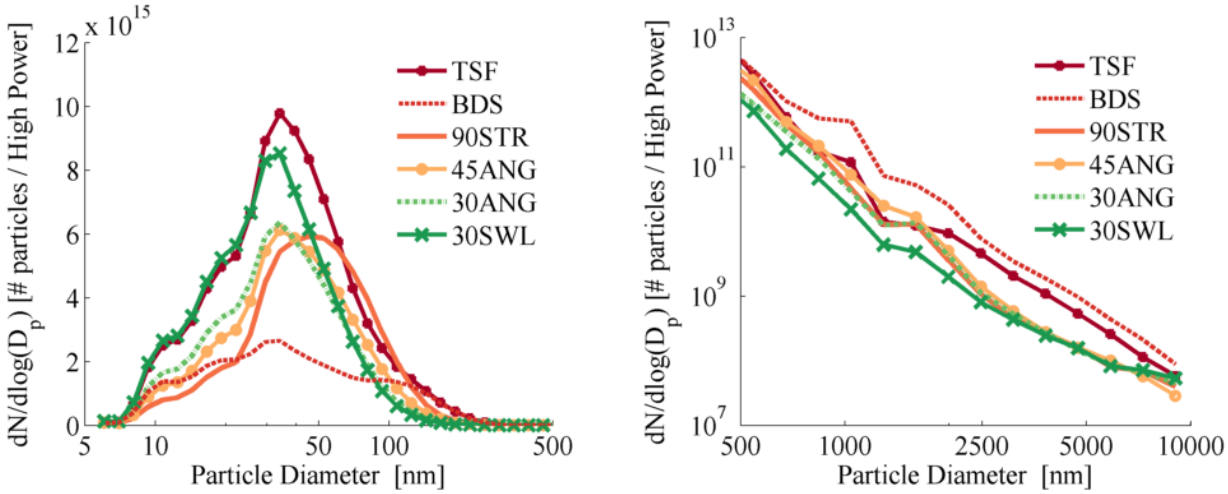

Figure 7.13: The size distribution of emitted particles for the high power phase.

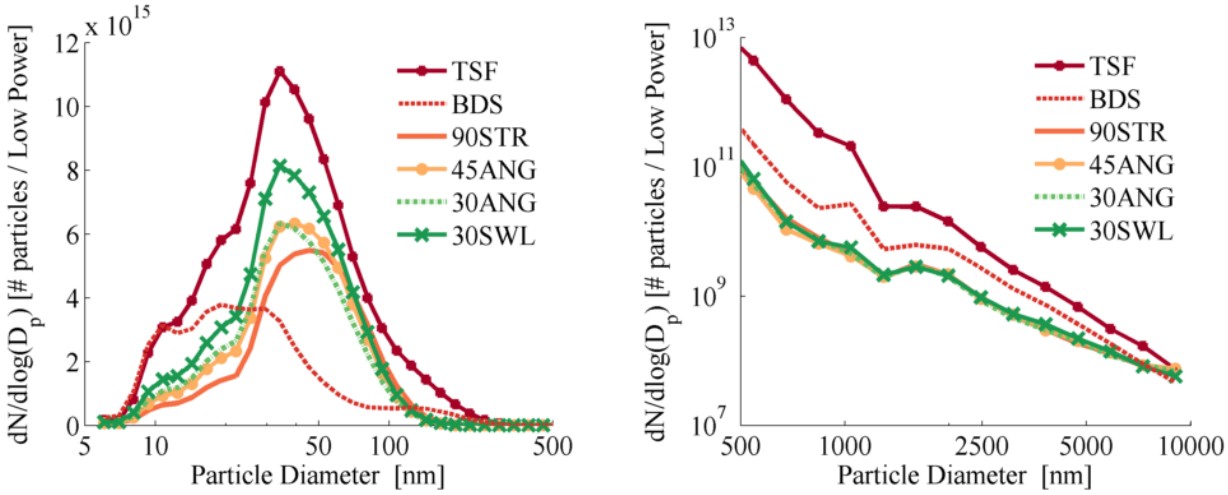

Figure 7.14: The size distribution of emitted particles for the low power phase.

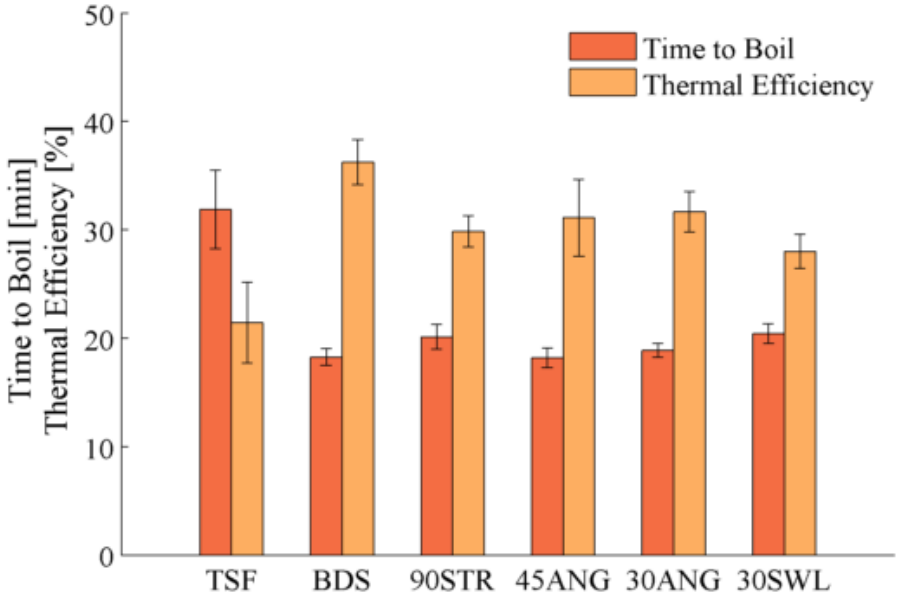

Figure 7.15: The time to boil and the thermal efficiency of the different halos and baselines.

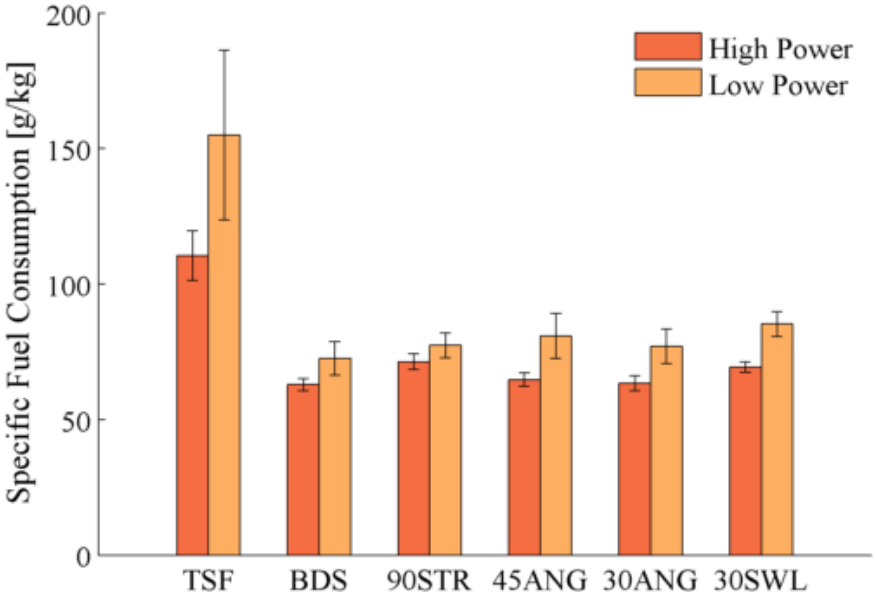

Figure 7.16: The specific fuel consumption of the different halos and baselines.

7.5 Discussion

Emissions and performance results are an important aspect of the evaluation because they are what actually impact the end users and environment. However, because the results provided in this chapter were recorded ex-situ, far downstream of the actual combustion and air injection being examined, this discussion section provides many hypothetical reasonings behind the results. In-situ results, explored in Chapters 8 – 9, will be presented to help evaluate these hypotheses.

7.5.1 High Power Phase

For the high power phase, the 30SWL emitted the least amounts of BC, $PM_{2.5}$, and CO mass emissions as well as having the highest MCE. This indicates the 30SWL increased turbulent mixing and residence time of the volatiles and particles in the flame zone while encouraging less smoldering combustion than the other halos, so soot oxidation and other reactions had time to occur before the gases cooled, leading to more complete combustion and less emitted BC, $PM_{2.5}$, and CO. However, the 30SWL had poor performance results compared to the BDS and the 30ANG, increasing time to boil and fuel consumption and decreasing thermal efficiency. Although the long residence time likely provided by the swirl would be beneficial for emissions reductions, it could allow the gaseous emissions time to cool prior to reaching the pot; the swirl also could increase interaction of the hot gaseous emissions with potential thermal sinks, such as walls. Too much cooling of the gases would reduce the thermal efficiency and therefore increase specific fuel consumption and time to boil.

The 90STR was the most polluting of the halos in the high power phase, emitting the most BC among the mixing strategies, more CO than the BDS, and a similar amount of $PM_{2.5}$ to the TSF. The injection angle of the 90STR likely promotes recirculation but not as much turbulent mixing as the other halos because it does not have a horizontal component to its injection angle. The lesser amount of turbulent mixing is likely why the 90STR had smaller reductions in BC emissions in the high power phase; the high burn rate rapidly produces many volatiles and particles so requires a large amount of mixing to achieve complete combustion. Also, the 90STR likely quenched the solid fuel combustion as it was angled directly downward, promoting smoldering combustion and leading to high CO emissions, a low MCE value, and probably a large amount of organic particles included in the total $PM_{2.5}$. The 90STR had similar performance to the 30SWL regarding time to boil, specific fuel consumption, and thermal efficiency. Besides the likely increase in smoldering combustion produced, it is also possible that the strong downward air injection blew combustion products under the grate where they were entrained with the cooler, room temperature air between the outer wall of the firebox and the stove body; the hot gases would be greatly cooled by this interaction, reducing thermal efficiency and limiting the number of reactions occurring in the combustion products.

The 30ANG and 45ANG reduced emissions to a lesser extent than the 30SWL but fared better in the performance metrics as the 30ANG was second only to the BDS. It is likely that the angled mixing strategies led to less interaction between the injected air and the solid wood than the 90STR and did not quench the fuel or increase smoldering, as shown by the high MCEs and lower CO and $PM_{2.5}$ emissions. The angled mixing strategy likely produced a great amount of turbulence (more so than the recirculation of the 90STR) to promote mixing of the gaseous combustion products, reducing BC and other products of incomplete combustion, without providing a long enough residence time for gaseous products to cool or creating excessive wall interactions which would reduce thermal efficiency. The overall positive results for the 30ANG indicate that it could be a good compromise for high power cooking to maintain the current performance level of the BDS, while still drastically reducing BC emissions.

7.5.2 Low Power Phase

The low power phase results follow different trends than the high power with the 90STR producing the greatest reduction in BC emissions. Because a lower temperature in the combustion chamber is adequate to maintain a simmer (as compared to bringing water to a boil), the gaseous fuel will be cooler as it rises through the firebox, especially with the halos diluting the gases with room temperature air. It is hypothesized that this is why the largest reductions in BC are seen with the 90STR in the low power phase; the 90STR forced gases to recirculate closest to the hot, solid fuel combustion. The angled halos emitted slightly more BC than the 90STR, as the lesser injection angle would not have interacted with the fuel bed as directly. The swirl halo, however, likely circulated the gases higher in the combustion chamber, where they would be cooler and promote fewer reactions, and thus produced significantly more BC.

It was seen that all halos increased the total CO emissions compared to the BDS, but this could be due to different reasons. The 30SWL produced more CO than the BDS but also had a higher MCE and specific fuel consumption. Therefore, the higher CO output from the 30SWL was probably due to the larger amount of fuel being consumed as opposed to incomplete combustion. The 90STR, on the other hand, had high CO emissions with a low MCE and low specific fuel consumption. In order to be emitting more CO than the 30SWL while consuming less fuel, the 90STR likely quenched the solid fuel combustion or otherwise impeded complete combustion. It is important to note that preheating the air prior to injection could provide a large improvement in the halo performance; the same mixing strategies without the greatly cooling effect of room temperature air could increase both the modified combustion and thermal efficiencies, especially in the cooler, low power phase. Therefore, future work examining the effects of the halos injecting preheated air warrants consideration.

7.6 Conclusions

Four halos were used to compare three mixing strategies with a traditional TSF and baseline BDS, identifying the positive and negative impacts those mixing strategies have on stove emissions and performance metrics during high and low power cooking cycles. The results were found to be quite different between the high and low power phases, elucidating the need to consider cultural cooking styles, such as frying (high power) or simmering (low power), of the intended dissemination region for a stove when choosing a mixing strategy. Future work examining different air flow rates and temperatures of the injected air are suggested, especially when identifying the impacts on UFPs and developing a stove for low-power simmering. Additional future work identifying the ratio of BC and organic material could be beneficial from an environmental perspective when attempting to determine the optical properties and atmospheric effects of particles from cookstoves.

The main goal of this chapter was to examine the impact of the mixing strategies on BC emissions. Drastic reductions in BC emissions were observed with the halos, so they appear to produce the desired result from that aspect of evaluation; however, the halos can also have less favorable impacts on CO emissions and performance metrics. Comparing the halos, the favorable and unfavorable results were quite distinct in the high power phase: the 30SWL had the lowest emissions but poor performance; the 30ANG had good emissions reductions and good performance; and the 90STR had comparatively poor emissions reductions and poor performance. Many hypotheses were posed estimating why these effects were seen and examining the differences between these three halos. Examining the differences in greater depth will help identify the desired and undesired components of each mixing strategy and help validate or invalidate the proposed hypotheses. Therefore, the next steps in this work, discussed in Chapters 8 – 9, focus on in-situ measurements to discover where soot formation and oxidation are occurring in the flame and the mixing characteristics that are enabling them.

8 Preparation for In-situ Measurements

8.1 Introduction

When evaluating cookstove performance, it is common practice to use an aerosol-based emissions measurement system, like that described in Section 3.1.2 and utilized in Chapter 7, sampling far downstream from the stove in a duct which captures the emissions (Jetter et al., 2012; Preble et al., 2014; MacCarty et al., 2010). Aerosol emissions measurements are useful when evaluating stove performance and impact on human health and the environment but are not as informative about what is occurring in the flame zone itself because impacts to the flame must be hypothesized from measurements taken far downstream (as was done in the discussion section of Chapter 7). Nonintrusive, in-situ measurements provide a better view of how design modifications, such as air injection, directly affect the combustion in a stove. Therefore, to gain a deeper understanding and clarify the key differences between the air injection mixing strategies described in Section 7.2, it was desired to conduct in-situ evaluations to attain spatially-resolved details of how the injected air affected the flame itself.

Laser diagnostic techniques are used for many in-situ flame evaluations because they are nonintrusive and able to withstand harsh flame conditions, such as high temperatures. Three spatially-resolved laser diagnostic techniques were chosen for the in-situ evaluations: 1. Particle image velocimetry (PIV) provides a quasi-instantaneous measurement of the velocity field of the injected air; 2. Laser-induced incandescence (LII) measures soot volume fraction in the flame; and 3. OH laser-induced fluorescence (OH-LIF) measures the concentration of hydroxyl radicals in the flame, which can indicate reaction zones. The three techniques are fully described in Sections 3.3 – 3.4. With these techniques, the aim was to provide a visualization of the flow profiles of the mixing strategies and determine where the soot was located within the flame and where it was being oxidized with each mixing strategy.

8.2 In-situ Measurement in a Wood-burning Stove

Solid fuel combustion systems, such as biomass cookstoves, can be quite difficult to analyze using laser diagnostic techniques due to the high variability of the system both spatially

and temporally. Therefore, the first step for the in-situ measurements was to identify if the flame in the wood-burning stove was consistent enough to be practical for evaluation with laser diagnostic techniques. A straightforward and easy-to-apply laser diagnostic technique, laser extinction (LE) (described in Section 3.2), was chosen as an initial evaluation of the variability of the wood combustion. Laser extinction is a line-of-sight technique for determining the soot volume fraction in a flame. Because it is a line-of-sight technique, LE is less spatially-resolved than the proposed methods (LII, OH-LIF, and PIV), but it could be used to quickly evaluate the temporal variability of the wood-burning system and indicate the feasibility of applying more complicated methods. Although it was desired to eventually evaluate the Halo Stove with the laser diagnostic techniques, the Berkeley-Darfur Stove (BDS), described in Section 2.1.2, was the wood-burning stove chosen for this initial assessment. The only difference between the BDS and Halo Stove is the air injection system (the halo), so the BDS served as a good starting case because it provided the same combustion characteristics of the Halo Stove without the additional complexity of the turbulence-inducing air injection. LE was also used to evaluate a single block of burning wood in order to obtain sample burn profiles of a relatively well-defined system and aid in understanding the more complex results from the BDS.

8.2.1 Experimental Setup and Protocol

The experimental setup consisted of an infrared laser and two photodiodes to record the attenuated and reflected signals; a detailed description of the system used for the wood-based trials can be found in Section 3.2.1. The fuel used was locally-sourced Australian Douglas fir, the same type of wood as the Halo Stove experiments performed in Chapter 7.

Berkeley-Darfur Stove

For the BDS trials, five pieces of 20 mm × 20 mm × 150 mm Douglas fir were stacked in a slightly askew pyramid as shown in Fig. 8.1. The wood was ignited from underneath the pyramid using a natural gas flame for three minutes; if the wood did not ignite in the first three minutes, 30 extra seconds of natural gas ignition were added to the test. The wood was allowed to burn untended; no sticks were moved or turned and the fire was not fed to minimize variability due to fire-tending. Data was recorded from the end of the natural gas ignition until no visible flame remained in the firebox.

Holes (6.35 mm diameter) were drilled in the wall of the stove body and the firebox, perpendicular to the firebox opening, to allow the laser beam to pass through the stove with minimal light pollution from the flame reaching the photodiodes. The beam was aligned to the center of the firebox and approximately 10 mm above the top wood stick in the pyramid. For some trials, a camera viewed the burning wood pile from the firebox opening (perpendicular to the laser) to obtain an average flame width; other trials viewed the flame through a hole cut directly above the hole for the laser to visually estimate when the laser was propagating through a flaming region.

Figure 8.1: Wood configuration consisting of 5 sticks stacked in a slightly askew pyramid used for the BDS LE trials as viewed from the firebox opening.

For the BDS case, the path length was known to be no larger than the inner diameter of the firebox (190 mm) so that was chosen as the optical path length. It is important to note that, in the majority of instances, the path length was much smaller than the firebox, so the calculated soot volume fractions are potentially significant underestimations. Time-averaged measurements were taken every 30 seconds.

Wood Block

Individual 20 mm cubes of wood were combusted using a continuous natural gas flame located 45 mm below the center of the block. The grain of the wood was parallel to the laser, which was aligned 10 mm above the surface of the wood block along the centerline of the block.

Two conditions were examined with the wood blocks. In the first condition, a single block was held by a clamp with a flame surrounding it ("open-flame" case), revealing the full temporal burn profile of the wood. In the second, a single block was placed on a flame limiter made of mesh with circular holes of 4 mm diameter spaced every 2 mm ("on limiter" case) to prevent direct contact of the natural gas flame with the wood so the block was being heated but not allowed to reach flaming combustion. This simulated the stage of wood combustion when the wood is releasing some volatiles but has not achieved the heat needed to transition to flaming combustion.

For the wood block trials, the optical path length was considered to be the width of the wood block, namely 20 mm. In general, this led to an overestimation of the path length and thus an underestimation of the calculated soot volume fraction. Time-averaged samples were taken every 15 seconds for the flame-limiting trials and every five seconds for the open-flame trials, allowing a visualization of the trends while averaging the fluctuations created by turbulence and an extremely variable flame. All trials were recorded with a video camera focused in-line with the laser, providing simultaneous data of the observational occurrences of flame and the measured emissions (attenuation).

Data Analysis

The soot volume fraction, or soot concentration, was calculated as described in Section 3.2. Results were background corrected by measurements collected without flame taken before and after each run. The light extinction coefficient, K_e, which is necessary for computing the soot volume fraction, is dependent on the fuel and laser wavelength. From the work done by Choi et al. (1995), the K_e value was chosen to be 9.0. This is likely to be an overestimation due to the differences in laser wavelengths between that work and this experiment (laser wavelengths of 633 nm versus 1064 nm, respectively).

8.2.2 Results and Discussion

Trials revealed great variation in both the temporal soot concentration profile of the wood blocks and the BDS as well as the test-to-test BDS results. Beginning by examining the relatively well-defined system, a typical, open-flame wood block trial is shown in Fig. 8.2a. From the observational videos of the case presented in this figure, it was determined that charring of the wood began almost immediately as the volatiles were released with lots of visible smoke prior to producing a full flame. During this stage (from $0-180$ seconds), the emissions measurements were quite sporadic, indicating soot emissions are higher and more variable while the wood is releasing volatiles than when the wood is fully ignited (time greater than 200 seconds). Once the exterior of the wood block fully caught fire (at approximately 200 seconds), the emissions measurements dropped dramatically, likely due to more complete combustion occurring in the flame zone. Only when the wood block was fully burning from the interior of the block (starting at approximately 330 seconds) was there any variation in the opacity. However, there was no visible smoke during this time, indicating these values relate solely to the release of soot. The ember then fully extinguished with a puff of smoke at around 480 seconds.

The results shown in Fig. 8.2b examine the precursor to the ignition stage by heating a 20 mm cubic wood block above a flame limiter. Only minor peaks in soot volume fraction occurred and the visual analysis showed very little charring of the block or opacity in the emissions. This indicates the wood block was releasing volatiles slowly without fully smoking or flaming.

Example data from two BDS trials are also shown in Fig. 8.2. Although the same protocol was followed for both trials, due to the variable nature of wood combustion, the results are quite different. Comparing the BDS results with the wood block results provides some clarity. Similar trends can be seen between the BDS trial shown in Fig. 8.2c and the open-flame wood block case shown in Fig. 8.2a. In the open-flame case, the fuel was allowed to fully flame and combust, indicating the similar peaks seen in the BDS trial are due to the top stick fully flaming and combusting in view of the laser. Observational data indicated the presence of smoke for the first 400 seconds. After this stage, the exterior of the top stick fully ignited along with the other sticks, greatly decreasing the laser light attenuation. At approximately 800 seconds, the fire combusted the entire stick prior to extinguishing. These trends are very

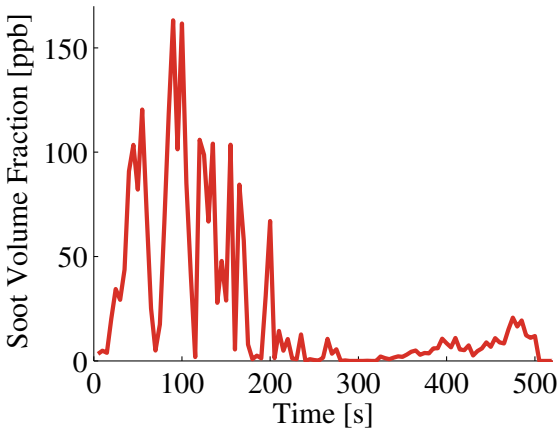

(a) Wood Block: Open-Flame

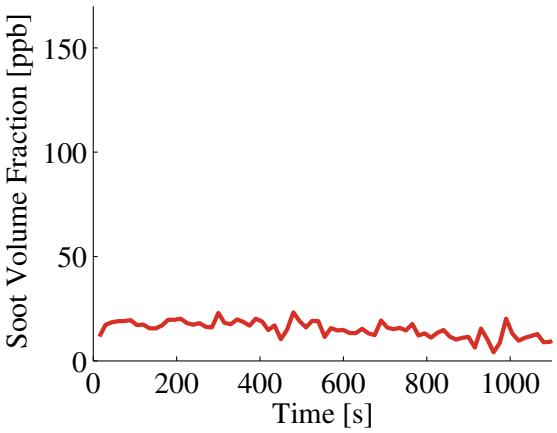

(b) Wood Block: On Limiter

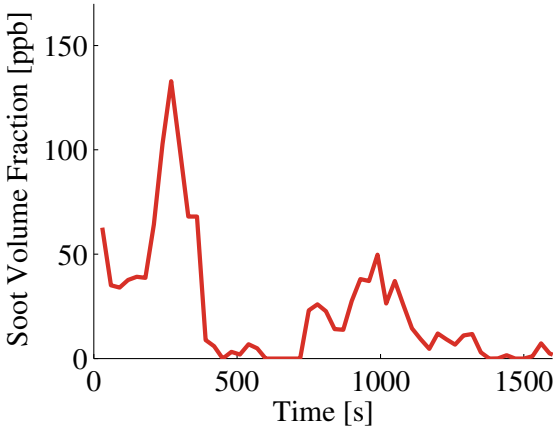

(c) BDS: Combustion in laser view

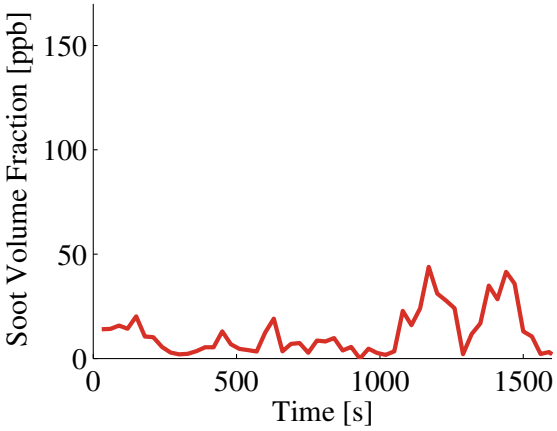

(d) BDS: Combustion out of laser view

Figure 8.2: LE wood-burning trials: (a) Typical results of the open-flame wood block trial. Even in the simplified case of the wood block, high variability is seen over the duration of the burn. (b) Example results with block resting on a flame limiter. Comparing the BDS results (c and d) to the wood block trials, it is apparent that in (c) the top stick fully combusts in view of laser and in (d) the top stick combusts out of view of the laser.

similar to those found for the open-flame wood block case. Then around 1000 seconds, a second peak occurs in Fig. 8.2c, likely due to soot emissions from the other combusting wood sticks. As evident in Fig. 8.2a and Fig. 8.2c, the stages of solid fuel combustion inherently produce an inconsistent temporal soot concentration which would make consistent results from averaged laser diagnostic techniques difficult.

The results shown in Fig. 8.2d are similar to those of the wood block with limiter (Fig. 8.2b); the attenuation is small, but emissions are measurable. This suggests that in some BDS trials, the top stick is never releasing smoke in view of the laser. However,

as all wood piles were burned to completion for each BDS trial, the top stick must have therefore burned outside of the path width of the laser, which could happen if the wood pile collapsed before the top stick was fully ignited. The peaks in soot volume fraction seen between 1000 – 1600 seconds are similar to the peak seen in Fig. 8.2c around 1000 seconds and are likely owing to the initiation of combustion of other sticks in the wood pile.

8.2.3 Conclusions

The in-situ soot volume fraction was found for the BDS using many trials and a simple laser diagnostic technique. High variability was seen in the soot volume fraction over the course of a burn for both a full wood stack in the BDS and a single piece of combusting wood. In addition, the results between tests for the BDS were highly irregular because the wood stack could combust differently every trial, sometimes collapsing or shifting as lower sticks charred and burned away, moving the flaming section out of view of the laser. Therefore, it was determined that the spatial and temporal variability in the wood stack combustion in a cookstove like the BDS would not produce in-situ results with any certainty without an unfeasible amount of trials. A more consistent, time-invariant flame was necessary to evaluate the effects of the halo mixing strategies.

8.3 Development of a Proxy Cookstove Burner for In-situ Measurements

Because a wood flame proved to be too variable for the desired in-situ measurements, the proxy cookstove burner (PCB) was developed. It was designed to produce a robust, spatially-repeatable, time-invariant, sooty flame similar to that of the Halo Stove. The final PCB was chosen to be a nonpremixed gas burner consisting of three pipes arranged like a trident with a line of holes on the top-facing side of each pipe (fully described in Section 2.1.3). As with any proxy system, the development of this final design consisted of trying to balance anticipated trade-offs between the original and proxy systems. Although the burner was still designed to provide a turbulent, variable flame, a gas burner was chosen because gas flames burn more repeatably than solid fuels. Gaseous fuel is comparatively homogeneous; the fuel burn rate can be controlled; and gas combustion inherently only consists of the flaming combustion stage versus the multiple stages of wood combustion (see Section 1.2.1 for full discussion). Also with a gas burner, the location of the base of the flame will remain constant, whereas the flames can traverse along a piece of wood as it burns, creating temporal and spatial variability. However, because the gas burner lacks the other stages of combustion, such as smoldering, and has a less diverse composition than pyrolysis gases from wood combustion, it will produce a different composition of emissions than a wood fire. Because this study is focused on in-situ soot emissions, the PCB was designed such that it produced as much or more soot than the Halo Stove, allowing the interactions between the injected air and

in-situ soot to be easily visualized, and focused less on other potential emissions or trends seen in the ex-situ results of Chapter 7. Liquefied petroleum gas (LPG) was chosen as the fuel because its primary component, propane, is a small-chain hydrocarbon and small-chain hydrocarbons, including propane, are typical pyrolysis gases from wood combustion (Di Blasi et al., 1999; Fagbemi et al., 2001; Bajus, 2010; Evans and Milne, 1987); however, unlike some small-chain hydrocarbons, propane still has the propensity to produce as much or more soot than a wood fire, especially when combusted in a nonpremixed flame. A nonpremixed flame, whether from solid or gaseous fuel combustion, requires the gaseous fuel or volatiles to interact with entrained air to combust, which produces an inefficiency that promotes products of incomplete combustion such as soot. The gas burner was chosen to be nonpremixed both because of the propensity towards soot formation and because then the gaseous fuel has to entrain air to combust, similar to the pyrolysis gases from the wood combustion in the Halo Stove.

Because the focus of the in-situ experiments was to view the effect of the air injection on the flame itself, the flame zone produced by the PCB was designed to mimic the flame zone of the Halo Stove. The hole and pipe spacing in the PCB encompassed a similar area as the Halo Stove firebox so the air injection from the halos would interact with the flames at similar points in both cases. The separation distance between the three pipes of the PCB allowed air to be entrained between them, similar to burning pieces of wood, and the PCB was elevated the same distance above the ground as the fuel grate of the Halo Stove so air could be entrained from below and between the burner pipes. Also, a 205 mm $\times$ 205 mm $\times$ 1 mm piece of sheet metal sat approximately 145 mm above the burner to mimic the bottom of the pot. However, to allow laser access without distorting air flow patterns, no vertical walls were included in the system. Laser access with vertical walls would involve either using windows, which would necessitate a redesign of the firebox to have straight walls because a circular firebox would require an unfeasible amount of alignment and calibration to avoid curvature effects, or using slits in the firebox walls, which would allow the laser sheet to pass through but would also allow air to be entrained non-symmetrically through the firebox walls, potentially obscuring the effects of the halo mixing strategies.

The three mixing strategies (90STR, 30ANG, and 30SWL, described in Chapter 7), mounted 130 mm above the PCB, were evaluated to ensure the PCB was emitting adequate quantities of soot. Three air flow rates (28.3, 35.4, and 42.5 L/min) were examined because interesting transitions occurred in this range in the preliminary Halo Stove results, discussed in Section 7.3. The LPG fuel was introduced at 5 L/min to produce a thermal power of 5 kW; the LPG flow rate was regulated using an Alicat mass flow controller which was inline with a compressed LPG supply.

8.3.1 Ex-situ Results of Proxy Cookstove Burner

Although the PCB was designed for in-situ measurements, ex-situ emissions measurements were collected to determine if the PCB was emitting as much or more soot than the Halo

Stove and also for comparison with the in-situ measurements (e.g. to be able to compare ex-situ and in-situ soot concentrations).

The experimental instrumentation used for ex-situ evaluation consisted of the same aerosol setup used in Chapter 7; it is described in Section 3.1.2. Each test was 5 minutes long with at least 2 minutes between tests to avoid lingering effects of the previous test conditions. Three tests were conducted per halo (90STR, 30ANG, and 30SWL), per air flow rate (28.3, 35.4, and 42.5 L/min). As the PCB combustion setup and air injection were ideally steady-state and repeatable, the data for all tests per case was analyzed as one large data set instead of as a comparison between tests. Therefore, although the metrics for evaluation were calculated as described in Section 4.4, they are presented as emission rates instead of emissions per test. The aethalometer data was calibrated as discussed in Section 4.4. Because the OPS was only calibrated for wood smoke, it was not used for this experiment. The DustTrak $PM_{2.5}$ data was calibrated using the equation: $PM_{2.5,filt} = 0.42PM_{2.5,DT} + 0.2$, which was developed by comparing the DustTrak and gravimetric filter data (shown in Fig. 8.3). Error bars on the graphs represent a 95% confidence interval calculated for a normal distribution.

Black Carbon

The black carbon (BC) results, shown in Fig. 8.4, confirm the PCB successfully emits as much or more BC than the Halo Stove, and also, all halos at all air flow rates drastically reduce BC compared to the baseline (no air injection) case. As the flow rate increased,

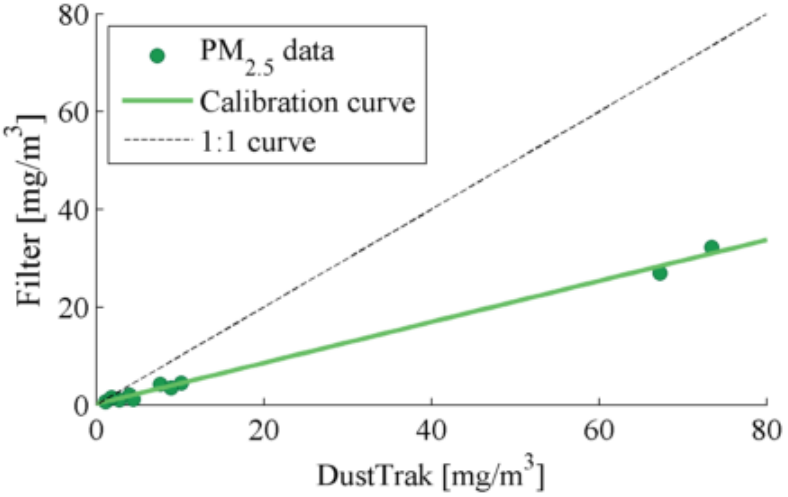

Figure 8.3: The $PM_{2.5}$ DustTrak data was compared to the $PM_{2.5}$ data from the gravimetric filters. The calibration curve was found to be: $PM_{2.5,filt} = 0.42PM_{2.5,DT} + 0.2$. Note, the two largest $PM_{2.5}$ values are from the baseline (no air injection) case and the smaller $PM_{2.5}$ values are from the halo cases.

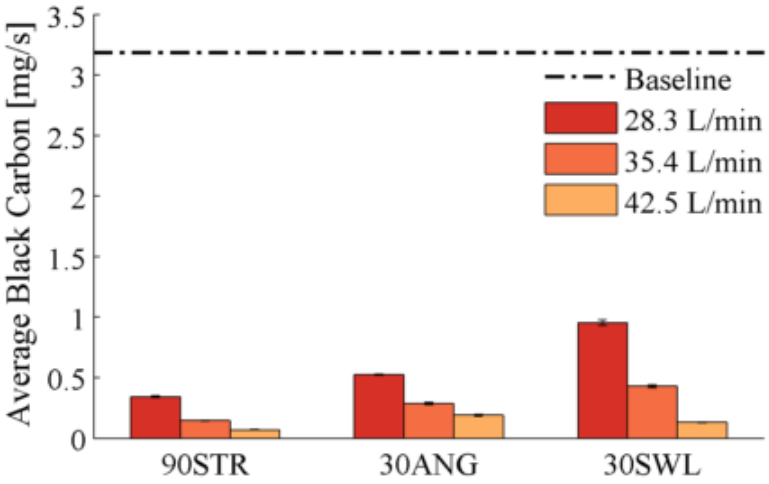

Figure 8.4: Black carbon (BC) emission rates from the PCB with different halos and air flow rates. Error bars represent 95% confidence intervals.

emitted BC concentration decreased. At the two lower flow rates, the 90STR reduced BC emissions the most, followed by the 30ANG and the 30SWL. At 42.5 L/min, the 30SWL reduced BC more than the 30ANG, with the 90STR still providing the largest reductions.

Carbon Monoxide

The carbon monoxide (CO) emissions are presented in Fig. 8.5. Like the BC results, all halos reduce CO at all air flow rates compared to the baseline. However, unlike the BC results, the CO results follow less of a trend. At the lowest flow rate, the 30ANG released over five times less CO than the 90STR and almost seven times less CO than the 30SWL. All halos released approximately the same amount of CO at 35.4 L/min. At 42.5 L/min, the 30SWL emitted the least amount of CO followed by the 90STR and then the 30ANG.

Although the gaseous flame removed the possibility of smoldering combustion, an important consideration is the effect of the air on the flame strain rate. If air strains the flame or quenches the flame too much, it could lead to local extinction. It could be expected as the air flow rates increase, the probability of locally extinguishing the flame also increases. A sign of flame extinction is an increase in CO emissions (Morr et al., 1975). The baseline case emitted three times the amount of CO as any of the halo cases so any quenching or strain effects appear to be small in this system. However, considering local extinction when examining the CO emissions from the PCB, some conclusions may be hypothesized. As the flow rate increased, the 30ANG emitted more CO, likely indicating that the injected air is locally extinguishing the flame because a higher air flow rate should improve turbulent mixing but it would also potentially cool or strain the flame zone. Conversely, the 30SWL produced the most CO at the lowest air flow rate and then less at the two higher; therefore,

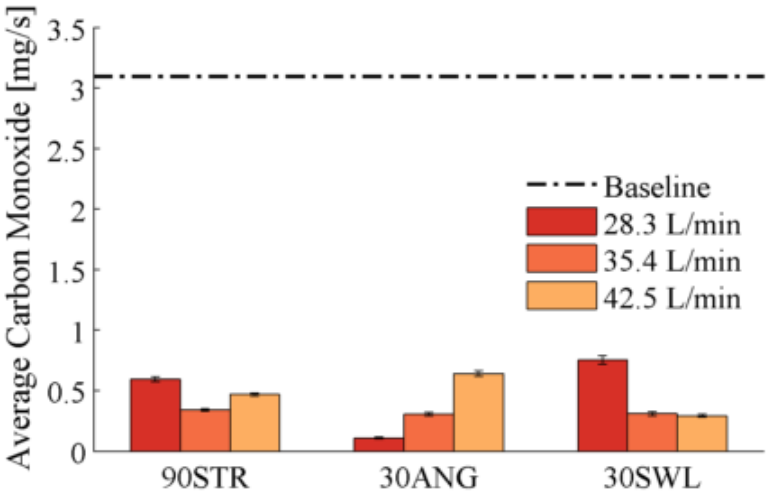

Figure 8.5: Carbon monoxide (CO) emission rates from the PCB with different halos and air flow rates. Error bars represent 95% confidence intervals.

it is likely the large CO emission at 28.3 L/min is due to a lesser amount of turbulent mixing than provided by the higher flow rates. The 90STR appears to be a combination of both poor mixing at the low flow rate and local extinction at the highest flow rate since its minimum occurs at 35.4 L/min.

$PM_{2.5}$ and Particle Size Distribution

The $PM_{2.5}$ emissions, shown in Fig. 8.6, closely resemble those of the BC emissions. All halos drastically reduced $PM_{2.5}$ compared to the baseline case. The 90STR provided the largest reductions at all three air flow rates. The 30ANG produced less $PM_{2.5}$ than the 30SWL at 28.3 and 35.4 L/min, but the 30SWL emitted less $PM_{2.5}$ at 42.5 L/min.

The similarity between the $PM_{2.5}$ and BC emissions is notable. Because it is a gas flame, the PCB consists solely of the flaming stage of combustion without the smoldering stage (as discussed in Section 1.2.1), unlike the wood-burning Halo Stove. It was noticed in the results of Section 7.4.2 that the emitted masses of $PM_{2.5}$ and BC for the wood-burning stoves were markedly different, potentially due to a high concentration of organic carbons (which would be recorded in the $PM_{2.5}$ measurements, but not the BC). Since organic carbons are more commonly emitted from smoldering combustion (Andreae and Merlet, 2001; Yokelson et al., 1997; MacCarty et al., 2008), theoretically the flaming combustion of the PCB should produce comparatively little organic carbon, meaning the $PM_{2.5}$ and BC mass measurements should be similar. This was indeed found to be the case.

The $PM_{2.5}$ results can be further examined in the particle size distribution results from 500 nm – 2.5 μm, shown in Fig. 8.7. Like the DustTrak $PM_{2.5}$ measurements, all halos reduced the number of particles compared to the baseline. Similarly, the different air flow

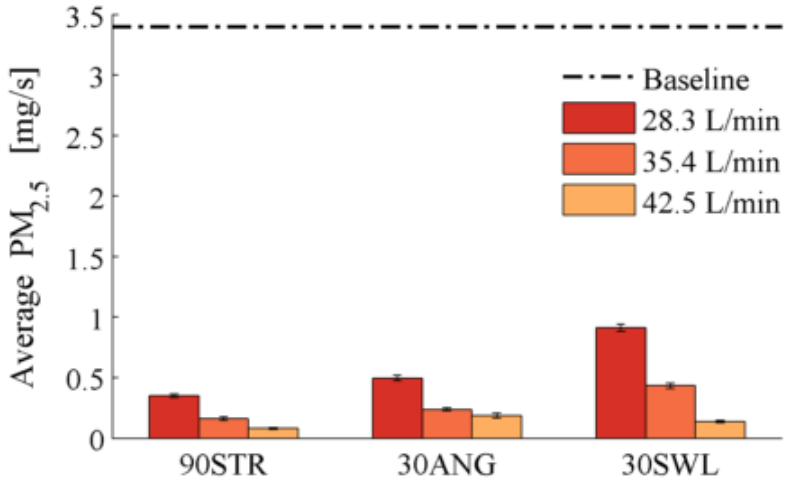

Figure 8.6: The $PM_{2.5}$ emission rates from the PCB with different halos and air flow rates. Error bars represent 95% confidence intervals.

rates appear to have the largest effect on the 30SWL because the particle size distribution changes noticeably between each flow rate. Note, above 5000 nm, too few particles were detected to provide valid results.

Although the primary goal of the PCB was to allow a visualization of the in-situ soot concentration, another original goal of the PCB design was to mimic the particle size distribution of the wood-burning Halo Stove in hopes of elucidating the mixing parameters that affect ultrafine particle (UFP) emissions. Several iterations of prototypes were developed which varied the number of pipes, number of holes in each pipe, pipe diameter, hole diameter, and pipe orientation (horizontal vs. vertical) in attempt to align the particle size distributions of the PCB baseline (no air) with the broad, multimodal distribution of the Halo Stove baseline (aka the BDS), seen in Figures 7.13a and 7.14a. However, the PCB baseline tended to be largely unimodal and peaked around 160 nm (shown in Fig. 8.8a). The only instances where the PCB baseline peaked in the smaller particle regime ($10-20$ nm), more similar to the Halo Stove, was when the burner fuel flow rate was so slow as to approach the lean flammability limit. As this flame was too weak to withstand additional air injection, it was not deemed feasible to achieve the same UFP distributions for the Halo Stove and PCB baselines. Perhaps as suggested by Hosseini et al. (2010), it is not possible for the pure flaming combustion of the PCB baseline to promote peaks in the ultrafine size regime. It is interesting to note, however, that the broader distribution seen for the BDS is somewhat mimicked by the 30ANG PCB and the 90STR PCB at 42.5 L/min; from the CO results, both of these cases were hypothesized to quench the flame, reducing that purely flaming combustion by potentially increasing local extinction. However, at 35.4 L/min (the same air flow rate as the Halo Stove trials), all of the PCB halos are largely unimodal and produce a peak around 100 nm; similarly, in the Halo Stove results, the distributions for the halos have

a single dominate peak which is centered between $30-50$ nm. Although the peak locations are slightly different, the particle distributions were deemed acceptable, especially as the UFPs are smaller than the wavelength of the laser beams used for the in-situ measurements.

8.4 Conclusions

Although the experiments conducted in Chapter 7 provided valuable information on the emissions and performance of the Halo Stove using the different mixing strategies, in-situ measurements in the flame zone are needed to help evaluate the hypotheses generated from the ex-situ examination of the Halo Stove. Often, laser diagnostic techniques are used for such in-situ measurements in combustion systems. To evaluate the feasibility of applying such techniques to the wood-burning Halo Stove, a simple laser diagnostic technique was applied to the Halo Stove baseline case. The wood fire was found to be too variable spatially and temporally to be used for the desired laser diagnostic techniques, so a proxy cookstove burner (PCB) was developed. Although differences are seen between the Halo Stove and the PCB, likely due to boundary conditions and potential for smoldering combustion conditions, the PCB produced as much or more soot than the Halo Stove and had a similar visual flame region. With the development of the PCB, it was now possible to record in-situ measurements using laser diagnostic techniques, discussed in Chapter 9.

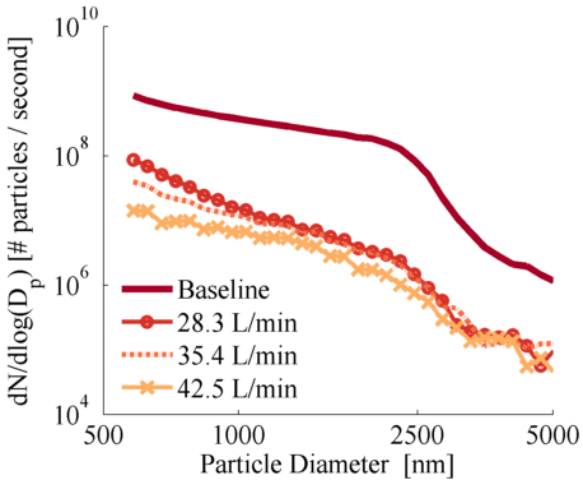

(a) 90STR particle size distribution

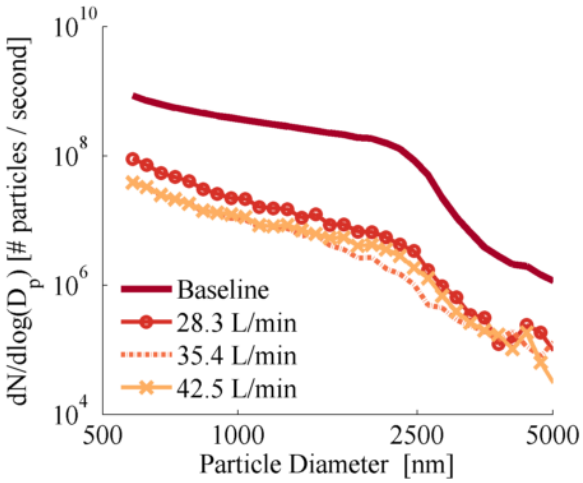

(b) 30ANG particle size distribution

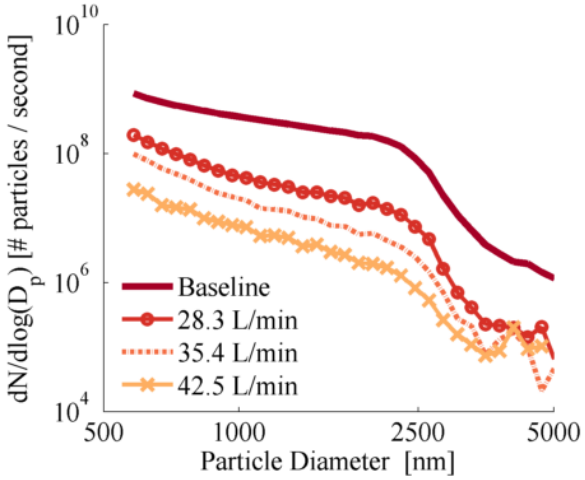

(c) 30SWL particle size distribution

Figure 8.7: The size distributions of emitted particulates from 500 – 5000 nm for the different halo and air flow rate cases of the PCB tests.

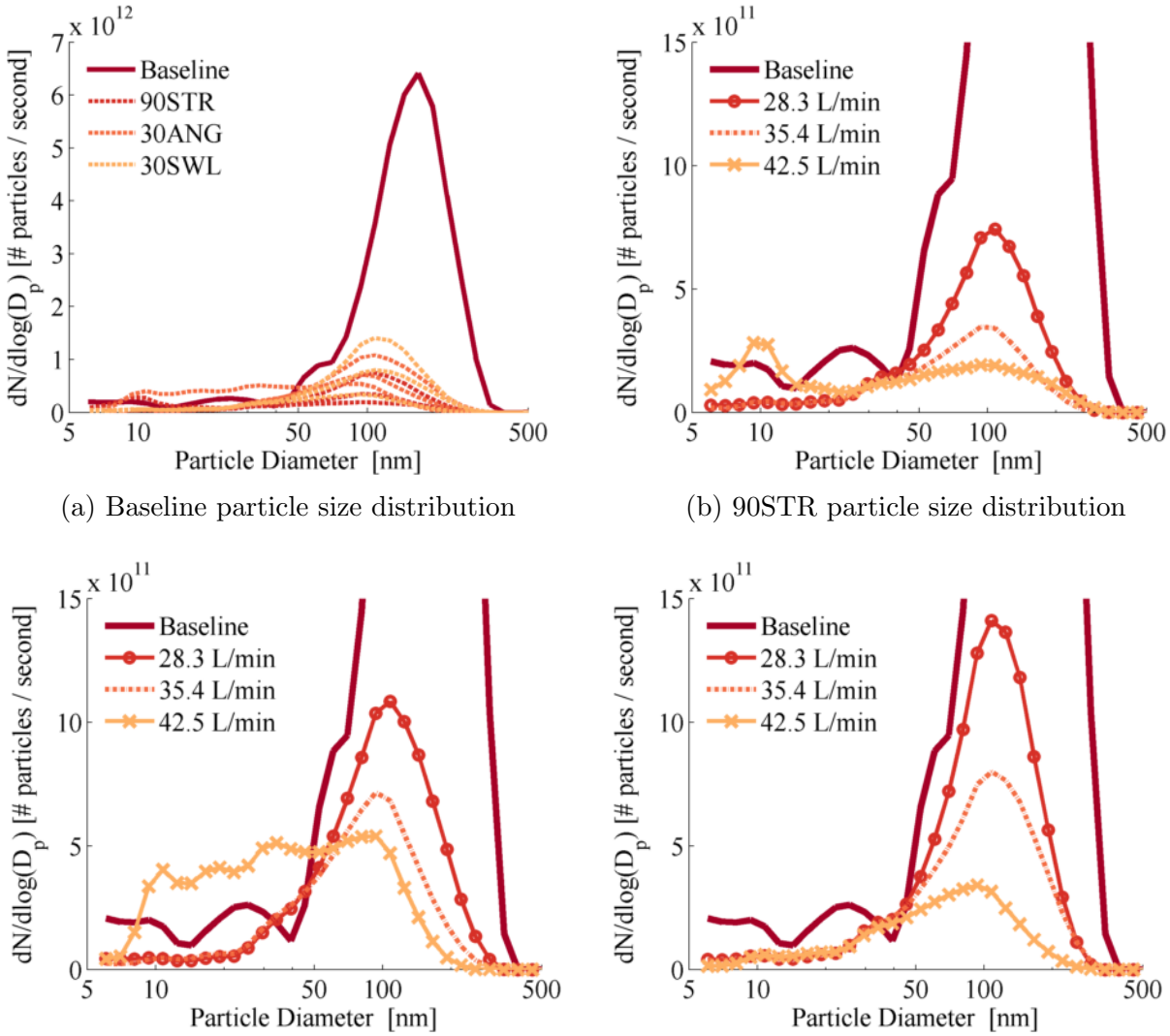

(a) Baseline particle size distribution

(b) 90STR particle size distribution

(c) 30ANG particle size distribution

(d) 30SWL particle size distribution

Figure 8.8: The size distributions of emitted particulates from 5 – 500 nm for the different halo and air flow rate cases of the PCB tests. Note, Fig. 8.8a shows the full baseline values. The other graphs have been scaled to reveal the differences in halos and air flow rates, so the baseline values have been cut on the y-axis.

9 In-situ Evaluation of the Halo Mixing Strategies

The proxy cookstove burner (PCB) (discussed in Chapter 8) was developed to enable the evaluation of the three halo mixing strategies (outlined in Chapter 7) using laser diagnostic techniques. Laser diagnostic techniques provide nonintrusive, in-situ measurements of the flame zone, which can offer a better view of how design modifications, such as air injection, directly affect the combustion in a stove. Four optical techniques were used to visualize the in-situ soot concentration, reaction zones, and flow profiles of the halo mixing strategies on the PCB: particle image velocimetry (PIV), laser-induced incandescence (LII), OH laser-induced fluorescence (OH-LIF), and luminescence.

9.0.1 General Experimental Setup

The proxy cookstove burner (PCB) and halo setup used for the ex-situ measurements in Section 8.3 was also used for all four optical techniques. The trident-like PCB, described in Section 2.1.3, was mounted approximately 50 mm above a base platform; this platform was mounted such that it could traverse vertically and horizontally, allowing the position of the PCB and halo system to be adjusted as needed for testing without disrupting the optical setups. Like the experiments conducted in Chapter 8, the LPG fuel was regulated at 5 L/min using an Alicat mass flow controller set to propane, which was inline with a compressed LPG supply.

The three mixing strategies (90STR, 30ANG, and 30SWL halos), described in Chapter 7, were chosen for evaluation with the same three air flow rates used in Chapter 8 (28.3 L/min, 35.4 L/min, and 42.5 L/min). The desired halo and the surrogate pot bottom were mounted 130 mm and 145 mm, respectively, above the PCB. The injected air was regulated using an Alicat mass flow controller set to air, which was inline with a compressed air supply.

9.1 Luminescence

Glowing soot particles formed in the fuel-rich regions of a flame produce a yellow luminescence (Warnatz et al., 2006). This luminescence can be recorded as a passive imaging

technique; a passive imaging technique uses the light from the flames to determine flame properties instead of an external source such as a laser (Ciatti, 2010). In this technique, the flame luminescence is observed and recorded using a light collection device, such as a camera or photodiode, which provides an estimation of soot in the flame based on the amount of light output, or luminosity. Note, the total luminescence from a flame not only includes soot luminescence but also includes contributions from the chemiluminescence of many other species, although these are often much weaker than soot luminescence. Therefore, luminescence measurements are a reasonable indicator of soot concentrations in the flame, but not a quantified measurement.

Luminescence is a straightforward, adaptable, and nonintrusive method. Passive techniques, such as luminescence, are especially useful for systems with limited optical access, as they require only one optical access window (Ciatti, 2010). Two limitations of luminescence are that it does not provide a quantitative concentration, only qualitative results which also include chemiluminescence components, and it has a strong dependence on the temperature in the flames. However, these qualitative results allowed for quick, straightforward comparisons between the different air injection modifications and visually provided insight on the locations of soot reduction in the entire flame region. Also the applicability of this technique to enclosed systems and the relatively inexpensive and straightforward setup could make it a feasible technique for in-situ measurements in cookstoves both in the lab and in the field. Therefore, another objective is to see how well the simple luminescence technique correlates to the more accurate and quantitative laser-induced incandescence (LII) technique (discussed in Section 9.3).

9.1.1 Experimental Setup

The PCB and mixing strategies were set up as described in the general experimental description of this chapter (Section 9.0.1). Images and movies of the flames under the different halo and air flow rate cases were taken using a digital SLR camera aligned with the center pipe of the PCB, the same location as the laser-induced incandescence (LII) camera (discussed in Section 9.3.1). Several exposure times, ISO settings, and aperture settings were assessed to achieve the highest signal output with limited saturation for all halo and flow rate combinations. The camera tests consisted of approximately 10 images per camera setting per air flow rate per halo as well as a 30 second movie per case. The camera settings f/16, ISO-1600, and 1/8000 exposure were found to reduce the amount of saturation in the images the most while still maintaining a signal-to-noise ratio of less than 2%, so were chosen to calculate the radial profiles of luminosity intensity. Although other settings at a lower ISO would give the same saturation results with a better signal-to-noise ratio, f/16 provided a good depth-of-field due to the strong out-of-plane nature of the flame and 1/8000 exposure reduced motion blur; the large f-number and short exposure time then required a high ISO to achieve the desired outputs.

Total light emitted from the flames was also recorded with a photodiode using National Instruments Signal Express LE software through a National Instruments cDAQ-9171

(4-channel, ±10 V). The photodiode allowed data capture at a sufficient rate to determine the frequency of the flame fluctuations and time-dependent statistics. Like the camera, the photodiode was aligned with the center pipe of the burner. No filter was used, so the photodiode detected broadband flame emission. The photodiode tests consisted of a 2.5 minute burn per air flow rate per halo along with 1 minute background (no flame) measurements before and after each case so the background noise could be removed from the total intensity before processing.

9.1.2 Results

Total Intensity

To compare the total amounts of in-situ soot for each halo and air flow case, the average total luminosity intensity, shown in Fig. 9.1, was calculated using the photodiode measurements. All halo cases decreased intensity compared to the baseline, with the 90STR halo leading to the largest reduction on average. As the measured intensity is taken as a proxy for the luminescing soot concentration in the flame, air injection through any halo appears to reduce soot within the flame. Furthermore, in general an increase in air flow through the halo appears to suppress soot formation or increase oxidation, consistent with the expected trend due to higher strain rates and enhanced mixing.

Intensity Radial Profiles

To visualize the effect of the different halos on the flames, mean profiles of the recorded intensity were developed from the luminescence images. Profiles of the intensity (integrated over the total flame height) from the centerline of the burner outward are shown in Fig. 9.2; note, these profiles are referred to in this work as radial profiles even though the flame is not axisymmetric. Each profile is the average of at least 10 still images and represents a viewing area of 238 mm × 185 mm. Example luminescence images for each halo are shown in Fig. 9.3. Note, unlike the images used to generate the radial profiles, these averaged images were formed from the movies recorded; the movies were taken at a more exposed camera setting which caused too much saturation for accurate radial profiles, but provides a brighter image and easier visual for the reader. Each movie-generated image is the average of approximately 1000 still frames and represents a viewing area of 238 mm × 162 mm. These sample images are for the lowest halo air flow rate (28.3 L/min). Averaged images for all cases at the camera settings used for the radial profiles, along with example instantaneous images, may be found in Appendix B.

The baseline case profile shown in Fig. 9.2 has two strong intensity peaks in the radial direction, one at the centerline and the other at approximately 40 mm. This corresponds to the flames from the center pipe and one of the outer pipes of the burner. In the images, it is the same with three strong flames shown in Fig. 9.3a.

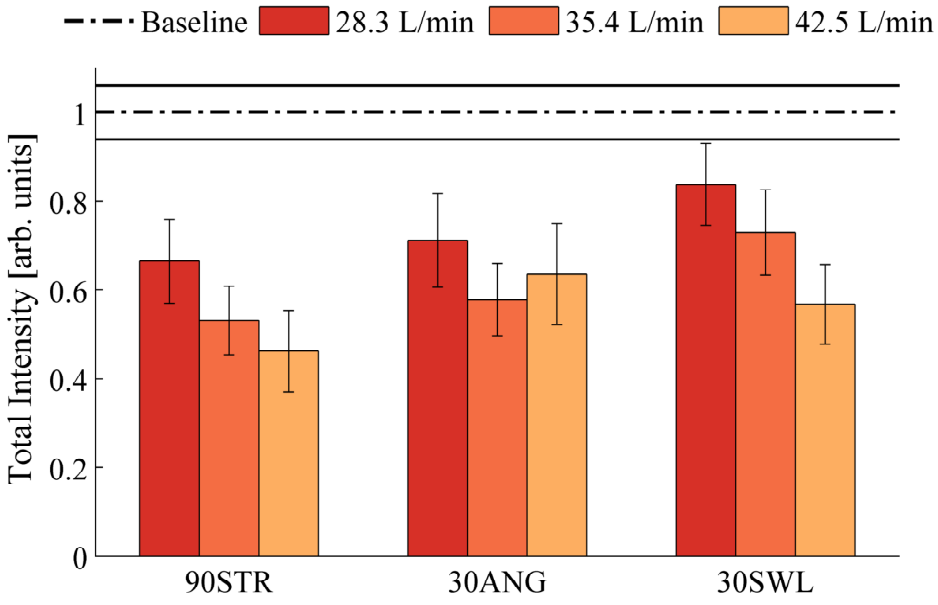

Figure 9.1: Total signal intensity of flames under different cases. All halos reduced soot compared to the baseline with the 90STR providing the largest reductions on average. Results have been normalized to the maximum (which is the baseline case) and error bars represent standard deviation.

The 90STR halo pushes these flames downward, theoretically increasing mixing and increasing soot oxidation. At low flow rates, like shown in Fig. 9.3b, flames still rise through the center of the 90STR halo, but as seen in Fig. 9.2a, the flames are suppressed and more uniform at higher flow rates. This explains the strong soot reduction shown in Fig. 9.1 and why the soot decreased as the air flow rate increased.

The 30ANG halo injects air toward the center of the burner and therefore primarily breaks up the fuel-rich zone in the center flame where the air converges, leading to the reduced intensity seen in Fig. 9.3c and explaining the improved soot reductions over the baseline in Fig. 9.1. However, it allows the flames from the outer pipes to rise up the outer edge of the injected air (around 40 mm in the radial direction of the profile shown in Fig. 9.2b), which is likely why the 90STR halo had larger reductions.

The 30SWL halo profile has two interesting trends apparent in its radial profile (Fig. 9.2c). A consistent peak is maintained along the centerline even with increased air flow. As this peak is not observed in the 30ANG halo case, it is due to the swirl effect caused by the tangential component of the 30SWL halo because the two halos are otherwise identical. Indeed, a swirling central vortex was visually observed during experiments. Similar to the 30ANG halo, the outer flame is present at low flow rates as the air injection does not greatly

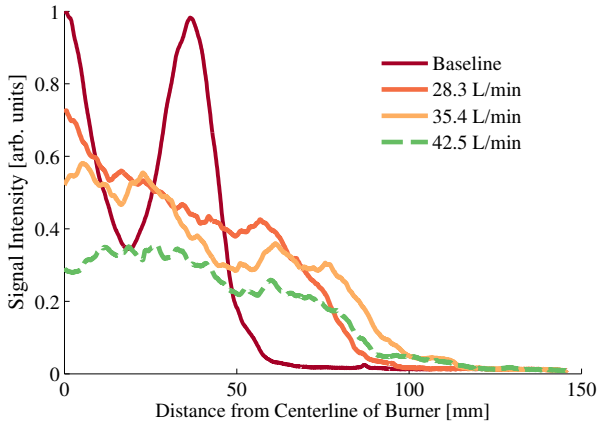

(a) 90STR radial profile

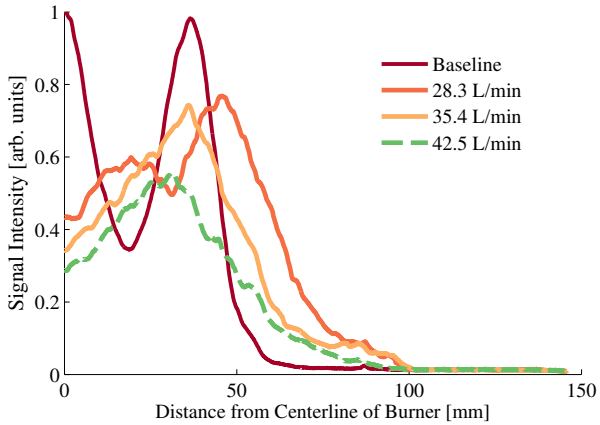

(b) 30ANG radial profile

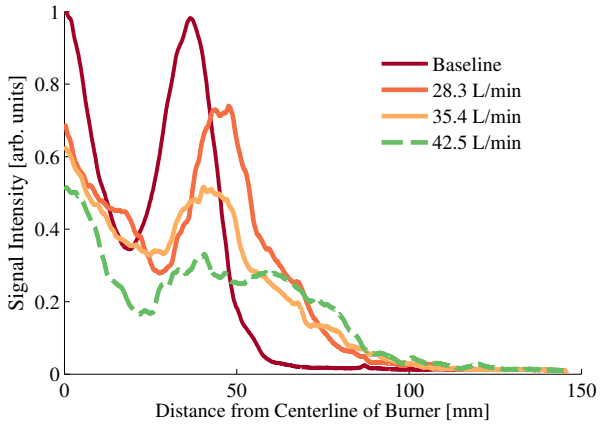

(c) 30SWL radial profile

Figure 9.2: Mean radial profiles of signal intensity for each halo. The baseline case is shown on all three graphs for comparison and measurements are normalized to the maximum.

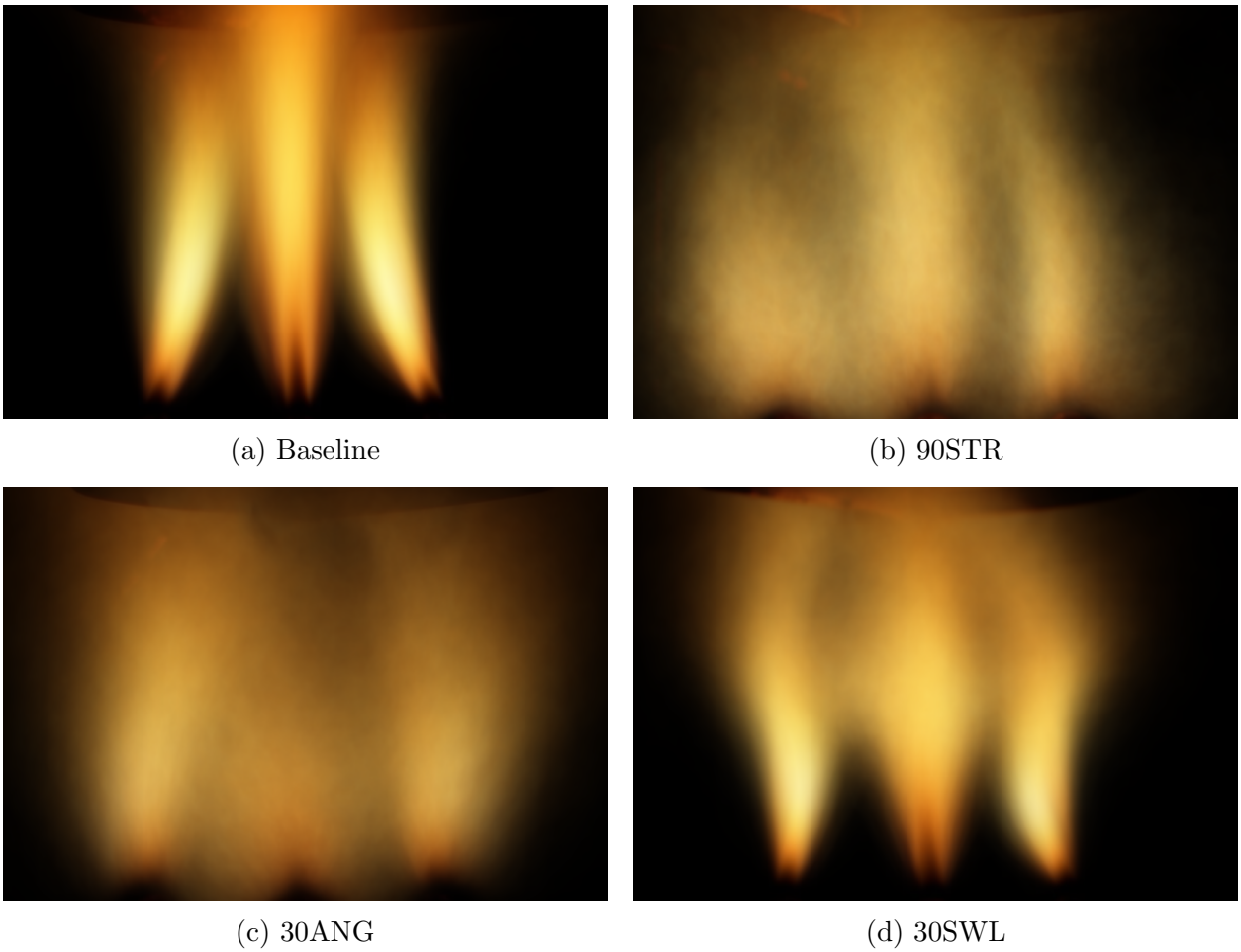

(a) Baseline

(b) 90STR

(c) 30ANG

(d) 30SWL

Figure 9.3: Example averaged images of flames in each halo case at the lowest air flow rate. Images represent a 238 mm × 162 mm viewing window.

impact the flames near the burner, shown in Fig. 9.3d. However, as seen in the profile, if the flow rate increases, this outer flame is reduced almost to the level of the 90STR halo as that soot is likely oxidized by air entrained by the central vortex. It is also important to note the difference in the 30SWL flames near the burner as compared to the 90STR and 30ANG halos. While the other halo average images are blurred throughout the lower flame region (indicating flame variability in the region), the 30SWL still has three separate and well-defined flames similar to the baseline case. This shows that the 30SWL at this air flow rate does not affect the base of the flames, and therefore, should not interact with the solid fuel combustion in the wood-burning Halo Stove, which may lead to increased emissions of products of incomplete combustion.

9.1.3 Discussion

In-situ vs. Ex-situ Soot

The soot emissions measurements discussed in Section 8.3.1 follow similar trends to the in-situ soot results shown in Fig. 9.1:

1. All halo and air combinations reduce soot in comparison to the baseline.
2. The 90STR halo performs best followed by the 30ANG and then the 30SWL.
3. As the flow rate of air increases, the soot decreases (within the limits of these experiments).

An important distinction may be made, however, in the level of soot reduction measured between the baseline and halo cases for the in-situ and ex-situ results. Luminescence only measures hot, luminescing soot in the flame; further oxidation may occur that is not captured by these measurements. As aerosol techniques measure the soot emitted from the stove, comparing luminescence and aerosol measurements can provide an idea of the amount of soot being oxidized outside of the flame front by each modification. This provides an idea of the effect of the air injection on the reduction of soot formation in the flame (low luminescence) versus the amount of soot that is formed and then oxidized. For environmental and human health reasons, it is desirable to reduce the soot emitted from a fire. However, the presence of soot within the flame is not entirely unwelcome because radiation from the in-situ soot can increase radiative heat transfer to a cooking pot, improving thermal efficiency.

The in-situ soot concentrations for the halos are less than the baseline, which indicates a portion of the soot emissions reduction is due to less soot formation in the halo cases. However, the relative difference between the baseline and halo measurements is drastically larger and more significant for the ex-situ results than for the in-situ. This is likely due to the air injection modifications performing as desired — soot still forms within the flame, resulting in high luminosity, but the increased turbulent mixing from the air injection oxidizes soot prior to its emission. These results help answer the question posed in Chapter 7 about whether the halo mixing strategies reduce BC emissions by decreasing soot formation or increasing soot oxidation. The difference between in-situ and ex-situ soot appears to confirm the halos are measurably increasing soot oxidation.

9.2 Particle Image Velocimetry (PIV)

Particle image velocimetry (PIV), described in Section 3.3, uses a series of images to visualize the movement of tracer particles in a system, thereby revealing the velocity profiles of the system. PIV was used to visualize the flow velocities of the injected air from the halo mixing strategies.

9.2.1 Experimental Setup and Data Analysis

The experimental setup (described in Section 3.3) primarily consisted of a 532 nm double-headed Nd:YAG laser (repetition rate of 10 Hz) which produced a laser sheet that spanned the region from the top of the PCB to the bottom of the halo. A MegaPlus-II CCD camera was aligned perpendicular to this laser sheet to capture the PIV images. There were three primary "flows" in the system: the fuel flow from the PCB, the air injected from the halo, and the air entrained into the measurement area by the first two flows. Ideally, all three of these flows would be seeded to capture the entire system. However, it was found that the fuel flow from the PCB was unable to be adequately seeded, even when using the ultrafine (0.2 μm) tracer particles, likely due to its low flow rate. The halo flow and general measurement area were successfully seeded with the halo and sieve seeders, respectively, described in Sections 2.4 and 3.3 using ultrafine titanium dioxide particles (0.2 μm). The experimental system was unenclosed to avoid affecting the bulk flow of entrained air in the system; therefore only the lowest air flow rate (28.3 L/min) was chosen for these evaluations to minimize particle losses outside of the measurement area.

Empirical trials found a pulse delay of 1 ms for the baseline (no air injection) cases and 200 μs for the air injection cases provided the correct timing between images to capture particle motion and a laser power of 90 – 100 mJ/pulse provided a strong signal intensity from the small tracer particles. The 90STR and 30ANG halo cases consisted of at least 474 image pairs per case, while the 30SWL halo cases consisted of over 700 image pairs per case. All image pairs were batch processed using PIVView 3.5 software using a single-pass interrogation algorithm to produce a velocity profile for that image pair. Images of a target grid (2 mm × 2 mm spacing) placed inline with the laser sheet in the measurement area were taken at least daily. These grid images allowed a calibration constant relating the number of image pixels per millimeter to be determined. The calibration constant, along with the pulse delay timings, allowed the PIV processing software to calculate quantified velocity outputs. An interrogation window of 64 × 64 was found to provide the desired level of detail for the velocity profile, so processing was conducted with a step size of 32 × 32 to allow for a 50% overlap. After the instantaneous velocity profiles were developed using PIVView 3.5, all velocity profiles for the same case were averaged to produce the final results for each case, presented here.

Velocity Errors due to Sieve Seeder

The sieve seeder was used to the seed the general measurement area in the halo tests. Because the sieve seeder used gravity to introduce particles into the measurement region, there was initially a slight downward velocity with those trace particles. This downward velocity was found to be 0.11 ± 0.08 m/s from PIV runs operating only the sieve seeder without air or fuel addition via a halo or the PCB, respectively. Unfortunately, the seed particles from the sieve seeder could not be distinguished from those of the halo seeder, and therefore, this intrinsic velocity of the sieve seeder particles could not be removed from the final results.

However, when examining the nonreacting flow results, it appears that the velocity of the halo air can still be distinguished from the surrounding air, even with the inclusion of a small gravitational velocity.

9.2.2 Results

Nonreacting Flow Measurements

Average velocity profiles for the three halo cases (90STR, 30ANG, and 30SWL) are presented in Figs. 9.4 – 9.6. For these cases, both the sieve and halo seeders were operating and the PCB was operating with LPG but was not lit (i.e. nonreacting or "cold flow"). Note that buoyancy effects of a lit, hot flame will not be captured in the nonreacting flow measurements.

Figure 9.4 shows the average velocity profile for the 90STR halo. In this figure, two downward flows are visible in the upper half of the image at approximately $x = \pm 50$ mm (where x is the radial distance). When the two downward flows reach $\sim 60 - 70$ mm height above burner (HAB), they begin to swirl and dissipate. Below HAB = 60 mm, the flow is chaotic across the radial distance, indicating turbulent flows and a potentially low seed density in this region. Increased turbulence could be indicative of the collision of the halo air and the PCB fuel, while a low density of seed particles could mean a fuel-rich area because the fuel flow is unseeded. Above 60 mm HAB, the center of the profile ($x = \pm 35$ mm) contains little velocity information, indicating that the injected air from the 90STR halo does not reach this region. These results align well with the luminescence results of Section 9.1. It was hypothesized that at low air flow rates, the flames still rise through the center of the burner with most of the fuel and halo air interactions taking place at the edges. The velocity profile from the PIV measurements appears to support this hypothesis with the turbulent lower outer regions and a relatively unaffected center region.

Figure 9.5 shows the average velocity profile for the 30ANG halo. A strong diagonal flow can be seen originating from the upper right corner of the figure. Note, the even spacing between the holes in the halo meant that two holes on opposite sides of the burner could not align with the beam line. Therefore, no clear air flow from the halo is seen in the upper left corner of the profile because that region is between holes in the halo and little of the injected air reaches that area. The injected air streams appear to begin intermingling around HAB = 100 mm because velocities are seen in the left half of the image, meaning the injected air has reached the laser plane. By ~ 80 mm HAB, the injected air flow has turned downward and is constrained in the central 40 mm of the burner, essentially the opposite of the 90STR halo. Outside of this central region, the flow profile is chaotic and sparse, indicating turbulent flow and/or less dense seeding. Overall, the velocity profile for the 30ANG shows a strong central flow of air and sparse, chaotic velocities in the outer regions, indicating the outer region is the primary location of the flames and the inner region is dominated by air from the halo. This corresponds well to the luminescence results which saw a low amount of soot in the center of the burner, meaning little visible flame and likely a high amount of injected

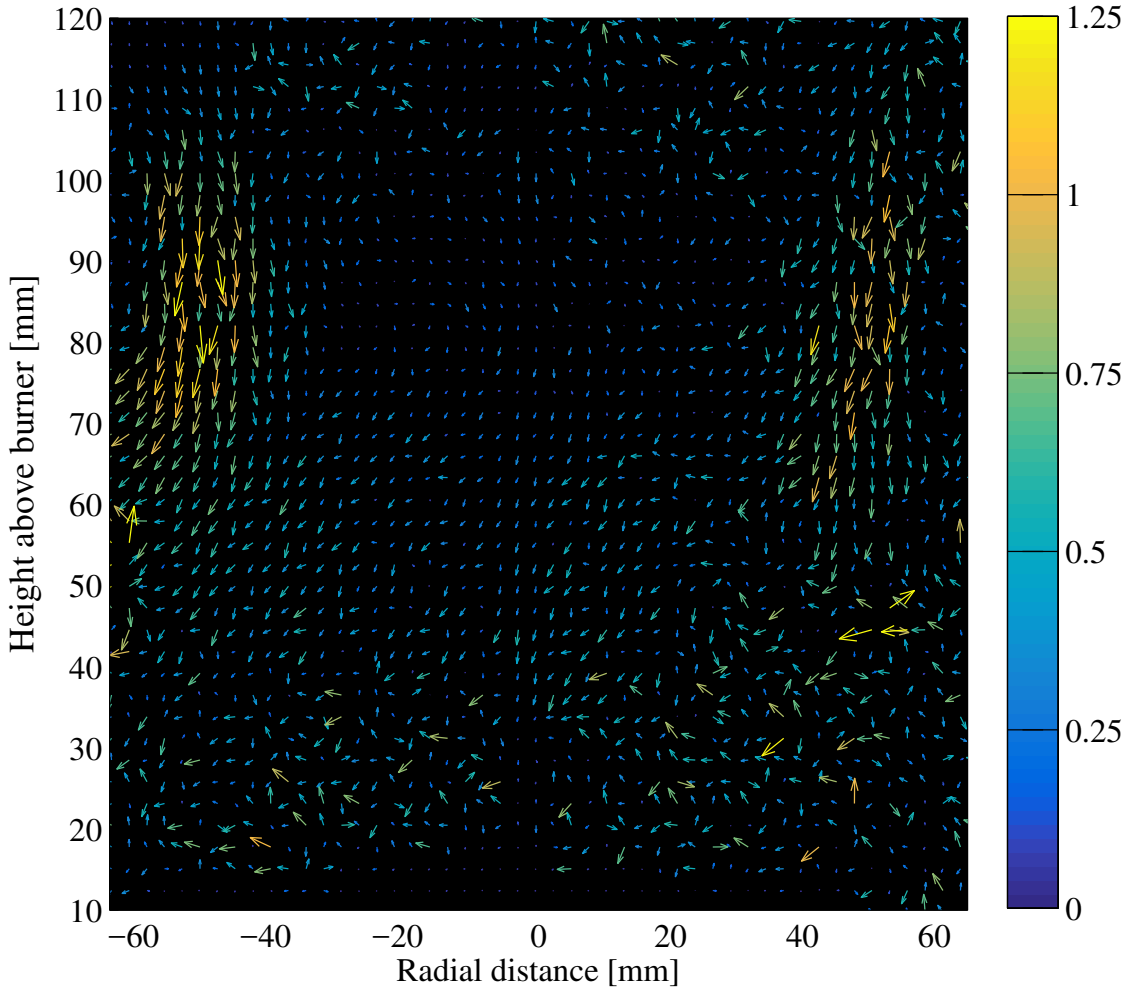

Figure 9.4: The average velocity profile for the 90STR halo with nonreacting flow. The center of the burner aligns with x = 0 mm in the radial distance. Units of the color bar are in m/s.

air, and increasing soot with increasing radial distance, indicating fuel-rich zones are near the edges of the measurement region.

The average velocity profile for the 30SWL halo is shown in Fig. 9.6. Like the 30ANG, a strong diagonal flow originates in the upper right corner of the profile. Again, the upper left corner lies between two injection holes and is therefore much sparser than the right corner; however, the swirling flow moves particles more quickly into the laser sheet than the 30ANG, allowing them to be seen as the less dense flow profile in the upper left corner. It is observationally known that the hole in the upper right corner angles the air toward the camera (out of the page) and the holes in the left hand corner angle the air away from the camera (into the page). It is likely part of this out-of-plane motion is captured in the slightly slower average velocities seen in the 30SWL results as compared to the 30ANG; these PIV

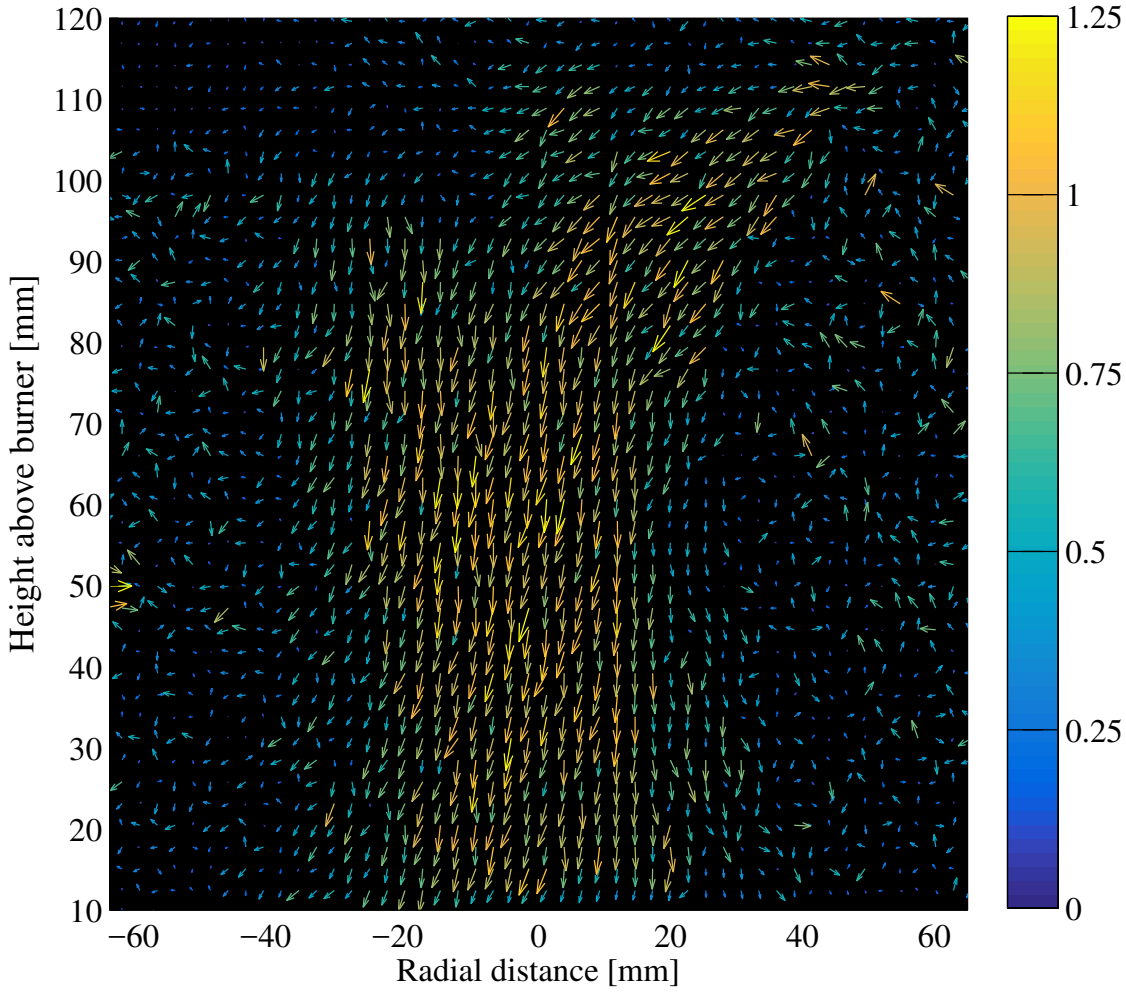

Figure 9.5: The average velocity profile for the 30ANG halo with nonreacting flow. The center of the burner aligns with x = 0 mm in the radial distance. Units of the color bar are in m/s.

measurements are two-dimensional and will therefore exclude the velocity magnitude in the third direction, making the overall velocity appear slightly slower.

In the lower half of the 30SWL profile, there is a downward flow centered around x = 0 mm. Although the downward flow appears similar to that of the 30ANG, the radial distance affected by the flow is broader, spanning more than 60 mm as opposed to 40 mm. Also to the left of center, the flow angles to the left, while to the right of center, the flow angles to the right. Additionally, the center of the upper half of the profile is largely empty. These differences are likely why the luminescence results still present a central flame for the 30SWL and not for the 30ANG. Although in two dimensions the injection angles of the 30ANG and 30SWL are the same, the slight angle of the 30SWL in the third dimension creates a vortex in the center of the halo as opposed to a centralized downward velocity

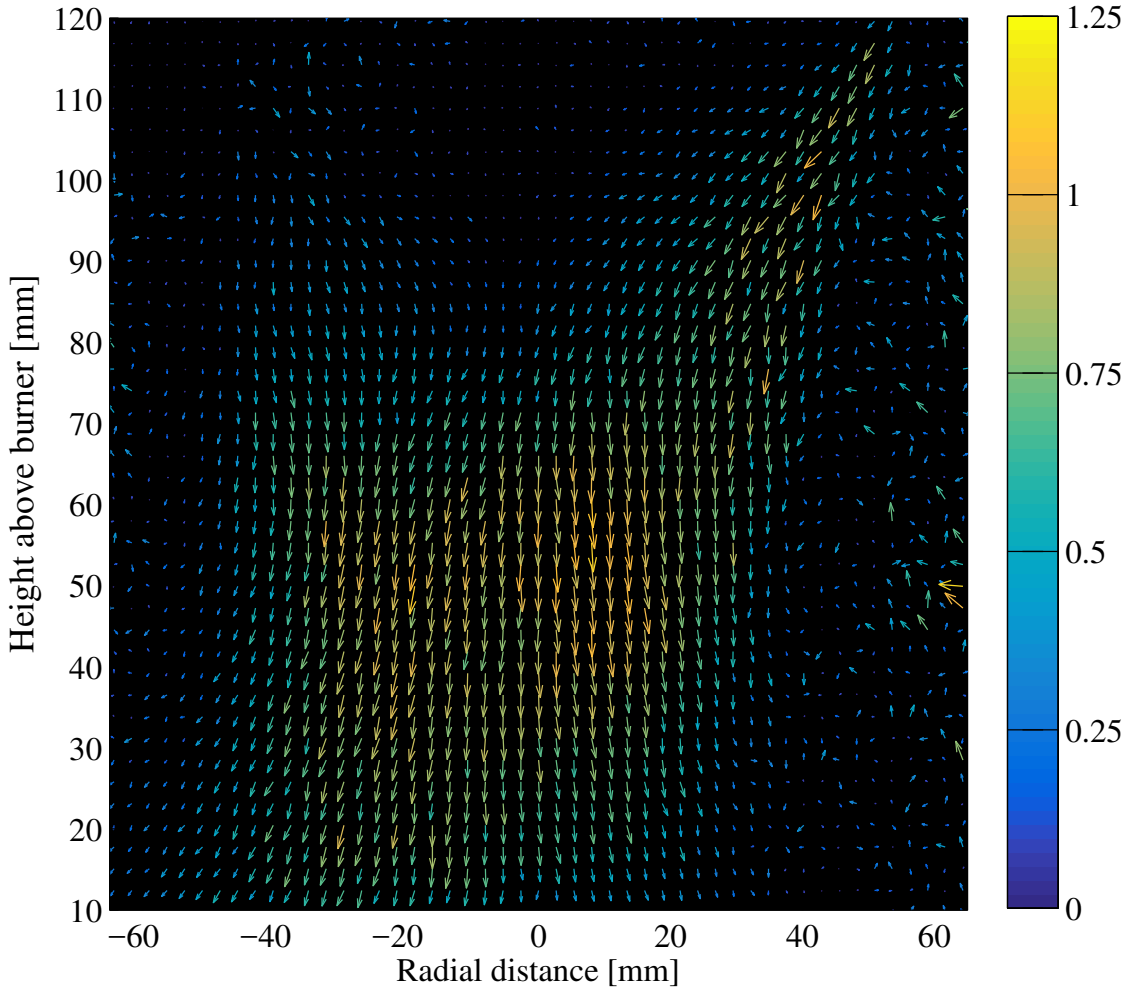

Figure 9.6: The average velocity profile for the 30SWL halo with nonreacting flow. The center of the burner aligns with x = 0 mm in the radial distance. Units of the color bar are in m/s.

like that of the 30ANG. The outer edges of the profile ($|x| > 40$ mm) appear to have a low seed density, indicating a richer fuel area because the fuel does not contain seed particles and would therefore greatly reduce seed density. This fuel flow on the outer edges of the profile also corresponds well to the luminescence results, which show a prominent flame zone around $|x| = 45$ mm.

Reacting Flow Measurements

The primary halo measurements are presented without the PCB fuel being lit, i.e. nonreacting or "cold flow". Because the velocity profiles are heavily dependent on the temperature of the gases in the system (e.g. buoyancy-induced flow), it is desirable and much

more representative of the system to have the fuel combusting (i.e. reacting or "hot flow"). Originally, measurements were recorded for all halos with a lit flame for this reason. However, reacting flow cases were found to result in large, empty portions of the instantaneous velocity profiles; these sections, which lacked measured flow velocities, coincided with the locations of bright flames. Visual inspection during experiments verified that the measurement region appeared to be well-seeded, thereby suggesting that the brightness of the flame obscured the scattered laser light of the small particles, even with the 532 nm filter in use. Due to the turbulent nature of the halo and PCB system, each instantaneous profile was unique; this uniqueness combined with the empty sections of the profiles produced unhelpful average flow profiles, presented in Figs. 9.7 – 9.9. Although sections of the initial air injection are visible in the 90STR and the 30SWL profiles, much of the profiles are void of usable velocities and therefore provide little information. Therefore, although it is less representative of the final system, it was decided that the primary results discussed and used for comparisons would be of the nonreacting flow cases.

Comparison of PIV Results and Luminescence Images

Because both PIV and luminescence images are visual, full-field techniques, it can be useful to compare them to provide a reality check for the laser-based PIV profiles using photos of the system. Therefore, this section compares the PIV velocity profiles with the images found in Fig. 9.3 as both measurements are of the 28.3 L/min flow rate case. Note, the PIV cases discussed are the nonreacting flow cases, while the luminescence images are from reacting flow cases. Although it is not a rigorous, quantitative comparison, comparing the PIV results and luminescence images also checks for any drastic differences occurring due to the increased temperature effects in the reacting flow cases.

The 90STR halo velocity profile (Fig. 9.4) showed an empty central region in the upper half of the profile surrounded by two downward flows that reach approximately halfway down the profile before becoming a sparse, chaotic, fuel-rich region. Similarly in the photo (Fig. 9.3b), the two outer flames rise approximately halfway up the image and the middle flame is left to burn relatively unaffected besides an increase in turbulence, providing an excellent opposite view to the PIV profile which highlights the location of the injected air.

The 30ANG profile (Fig. 9.5) showed strong diagonal flows which collided and formed a single downward column in the center of the measurement region surrounded by sparse, chaotic regions. Comparing with the luminescence photo (Fig. 9.3c), the center of the visible flame appears to have a hole punched in it where that strong downward air column is located. The flames then rise up along either side of that hole, aligning with where the velocity profile is relatively empty and disorganized in the PIV profile.

The 30SWL profile (Fig. 9.6) has strong diagonal flows which appear to twist around a central vortex. There are relatively few velocity measurements shown outside of the vortex flow, so the area appears to have low seed density (indicating a high fuel and/or low halo air presence) as opposed to a chaotic flow profile (indicating high turbulence). As seen in

Fig. 9.3d, the halo air does produce a swirl, but does not produce the same amount of turbulence as the 90STR or 30ANG, especially at low HABs.

9.2.3 Discussion

Applying PIV to the halo and PCB system encountered some challenges. The low fuel flow rate and large pressure drops of the PCB system did not allow for that flow stream to be seeded using the designed seeder. This meant that large sections of each image (where the fuel flow was dominant) did not contain an adequate number of seed particles and therefore lacked accurate flow profiles. Future research is necessary to identify how to adequately seed the fuel flow to remedy this issue. Large sections of images also lacked velocity profiles when the fuel was lit (i.e. reacting flow) because the luminescence of the flame obscured the light scattering of the small particles in the halo air flow. Therefore, the primary halo measurements examined here use a nonreacting, non-luminescing fuel flow; however, a nonreacting flow can produce different flow velocities than reacting flow due to effects of temperature-induced buoyancy. To assess any major discrepancies arising from using cold instead of hot flow, the nonreacting flow PIV results were compared to the reacting flow luminescence images, which are another full-field visual technique. Results of the two techniques appear to be well-matched, so it is assumed that the general flow profiles produced from the PIV measurements are correct. There are obvious limitations to applying two-dimensional PIV to highly three-dimensional flows, like those produced by the halo mixing strategies; however, useful insight into the mixing strategies has still be gained. Also, the application of two-dimensional PIV identified key challenges for future work, such as the need for a better seeding system for the fuel flow. Alternative methods of approximating flow profiles, such as computational fluid dynamics, as well as three-dimensional PIV would also be beneficial directions to explore to help reduce the uncertainty in the PIV image velocity profiles.

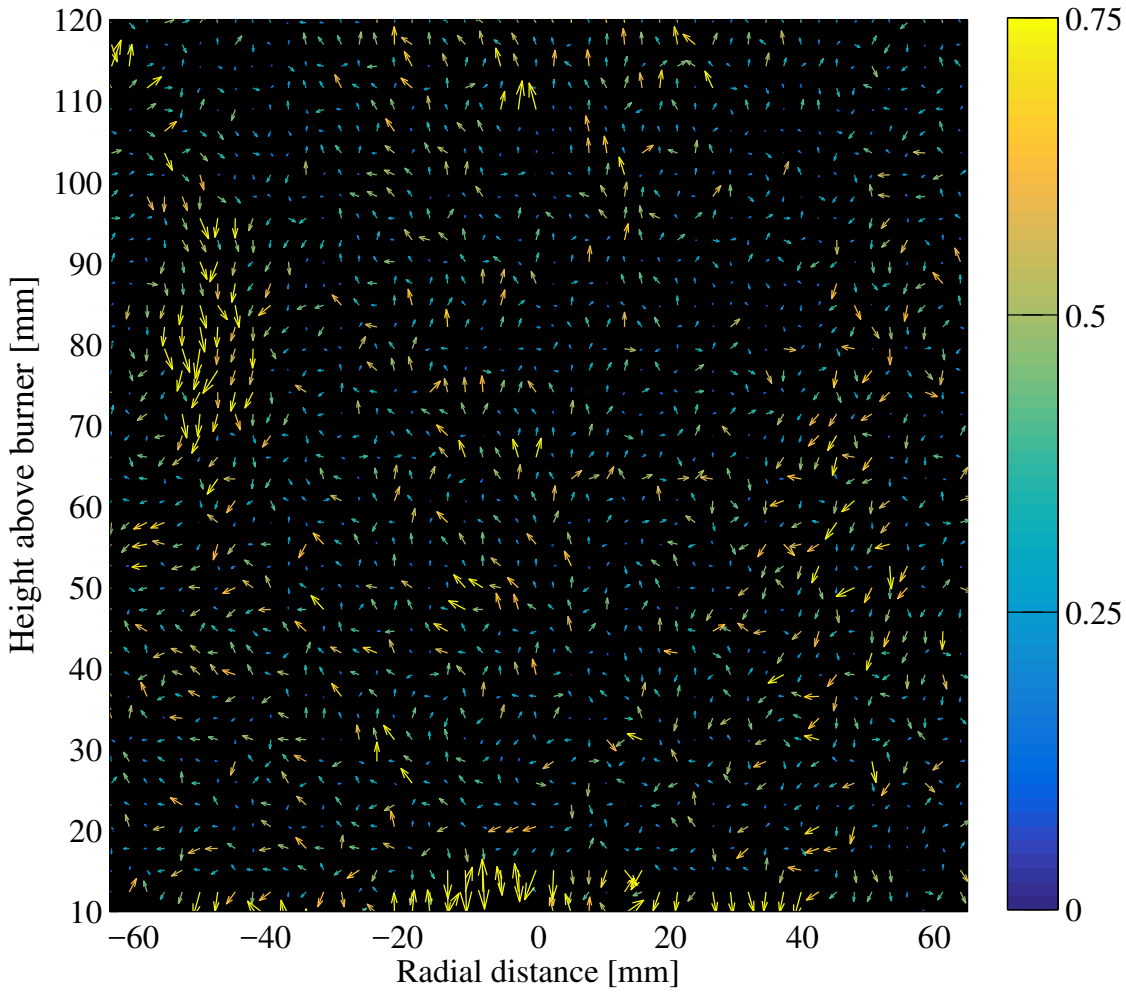

Figure 9.7: The average velocity profile for the 90STR halo with reacting flow. The center of the burner aligns with x = 0 mm in the radial distance. Units of the color bar are in m/s.

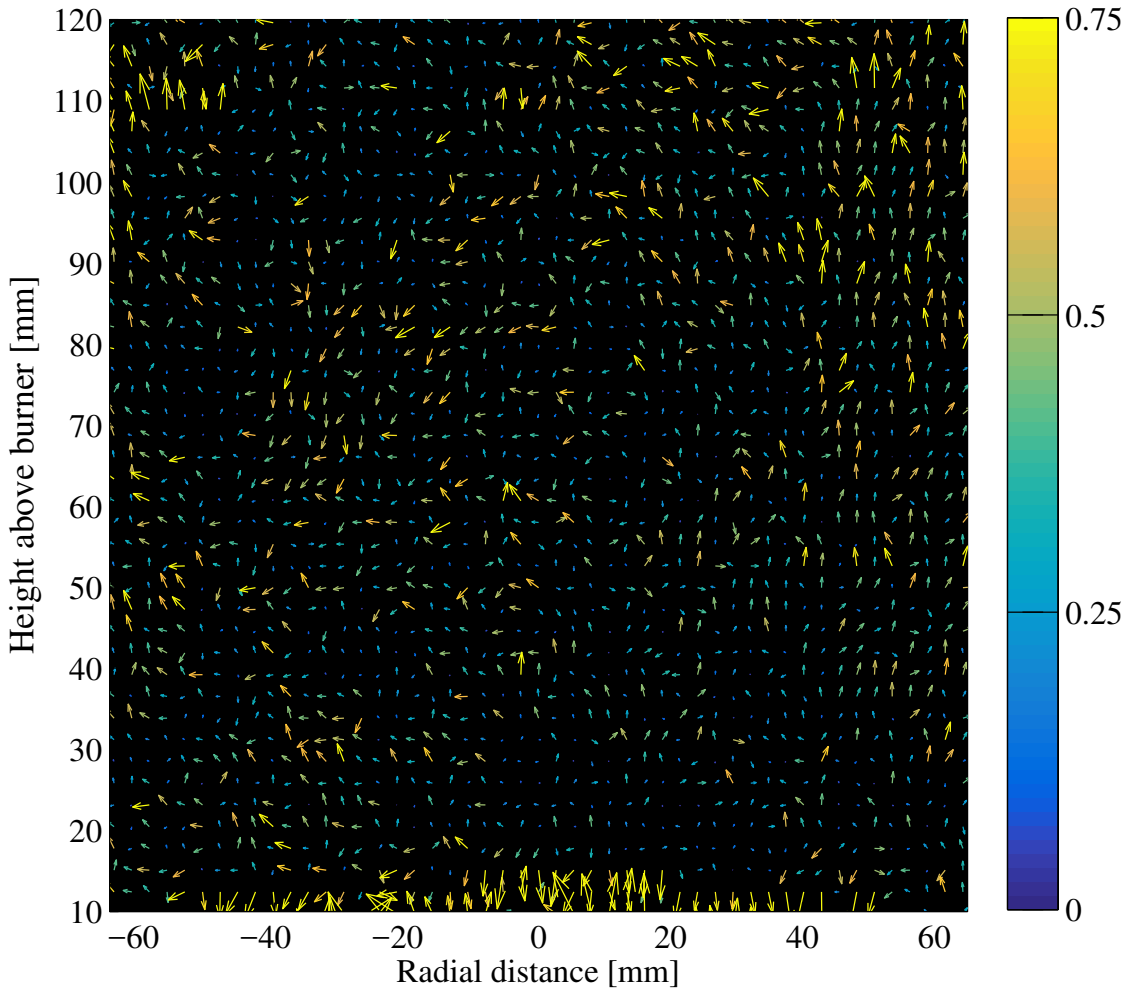

Figure 9.8: The average velocity profile for the 30ANG halo with reacting flow. The center of the burner aligns with x = 0 mm in the radial distance. Units of the color bar are in m/s.

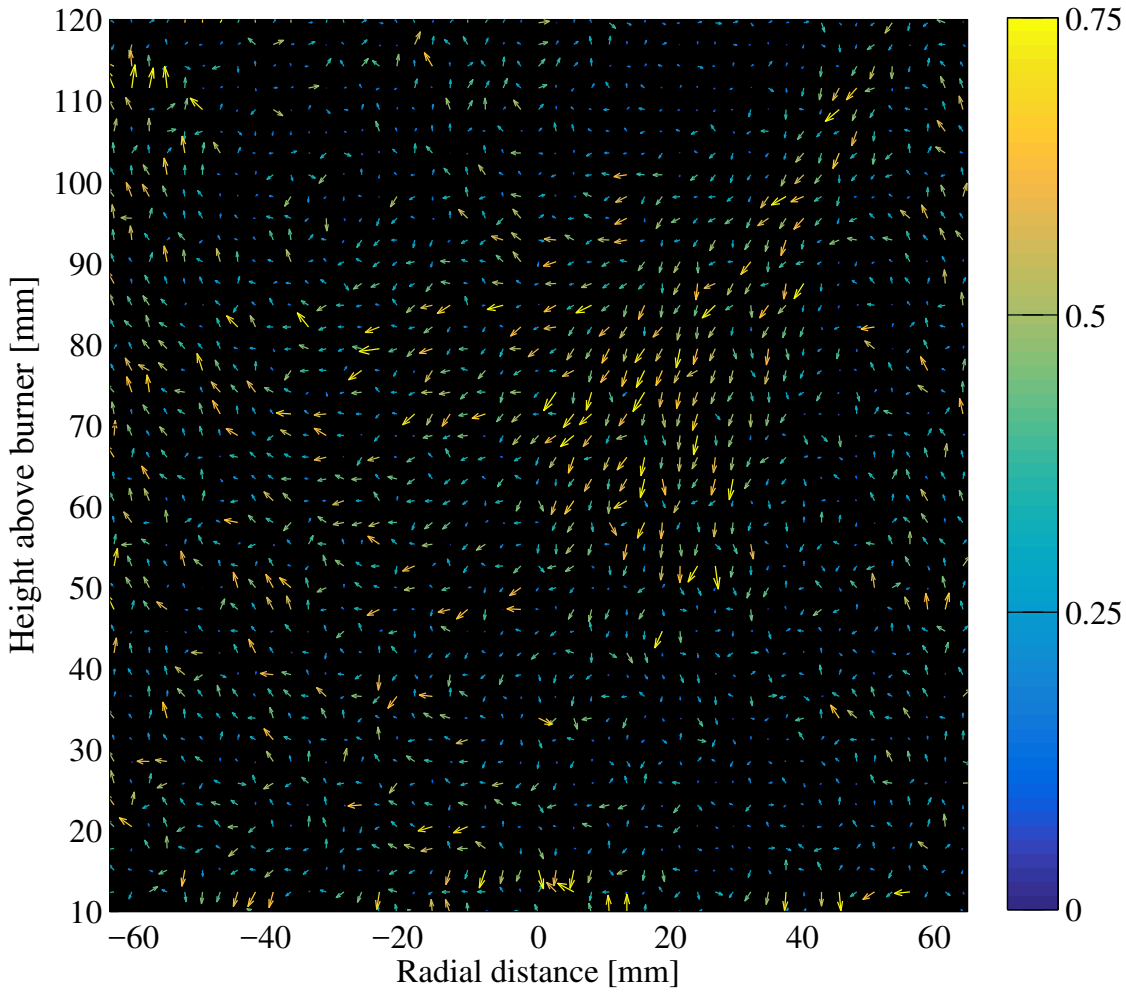

Figure 9.9: The average velocity profile for the 30SWL halo with reacting flow. The center of the burner aligns with x = 0 mm in the radial distance. Units of the color bar are in m/s.

9.3 Simultaneous OH-LIF and LII

Laser-induced incandescence (LII) and laser-induced fluorescence of the hydroxyl radical (OH-LIF), both described in Section 3.4, were conducted simultaneously to evaluate the spatial concentrations of soot and OH in the flame zone for each halo and air flow rate case. If calibrated, LII provides quantitative measures of soot concentration, and OH is a marker of the reaction zone of a flame (Santoro, 1994; Xu et al., 2003; Garo et al., 1990); therefore, the simultaneous use of LII and OH-LIF theoretically allows for identifying where the soot is located in the flame and the reaction zone, where the soot is potentially oxidized. The goal of this experiment was to compare the results of the different halo and air flow rate cases to identify any key differences and potential benefits of the mixing strategies and to enable better understanding of the hypotheses posed in Chapters 7 and 8.

9.3.1 Experimental Setup and Protocol

As with the experiments conducted in Chapter 8 and the other laser experiments conducted in this chapter, the PCB and mixing strategies were used as described in the general experimental setup (Section 9.0.1). The LII and OH-LIF laser systems (fully described in Section 3.4.2) produced coplanar laser sheets perpendicular to the ICCD cameras; the PCB was oriented with the pipes perpendicular to the laser sheets (inline with the cameras) such that the laser sheets crossed the midline of the flaming section of burner (center of the burner holes). In addition to the PCB, the slot burner (described in Section 2.1.3) was located along the beam line just prior to the PCB to provide the reference flame necessary to correct for power fluctuations in the OH-LIF beam (discussed in Section 4.5). The alignment of the OH-LIF and LII laser sheets was checked prior to testing each day and corrected as necessary. Also, the OH-LIF and LII laser powers and alignments were periodically checked throughout testing to avoid and correct any drift in the system. The timing of the LII and OH-LIF laser systems and cameras were controlled using the timing system described in Section 3.4.2. Each laser power was controlled by varying the delay time between the flashlamp and Q-switch through this timing system. The LII was prompt and the gate widths of the LII and OH-LIF cameras were 50 ns and 100 ns, respectively.

Several images were collected every day before and after testing to allow for calibrations and corrections as well as to check for system errors. The goals of these images included checking for signal interference due to background noise, flame luminosity, and laser intensity; acquiring images of the target grid for matching, parallel wires for rotation correction, signal uniformity for vignetting effects, and field-of-view for burner alignment; and checking and optimizing laser powers, beam heights, and synchronicity of the two imaging systems. For each case studied, off-wavelength OH-LIF images (500 per case) were recorded at the end of each test day for comparison with the day's measurements to assess interference from other species. The full use of these images in the data processing is described in Sections 4.5 and 9.3.2.

Laser extinction (LE) measurements were collected before and after testing every day for quantifying the LII measurements, using the experimental setup for LII calibration described in Section 3.2.1. To acquire the measurements needed for quantification, a highly and uniformly sooting, flat-flame burner (described in Section 2.1.3) was set up in place of the PCB. The flat-flame burner was centered inline with the LII laser sheet for the LII measurements and rotated slightly to be centered on the LE beam for the LE measurements so the two techniques would measure the same flame location, although not simultaneously. The LE measurements consisted of one minute of continuous data collection of the transmitted and incident beams without flame (background) and another one minute with flame; the LII test collected 250 images. These measurements were then processed and corrected as discussed in Sections 3.2 and 4.5 to produce calibration constants to quantify the daily LII measurements.

Because the distance between the PCB and halo was much larger than a feasible size for the OH-LIF and LII laser sheets (which is dependent on the size of available optics), measurements were taken at three heights above the burner (HAB): 10 mm, 25 mm, and 40 mm as measured from the bottom of the laser sheet to the top of the PCB pipes. As the laser sheets were $\sim$20 mm high, these three heights represent the bottom half of the distance from the PCB to the halo. Examining this region helps evaluate the impact of the air injection on the fuel bed. Also, visual observation of the flames in the upper half of the region showed extremely high variability and often contained little to no visible flame at the higher air flow rates. Therefore, the lower half of the region was chosen for evaluation using the three HABs.

Each test case consisted of 5 – 10 runs and each run collected 500 images of the measurement region, so the data for each case (halo, air flow, and HAB) consists of approximately 2,500 – 5,000 images with the exception of the baseline (no air injection) cases. Unlike the other cases, baseline cases were recorded multiple times every test day to provide a check of the optical and imaging systems throughout the day and across the test days; therefore, the baseline case results consist of approximately 11,500 images. After the corrections and calibrations discussed in the next section were conducted, the instantaneous results for each case were averaged to make radial profiles of the soot concentration and OH-LIF signal intensity.

9.3.2 Data Interpretation

To complete the OH-LIF/LII experiments and fully interpret the data, information regarding the laser powers and potential interferences needed to be collected and evaluated as discussed in the following sections.

Laser Power Variability

Laser power can slightly vary with each pulse (i.e. shot-to-shot variability) which in turn will affect the intensity of the signal to be measured. For OH-LIF, this shot-to-shot variability

could be relatively easily corrected for in image processing due to the availability of a reference burner (discussed in Section 4.5) as long as the OH-LIF laser was operating such that laser power is linearly proportional to the measured signal. Therefore, it was necessary to check the relation between the signal intensity and the laser power to ensure OH-LIF operation in the linear regime.

In these tests, the OH-LIF signal intensity was measured while the amount of laser power was varied by placing UV fused silica metallic neutral density filters (optical densities of 0.1, 0.2, 0.3, and 0.5) in the beam prior to the measurement region. The power was recorded just prior to the final beam block of the system (shown in Fig. 3.6); the laser power used was the same as that used for the experiments conducted in the results section ($\sim$10 mW). As seen in Fig. 9.10, reductions in laser power scale linearly with the signal intensity, allowing for shot-to-shot variability corrections for laser power.

In the LII system, laser power can have a large impact on the detected LII signal because at low fluence, the peak LII signal rises as the laser fluence rises (Schulz et al., 2006). However, as the fluence increases, so does the temperature. At a certain temperature ($\sim$4000 K), the mass loss and evaporative cooling caused by soot sublimation balances out with the increasing laser fluence, so the peak LII signal stops increasing with laser fluence (Schulz et al., 2006). Laser fluences within this "plateau" region are typically chosen for

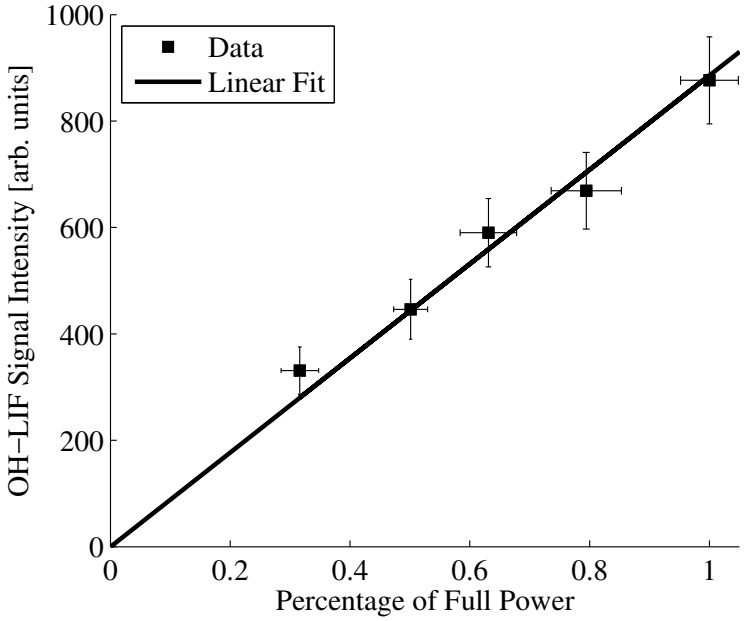

Figure 9.10: The average OH-LIF signal intensity versus the average percentage of laser power. As can be seen, the OH-LIF signal and laser power scale linearly, allowing for straightforward corrections in shot-to-shot variability of the laser. Error bars represent standard deviation.

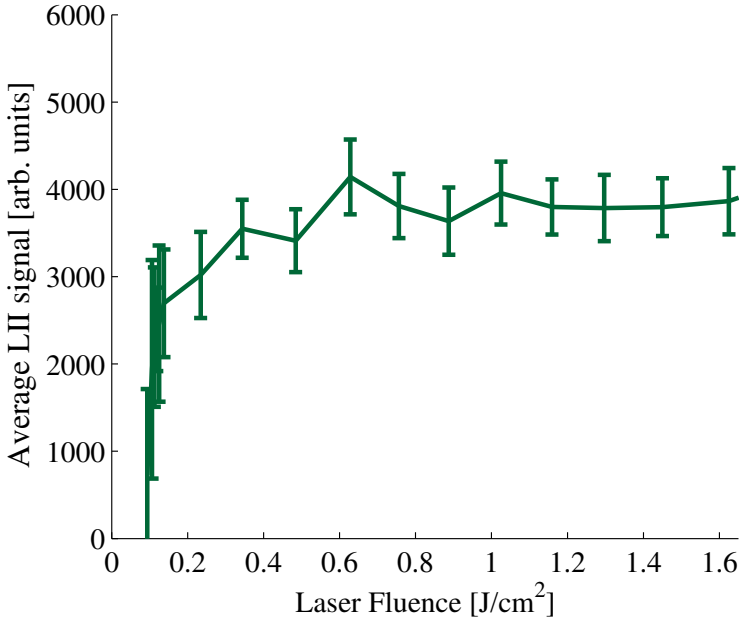

Figure 9.11: LII signal intensity versus the laser fluence. Note, the signal intensity becomes level past a certain laser fluence; this is often referred to as the LII fluence plateau. Error bars represent standard deviation.

LII measurements so any variability in the laser fluence does not affect the peak LII signal. However, as the fluence increases in the plateau region, so does the amount of sublimation of particles and potential for changes in the soot morphology (Moreau et al., 2004) so a balance along the plateau must be found. To evaluate the correct laser power to use for the LII experiments conducted in this work, measurements were taken at incremental laser fluences, shown in Fig. 9.11. The onset of the plateau appears to be around $0.4-0.6$ J/cm^2, which is in good agreement with other works, which estimate the onset of the plateau around 0.3 J/cm^2 and above for a 1064 nm excitation beam (Axelsson et al., 2000; Vander Wal, 1996; Schulz et al., 2006). A laser energy of 162 mJ/pulse, which was equivalent to ~ 1 J/cm^2, was chosen for these experiments; therefore, the shot-to-shot variability of the laser should not affect signal intensity as the measurements were taken within the plateau region.

Beam Attenuation

As the laser passes through the flame, some of its energy is attenuated by soot and other particles (which is the entire concept of extinction, described in Section 3.2). It is possible therefore for the laser energy to drop as it passes through a flame, especially if it is a heavily-sooting flame, affecting the uniformity of the resulting measurements. To check for this effect in the PCB, the power of the LII laser after it had passed through the flame was measured as well as the laser power at the same location without any flame; a difference

Table 9.1: Laser energy data for the LII laser at 10 mm, 25 mm, and 40 mm above the burner with and without a flame. Power measurements were recorded after the flame zone to assess the amount of attenuation as the beam passed through the flame. The error shown is the standard deviation.

	LII Laser Energy $\left[\frac{mJ}{pulse}\right]$
No Flame	1.55 ± 0.004
HAB = 10 mm	1.55 ± 0.022
HAB = 25 mm	1.51 ± 0.021
HAB = 40 mm	1.48 ± 0.026

in laser power would show the level of interference from the attenuation through the flame. Measurements were taken at the three flame heights to be used for the final experiments (HAB = 10 mm, 25 mm, and 40 mm). Each measurement result, shown in Table 9.1, is the average laser power during a 90 second period. It was found that attenuation contributed to less than a 5% drop in laser energy over the width of the flame at all heights, which was deemed acceptable.

Signal Trapping

Because the flame zone is three-dimensional, not solely a 2-D sheet like the laser, many reactions, radiative emissions, and particles exist between the measurement region and the ICCD camera of the LII system. Therefore, similar to the beam attenuation, the generated signal intensity of the luminescing soot in the laser plane can be obscured or absorbed prior to reaching the camera. This is commonly referred to as signal trapping. To assess the amount of signal trapping occurring in these experiments, the flat-flame burner (described in Section 2.1.3), typically used for the LII calibration, was utilized as a uniform, symmetric soot source. The flat-flame burner was operated with a premixed ethylene and air mixture (2 L/min of ethylene, 10 L/min of air). Because the flat-flame burner produces higher quantities of soot than the PCB, signal trapping measured with the flat-flame burner is an overestimate of this interference. LII measurements were recorded traversing the length of the burner, with 0 mm being the closest end of the burner to the camera and 25 mm being the typical location of the laser sheet for the LII calibration tests. The laser sheet (which was perpendicular to the LII camera as in the LII schematic (Fig. 3.6)) was incrementally moved from 15 mm from the end of the burner to 35 mm away; the results are shown in Fig. 9.12. It can be seen that the signal intensities across the burner are relatively equivalent. If a significant amount of signal trapping was occurring, the signals recorded closer to the camera should have a higher intensity than those recorded farther away. Because this is not seen to be the case in Fig. 9.12 and these measurements should overestimate the interference, effects of signal trapping in the system were deemed to be negligible.

Soot Intermittency

When measuring the in-situ soot concentration in the flame, the standard deviation, or variability, of the soot concentration can help describe the intermittency of the soot in the system. The average maximum LII signal intensity and its standard deviation were found for each case; the normalized standard deviations for the different heights above the burner (HABs) are presented in Table 9.2. The full table of averages and standard deviations may be found in Appendix D.

It can be seen in Table 9.2 that the standard deviations are fairly similar across all cases for HAB = 10 mm. This suggests that there is little difference in the level of intermittency between the baseline and halo cases at that height. As the HAB increases, so does the difference between the standard deviations of the baseline and the halo cases. Averaging the standard deviations for the halo cases, it can be seen that at HAB = 10 mm, the difference from the baseline is only ∼9%, but at HAB = 25 mm, it is ∼28%, and at HAB = 40 mm, it is ∼35%. It is understandable that there would be little variability in the signal at HAB = 10 mm; that measurement region is near the top of the PCB where the flames have had little opportunity to interact with each other or the injected air from the halos (if applicable). As the HAB increases, the opportunity for interaction will increase, leading to greater variability in the flame location and a higher level of soot intermittency in the system.

Interference from Polycyclic Aromatic Hydrocarbons

Interference in the OH-LIF signal can occur due to soot luminescence and polycyclic aromatic hydrocarbon (PAH) fluorescence, which obscures the genuine OH concentration profile. Previous studies have found that the fluorescence of PAH is likely to occur from excitation in the UV spectrum where OH-LIF is performed (Leipertz et al., 2002; Vander Wal, 1996). A bandpass filter was used with the OH-LIF camera to limit extraneous light and help address the issue. To evaluate the amount of this interference, daily measurements were taken with the OH-LIF laser being operated at a wavelength that would not induce OH fluorescence ("off-wavelength"); therefore, any measured signal would be due to interference from other sources, such as soot or PAH. The baseline case produces the most soot and is therefore expected to have the largest soot and PAH interference. Measurements recorded at different HABs for the baseline (no air) case are shown in Figs. 9.13 – 9.15 as the upper bound of the potential interference (see Appendix C for all cases). The top plot in each figure shows the average measured interference found when the OH-LIF laser is driven off-wavelength. The middle plot shows the average OH-LIF signal prior to the laser power variability corrections discussed in Section 4.5, as well as the same OH-LIF signal with the measured off-wavelength signal subtracted. Note, since the OH-LIF reference flame was not visible in the off-wavelength measurements (because it did not produce measurable amounts of soot or PAH to cause interference), the off-wavelength signal itself could not be corrected for laser variations. Therefore, the uncorrected OH-LIF signal minus the off-wavelength from

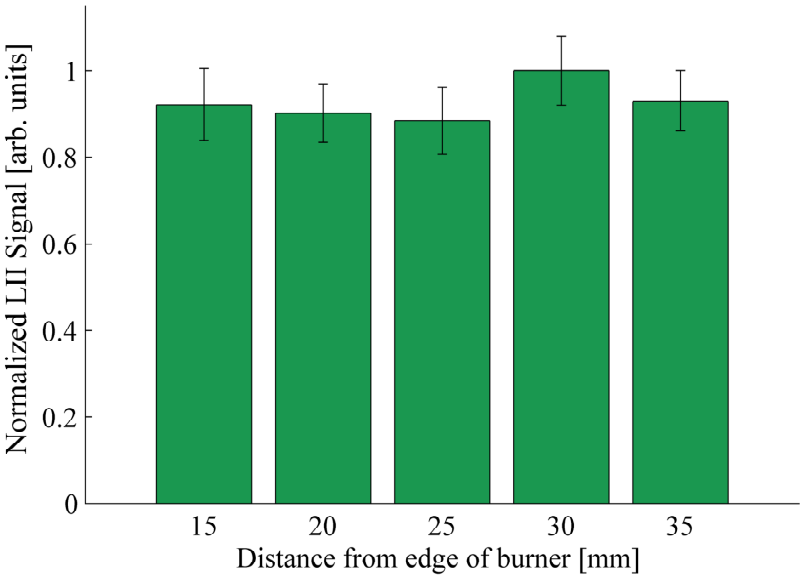

Figure 9.12: The LII signal measured at different distances away from the LII camera (0 mm is the closest edge of the burner to the camera). Error bars represent standard deviation.

Table 9.2: The normalized standard deviations of the maximum LII signal intensities per case. Values have been normalized to the maximum from their respective HAB.

Halo	*Air Flow*	*Normalized Standard Deviation [arb. units]*		
		HAB = 10 mm	*HAB = 25 mm*	*HAB = 40 mm*
Baseline	No Air	0.86	0.70	0.67
90STR	28.3 L/min	0.98	0.82	0.89
	35.4 L/min	0.84	0.79	0.97
	42.5 L/min	1.00	0.97	0.98
30ANG	28.3 L/min	0.95	0.94	0.95
	35.4 L/min	0.88	0.97	0.95
	42.5 L/min	0.96	0.98	1.00
30SWL	28.3 L/min	0.99	0.94	0.96
	35.4 L/min	0.94	1.00	0.94
	42.5 L/min	0.94	0.93	0.95

the middle plot was corrected to produce a "final" OH-LIF minus off-wavelength result which is shown in the bottom plot in each figure along with the final recorded OH-LIF signal.

The results reveal that the impact of the PAH interference on the OH-LIF signal can be quite drastic, as in many instances the entirety of the OH-LIF signal is comprised of interference from other species. Unfortunately, the interference from soot and PAH can vary dramatically from image to image and off-wavelength measurements could not be recorded simultaneously with the experimental data; therefore, such interference could not be removed from the final averaged data presented in the results. However, strong PAH occurs in the fuel-rich section of the reaction zone, so even the high interference levels can be a marker of the reaction, although not the fuel-lean, oxidizing region. Therefore, it is stressed that the final OH-LIF data presented contains substantial interference and care must be taken when trying to draw conclusions from the averaged results.

Data Confidence

Flames from the PCB were intended to mimic a wood-burning fire and therefore they were intentionally turbulent. Because of this turbulence, numerous replicate measurements were collected to counteract some of the variability in averaged measurements. Between 2,500 and 5,000 images were collected for each case studied with the exception of the baseline cases, which had 11,500 images recorded. To check if enough measurements were recorded, the 95% confidence intervals (assuming a normal distribution) were calculated for the OH-LIF and LII measurements. The 95% confidence intervals were found to be less than 0.15% of the average values, indicating a high level of confidence in the results and that enough tests were conducted.

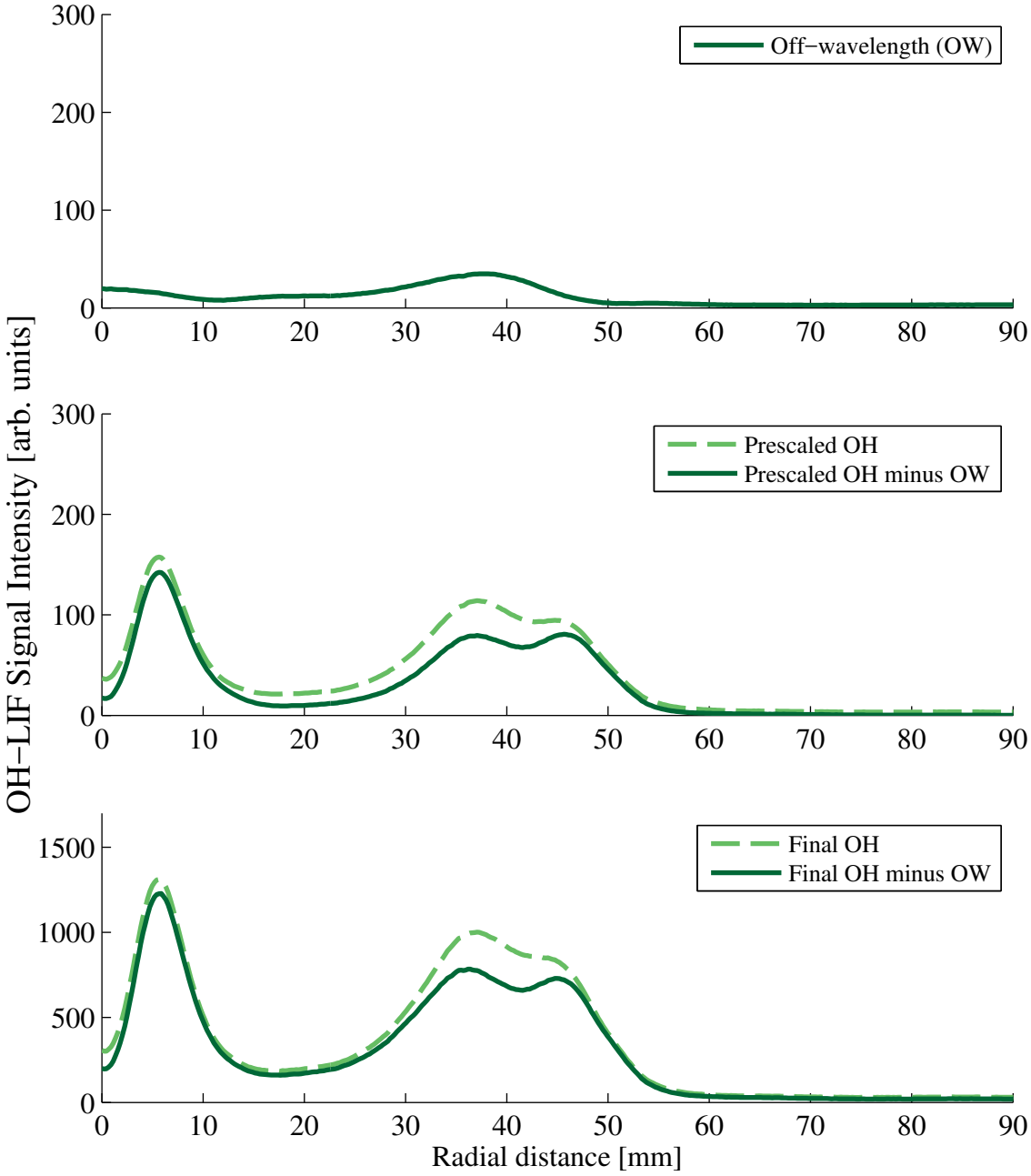

Figure 9.13: OH-LIF results outlining interference from other species for the baseline case measured 10 mm above the burner.

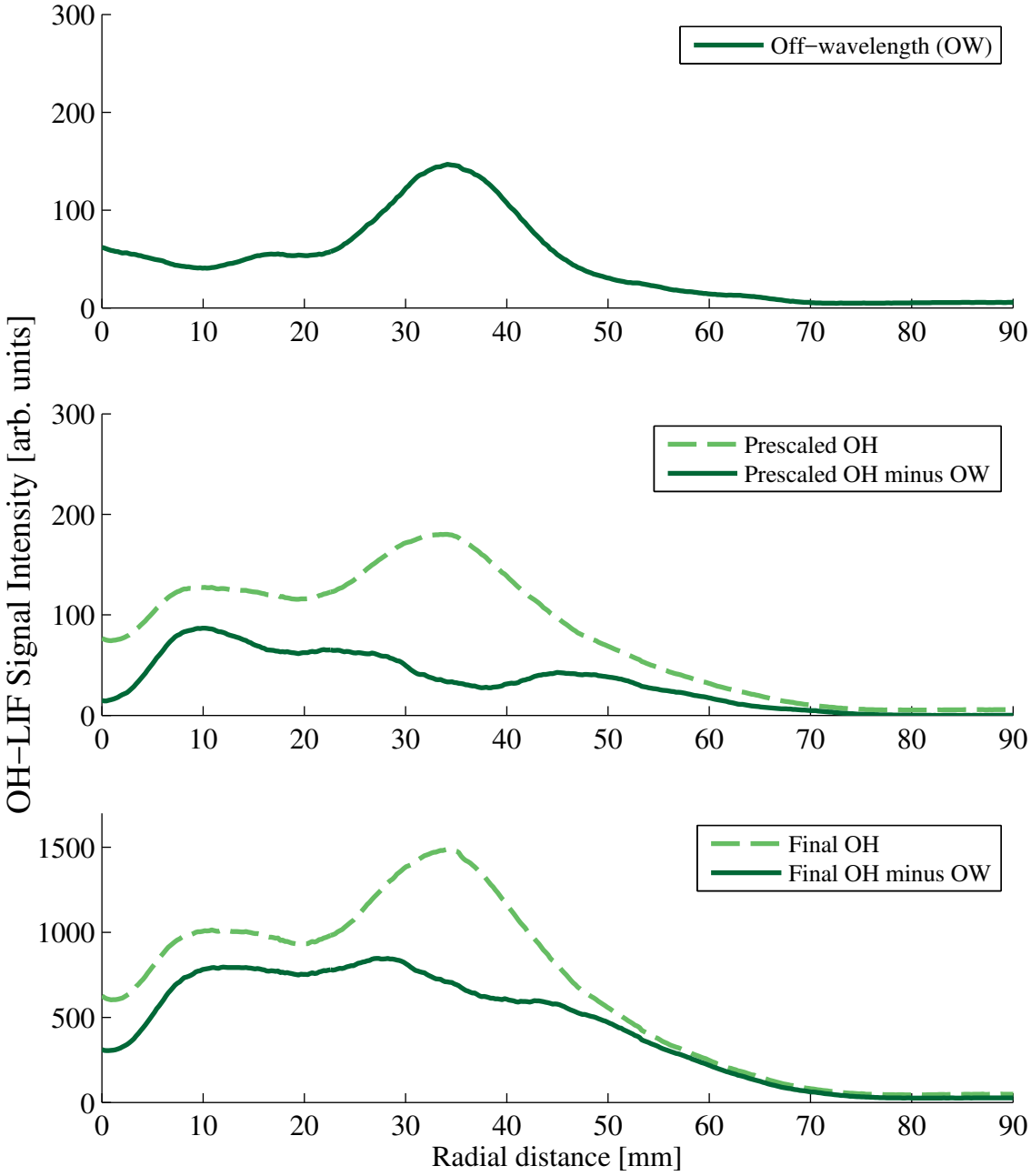

Figure 9.14: OH-LIF results outlining interference from other species for the baseline case measured 25 mm above the burner.

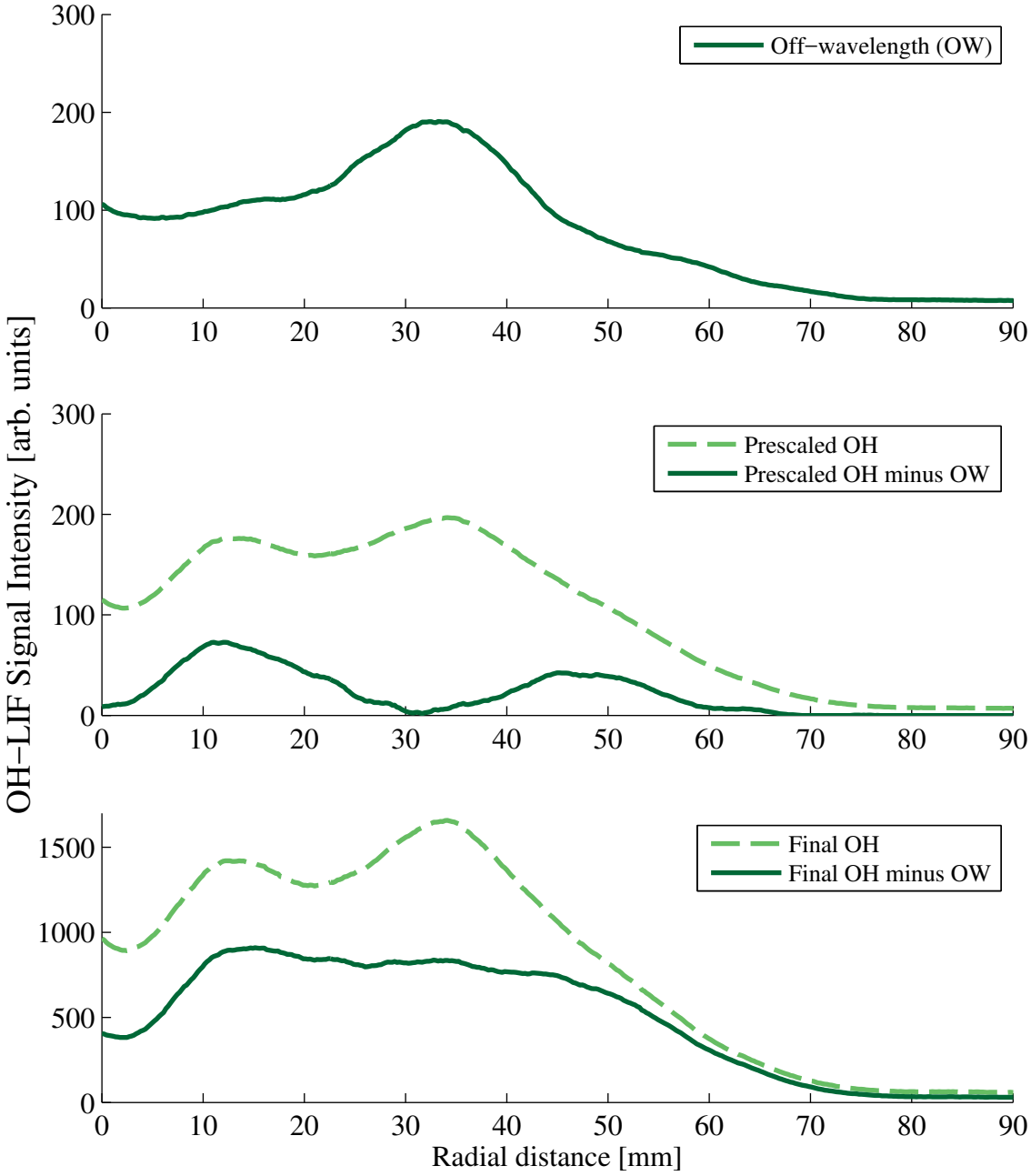

Figure 9.15: OH-LIF results outlining interference from other species for the baseline case measured 40 mm above the burner.

9.3.3 Results of the LII and OH-LIF experiments

Simultaneous LII and OH-LIF images were recorded in this work. The averages of these instantaneous images are presented in this section as average radial profiles of the quantified soot concentration and normalized OH-LIF signal intensity. A more detailed analysis of the instantaneous images would provide greater information into the soot concentrations and reaction zones in the highly-variable flames; however, that analysis is outside of the scope of this work so is not presented here. Figures 9.16 – 9.18 show the radial profiles of the average soot concentrations; each figure represents a single halo and each subplot represents a different HAB (10 mm, 25 mm, and 40 mm). Each subplot shows the baseline (A0) and three air flow rate cases (A1 = 28.3 L/min, A2 = 35.4 L/min, and A3 = 42.5 L/min) from the centerline of the burner (x = 0 mm) to the outer edge. The y-axis scale is held constant for all subplots to allow easy comparison between halos and HABs.

The same radial profiles of the average soot concentration are plotted in Figs. 9.19 – 9.27 along with the normalized OH-LIF signal intensities (which still include signal interference); each figure represents a single halo and air flow case and each subplot represents a different HAB. The OH-LIF signal has been normalized to the maximum OH-LIF signal for all cases. The y-axis scales vary by HAB to allow easy comparison between the LII and OH-LIF profiles. Simultaneous LII and OH-LIF measurements can provide a view of the reaction zone locations in a flame, indicated by areas of soot concentration surrounded by OH concentration (i.e. a peak in soot concentration in a radial profile would have a peak in OH concentration on either side for a straightforward nonpremixed flame case). Therefore, the location of the OH-LIF signal in comparison to the LII signal, or soot concentration, is important for the discussion of the location of reaction zones. However, it is important to note that the intent of the halo mixing strategies is to break-up large fuel pockets and induce mixing of fuel and air to promote soot oxidation. This would mean that the soot is in smaller, temporally- and spatially-transient pockets that are mixing with the injected and entrained air flows, as opposed to a well-defined, stable, nonpremixed flame. The transitional nature of the system means that each instantaneous measurement will be unique – an area of high soot concentration in one image could be a reaction zone in another. Therefore, clear cut localized flame fronts and reaction zones are unlikely to be observed in the average profiles. Also, it is necessary to remember the large amount of PAH interference observed in the error assessments; this interference can drastically obscure the OH concentration locations.

Results of the Baseline Case

Examining the average soot concentrations of the baseline cases shown in Figs. 9.16 – 9.18, the visible flame regions of the PCB are easy to identify. A clearly defined peak is centered around x = 0 mm (where x is the radial distance), corresponding to the middle pipe of the PCB. Another peak is visible around x = 35 – 40 mm representing an outer pipe of the PCB. The soot concentration is seen to increase as it progresses upwards in the flame (i.e. as the

HABs increase), reaching a maximum average of 150 ppb. This is expected as the soot forms and grows in the lower half of a nonpremixed flame, as discussed in Section 1.3.3.

The soot concentration and OH-LIF profiles for the baseline case are shown in Figs. 9.19 – 9.27). At $x \approx 35$ mm, there is a well-defined peak at all HABs. This peak in the OH-LIF profile aligns well with a peak in the soot concentration and therefore is likely interference from PAHs and soot. However, the OH-LIF signal for the baseline case also contains peaks unrelated to the soot concentration which probably represent OH concentrations in the flame zone. At 10 mm HAB, the peaks in OH-LIF signal that do not correspond to a spike in soot concentration are visible around 8 mm and 45 mm bordering the peaks in soot concentration. At the two higher HABs, the OH concentration peak at ~ 8 mm has become more diffuse, encompassing approximately 12 mm of the radial distance. The OH concentration peak at $x = 45$ mm does not exist at the higher HABs, but the peak in the OH-LIF signal at $x = 35$ mm is disproportionately broader than the same peak in the soot concentration. Therefore, the details of the OH concentration are hidden within the larger peak attributed to PAH interference, but there could still be reaction zones on the outer edges of that peak. The broadening of the OH peaks could indicate that the reaction zones are wider at the higher HABs. Also, widening of the peaks could be due to the increased variability of the flames as the HAB increases. At higher HABs, the flames flicker and intermingle so the reaction zones will move spatially, meaning the peaks of the averaged values will decrease in magnitude but increase in radial distance.

Results of the 90STR Cases

Figure 9.16 presents the radial profile of the average soot concentration for the 90STR halo. The 90STR profiles at all air flow rates perform quite differently from the baseline case. For the HAB = 10 mm case from the centerline to $x = 35$ mm, there is generally a higher soot concentration than the baseline case for all air flow rates, but there is no peak at the centerline. As radial distance increases, however, so does the average soot concentration, producing a broad peak toward the outside of the burner ($x > 50$ mm). At HAB = 25 mm, a visible valley in the soot concentration begins to appear between $15 < x < 30$ mm, where a peak existed in the baseline case. Like the HAB = 10 mm profile, a diffuse peak occurs toward the outside of the PCB (approximately $x > 50$ mm). The HAB = 40 mm profile follows the HAB = 25 mm trend, except near the centerline where a rise in soot concentration occurs. These trends generally become more extreme as the air flow rate increases.

The average OH-LIF profiles along with the soot concentrations for the 90STR are shown in Figs. 9.19 – 9.21. At HAB = 10 mm for all air flow rates, the OH-LIF signal generally tracks with the LII signal for $x = 0 - 50$ mm, making it impossible to distinguish the OH concentration from the PAH interference. At $x > 50$ mm, however, the soot concentration peaks but the OH-LIF signal does not. Instead the OH-LIF signal remains relatively constant until the soot concentration peak begins declining around $x = 75$ mm, at which point the OH-LIF signal also declines at a similar rate. Because the OH-LIF signal is expected to increase due to increased interference from PAH and soot but instead remains

constant, another factor must be decreasing as the interference increases – OH concentration. After ~50 mm, the OH concentration is depleting, likely due to oxidizing soot; as the OH concentration lessens, the soot concentration can rise, which will also lead to a rise in the PAH/soot interference in the OH-LIF signal so a change is not seen in the overall profile even though the OH concentration is likely depleting. This effect, seen at the 10 mm height, is accentuated at higher air flow rates which have larger peaks in average soot concentration but similar OH-LIF trends. The two higher HABs have less defined peaks in OH-LIF signal intensity; instead the noticeable difference between the soot concentration and OH-LIF signal occurs in the soot concentration valley (x = 10 – 50 mm). The soot concentration drops disproportionately more than the OH-LIF signal. This discrepancy is likely due to a higher concentration of OH in the area, like that seen in the baseline case, which is oxidizing the soot.

Results of the 30ANG

The average radial profiles of soot concentration for the 30ANG halo are presented in Fig. 9.17. At HAB = 10 mm, there is little soot in x < 40 mm with concentrations of ~10 ppb. At x > 40 mm, a small, broad peak begins which increases as the air flow rate increases. A similar profile occurs at HAB = 25 mm except that the broad peak is shifted slightly towards the center of the burner and there is little difference between the air flow rates. Finally, at HAB = 40 mm, the peak is shifted even farther towards center for the 28.3 L/min case and moves outward as the air flow rate increases.

Comparing the soot concentrations with the averaged OH-LIF signal intensity profiles in Figs. 9.22 – 9.24 unfortunately does not reveal any noticeable differences. Therefore, it is not possible to distinguish the OH concentration from the PAH interference at any point for the 30ANG halo cases using the averaged profiles.

Results of the 30SWL

Unlike the 90STR and the 30ANG cases, the radial profiles of average soot concentration for the 30SWL (shown in Fig. 9.18) resemble the baseline case results. The soot concentrations of the lowest air flow rate case at all HABs are generally less than the baseline, but the peaks of the 28.3 L/min case align well with the peaks in the baseline case. As the air flow rate increases, the outer peak (x ≈ 35 mm) is reduced and shifted toward the center of the PCB; this effect is most apparent in the HAB = 40 mm cases. All cases of the 30SWL halo continue to maintain a peak in soot concentration in the center of the burner.

More so than the other two halos, the 30SWL OH-LIF profiles (shown in Figs. 9.25 – 9.27) maintain the features seen in the baseline case and allow for distinction between the OH concentration and potential PAH interference. Figure 9.25 contains the profiles for the lowest air flow case (28.3 L/min). In this figure, the HAB = 10 mm case reveals a slightly smaller intensity with an almost perfectly identical trend to the baseline. At HAB = 25 mm, the outer peak (x = 30 – 40 mm) is similar to the baseline but the more diffuse peak from x = 5 – 20 mm

begins to deviate. By HAB = 40 mm, the inner peak completely disappears while the outer peak becomes larger. Similar trends are seen for the 35.4 L/min case (Fig. 9.26) with the exception of the HAB = 40 mm case. In that case, the outer peak of soot concentration has decreased from the 28.3 L/min case, however, the OH-LIF signal has increased. This indicates an increased OH concentration in the region, which likely highlights an area of soot oxidation in the flame occurring because of the injected air. By 42.5 L/min, the outer OH peak has decreased in magnitude compared to the 35.4 L/min case, but still does not follow the trend of the soot concentration. The soot concentration is biased towards the center of the burner and is lacking the outer peak of the baseline and lower air flow cases; however, the central peak has not increased as the air flow increased (which would be the case if the soot was simply pushed towards the center). Therefore, it is likely many reactions are occurring in this region (x = 15 – 30 mm), oxidizing much of the soot and slightly reducing the OH-LIF signal due to decreased PAH interference.

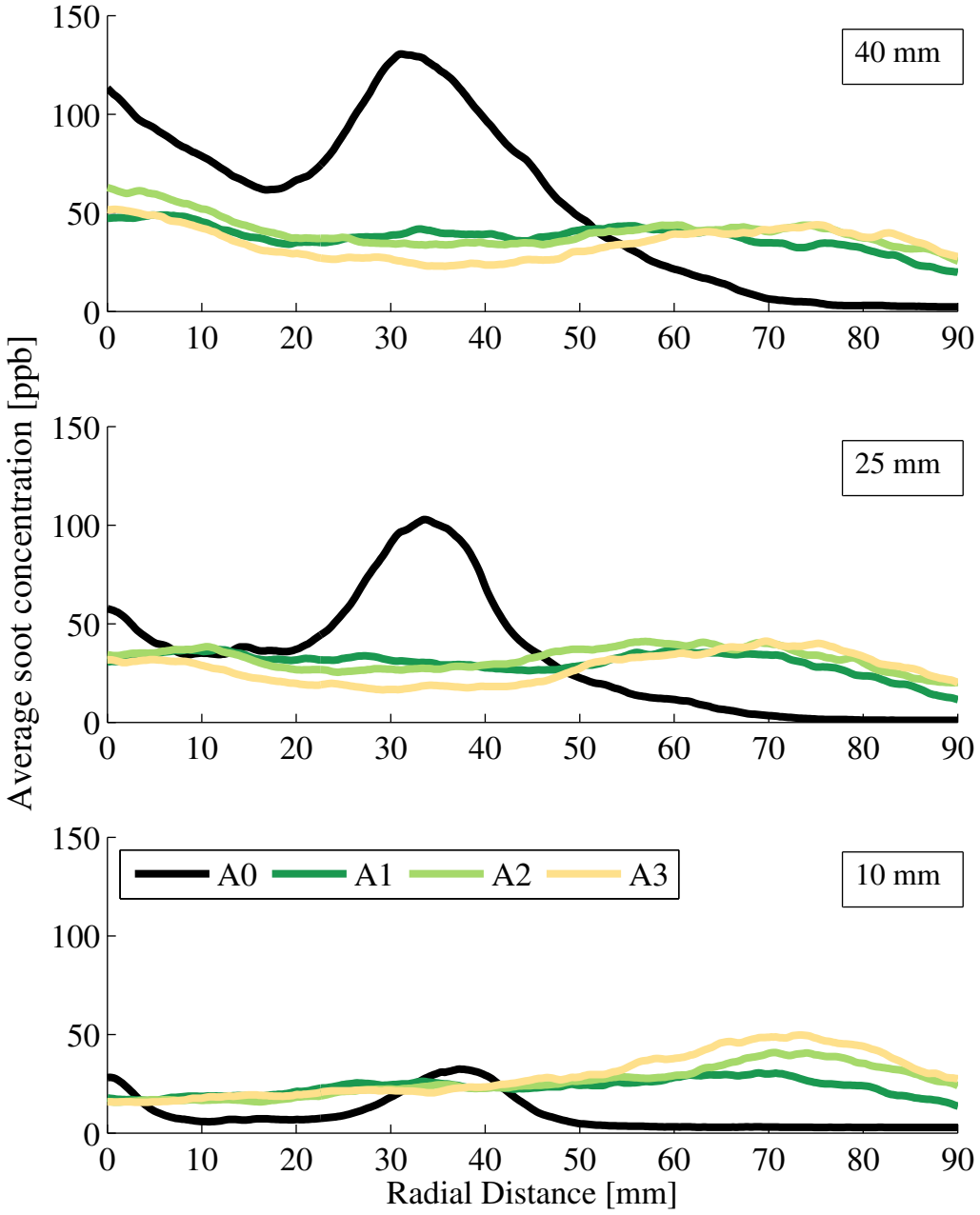

Figure 9.16: 90STR halo: Average radial profiles of the soot concentrations for the baseline (A0) and three air flow rate cases at the three HAB locations. Note, A1 = 28.3 L/min, A2 = 35.4 L/min, and A3 = 42.5 L/min.

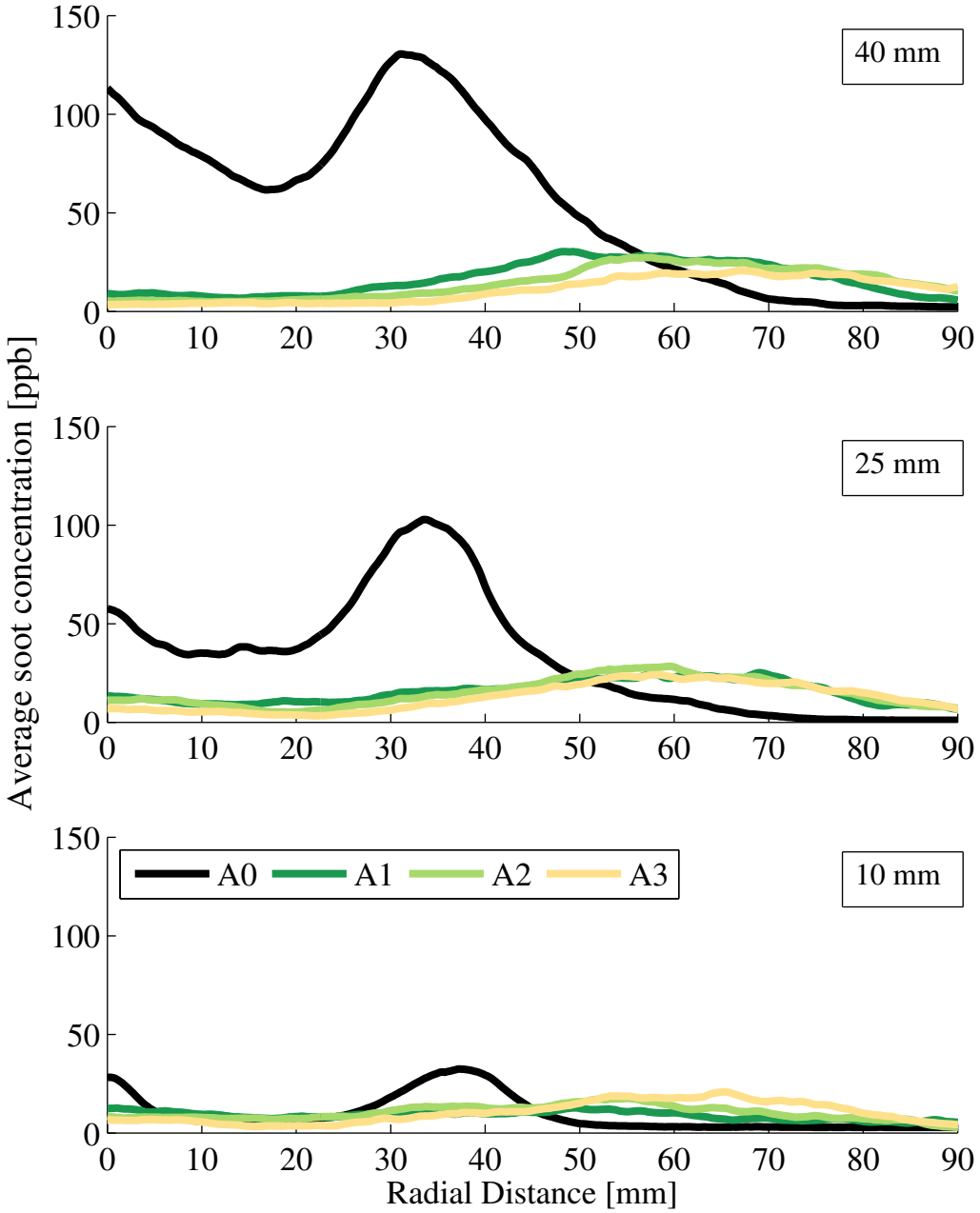

Figure 9.17: 30ANG halo: Average radial profiles of the soot concentrations for the baseline (A0) and three air flow rate cases at the three HAB locations. Note, A1 = 28.3 L/min, A2 = 35.4 L/min, and A3 = 42.5 L/min.

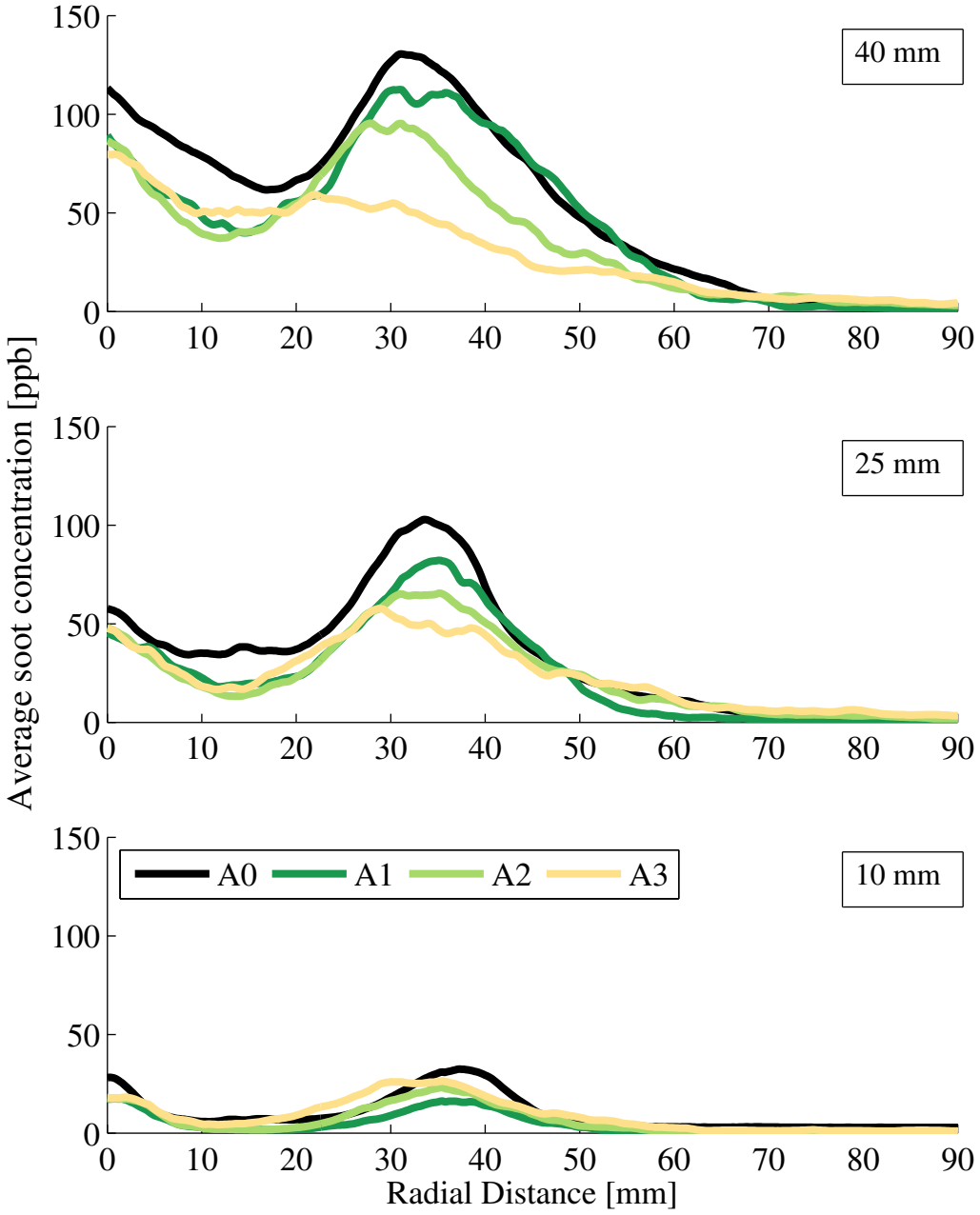

Figure 9.18: 30SWL halo: Average radial profiles of the soot concentrations for the baseline (A0) and three air flow rate cases at the three HAB locations. Note, A1 = 28.3 L/min, A2 = 35.4 L/min, and A3 = 42.5 L/min.

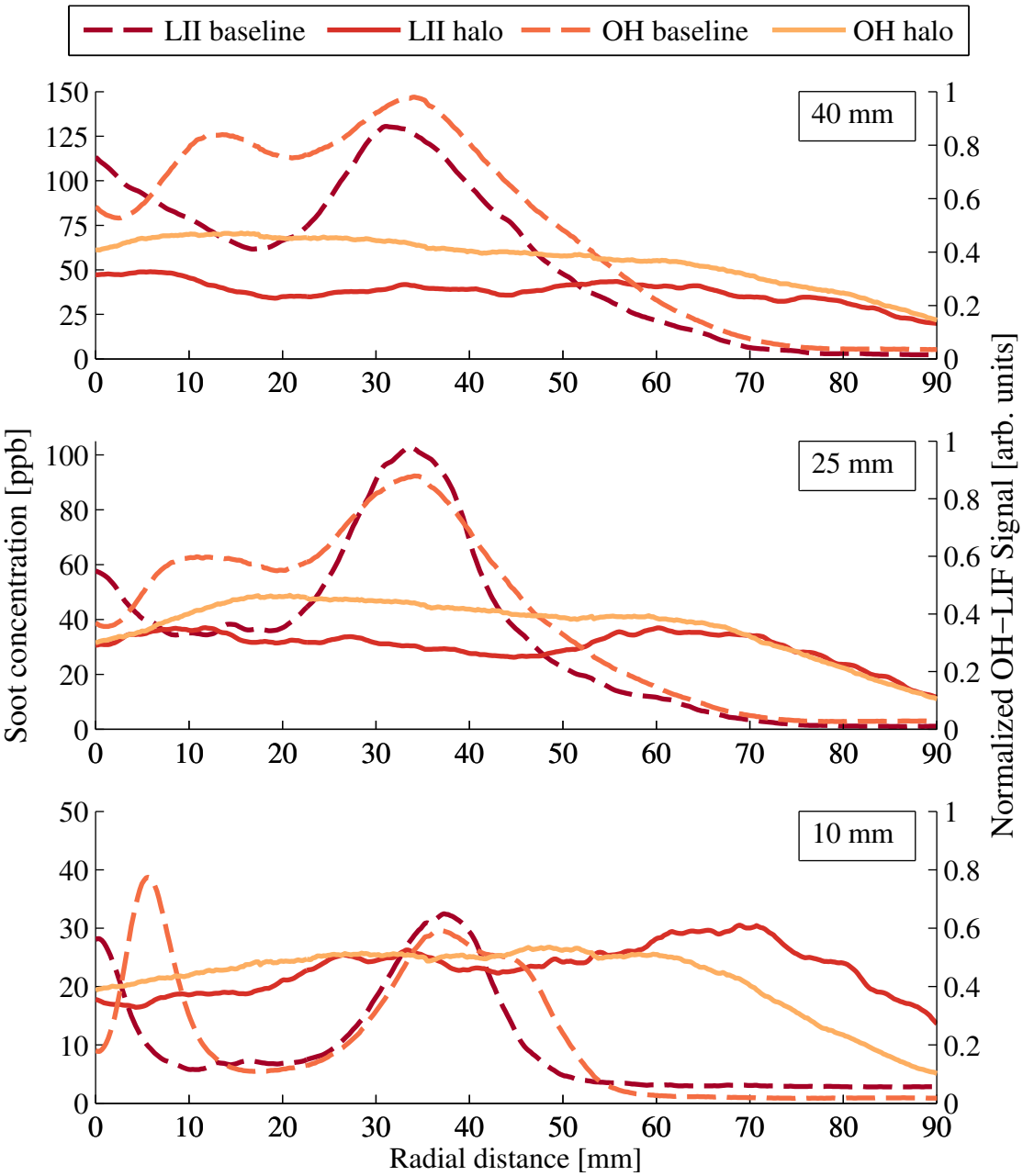

Figure 9.19: Average OH-LIF and LII radial profiles for the 90STR halo at 28.3 L/min, as well as the baseline case, for the three HABs. Note, the OH-LIF signal is normalized and still contains interference from other species such as PAH.

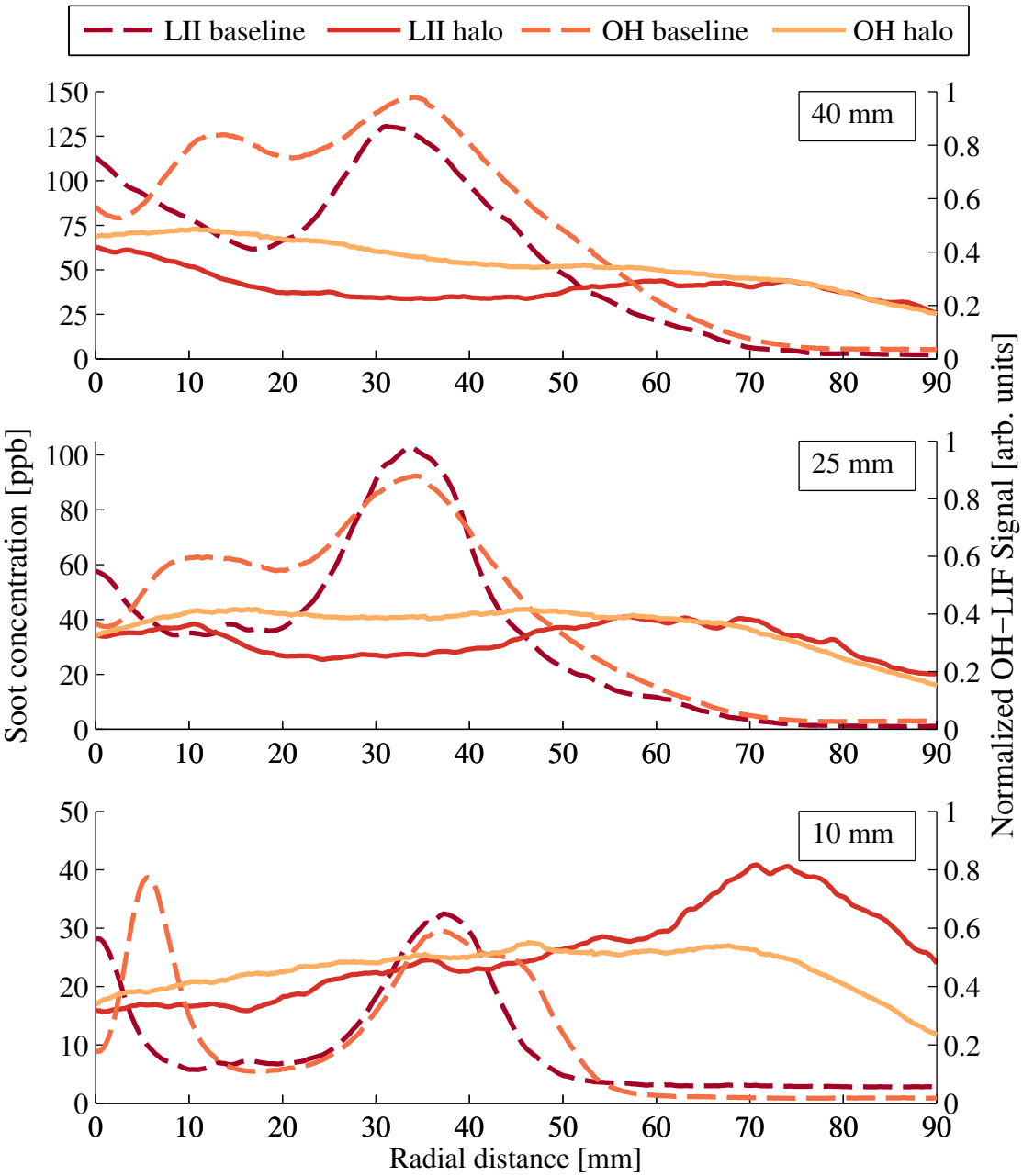

Figure 9.20: Average OH-LIF and LII radial profiles for the 90STR halo at 35.4 L/min, as well as the baseline case, for the three HABs. Note, the OH-LIF signal is normalized and still contains interference from other species such as PAH.

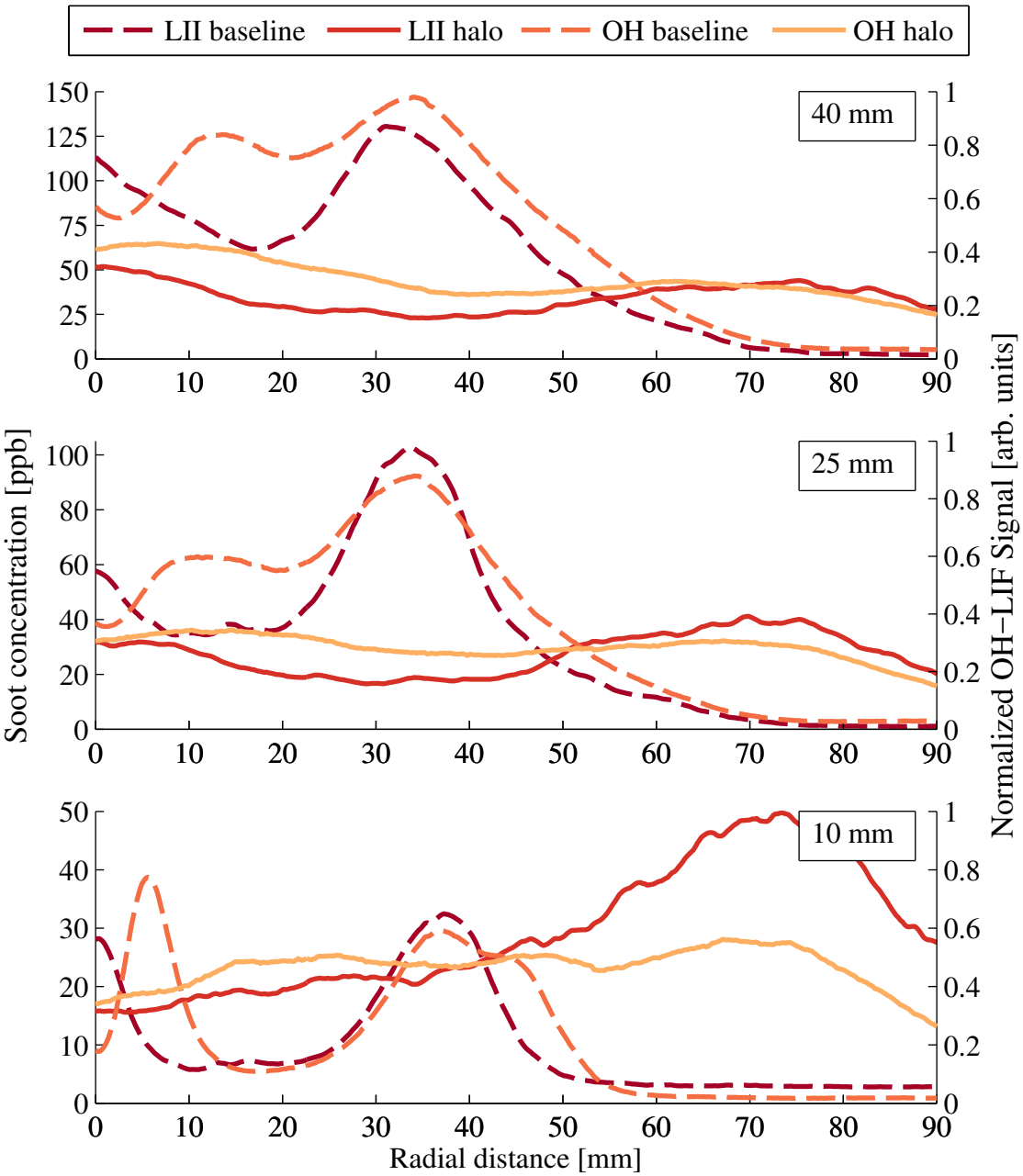

Figure 9.21: Average OH-LIF and LII radial profiles for the 90STR halo at 42.5 L/min, as well as the baseline case, for the three HABs. Note, the OH-LIF signal is normalized and still contains interference other species such as PAH.

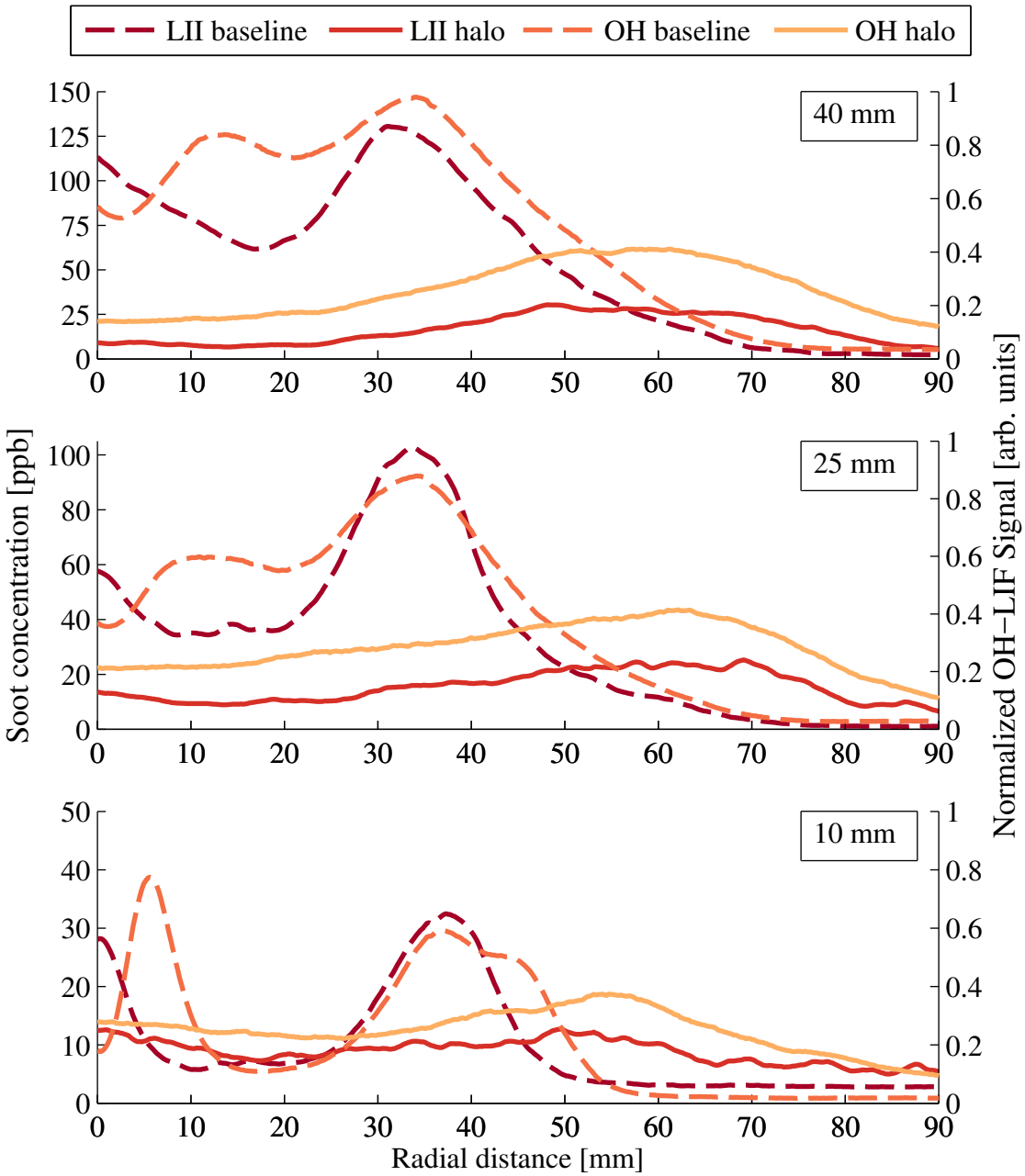

Figure 9.22: Average OH-LIF and LII radial profiles for the 30ANG halo at 28.3 L/min, as well as the baseline case, for the three HABs. Note, the OH-LIF signal is normalized and still contains interference other species such as PAH.

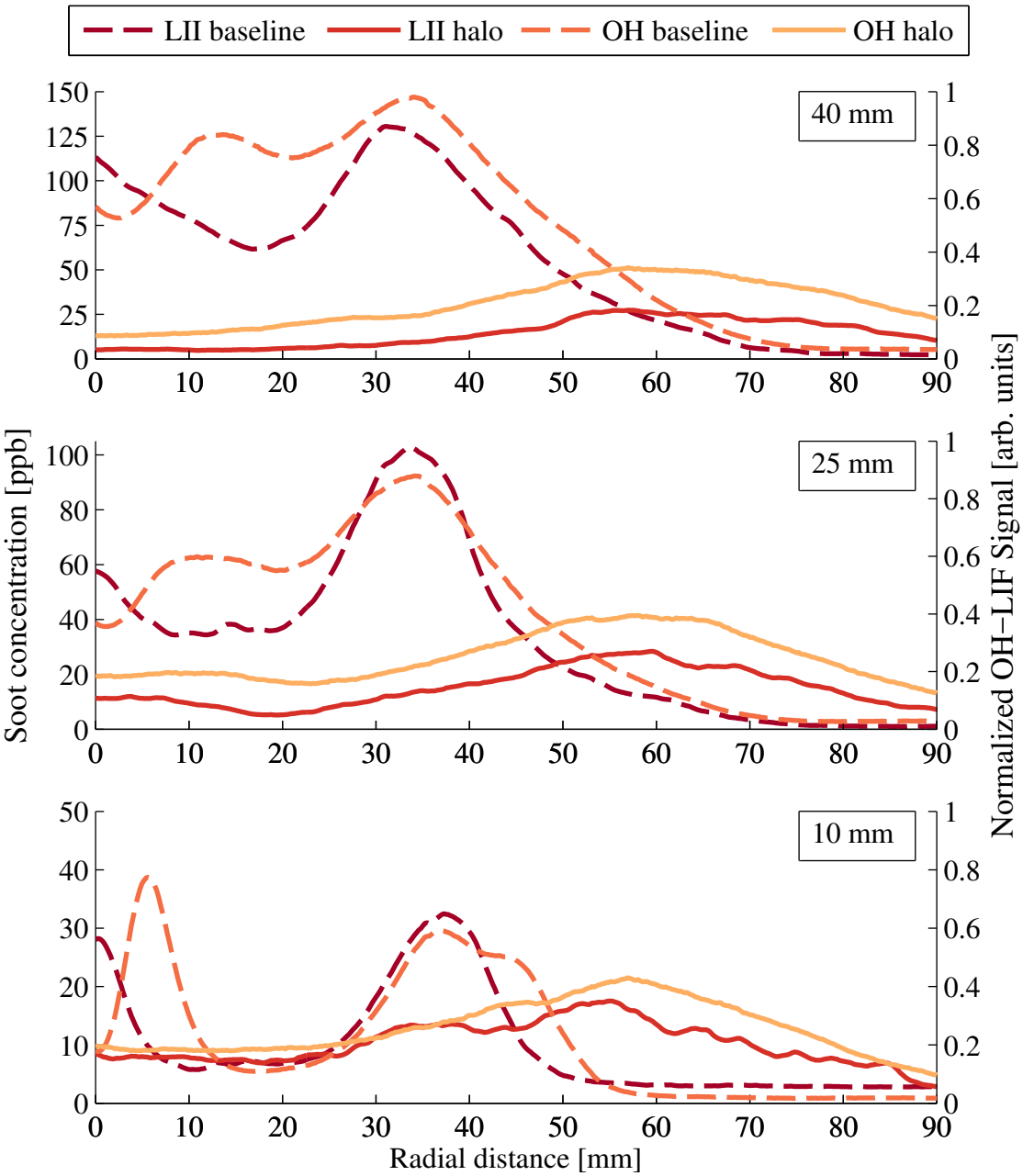

Figure 9.23: Average OH-LIF and LII radial profiles for the 30ANG halo at 35.4 L/min, as well as the baseline case, for the three HABs. Note, the OH-LIF signal is normalized and still contains interference other species such as PAH.

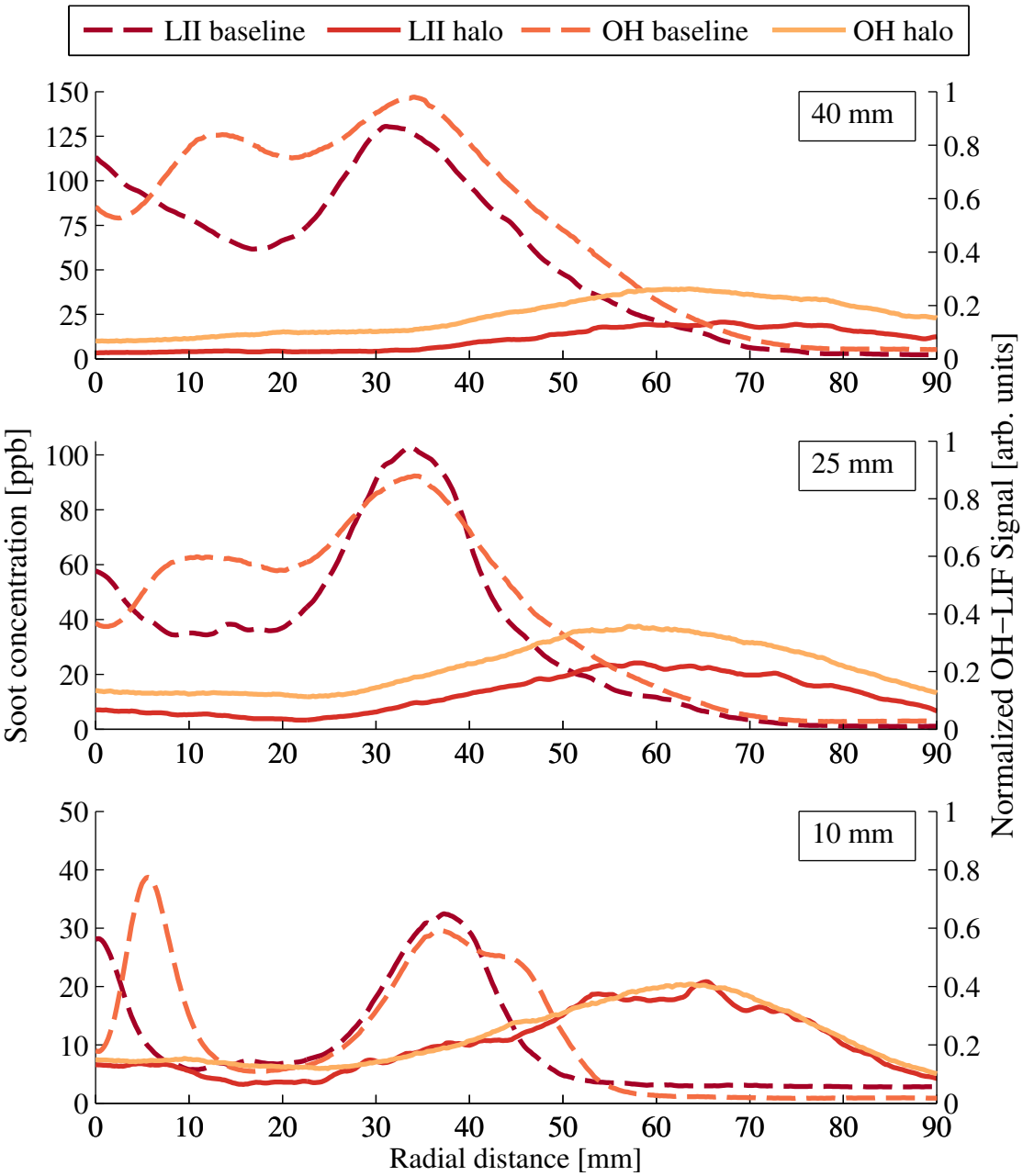

Figure 9.24: Average OH-LIF and LII radial profiles for the 30ANG halo at 42.5 L/min, as well as the baseline case, for the three HABs. Note, the OH-LIF signal is normalized and still contains interference other species such as PAH.

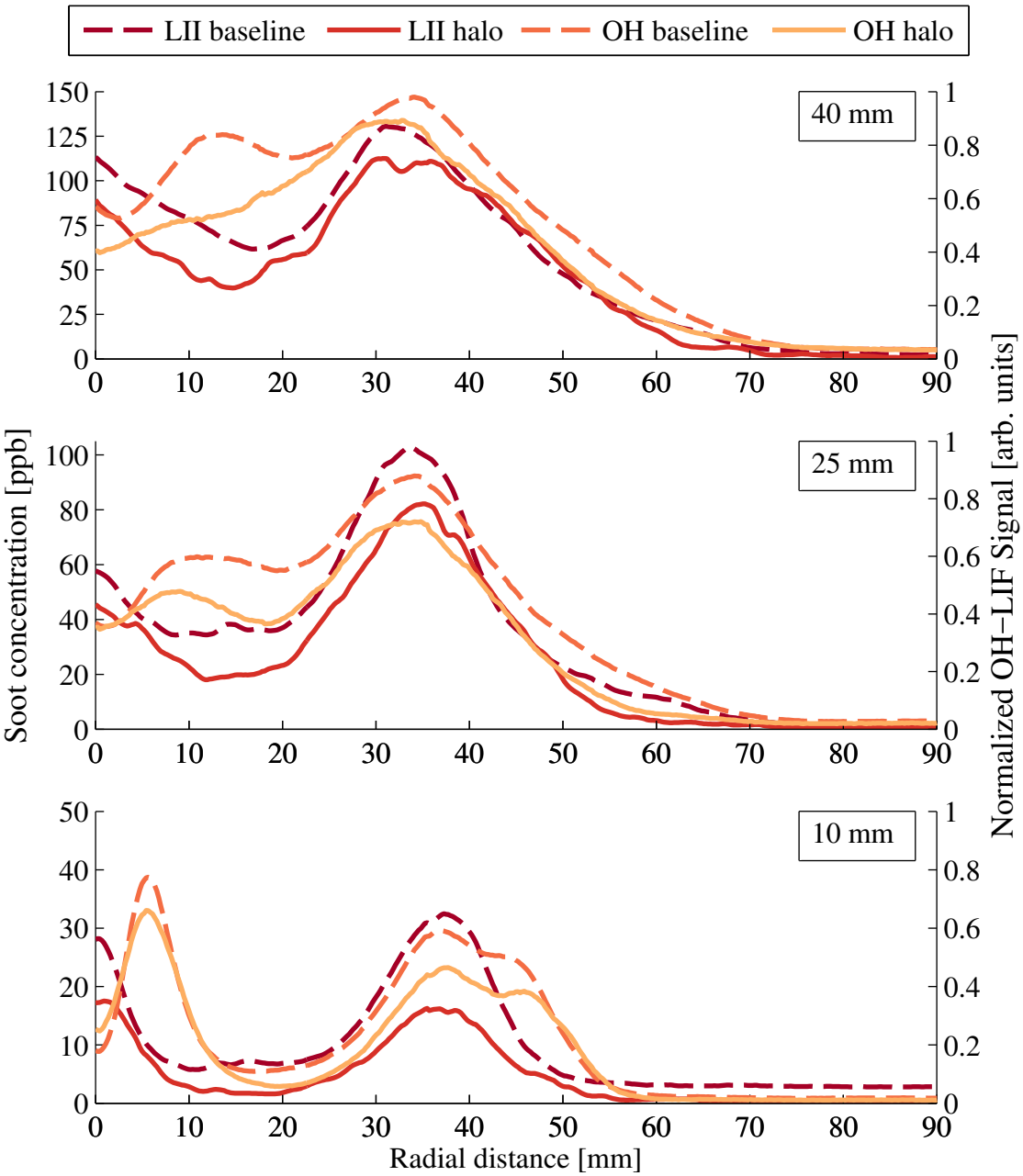

Figure 9.25: Average OH-LIF and LII radial profiles for the 30SWL halo at 28.3 L/min, as well as the baseline case, for the three HABs. Note, the OH-LIF signal is normalized and still contains interference other species such as PAH.

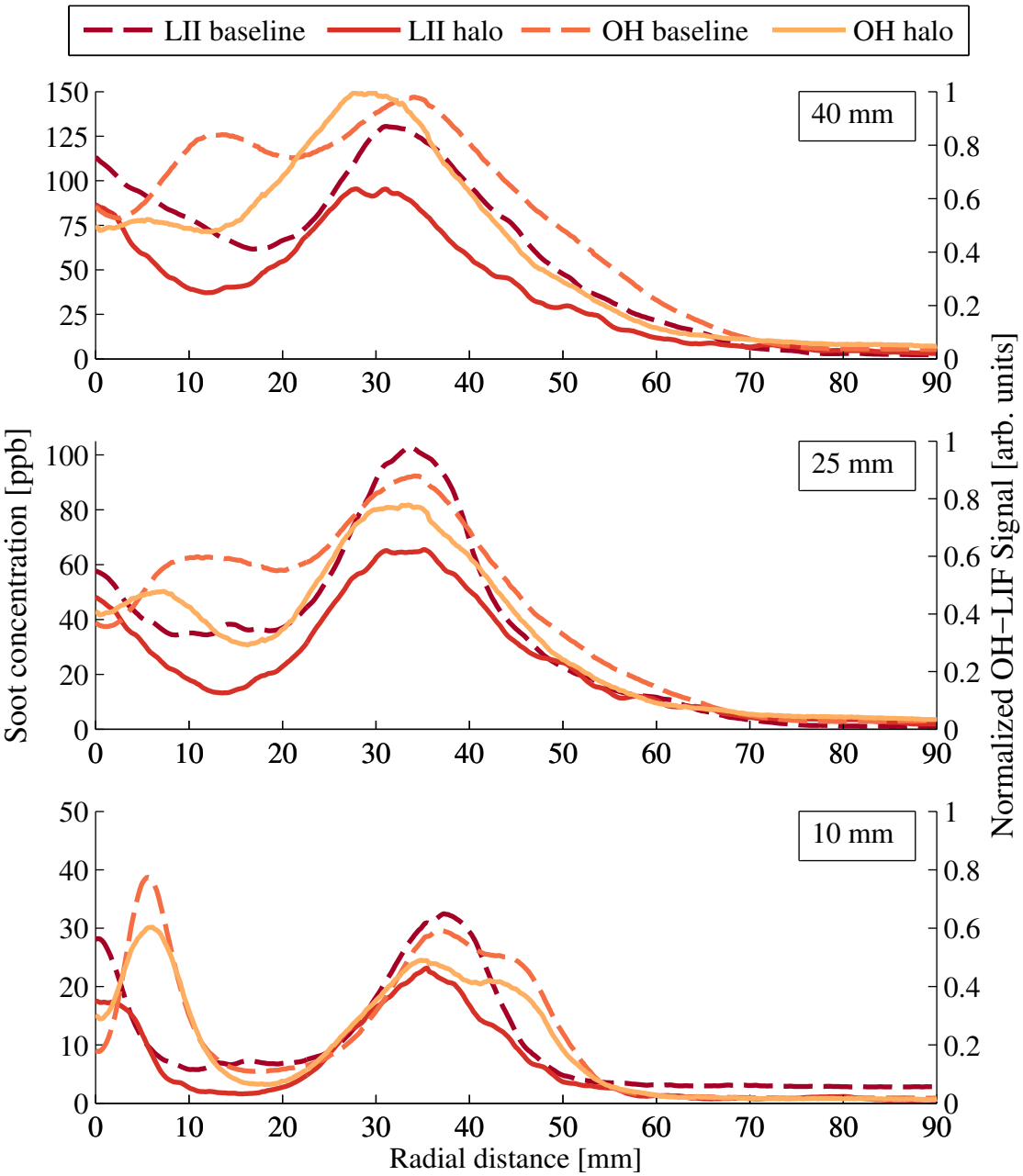

Figure 9.26: Average OH-LIF and LII radial profiles for the 30SWL halo at 35.4 L/min, as well as the baseline case, for the three HABs. Note, the OH-LIF signal is normalized and still contains interference other species such as PAH.

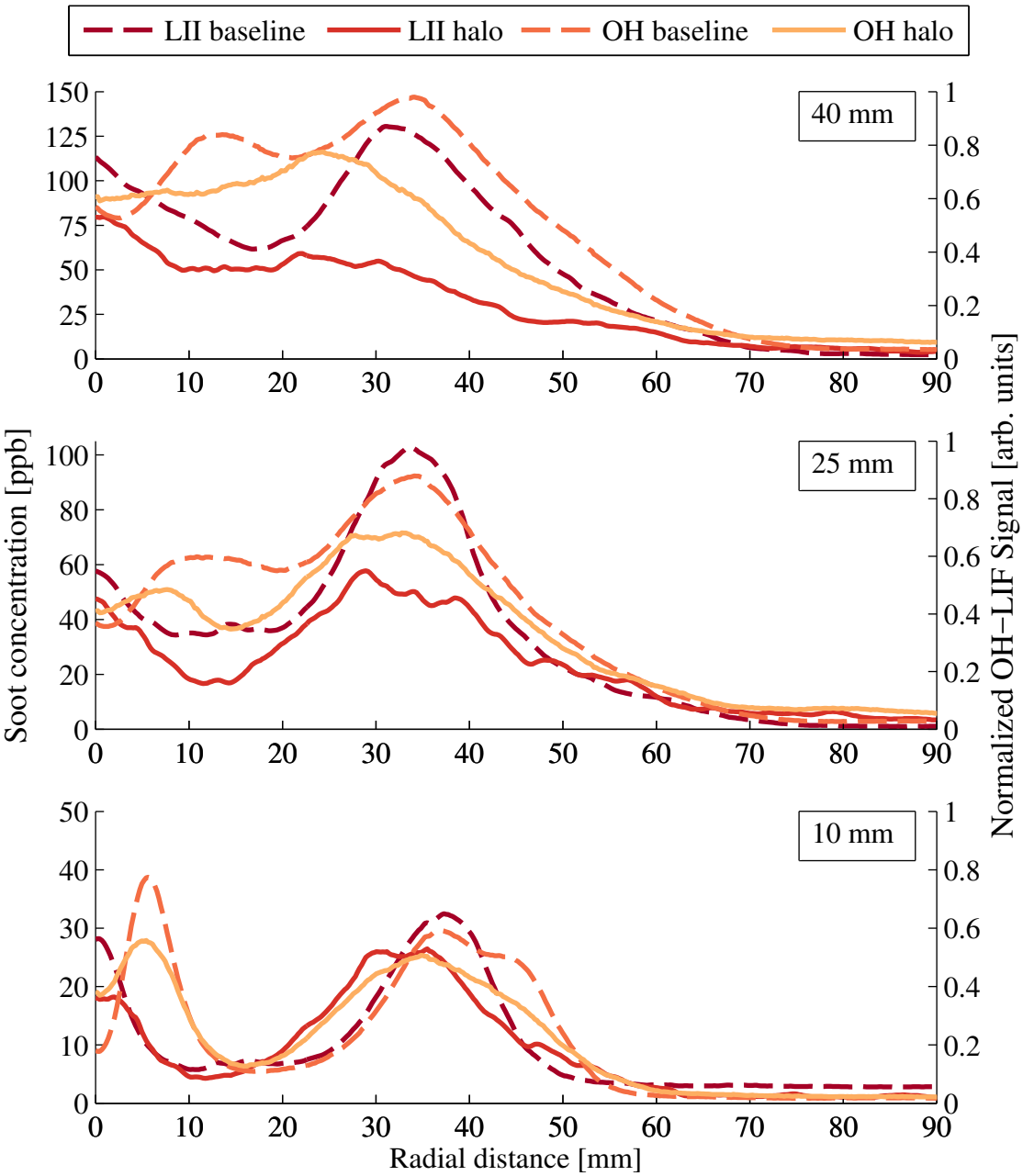

Figure 9.27: Average OH-LIF and LII radial profiles for the 30SWL halo at 42.5 L/min, as well as the baseline case, for the three HABs. Note, the OH-LIF signal is normalized and still contains interference other species such as PAH.

9.4 Discussion

In attempt to provide greater insight into the impact of the mixing strategies on the flame zone, this section compares the results of the four measurement techniques used in this chapter, as well as the ex-situ measurements of the Halo Stove and the PCB from Chapters 7 and 8, respectively.

90STR It was found that the 90STR velocity profile (Fig. 9.4) does not contain any strong flow profiles for HAB < 60 mm. Although higher HABs exhibit two downward flows, around HAB $= 60$ mm those streams largely disappear, likely leaving an area of turbulent mixing where the downward air streams and upward fuel streams interact. For the same 28.3 L/min case, the soot concentration profiles do not present any sharp peaks in soot concentration, instead exhibiting a relatively broad profile, as would be expected from the average profile of highly variable measurements, like those found in turbulent systems. As the air flow rate increases, the peaks and valleys seen at HAB $= 25$ mm and 40 mm in the soot concentration become more pronounced while the OH-LIF intensity remains consistent. The increased difference between the LII profile valleys and the OH-LIF intensity implies that there is a larger concentration of OH in that region as the air flow rate increases. Therefore, it is likely that the higher air flow rates are introducing more oxygen into the region (x $= 15-50$ mm, HAB $\approx 25-60$ mm), which could oxidize the soot there and result in the soot concentration valley in the profile. However, in the lower HAB region (10 mm), soot concentration increases as the air flow rate increases, potentially due to soot being recirculated back into the lower HABs by the injected air.

The luminescence images shown in Appendix B confirm that as the 90STR air flow rate increases, the luminous flame is confined to the lower half of the image, where it also becomes slightly broader than the baseline. In Section 8.3.1, the 90STR halo was found to be the least emitting halo for black carbon. At first, the LII results seem contrary to this, because there is a high total amount of soot compared to the other cases, especially the 30ANG. Looking at the luminescence images, however, it is readily apparent that the amount of luminous soot remaining in the measurement area stays relatively constant for HAB < 60 mm (where the LII measurement is taken) but drops dramatically for HAB > 60 mm (which would not be included in the LII measurements). Much more luminous soot remains visible for the 30ANG and 30SWL cases at the upper HABs than the 90STR.

The luminous flame is only visible in the lower half of the image for the 42.5 L/min case (in which the effects of a halo will be most pronounced). This indicates that the soot is either being recirculated into the lower half of the measurement region or is being released to the upper regions where it is either cooled such that it is no longer luminescing or oxidized. LII measurements in this higher measurement region would answer if the soot is being oxidized or simply cooled. However, based off of the low soot emissions in the Chapter 7 and 8 results, it seems likely the latter is occurring and the 90STR is oxidizing soot as desired.

The ex-situ results for the 90STR halo show high carbon monoxide (CO) emissions relative to the other two halos across all flow rates. Emissions of carbon monoxide indicate incomplete combustion and it was thought in Chapters 7 and 8 that they also indicate local extinction in the flames of the 90STR halo. Although an increase in smoldering combustion is not possible with the gas burner, local extinction can occur if the injected air quenches the flame. Exploring the area near the top of the PCB provides some indication of the halo effects on the wood combustion in the Halo Stove. Therefore, although it is difficult to quantify the level of turbulence in the lower measurement region from the PIV images due to inadequate seeding of the fuel flow, looking at the LII soot concentration results at HAB = 10 mm can help assess the potential for local extinction at the top of the PCB and increased smoldering combustion due to the 90STR halo air injection. As seen in Fig. 9.16, the soot concentration profiles for the 90STR halo at all air flow rates are noticeably different from the baseline case. This indicates that the injected air is affecting the bases of the flames, which could mean cooling or extinguishing portions of them. As the air flow rate increases, the difference with the baseline is more pronounced. Even if the increased air and turbulence at HAB = 10 mm are not quenching the flames, the results likely indicate that the 90STR air flow directly impacts the combusting wood in the Halo Stove. This could lead to an increase in smoldering combustion and therefore the high CO emissions seen in Fig. 7.10. Therefore, although the dramatic decrease seen in the emitted soot is desirable, it would be prudent in future work to evaluate the emissions at lower air flow rates than covered in this work for this mixing strategy to see if interactions with the flame base can be avoided.

30ANG The soot concentration profiles of the 30ANG halo (Fig. 9.16) showed very low concentrations of soot ($\sim$10 ppb) in the center 40 mm of the burner. Then as radial distance increased, the soot concentration increased. At higher HABs, the PIV measurements (Fig. 9.5) show a diagonally-introduced flow, but by HAB = 60 mm (which is where the LII measurements begin), the flow has become a centralized, downward flow. This central core of injected air explains the low soot concentrations seen in the LII measurements, as the soot would either be oxidized or pushed out of the region. Unfortunately, the large interference from other species did not allow any insight into the OH-LIF measurements and reaction zone locations in the flames when using the averaged profiles. Further analysis of instantaneous images in future work should provide deeper insights into the reaction zone locations. Outside of the central core in the PIV measurements, the velocity profile is sparse and disorganized, indicating it is primarily fuel (which is unseeded) and likely a flame zone. This flame zone is confirmed both visually in the luminescence image (Fig. 9.3c) as well as the soot concentration profiles, assuming a high soot concentration equals the location of a visible flame.

The strong downward flow shown in the PIV velocity measurements does raise a flag that the injected air might be quenching the base of the flames. Examining the HAB = 10 mm results for the LII measurements (Fig. 9.16), the halo air results are noticeably different than the baseline for all flow rates and display a peak which increases as the air flow rate increases.

As with the 90STR halo, this could indicate some soot is being recirculated by the injected air or more likely that the central flow stream is quenching the middle flame of the PCB. The CO results from the PCB ex-situ measurements, shown in Fig. 8.5, do appear to indicate quenching as the emitted CO decisively increases with increased air flow rate. Meanwhile, the Halo Stove results, shown in Fig. 7.10, show that the 30ANG reduces CO emissions in the high power phase and increases CO emissions in the low power phase, compared to the baseline. The results of the PCB indicate the air flow is directly impacting the wood fuel and therefore should be increasing the amount of smoldering combustion. Although it cannot be known for sure, it appears as though the more centralized interaction of the 30ANG is favorable to the ring of impinging air from the 90STR for emitting less CO, perhaps because it only increases smoldering combustion in a one localized region (i.e. the center of the fuel bed). Overall, it appears as though the air flow rates are too high for the 30ANG and lower flow rates should be explored; however, if only high power cooking is desired, the higher air flow rates could be acceptable.

30SWL The LII soot concentration profiles for the 30SWL reveal that all cases maintain the central flame, but the outer flame is reduced and shifted inwards as the air flow rate increases, especially at higher HABs. In Fig. 9.3d, which is the 30SWL at 28.3 L/min, the top half of the flames are affected by the injected air, but the closer regions to the PCB are largely unaffected. This helps explain the average LII soot concentration results – the measured HABs only encompass the lower half of the measurement region, where little air injection effects are visible in the 28.3 L/min case, so the 30SWL LII radial profile looks quite similar to the baseline. As seen in the images in Appendix B, at higher air flow rates, the swirling flow affects the lower regions of the flame which is why the soot concentration profiles begin to deviate from the baseline case, especially at HAB = 40 mm. Similarly, as the air flow rates increase, the soot concentration profiles for the 30SWL show the soot concentrations decreasing around the position of the outer flame and increasing toward the middle of the burner. This is validated in the luminescence images, which show a tall center flame for all cases and shrinking outer flames.

Both the 90STR and the 30ANG halos appear to reach the base of the flames to some degree as seen by examining the HAB = 10 mm cases of the LII results. The HAB = 10 mm results for the 30SWL, however, do not show signs that the injected air is affecting the base of the flames – the profiles appear to match the baseline case quite well, suggesting that the injected air or turbulence from it has not reached that HAB. The CO emission results for the PCB, shown in Fig. 8.5, reflect a lack of quenching as the total emitted CO actually drops with higher air flow rates. Therefore, the higher air flow rates appear to improve mixing and promote complete combustion (thus reducing the soot and CO emissions) without quenching the flame. In fact, changes in the air flow rate have the greatest affect in the 30SWL cases – across the majority of metrics, including in-situ and ex-situ soot concentrations and emissions of CO, fine particles, and ultrafine particles, as the air flow rate increases, the measured variable decreases. This indicates that as long as the swirling flow can be successfully

contained, the higher flow rates evaluated in this work are favorable for emissions reductions, producing emissions reductions comparable to the 90STR halo without producing adverse quenching effects.

Viability of Luminescence

Both luminescence and LII were used in this work to determine soot concentration profiles. Although LII is a more scientifically-rigorous, established technique than luminescence, it requires expensive, cumbersome equipment and highly trained personnel to collect the measurements. It is not suitable for field measurements and also it requires several optical access points to the desired flame zone, so would often require design modifications of the system if attempting to evaluate an enclosed cookstove. Luminescence, on the other hand, does not produce quantitative soot concentration profiles, but the measurements only require a high quality, commercially-available camera and a photodiode system. This makes luminescence a more practical and feasible technique for average stove designers. The real world system can be evaluated without modification as long as the flame zone is fully visible and the environment is dark. Therefore, a desire of this work is to assess the validity of using luminescence when comparing cookstove designs. The technique is not proposed as a replacement for LII when desiring scientifically-rigorous, quantified soot concentrations, but the ease and simplicity of the technique would make it ideal for quick comparisons during prototyping and early evaluation stages.

Average radial profiles of the luminescence and LII signal intensities are presented in Figs. 9.28 – 9.31 in order to compare the results of the two techniques and evaluate the validity of luminescence. In these figures, the luminescence and LII profiles have been normalized to their respective baseline cases and are overlaid on a single plot per halo per air flow rate for ease of comparison. Because luminescence is a full field technique and LII has discrete measurement heights, both data sets have been modified from their presentations in previous sections so they may be compared. The three HAB cases for each LII measurement have been averaged into a single profile representing the total region measured (HAB = 10 – 60 mm). Similarly because the LII measurements only account for the lower half of the luminescence measurement region, the luminescence data from only HAB = 10 – 60 mm has been included when developing the profiles.

The LII and luminescence results of the baseline case are shown in Fig. 9.28. The results were found to match well. The central and outer peaks are well-defined and near perfectly aligned. It is important to note that luminescence requires the soot to be hot in order to be recorded while LII does not directly depend on the local gas temperature. This is seen in Fig. 9.28 as the luminescence signal is less than the LII signal near the edges of the flames where the gases will be cooler. Figure 9.29 shows the radial profiles of the LII and luminosity intensities for the 90STR halo. The approximate concentrations are similar between the two. However, the LII result appears to show small peaks and valleys, while the luminescence result consistently decreases with radial distance. It is important to note that LII is a planar technique, only capturing a thin slice of the soot concentration, whereas

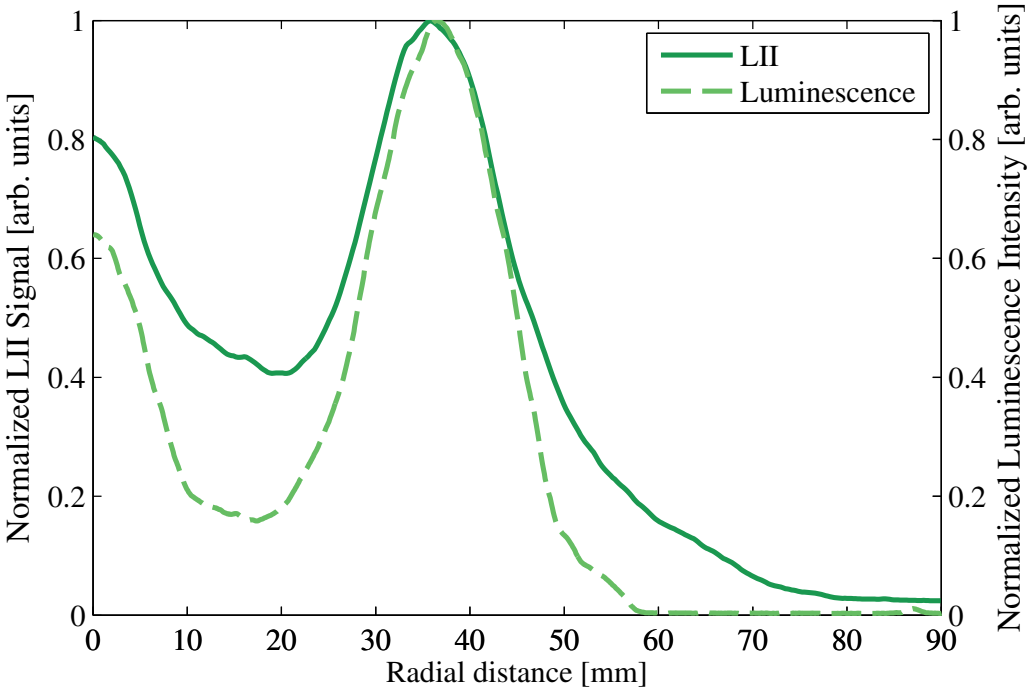

Figure 9.28: Radial profiles of the normalized LII and luminescence intensity data from the center of the burner to the edge for the baseline (no air) case. Both sets of data have been normalized to their respective baseline cases.

luminescence will capture out-of-plane soot radiation as well as other luminescing species. In a highly turbulent and three-dimensional system such as the PCB, it could be that the luminescence is more accurately capturing the overall flame tendencies. It is observationally known that the LII laser sheet was aligned with holes in the burner, thus providing larger peaks than is likely average throughout the flame. Therefore, it is possible that although the soot concentration is increasing at that local point in the single measured plane, total soot concentration at that radial distance is decreasing on average. The 30ANG luminescence and LII results do not track as well as the baseline and 90STR results, as seen in Fig. 9.30. The luminescence has peaks around $x = 30 - 60$ mm whereas the LII peaks around $x = 50 - 80$. Many possibilities exist for this difference in profile (e.g. that LII only records a thin slice of soot concentration) and future work is required to explore why this case deviates more than the others. Lastly, although not perfectly aligned, the trends of the 30SWL luminescence and LII results (shown in Fig. 9.31) match well. Both cases exhibit defined peaks at 28.3 L/min which then broaden and decrease as the air flow rate increases.

Overall, luminescence appears as though it could be a useful substitute for LII when desiring quick, comparative assessments of designs and prototypes. It correlates well for the well-defined flame of the baseline case. However, for some of the more turbulent cases,

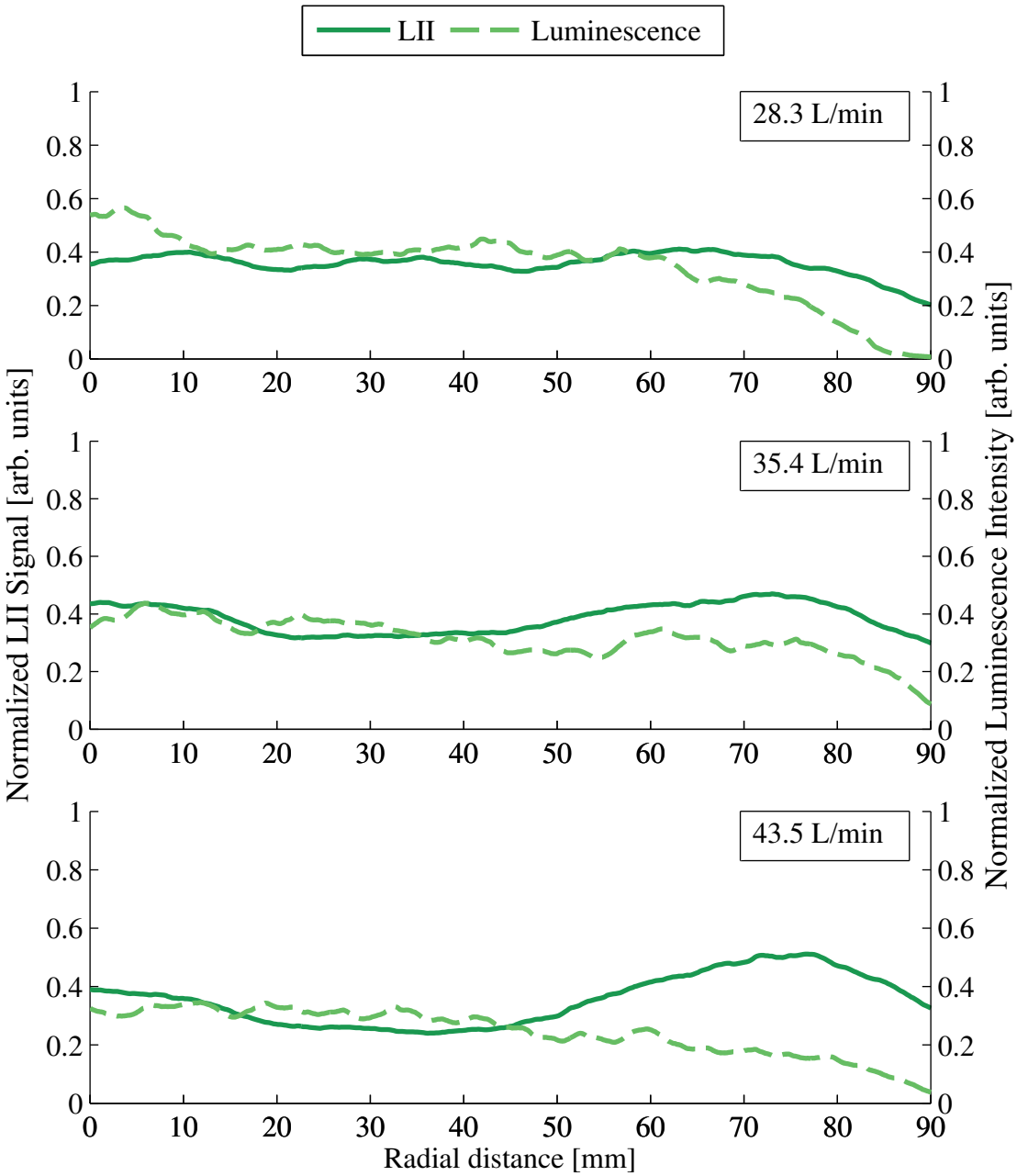

Figure 9.29: Radial profiles of the normalized LII and luminescence intensity data from the center of the burner to the edge for the 90STR halo cases. Both sets of data have been normalized to their respective baseline cases.

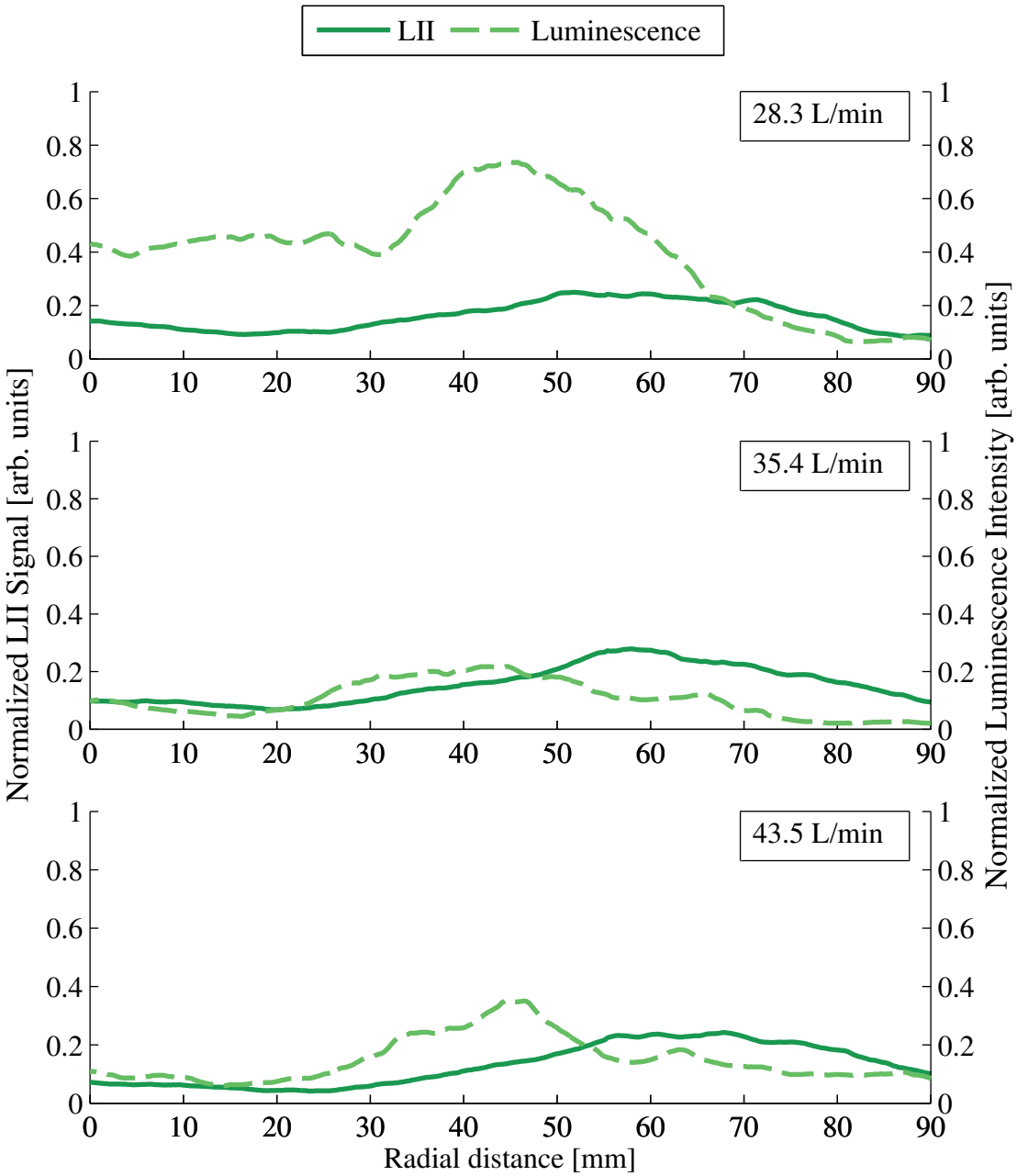

Figure 9.30: Radial profiles of the normalized LII and luminescence intensity data from the center of the burner to the edge for the 30ANG halo cases. Both sets of data have been normalized to their respective baseline cases.

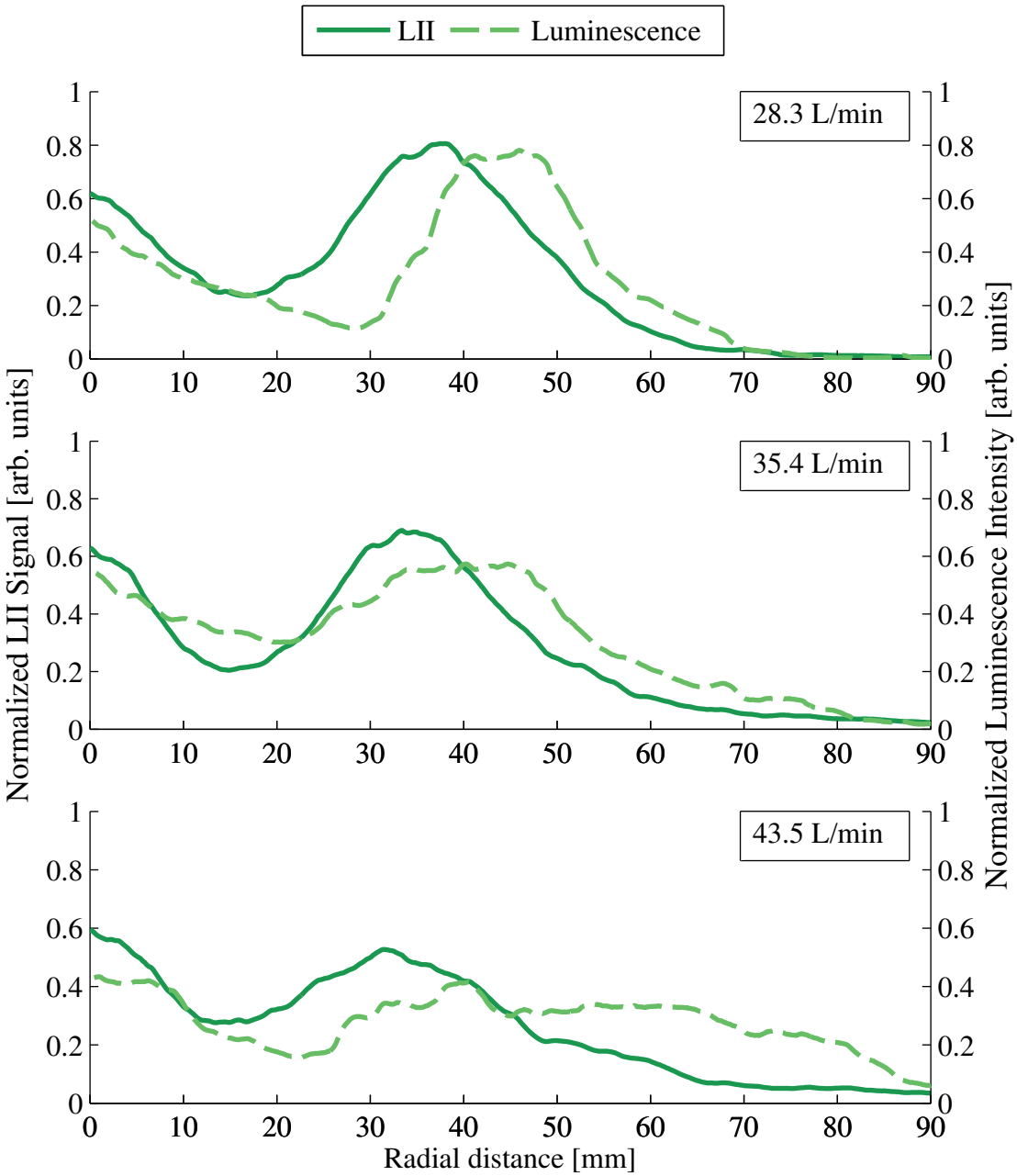

Figure 9.31: Radial profiles of the normalized LII and luminescence intensity data from the center of the burner to the edge for the 30SWL cases. Both sets of data have been normalized to their respective baseline cases.

such as the 30ANG halo, it did not match well. It is unknown if the errors in the more turbulent cases are due to limitations of the luminescence technique or flaws with the LII data due to its constrained, two-dimensional nature. Also, estimations had to be taken when calculating these results because the two techniques did not cover the same measurement area. To better understand the differences between the LII and luminescence measurements, future LII experiments should traverse the flame zone, recording soot concentrations closer to and farther away from the camera, instead of solely in the center of the burner. If these measurements were then combined, it would provide insight into the luminescence results, which record luminosity from the entire flame region not just a single, thin sheet like LII.

9.5 Summary of the In-situ Results

This chapter used four optical techniques to collect in-situ data on the PCB/halo system to help provide insight into the differences between the mixing strategies. It was found that the anticipated flow profiles of the mixing strategies were generally confirmed by the PIV results, although only the 28.3 L/min case could be evaluated. In addition, the soot concentration profiles found using LII and luminescence appear to correspond well to the PIV measurements as well as the ex-situ results of Chapters 7 and 8, providing additional data about the systems.

Several challenges were encountered when setting up and executing the PIV experiment; some were resolved or mitigated, others were not. Future work on the specific system used in these experiments includes developing an enclosure so higher air flow rates may be evaluated, incorporating better filtering to reduce interference from soot so reacting flow may be used, and creating a method of adequately seeding the fuel flow from the PCB. Because the mixing strategies introduce a highly three-dimensional flow that was not well-captured with the two-dimensional PIV, three-dimensional PIV is a logical and beneficial next step for evaluating the flow velocities in the system. The OH-LIF measurements, which were recorded simultaneously with the LII to help identify reaction zones in the flames, encountered high amounts of interference from other species, such as PAH and soot. This interference obscured the majority of the OH-LIF signal in the averaged profiles, so little was confirmed about reaction zone locations in the flames in this work. Future analysis of the instantaneous OH-LIF and LII images should provide a better understanding of the location of reaction zones.

Drawing from the conclusions of the in-situ results, some reasonings may be made about the ex-situ measurements in Chapters 7 and 8. Although the 90STR halo had the greatest reductions in total soot emissions for the PCB trials conducted in Chapter 8, the halo also appeared to quench the flame and promote incomplete combustion. The air flow rates tested therefore seem to be too high for this mixing strategy and lower flow rates should be examined to see if the adverse effects of quenching can be avoided. However, if the trends apparent in Chapter 8 continue, the black carbon emissions will not be as greatly reduced using lower air flow rates. The 30ANG performed similarly to the 90STR for the PCB

measurements, reducing soot and increasing CO with increasing air flow rates, indicating that for these cases soot oxidation comes at the cost of quenching the flame. The low power 30ANG Halo Stove results appeared to agree with the PCB results, but the high power are contradictory in regards to CO emissions. Therefore, although the measured air flow rates are too high for the low power phase of the 30ANG, perhaps they are appropriate for high power cooking. Future work should explore lower velocities for these two designs (90STR and 30ANG) so the injected air has a lesser effect on the base of the flames. Lower velocities can also be preferable for a real world stove system as they would likely require less pressure to inject the air. Unlike the 90STR and the 30ANG, the 30SWL performed well in emissions reductions, especially at the higher air flow rates, and did not appear to quench the flames. If a system is enclosed and desiring higher flow rates, the 30SWL mixing strategy appears most favorable out of these mixing strategies from an emissions perspective. However, it is important to remember the slow cooking time found for this halo in Chapter 7, which could make it undesirable to end-users. Comparing the ex-situ and in-situ soot emissions, it was found that all halos performed as desired in regard to soot emissions reductions; soot still formed in the flame, providing the desired radiative heat transfer, and was then largely oxidized prior to leaving the flame region.

In addition to examining the mixing strategies, luminescence was evaluated as a potential technique for cookstove evaluation. It is desirable to have luminescence available as a field technique, due to its ease of use and practicality. Intensity profiles representing soot concentration were found using both LII and luminescence and compared. The results from the comparison are promising but further work should be conducted to verify the technique.

10 Summary and Future Work

The goal of this work was to examine a few current applications of air flow modifications in biomass cookstoves in order to develop a better scientific understanding of the positive and negative impacts of those modifications for stove designers. The specific topics included:

1. Passive modifications to improve overall thermal efficiency in charcoal stoves as compared to the traditional Haitian stove;
2. A passive ignition aid, known as a lighting cone, to increase draft through the shallow charcoal bed of a traditional Haitian stove; and
3. Air-induced turbulent mixing strategies, referred to as halos, to reduce soot emitted from a wood-burning stove, focusing on injection angle and air flow rate.

A side aim of this work was to explore the technical feasibility and challenges of applying laser diagnostic techniques to high sooting, temporally- and spatially-variable flames such as those in biomass combustion systems. In this work, all air flow modifications achieved their primary intended benefit: all improved stoves in Chapter 5 reduced fuel consumption, the lighting cone decreased ignition time by over 50%, and the halo-based mixing strategies drastically reduced soot emissions. Several positive and negative side effects for each modification were also discovered in evaluations.

The improved stoves in Chapter 5 were designed to reduce convective heat losses to the environment and to direct air toward the cooking pot in attempt to reduce fuel consumption. Some stoves also featured doors so the air entrained from under the charcoal bed could be controlled. It was found that all improved stoves did save fuel compared to the traditional Haitian stove as desired, but they might face adoption issues due to slow cooking speeds. Because this work was performed as part of the short-term relief effort after the major 2010 Port-au-Prince earthquake, only a few stoves were evaluated. Future work assessing the performance and usability of more stoves either already in use or intended for dissemination in Haiti would be beneficial for long-term relief efforts.

Chapter 6 evaluated an ignition aid known as a lighting cone, which is used in various countries around the world. The lighting cone is designed to increase draft through a charcoal bed during ignition in order to increase the exposure of the charcoal bed surface to fresh air and protect it from heat losses due to wind. The lighting cone was found to work as desired – ignition time was reduced by over 50%, charcoal consumption was reduced by over

40%, and carbon monoxide emissions were reduced by over 50%. Additionally, the number of ultrafine particles was greatly reduced using the lighting cone as compared to the traditional ignition method. It would be interesting to see in future work if a lighting cone provides the same benefits for other hard to light stoves. If so, lighting cone use could prove extremely beneficial, especially since slow ignition time can be a barrier for adoption.

Chapters 7 – 9 examined the effects of different air-induced turbulent mixing strategies, focusing specifically on the effect of the secondary air injection angle and air flow rate. The results of Chapter 7 revealed that none of the halo mixing strategies improved specific fuel consumption during the low power (simmer) phase compared to the unmodified Berkeley-Darfur Stove (BDS); however, all mixing strategies did improve specific fuel consumption compared to the traditional three-stone fire (TSF). This indicates the halo stoves benefited from the same improvements as the BDS but the air injection did not improve performance. Also, while stoves with air injection dramatically reduced black carbon (BC), they produced more CO and $PM_{2.5}$ than the BDS. The large disparity between BC and $PM_{2.5}$ values indicates a high amount of organic carbons being released. Both CO and organic carbons are primarily produced during smoldering combustion, so the mixing strategies initially appear to be directly impacting the fuel bed and increasing the smoldering combustion rate during low power. It is interesting to note though that the 30SWL halo has a comparable modified combustion efficiency to the BDS; this likely means that the increased emissions seen from the 30SWL are due a decreased thermal efficiency and long burn time, as opposed to quenching the flame. In either case, it would be interesting in future work to examine the effect of preheating the secondary air to reduce the cooling effect of the injected air in the combustion chamber. While preheating the secondary air a few hundred degrees is unlikely to make an impact in the hot, high power burns, it could make a noticeable difference in the much cooler, largely smoldering combustion of the low power phase.

In the high power tests in Chapter 7, the stoves with air injection dramatically decreased soot emissions and performed better than the traditional TSF and comparable or worse than the unmodified BDS for time to boil, specific fuel consumption, and thermal efficiency. The dramatic decrease in soot was not mirrored in the $PM_{2.5}$ emissions, revealing potentially high concentrations of emitted organic carbons. It would be beneficial in future work to quantify the emitted ratio of black carbon to organic carbon through the use of gravimetric quartz filter measurements instead of speculating. Comparing the soot emissions measurements of the proxy cookstove burner (PCB) discussed in Chapter 8 with the in-situ luminescence measurements taken in Chapter 9 does reveal that all halos appear to be operating as desired; soot is produced in the flame, which increases radiative heat transfer to a cooking pot, but is oxidized prior to leaving the combustion zone.

For the high power phase, the 90STR halo promoted higher soot concentrations lower in the flame zone, appearing to form and recirculate soot in the lower regions prior to oxidation as predicted by Shelton (1983). As expected, injecting air straight down towards the fuel using the 90STR halo appeared to greatly interact with the fuel bed. High CO emissions and noticeable effects from the injected air at the base of the flame in the LII measurements indicate the injected air is reaching the fuel source and either increasing smoldering or

quenching the combustion. One would expect that a lower air flow rate would decrease the impacts of the impinging air on the fuel, but it is not known for certain due to the variable CO emission trends with air flow rates seen in Chapters 7 and 8 for the 90STR halo. Based on that data, it appears as though an air flow rate around 28.3 – 35.4 L/min would be best for balancing higher CO emissions with low BC and $PM_{2.5}$.

The 30SWL had the largest emissions reductions for BC, $PM_{2.5}$, and CO in the high power phase as well as the best modified combustion efficiency, indicating it likely increased turbulent mixing and residence time, similar to the swirling flow in industrial burners (Yin et al., 2008; Suri and Horio, 2010). However, the poor thermal efficiency might indicate the residence time was too long if gases had time to cool after leaving the hot flame zone but prior to reaching the pot; additionally, the 30SWL would have increased the interaction of the hot gases with the cool walls, which also would have reduced thermal efficiency. The laser experiments of Chapter 9 show a central vortex, which would have entrained air and increased residence time without quenching or local extinction. For high power combustion, therefore, the highest flow rate appears to be the best. It is not certain, however, at what point the flow rates higher than those studied in this work will transition from being beneficial to quenching the flames.

The results of the high power test for the 30ANG appear to make it a good compromise of the air injection designs; it does not achieve as large of emissions reductions as the 30SWL, but it also does not negatively impact stove performance as greatly. However, the laser-based measurement results do indicate the 30ANG quenches the center of the flame and the CO emissions appear to confirm, especially as air flow rate increases. This indicates slower air flow rates or air velocities could reduce the negative impacts of the injected air; however, if the trend seen in Chapter 8 holds true, then slower air flow rates will not reduce BC as effectively. Examining the trend in released emissions as the injection angle decreases from the 90STR to the 45ANG to the 30ANG in Chapter 7, the CO emissions decrease and so do the $PM_{2.5}$ and BC emissions. This trend suggests an even smaller injection angle than 30° could be more beneficial for emissions reductions and would avoid adverse quenching effects because the air injection would be directed farther away from the solid fuel.

Many challenges and uncertainties arose when applying the laser-based techniques of Chapters 8 and 9 to the turbulent mixing systems. First, in Chapter 8, laser extinction was conducted in the BDS to assess the feasibility of applying laser diagnostic techniques to the wood-burning stove. It was decided that using the actual wood-burning stove would not be feasible because of the highly variable combustion and the limited optical access of the enclosed stove. Although techniques such as LII could potentially handle the variability, a prohibitively large number of images for the scope of this work would need to be taken to ensure high confidence in the data. Therefore, a proxy burner was developed for the laser-based diagnostics of the system. Also, all laser techniques utilized in this work were one- or two-dimensional techniques. Because the halo mixing strategies tend to promote a great deal of out-of-plane motion, only visualizing in two dimensions did not provide the whole picture and much had to be hypothesized when comparing results. Future experiments examining multiple locations along the burner (as opposed to solely through the centerline) or utilizing

a top-down view would provide a more complete picture of soot concentration and oxidation in the flames. Three-dimensional laser diagnostic techniques would also help resolve many of the hypotheses left unanswered by the two-dimensional experiments.

The OH-LIF results conducted in Chapter 9 had a high level of interference from other species, likely PAH and soot. Because it was not possible to record the interference simultaneously with the OH-LIF measurements and the flame dynamics are extremely variable in this system, the interference was unable to be removed from the averaged OH-LIF radial profiles. Therefore, only limited information about the OH concentration was found using the averaged profiles in this work. Further analysis of the simultaneous LII and OH-LIF instantaneous images will enable better distinction between OH concentrations and interference from soot and PAH and therefore, provide deeper insight into the locations of reaction zones in the flames, but this analysis is beyond the scope of this work. Also, although filtering was used on the OH-LIF camera, a better system for reducing interference should be developed for future experimental work.

Although only sporadic and limited amounts of visible flame were visually observed in the upper half of the measurement region for some of the cases, it would be interesting to record LII and OH-LIF measurements in this zone in future work. Soot concentrations from the upper half of the measurement region, compared with the lower half measurements taken in this work, could provide insight into the amount of soot oxidation versus formation reduction occurring due to each halo. Also, better profiles of OH concentrations might be achievable in this region if there is less intense PAH interference, which is a possibility farther downstream since PAH tends to be formed in the initial ignition region by the burner where this set of measurements was taken.

Although the results of this work found useful information from the two-dimensional PIV measurements, three-dimensional PIV measurements would be better suited for the highly three-dimensional flows of the turbulence-inducing mixing strategies. The two-dimensional PIV experiments also highlighted challenges and necessary changes for future PIV measurements of this system. It is recommended the experiment be entirely enclosed to avoid particle losses from the system, reduce air interference from ambient sources, and allow seeding of the entire measurement volume without introducing uncertainty from gravitational settling. However, it is important that this enclosure is designed such that it does not affect the bulk flow of entrained air into or out of the measurement region so the effects of the air injection are not obscured. Additionally, further development is needed in order to seed the slow fuel flow and provide additional filtering to reduce interference from the luminescence of reacting flows. This would provide more detailed velocity profiles in the regions of the PIV images that are not well-defined from the results of this work (such as the lower half of the 90STR case).

Modifying the air flow in a biomass stove to improve combustion efficiency is promising but complicated. As seen in this work, there are several positive and/or negative side effects for each modification as well as challenges and barriers that must be overcome prior to implementation. However, each air flow modification achieved its primary intended benefit:

all improved stoves in Chapter 5 reduced fuel consumption, the lighting cone decreased ignition time by over 50%, and the halo-based mixing strategies drastically reduced soot emissions. As researchers continue to develop and hone these designs, air flow modifications in improved cookstoves have a strong potential to decrease the harmful emissions created from the simple, unavoidable act of cooking.

A Data Tables

A.1 Haiti Stove Comparison Results

This section contains the data tables for the Haiti stove tests discussed in Chapter 5. The means and 95% confidence intervals (calculated using the Student's t-distribution) of the results from the water boiling and controlled cooking tests are presented in Tables A.1 and A.2, respectively. Note, TtB_{cold} and TtB_{hot} are the times to boil for the cold and hot start phases, respectively, η_{th} is the thermal efficiency, SFC is the specific fuel consumption, and MCE is the modified combustion efficiency.

Table A.1: The water boiling test data from the Haiti stove comparison tests.

Stove	TtB_{cold} $[min]$	TtB_{hot} $[min]$	η_{th} [%]	*SFC* $[g/kg]$	*Total CO* $[g]$	*MCE* [%]
EcoRecho	50.1 ± 35.4	30.3 ± 3.9	31.4 ± 23.8	477.8 ± 166.3	178.6 ± 23.1	89.2 ± 1.8
Mirak	52.9 ± 21.4	42.9 ± 19.6	28.3 ± 10.5	506.8 ± 149.4	131.4 ± 25.0	92.0 ± 0.8
Prakti	47.4 ± 9.4	33.8 ± 13.6	37.8 ± 5.9	423.0 ± 249.6	123.5 ± 30.3	91.2 ± 1.1
Traditional	32.4 ± 10.8	27.4 ± 5.9	23.8 ± 4.2	866.7 ± 279.9	150.5 ± 30.0	92.0 ± 0.5

Table A.2: The controlled cooking test data from the Haiti stove comparison tests.

Stove	*SFC* $[g/kg]$	*Total CO* $[g]$	*MCE* [%]
EcoRecho	99.8 ± 9.7	92.7 ± 16.7	91.6 ± 1.4
Mirak	110.7 ± 13.8	99.0 ± 22.9	92.2 ± 1.5
Prakti	77.4 ± 10.9	69.0 ± 20.4	92.8 ± 2.0
Traditional	144.8 ± 19.1	127.6 ± 15.5	91.7 ± 0.9

A.2 Lighting Cone Results

Table A.3 presents the means and 95% confidence intervals (calculated using the Student's t-distribution) of the results from the lighting cone tests conducted in Chapter 6. Note, TtL is the time to light and FC is the total fuel consumed.

Table A.3: Performance and emissions data for the lighting cone tests.

Stove	*TtL* $[s]$	*FC* $[g]$	*CO* $[g]$	$PM_{2.5}$ $[mg]$	*BC* $[mg]$
Baseline	414 ± 46.3	28 ± 4.1	3.0 ± 0.5	538.0 ± 148.1	59.7 ± 16.1
Cone	193 ± 30.7	16 ± 1.5	1.2 ± 0.3	344.9 ± 170.1	66.6 ± 23.2

A.3 Halo Stove Results

Halo Stove Preliminary Trials

This section presents the results of the preliminary Halo Stove experiments, discussed in Section 7.3. Note, the results have been normalized to the maximum, which is the baseline (i.e. 0 L/min) case for the black carbon and $PM_{2.5}$ results and the 90STR 56.6 L/min case for the CO results.

Table A.4: Black carbon data for the preliminary Halo Stove tests.

	Baseline	*90STR*	*45ANG*	*30ANG*	*30SWL*
Baseline	1	–	–	–	–
14.2 L/min	–	0.78	0.63	0.54	0.29
28.3 L/min	–	0.22	0.31	0.17	0.09
42.5 L/min	–	0.06	0.11	0.09	0.08
56.6 L/min	–	0.10	0.07	0.06	0.11

Table A.5: $PM_{2.5}$ data for the preliminary Halo Stove tests.

	Baseline	*90STR*	*45ANG*	*30ANG*	*30SWL*
Baseline	1	–	–	–	–
14.2 L/min	–	0.51	0.36	0.28	0.18
28.3 L/min	–	0.41	0.22	0.13	0.06
42.5 L/min	–	0.40	0.10	0.11	0.09
56.6 L/min	–	0.31	0.11	0.10	0.09

Table A.6: CO data for the preliminary Halo Stove tests.

	Baseline	*90STR*	*45ANG*	*30ANG*	*30SWL*
Baseline	0.98	–	–	–	–
14.2 L/min	–	0.66	0.50	0.54	0.36
28.3 L/min	–	0.59	0.54	0.43	0.27
42.5 L/min	–	0.77	0.46	0.75	0.65
56.6 L/min	–	1.00	0.64	0.84	0.79

Halo Stove Comparison Trials

This section presents the results of the final Halo Stove experiments, discussed in Section 7.4, which compare the halo mixing strategies with two baseline stoves (TSF and BDS) using a modified water boiling test. Note, the error is a 95% confidence interval calculated using the Student's t-distribution.

Table A.7: Performance data for the Halo Stove comparison tests. Note, hp represents the high power phase, lp represents the low power phase.

Stove	*Time to Boil* $[min]$	*Thermal Efficiency* [%]	SFC_{hp} $[g/kg]$	SFC_{lp} $[g/kg]$
TSF	31.8 ± 3.6	21.4 ± 3.7	110.4 ± 9.1	154.9 ± 31.3
BDS	18.3 ± 0.8	36.2 ± 2.1	62.9 ± 2.3	72.6 ± 6.2
90STR	20.1 ± 1.1	29.9 ± 1.4	71.3 ± 2.8	77.4 ± 4.6
45ANG	18.2 ± 0.9	31.1 ± 3.5	64.8 ± 2.5	80.8 ± 8.3
30ANG	18.9 ± 0.6	31.7 ± 1.9	63.5 ± 2.7	76.9 ± 6.4
30SWL	20.4 ± 0.9	28.0 ± 1.6	69.4 ± 1.9	85.3 ± 4.5

Table A.8: Emissions data for the Halo Stove comparison tests. Note, hp represents the high power phase, lp represents the low power phase.

Stove	BC_{hp} $[mg]$	BC_{lp} $[mg]$	$PM_{2.5,hp}$ $[mg]$	$PM_{2.5,lp}$ $[mg]$	CO_{hp} $[g]$	CO_{lp} $[g]$
TSF	725.6 ± 58.5	750.4 ± 123.2	1463.2 ± 258.3	1171.9 ± 291.7	20.3 ± 3.1	29.7 ± 5.1
BDS	806.1 ± 78.1	333.3 ± 46.7	1290.9 ± 90.0	543.2 ± 54.0	12.1 ± 2.0	13.4 ± 3.2
90STR	87.2 ± 5.9	37.5 ± 4.4	2009.6 ± 293.6	1163.5 ± 96.2	16.1 ± 1.4	18.4 ± 0.8
45ANG	77.9 ± 17.3	39.7 ± 9.4	1366.8 ± 193.2	930.5 ± 285.1	12.4 ± 1.8	19.6 ± 0.5
30ANG	69.1 ± 8.8	44.4 ± 5.8	903.0 ± 199.7	815.8 ± 100.6	9.5 ± 0.8	17.9 ± 1.5
30SWL	58.7 ± 5.2	62.3 ± 10.1	851.5 ± 89.3	1038.0 ± 152.5	7.4 ± 0.5	16.0 ± 0.9

A.4 Proxy Cookstove Burner Results

This section presents the emissions results for the proxy cookstove burner tests using the three halo mixing strategies, discussed in Section 8.3.1. Note, the error is a 95% confidence interval calculated using a normal distribution.

Table A.9: Emissions data for the 90STR halo with the proxy cookstove burner.

Air Flow Rate	$BC\ [\mu g/s]$	$PM_{2.5}\ [\mu g/s]$	$CO\ [mg/s]$
Baseline	3185.5 ± 20.5	8030.6 ± 58.6	3095.9 ± 19.1
28.3 L/min	344.8 ± 6.2	786.5 ± 37.7	594.4 ± 19.5
35.4 L/min	147.8 ± 2.9	336.8 ± 35.6	342.6 ± 9.2
42.5 L/min	70.9 ± 1.5	144.1 ± 16.7	469.9 ± 14.0

Table A.10: Emissions data for the 30ANG halo with the proxy cookstove burner.

Air Flow Rate	$BC\ [\mu g/s]$	$PM_{2.5}\ [\mu g/s]$	$CO\ [mg/s]$
Baseline	3185.5 ± 20.5	8030.6 ± 58.6	3095.9 ± 19.1
28.3 L/min	526.0 ± 7.0	1130.3 ± 53.0	110.1 ± 8.2
35.4 L/min	287.4 ± 11.1	516.2 ± 29.8	307.4 ± 13.6
42.5 L/min	191.6 ± 7.0	395.3 ± 52.1	642.6 ± 22.1

Table A.11: Emissions data for the 30SWL halo with the proxy cookstove burner.

Air Flow Rate	$BC\ [\mu g/s]$	$PM_{2.5}\ [\mu g/s]$	$CO\ [mg/s]$
Baseline	3185.5 ± 20.5	8030.6 ± 58.6	3095.9 ± 19.1
28.3 L/min	955.6 ± 23.5	2120.7 ± 68.8	755.0 ± 36.5
35.4 L/min	431.4 ± 12.2	982.1 ± 49.3	311.3 ± 17.3
42.5 L/min	133.3 ± 2.9	277.5 ± 24.9	295.1 ± 10.3

B Luminescence images

This appendix contains the averaged luminescence images for all cases discussed in Section 9.1, which are shown in Fig. B.1. The cases include the baseline (no air) and three halo (90STR, 30ANG, and 30SWL) cases at three air flow rates (28.3 L/min, 35.4 L/min, and 42.5 L/min). The averaged images are made from approximately 10 still images and represent a viewing area of 238 mm $\times$ 185 mm. These images were taken at camera settings: f/16, ISO1600, and 1/8000.

Also contained in this appendix are example instantaneous images of each case (shown in Fig. B.2) to provide a better view of flame structure. The camera settings are the same as the averaged images.

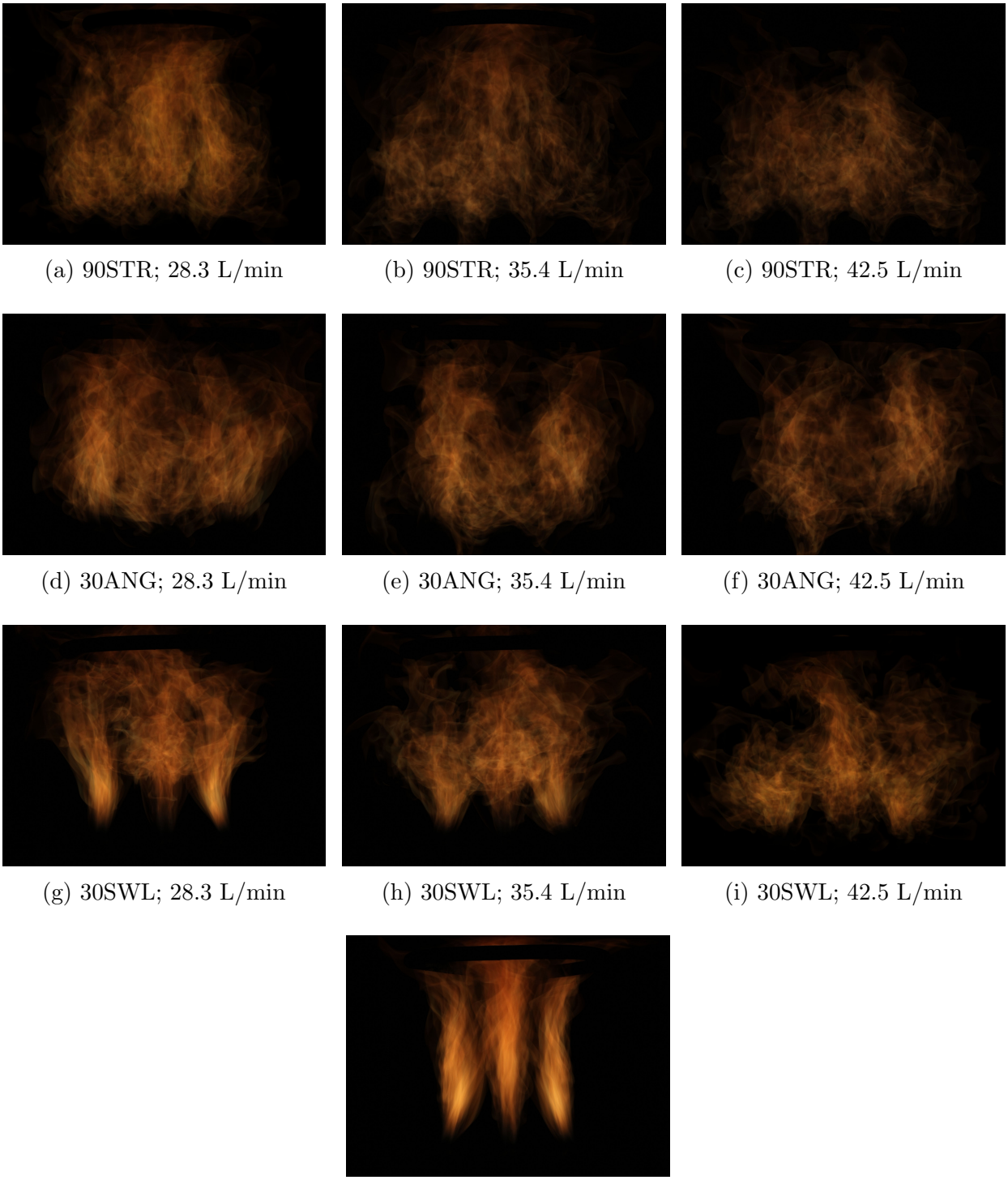

(a) 90STR; 28.3 L/min (b) 90STR; 35.4 L/min (c) 90STR; 42.5 L/min

(d) 30ANG; 28.3 L/min (e) 30ANG; 35.4 L/min (f) 30ANG; 42.5 L/min

(g) 30SWL; 28.3 L/min (h) 30SWL; 35.4 L/min (i) 30SWL; 42.5 L/min

(j) No air added

Figure B.1: Averaged luminescence images for the 90STR, 30ANG, 30SWL, and baseline.

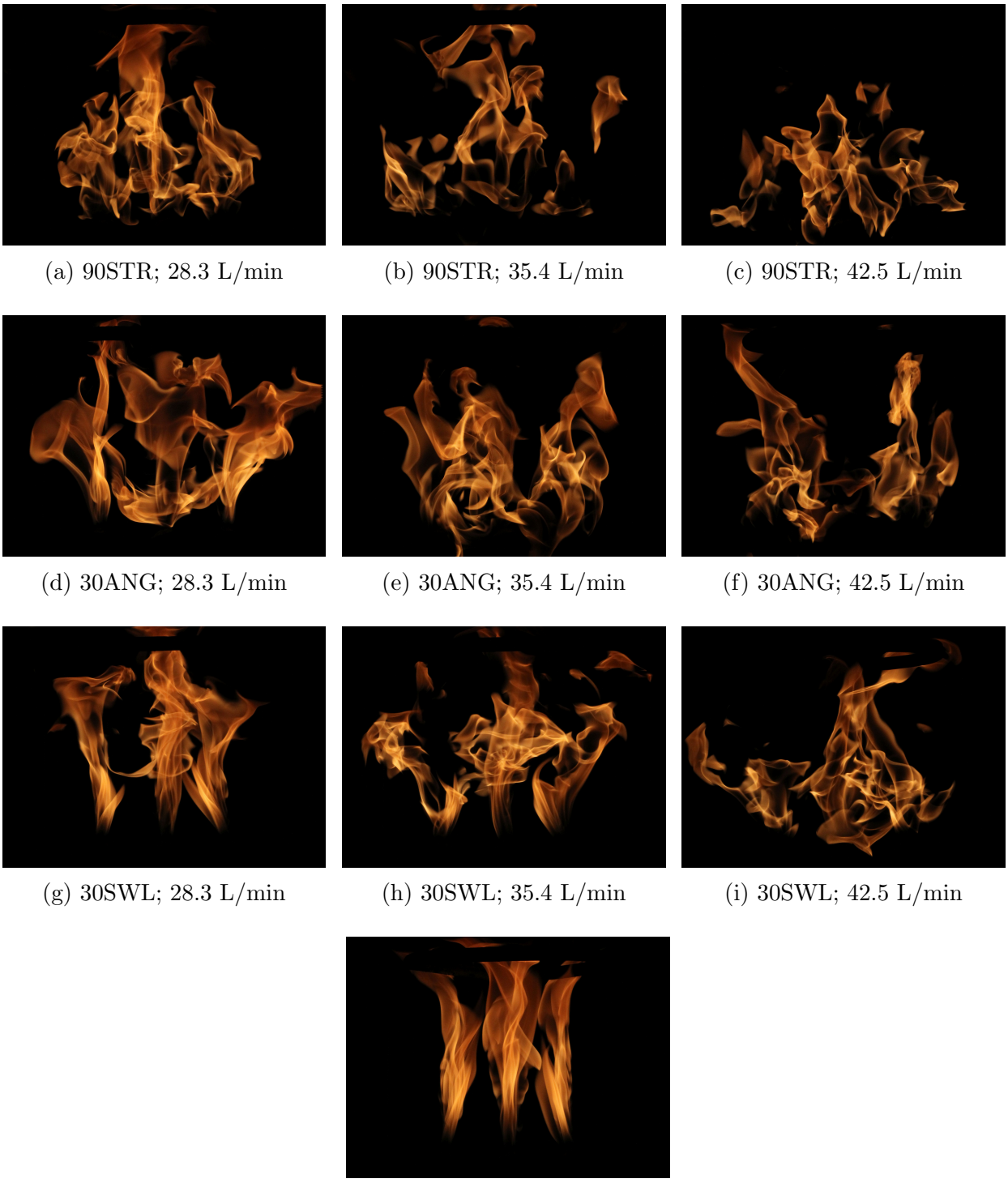

(a) 90STR; 28.3 L/min (b) 90STR; 35.4 L/min (c) 90STR; 42.5 L/min

(d) 30ANG; 28.3 L/min (e) 30ANG; 35.4 L/min (f) 30ANG; 42.5 L/min

(g) 30SWL; 28.3 L/min (h) 30SWL; 35.4 L/min (i) 30SWL; 42.5 L/min

(j) No air added

Figure B.2: Sample instantaneous luminescence images for the 90STR, 30ANG, 30SWL, and baseline.

C OH-LIF Interference Images

This appendix contains the profiles discussed in Section 9.3.2 which compare the recorded OH-LIF signal and the identified interference due to other species. The interference was judged by slightly changing the laser wavelength (or going off-wavelength) such that it would not cause OH fluorescence; any remaining signal is interference from other species, likely soot or polycyclic aromatic hydrocarbons (PAHs).

Each figure contains three plots. The top plot is the interference (or off-wavelength signal). The middle plot shows the average OH-LIF signal prior to the laser power and shot-to-shot variability corrections discussed in Section 4.5, as well as the same OH-LIF signal with the measured off-wavelength signal subtracted. The bottom plot contains the "final" OH-LIF minus off-wavelength result along with the final recorded OH-LIF signal.

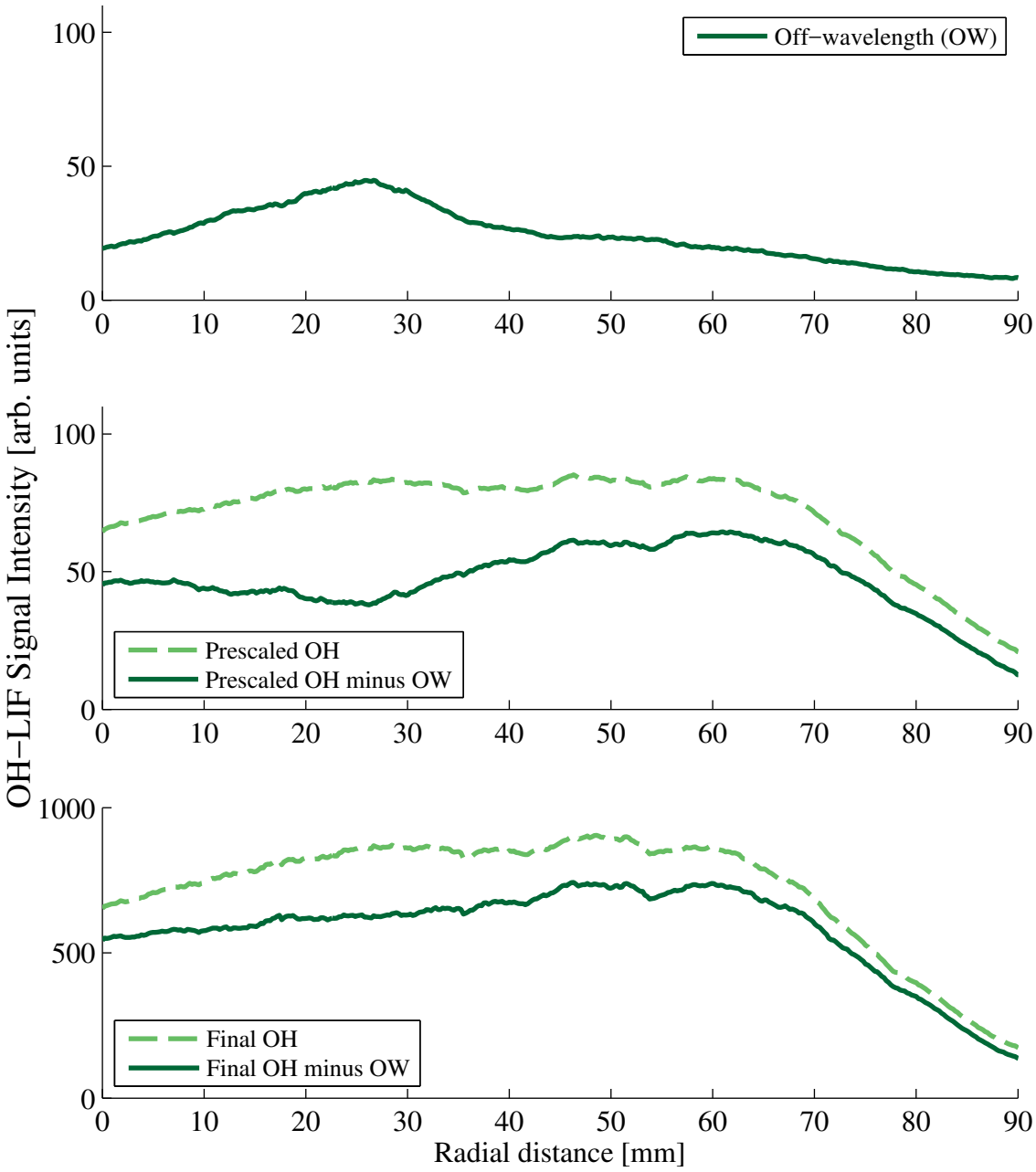

Figure C.1: OH-LIF results for the 90STR halo at 28.3 L/min measured 10 mm above the burner.

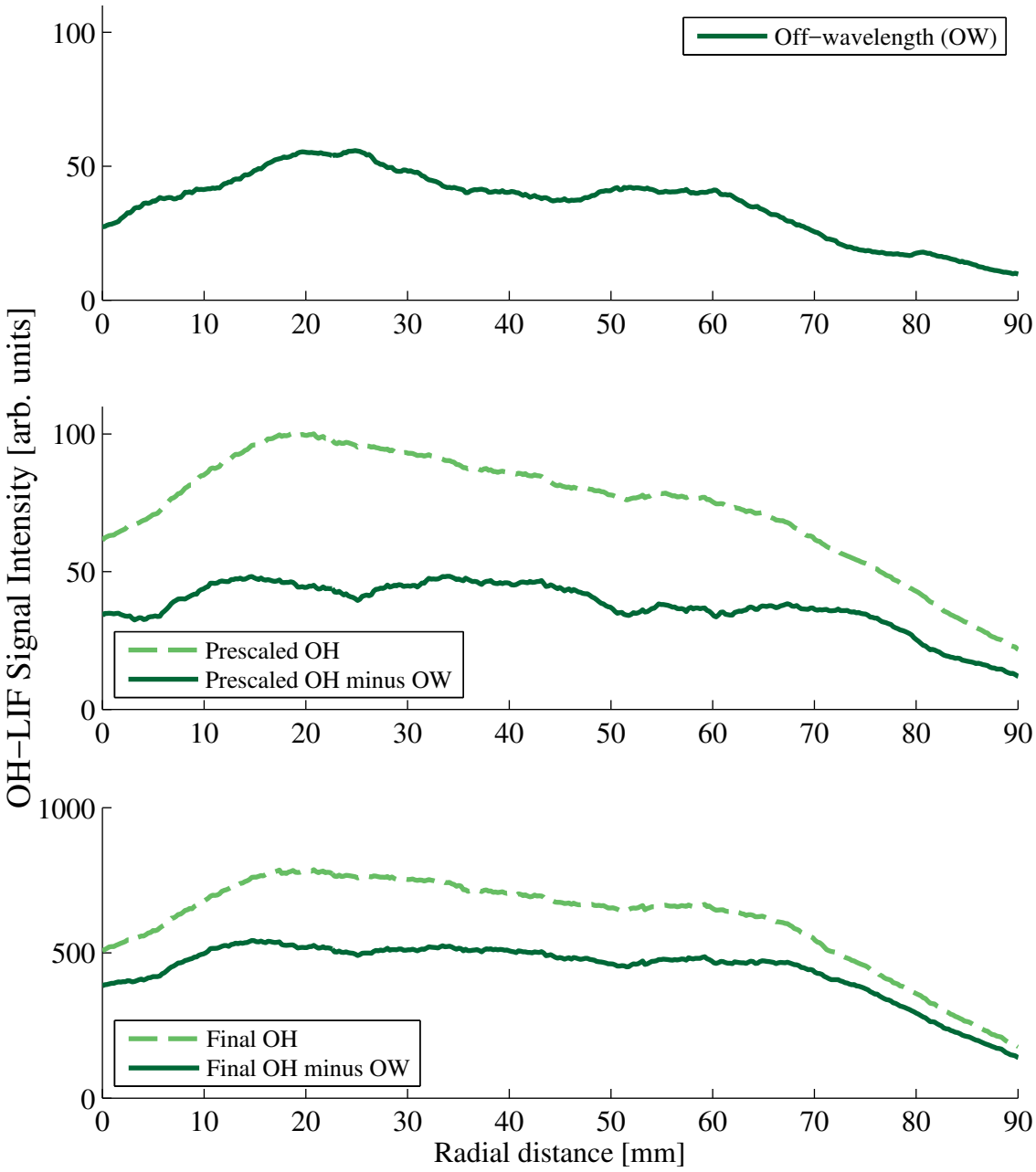

Figure C.2: OH-LIF results for the 90STR halo at 28.3 L/min measured 25 mm above the burner.

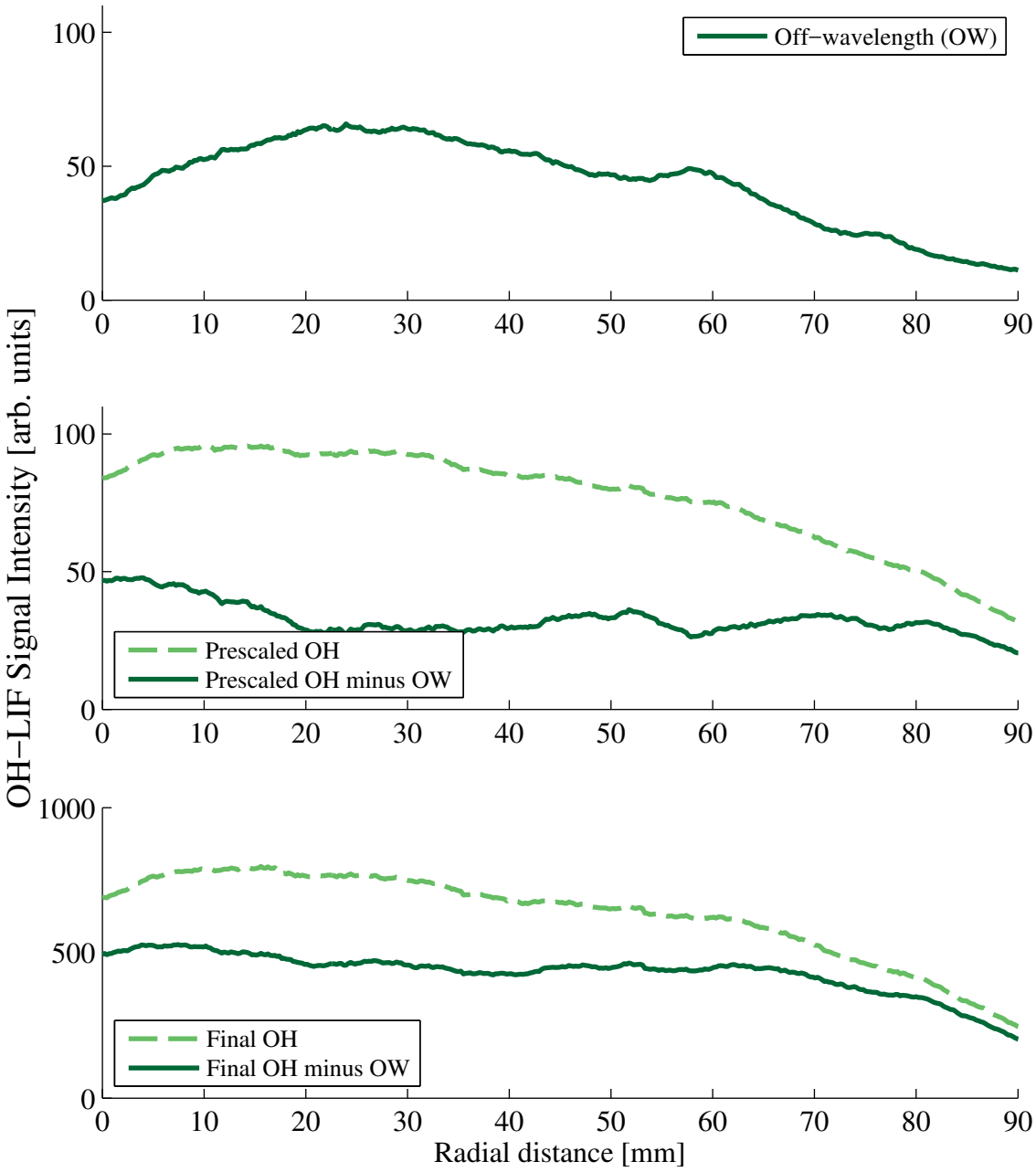

Figure C.3: OH-LIF results for the 90STR halo at 28.3 L/min measured 40 mm above the burner.

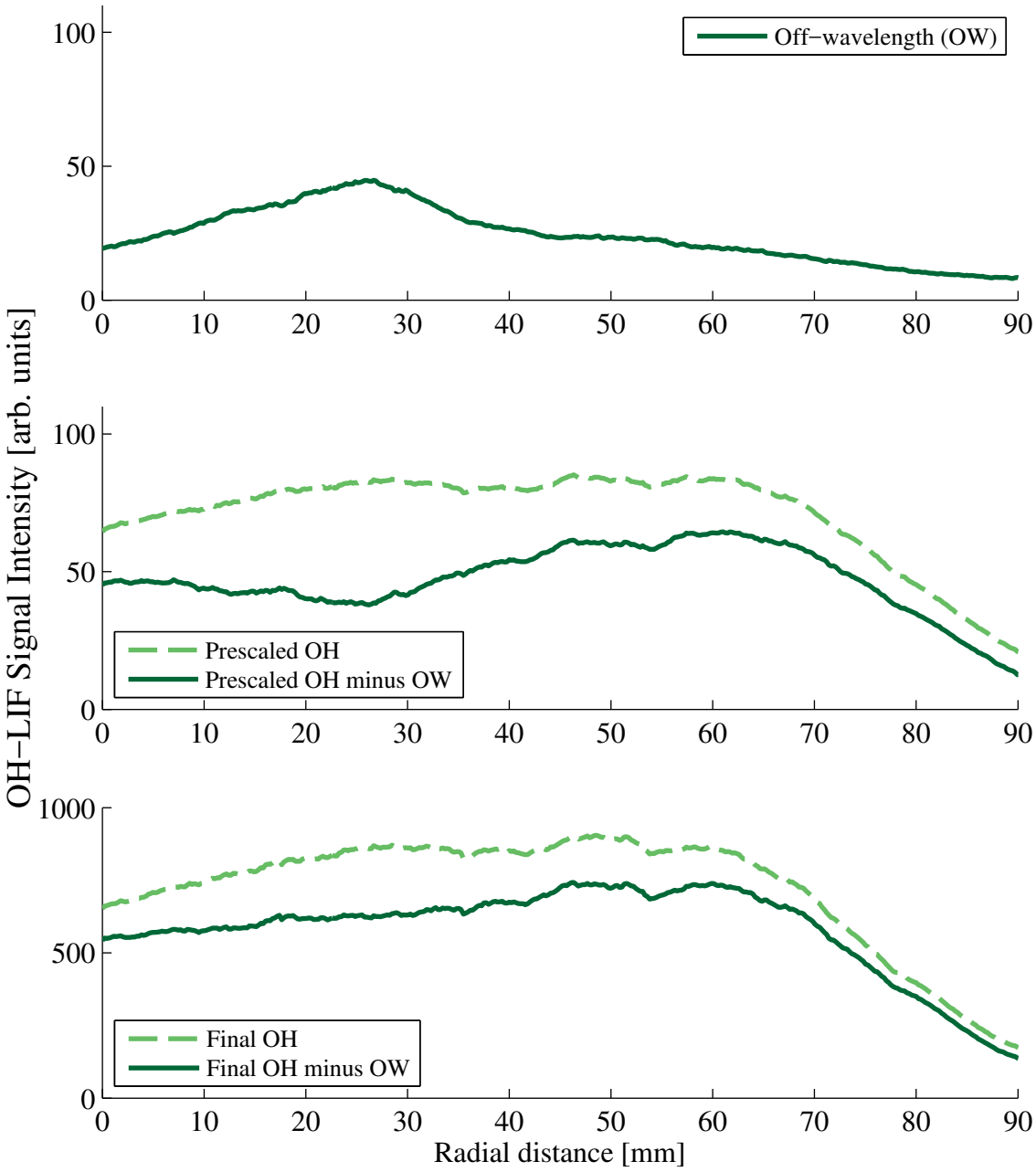

Figure C.4: OH-LIF results for the 90STR halo at 35.4 L/min measured 10 mm above the burner.

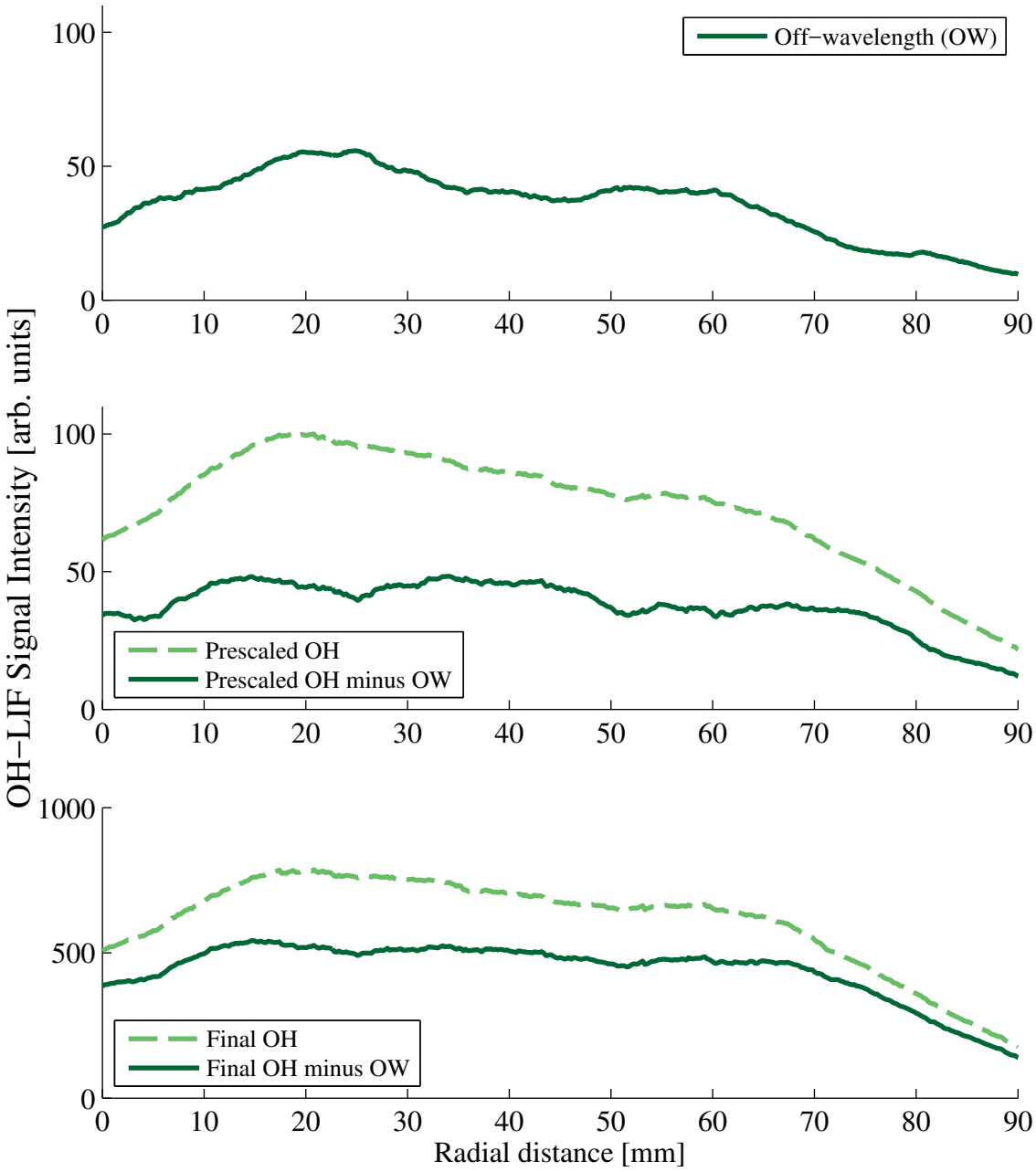

Figure C.5: OH-LIF results for the 90STR halo at 35.4 L/min measured 25 mm above the burner.

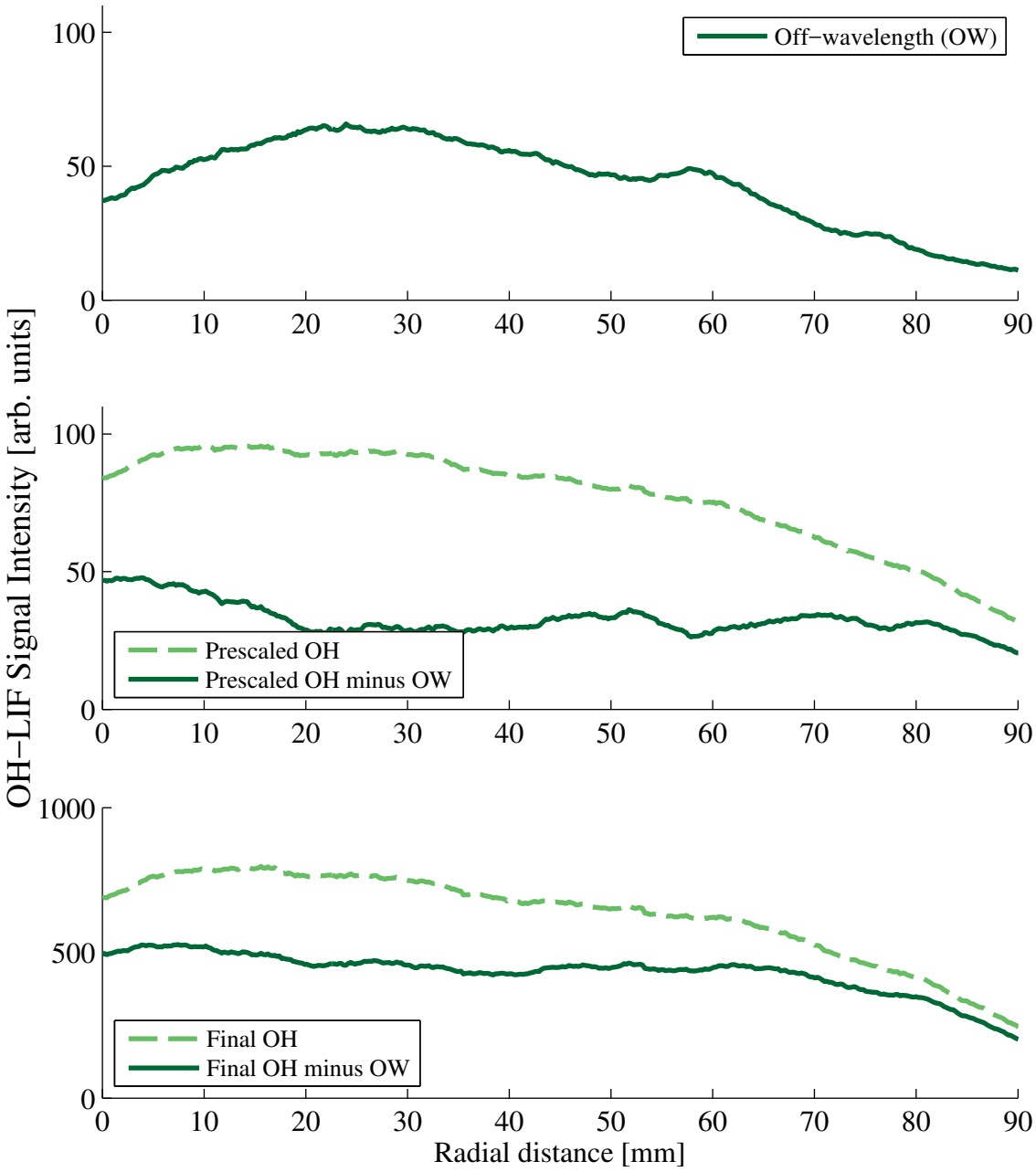

Figure C.6: OH-LIF results for the 90STR halo at 35.4 L/min measured 40 mm above the burner.

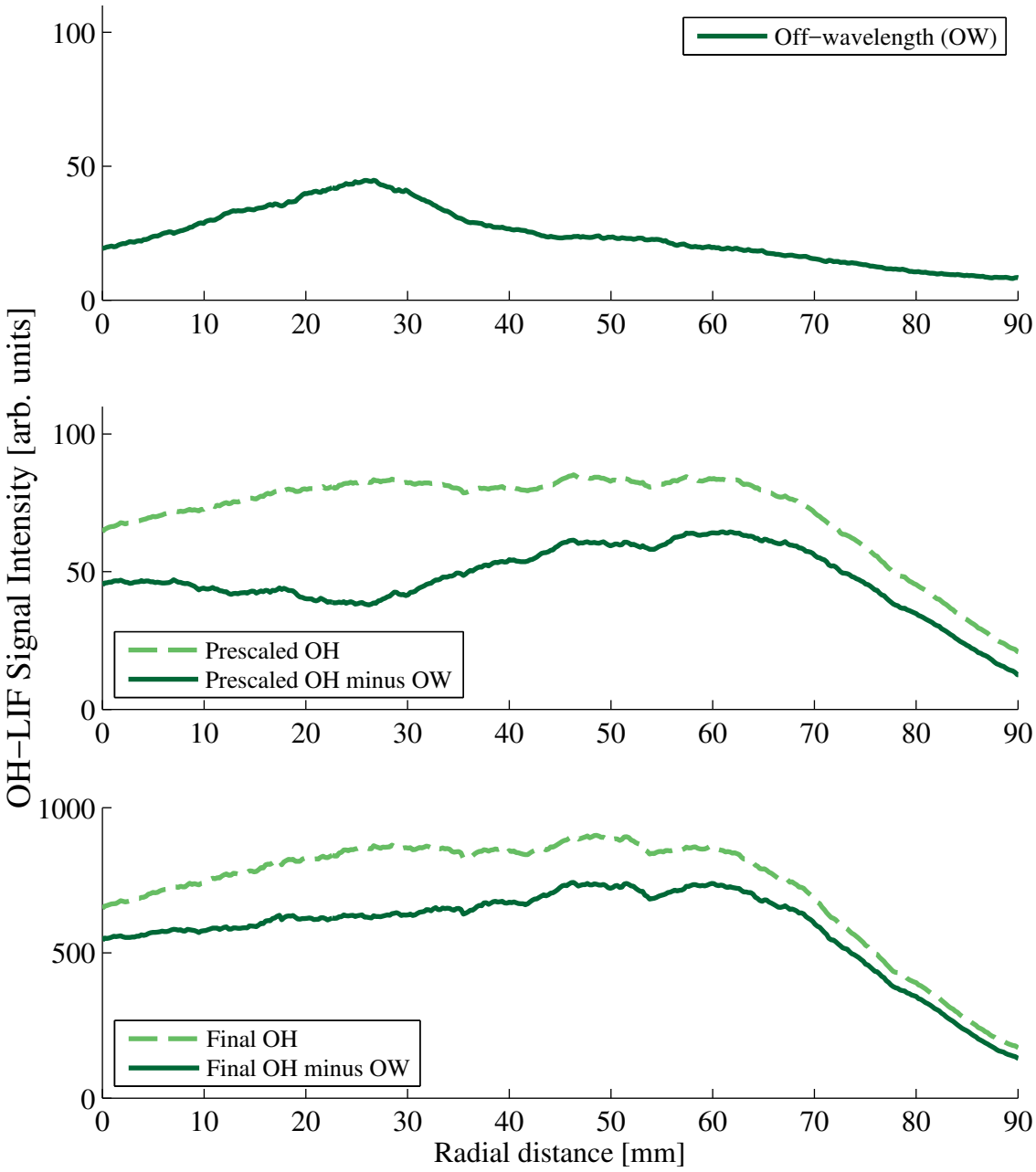

Figure C.7: OH-LIF results for the 90STR halo at 42.5 L/min measured 10 mm above the burner.

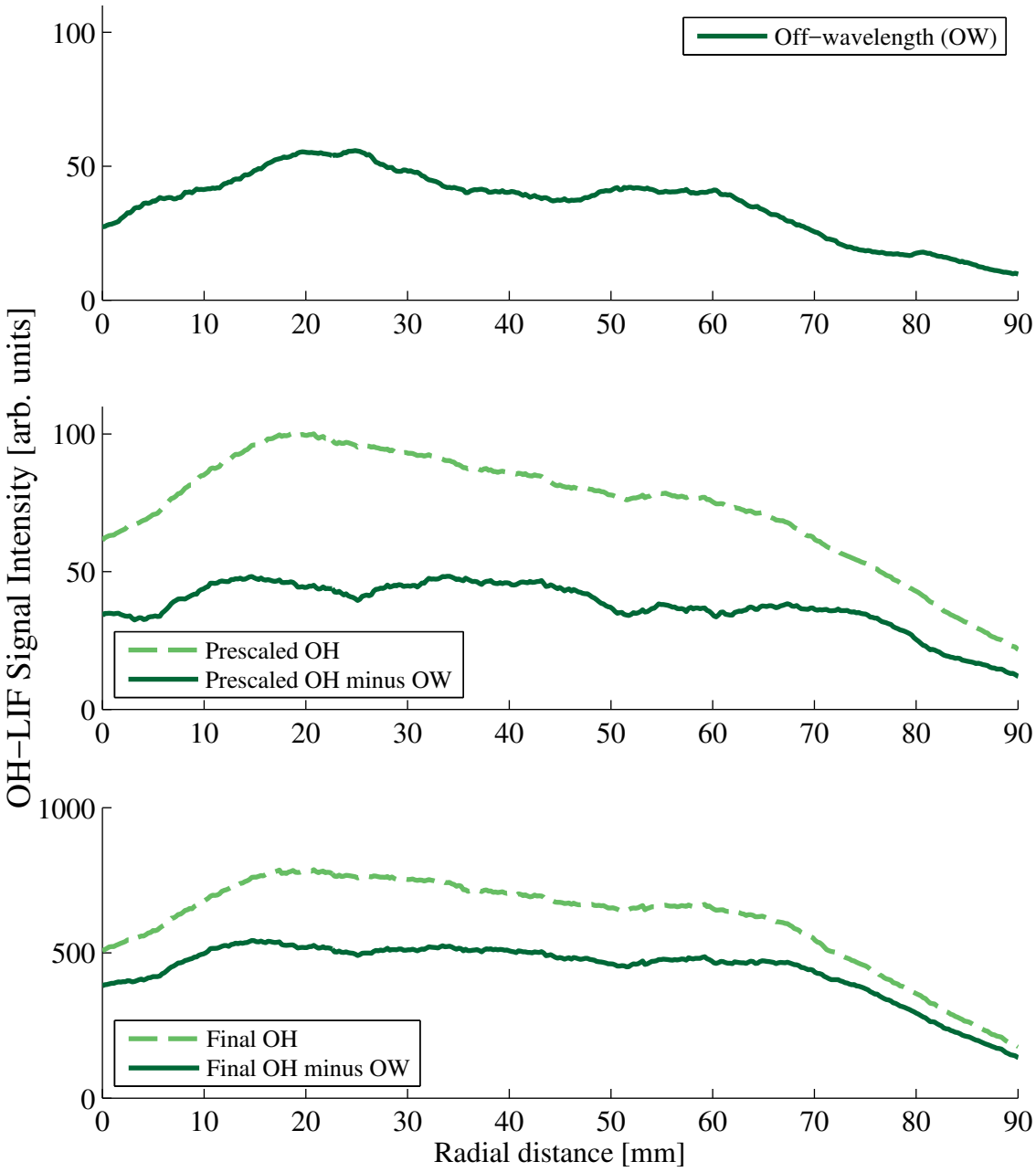

Figure C.8: OH-LIF results for the 90STR halo at 42.5 L/min measured 25 mm above the burner.

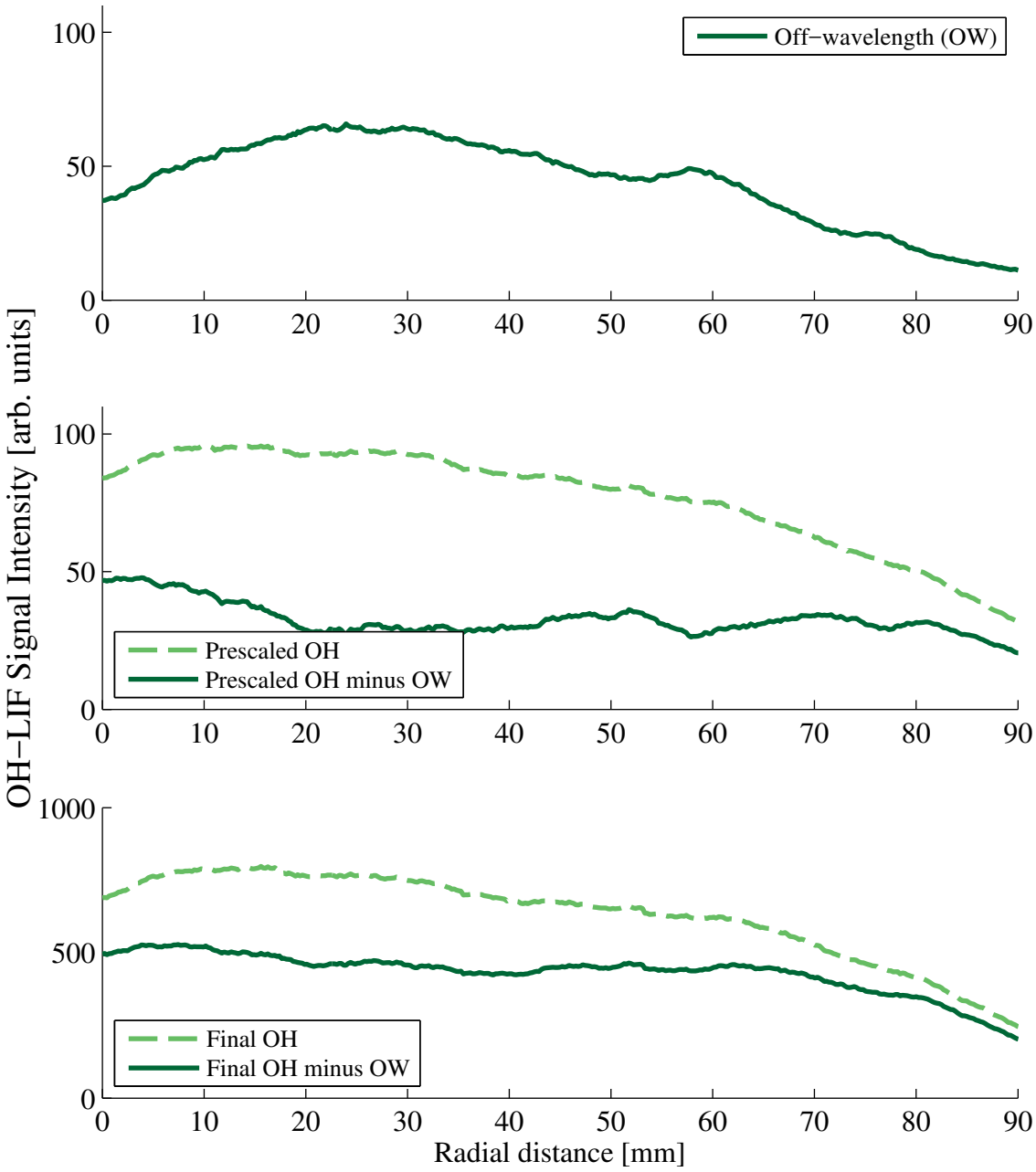

Figure C.9: OH-LIF results for the 90STR halo at 42.5 L/min measured 40 mm above the burner.

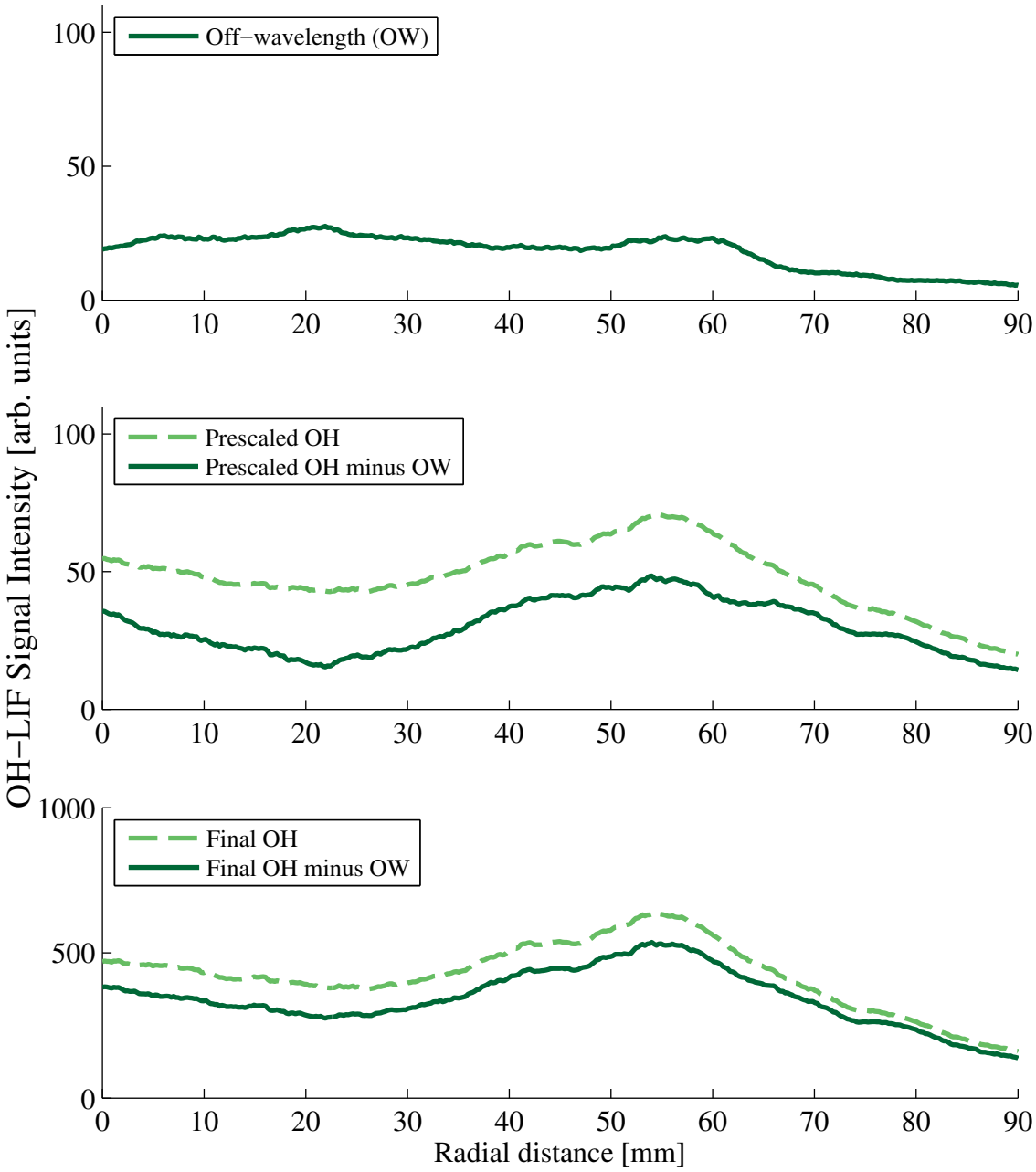

Figure C.10: OH-LIF results for the 30ANG halo at 28.3 L/min measured 10 mm above the burner.

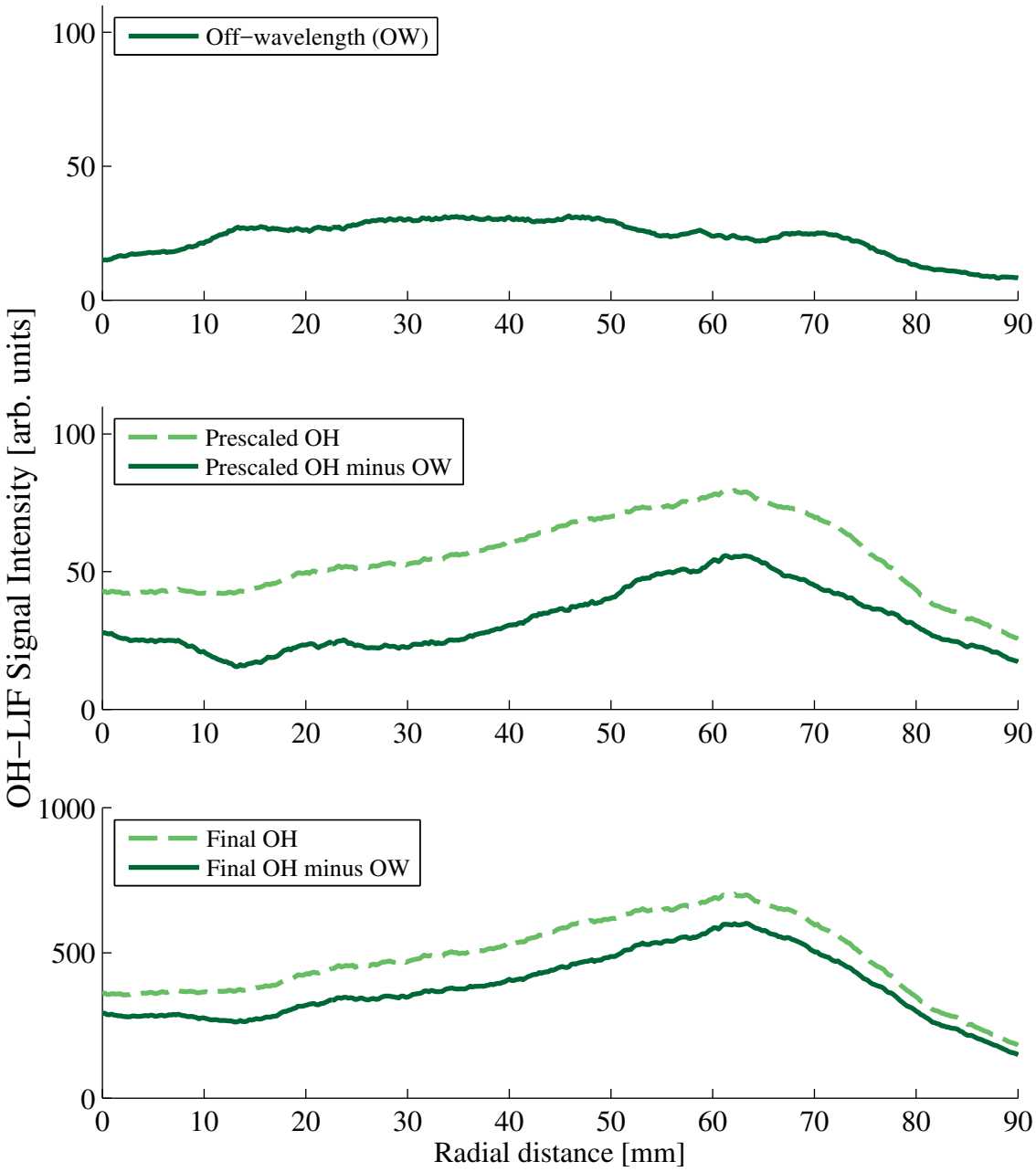

Figure C.11: OH-LIF results for the 30ANG halo at 28.3 L/min measured 25 mm above the burner.

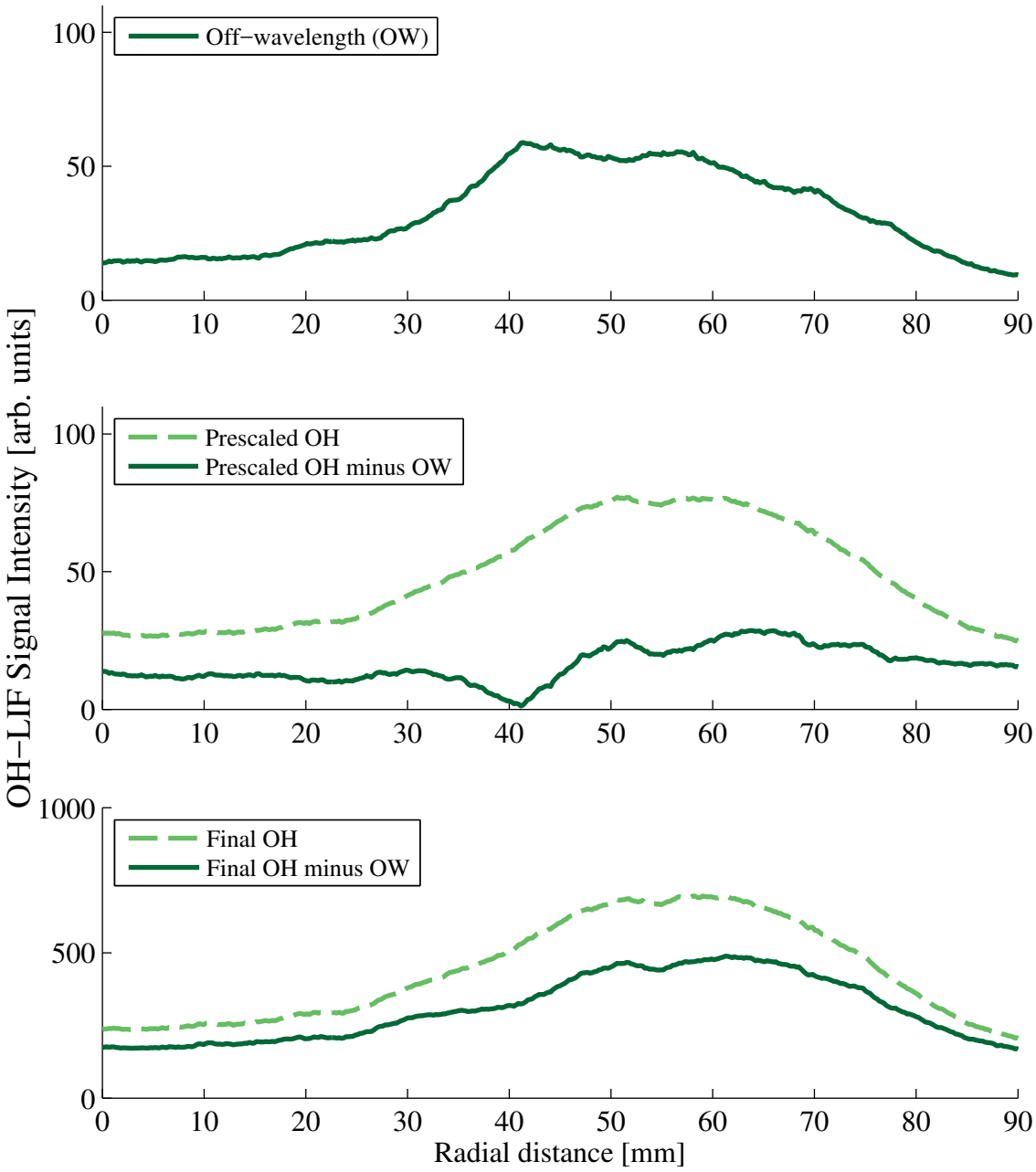

Figure C.12: OH-LIF results for the 30ANG halo at 28.3 L/min measured 40 mm above the burner.

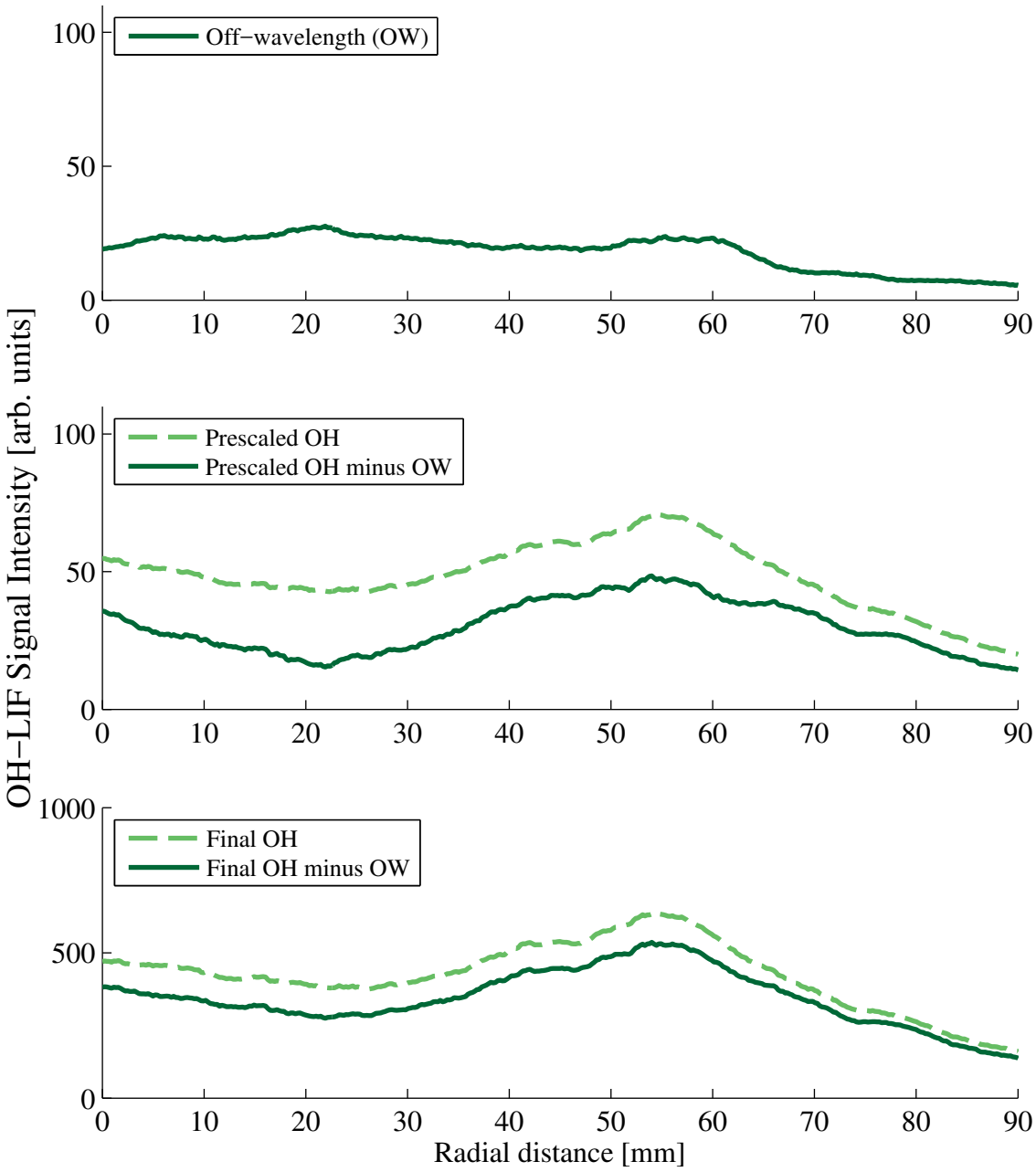

Figure C.13: OH-LIF results for the 30ANG halo at 35.4 L/min measured 10 mm above the burner.

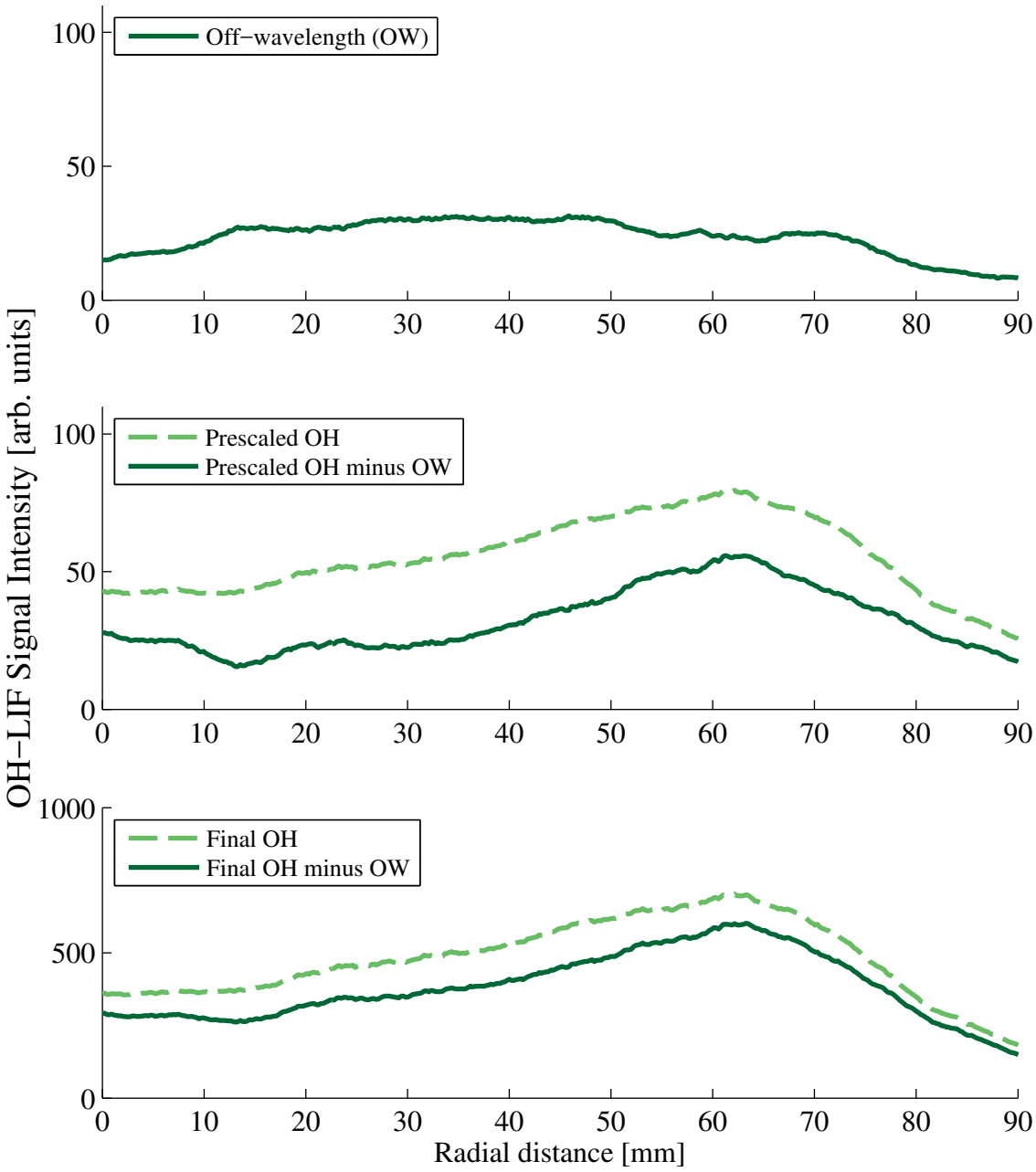

Figure C.14: OH-LIF results for the 30ANG halo at 35.4 L/min measured 25 mm above the burner.

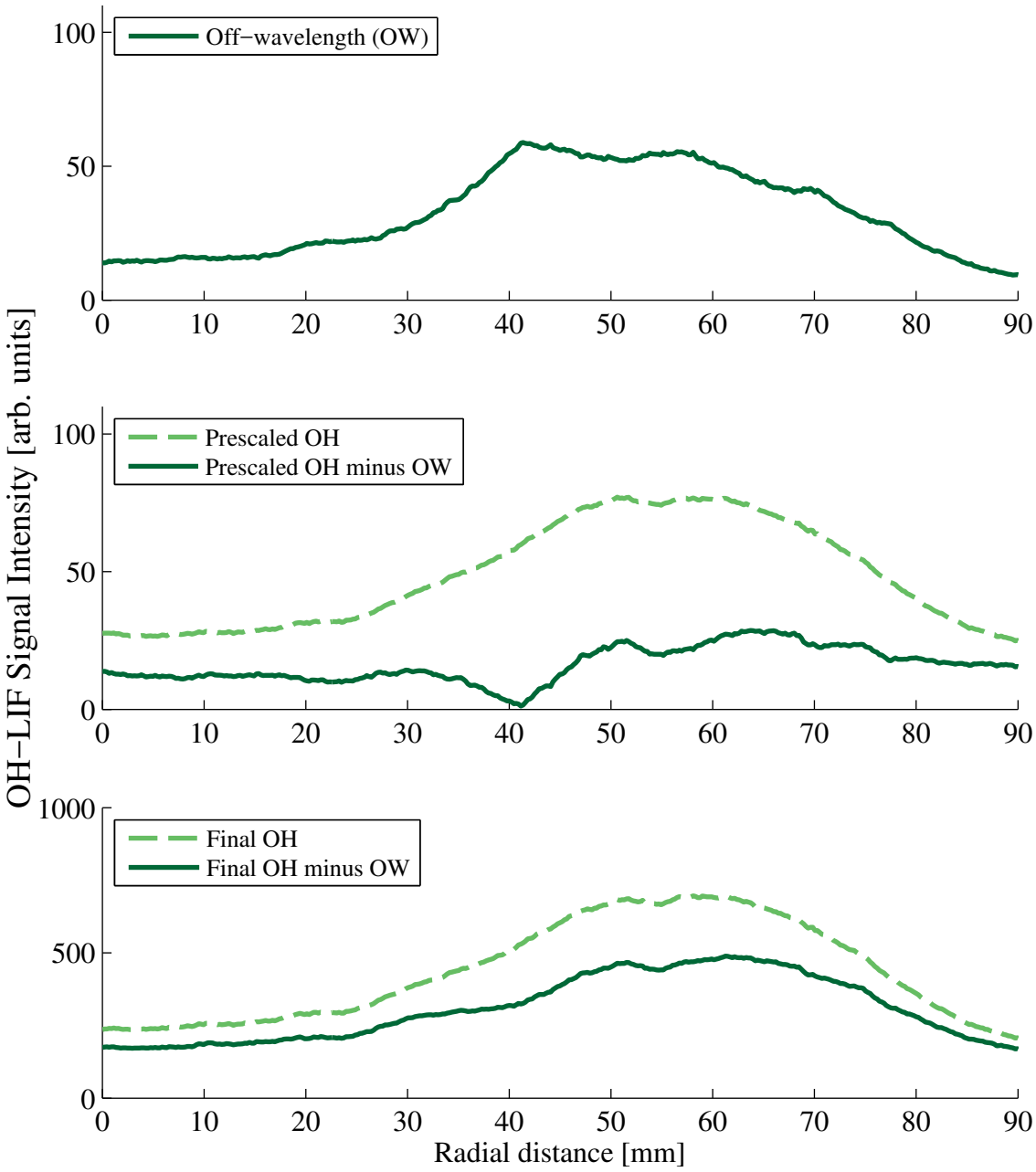

Figure C.15: OH-LIF results for the 30ANG halo at 35.4 L/min measured 40 mm above the burner.

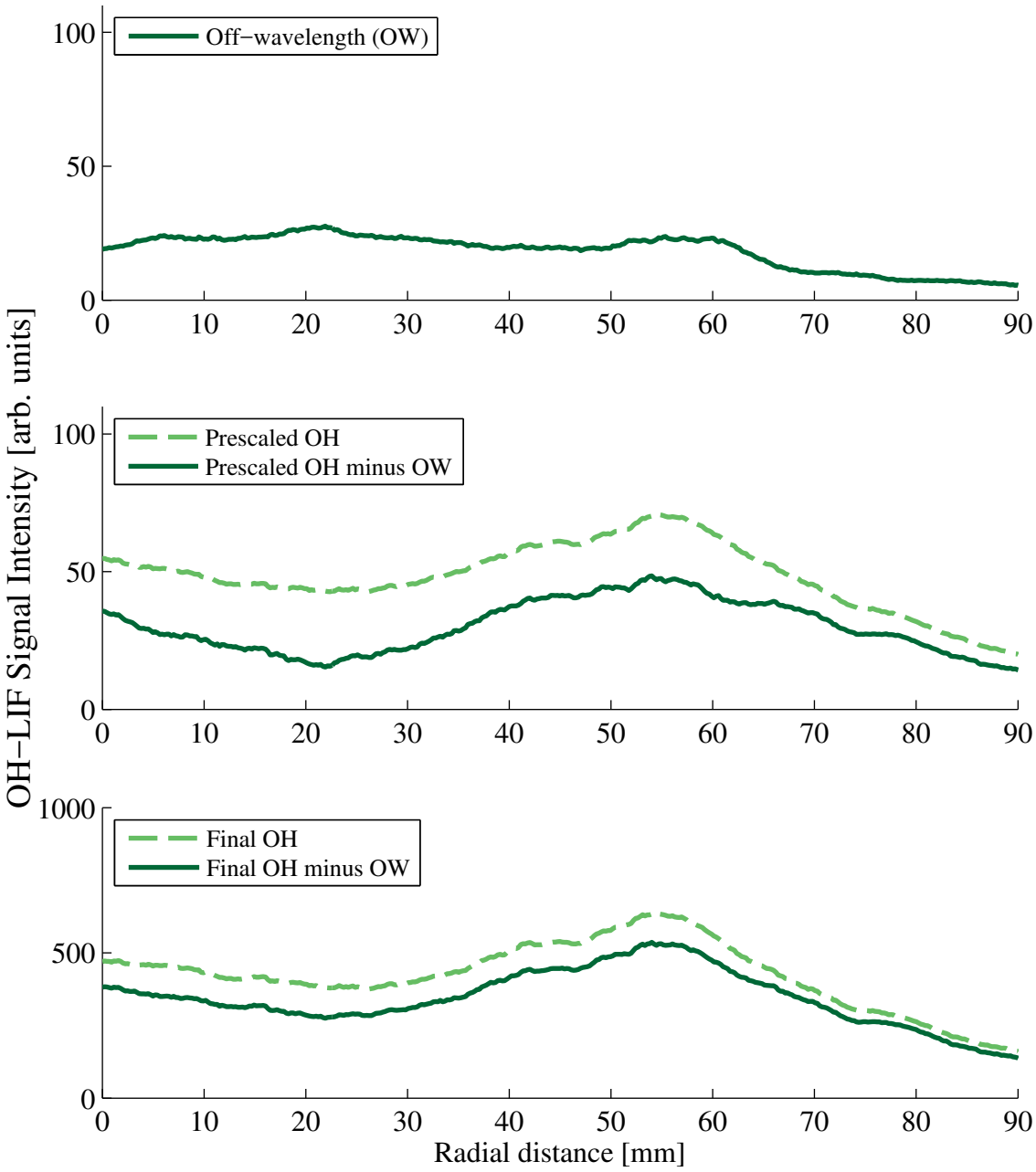

Figure C.16: OH-LIF results for the 30ANG halo at 42.5 L/min measured 10 mm above the burner.

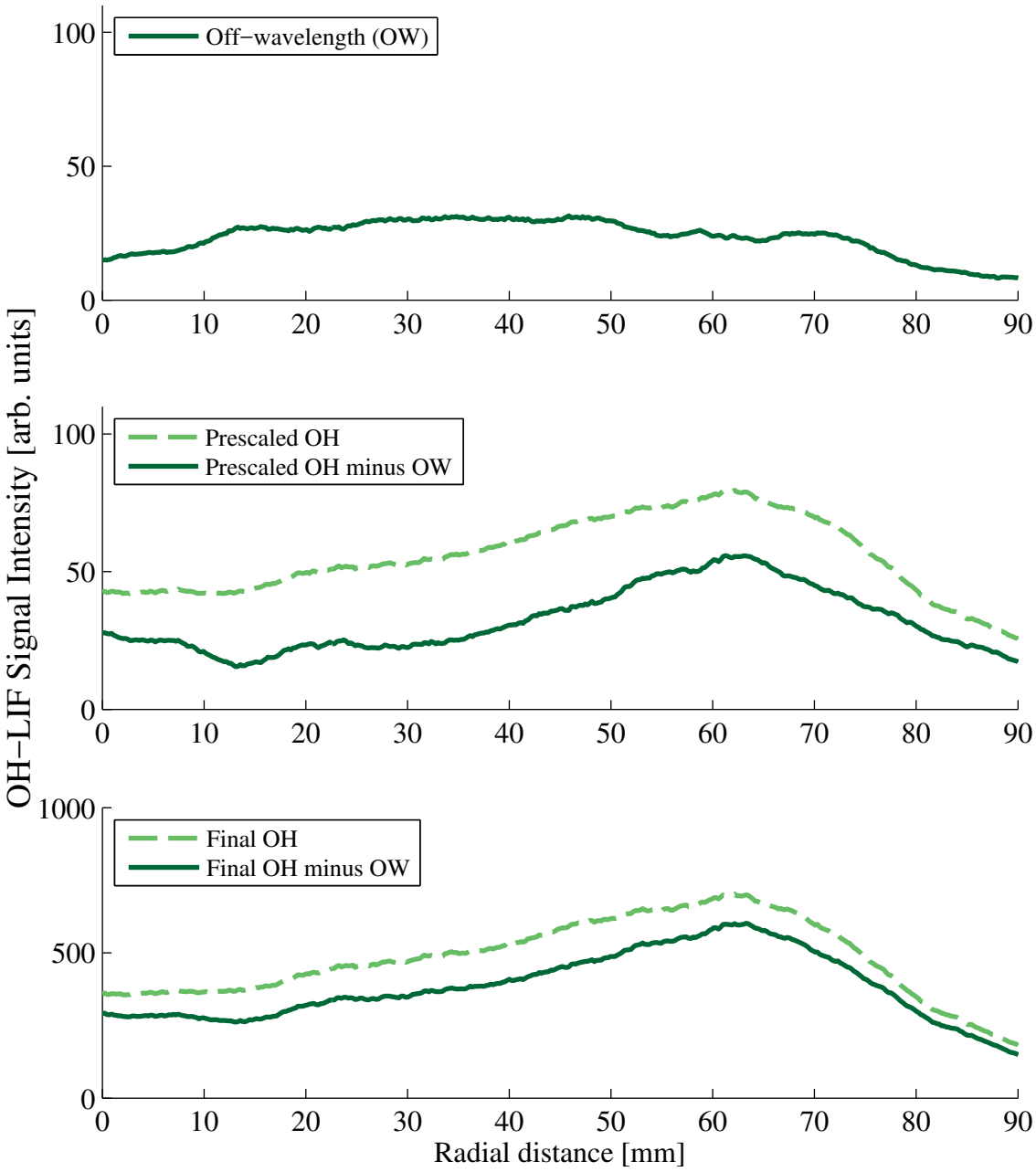

Figure C.17: OH-LIF results for the 30ANG halo at 42.5 L/min measured 25 mm above the burner.

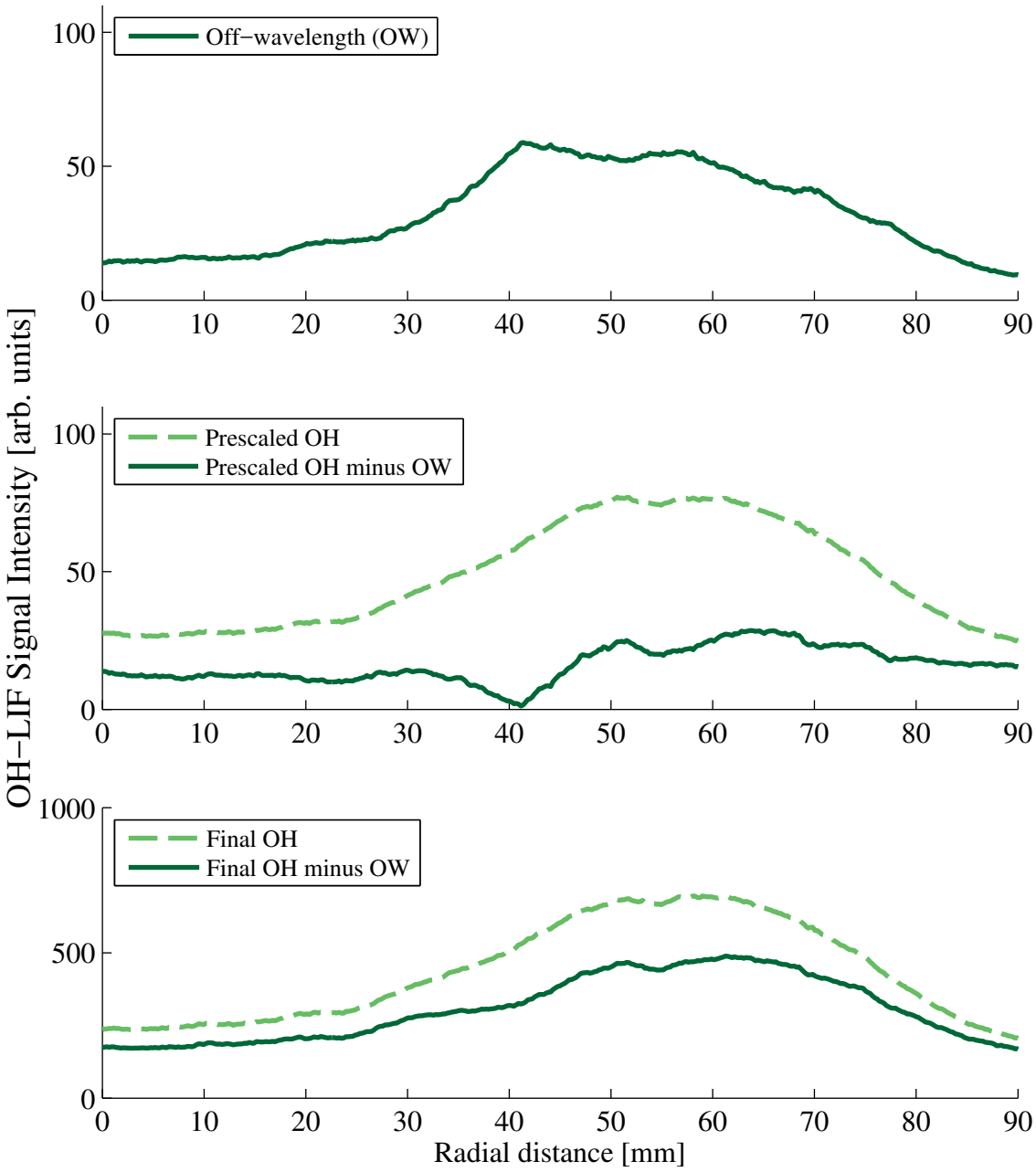

Figure C.18: OH-LIF results for the 30ANG halo at 42.5 L/min measured 40 mm above the burner.

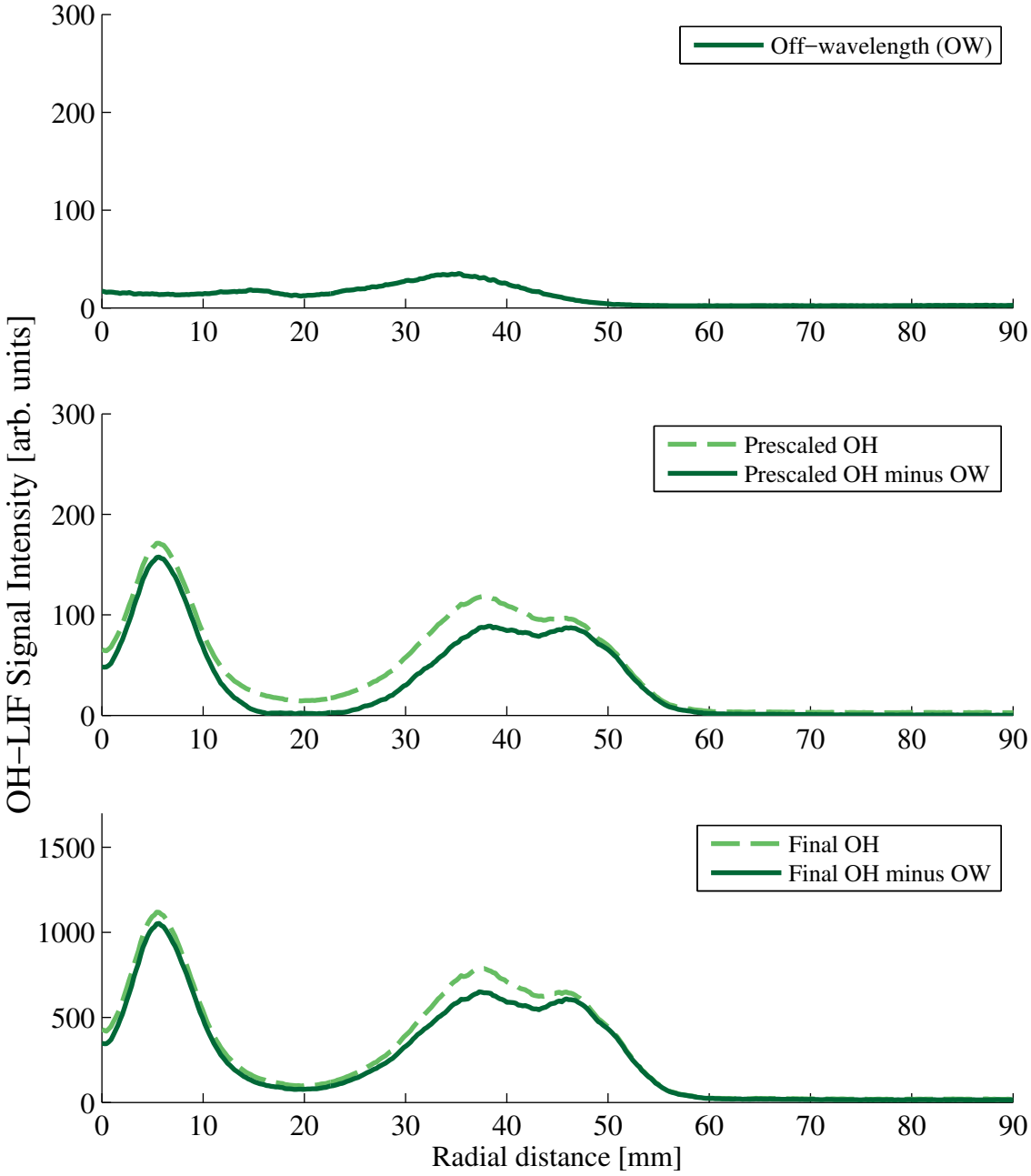

Figure C.19: OH-LIF results for the 30SWL halo at 28.3 L/min measured 10 mm above the burner.

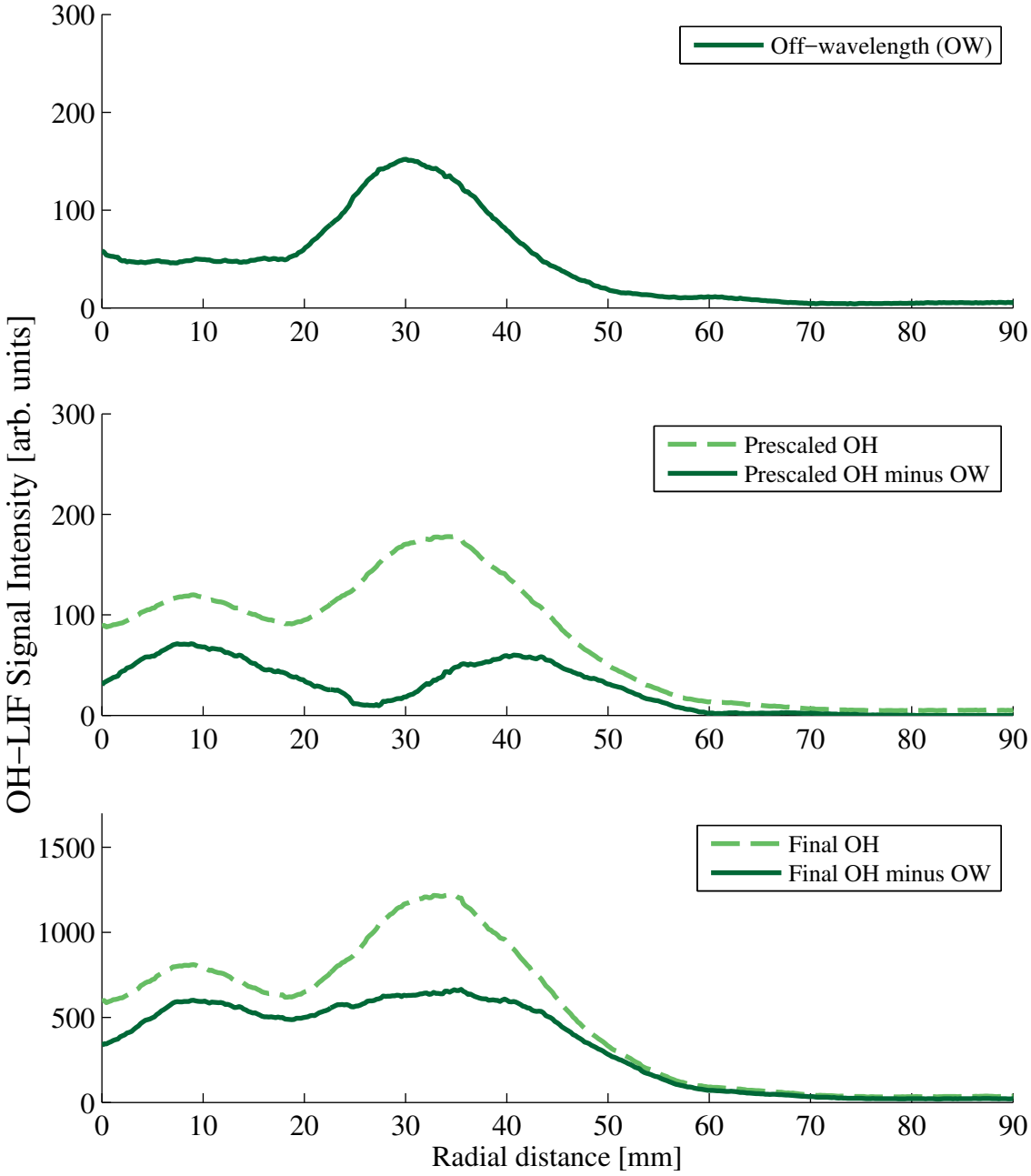

Figure C.20: OH-LIF results for the 30SWL halo at 28.3 L/min measured 25 mm above the burner.

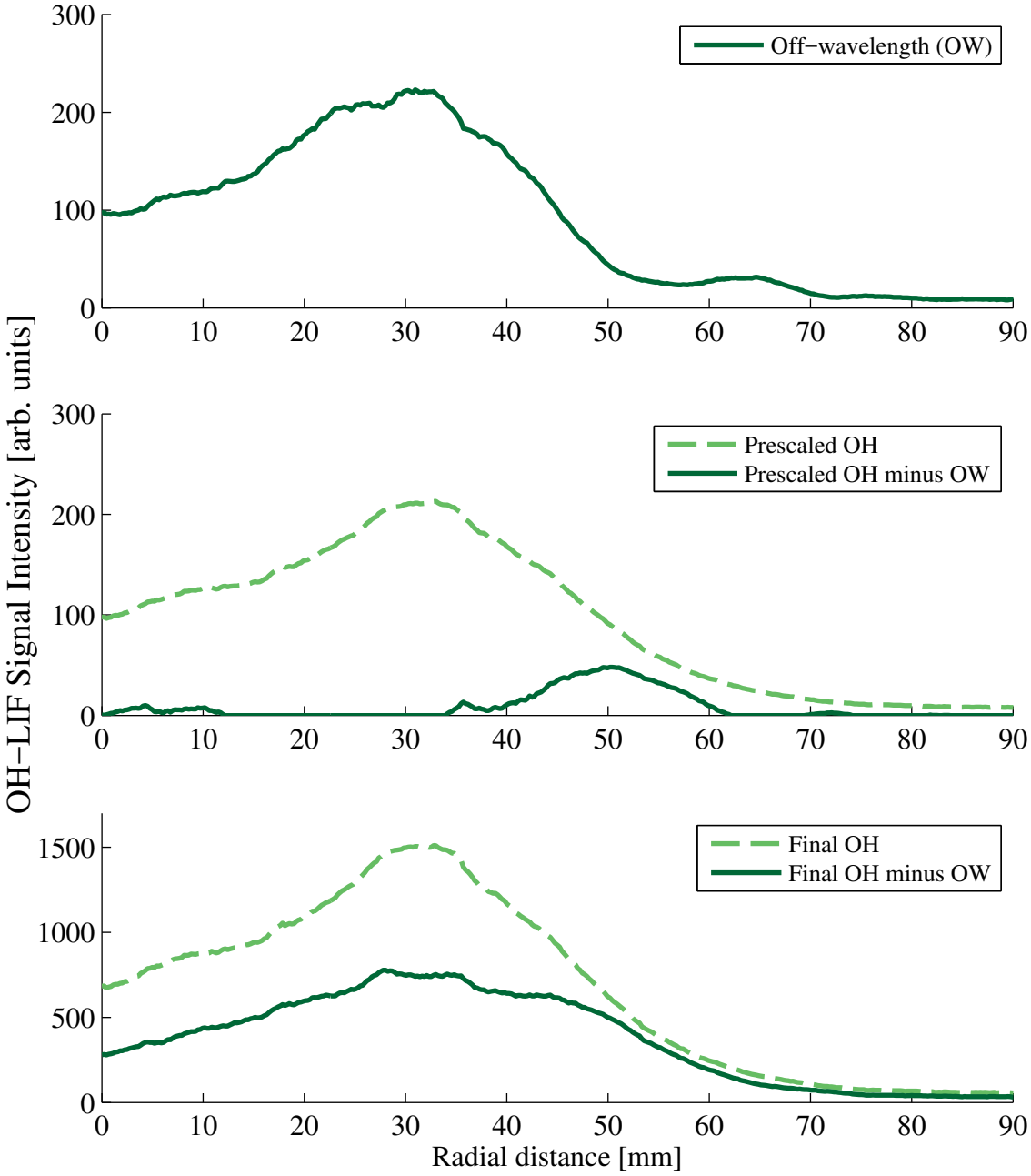

Figure C.21: OH-LIF results for the 30SWL halo at 28.3 L/min measured 40 mm above the burner.

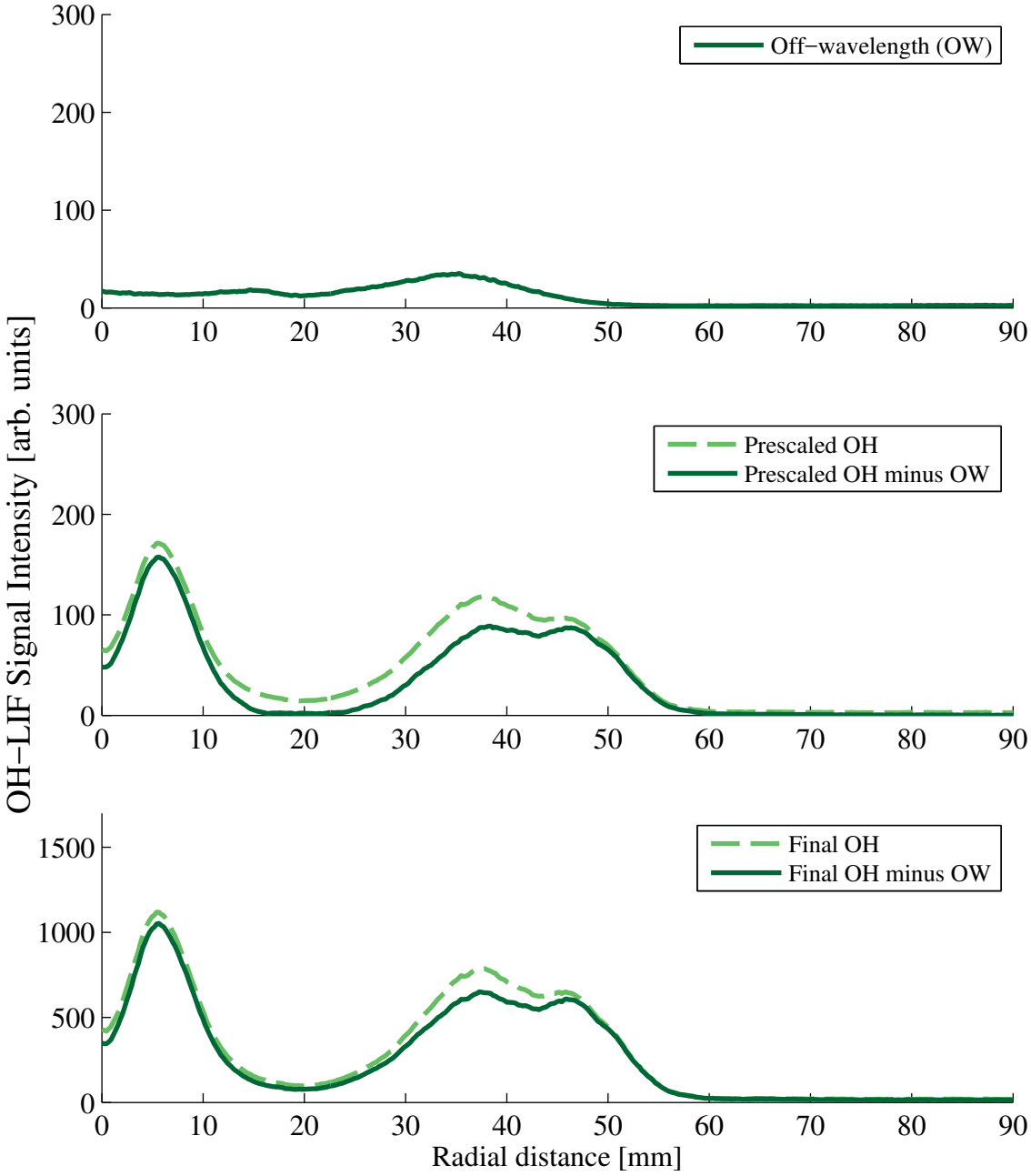

Figure C.22: OH-LIF results for the 30SWL halo at 35.4 L/min measured 10 mm above the burner.

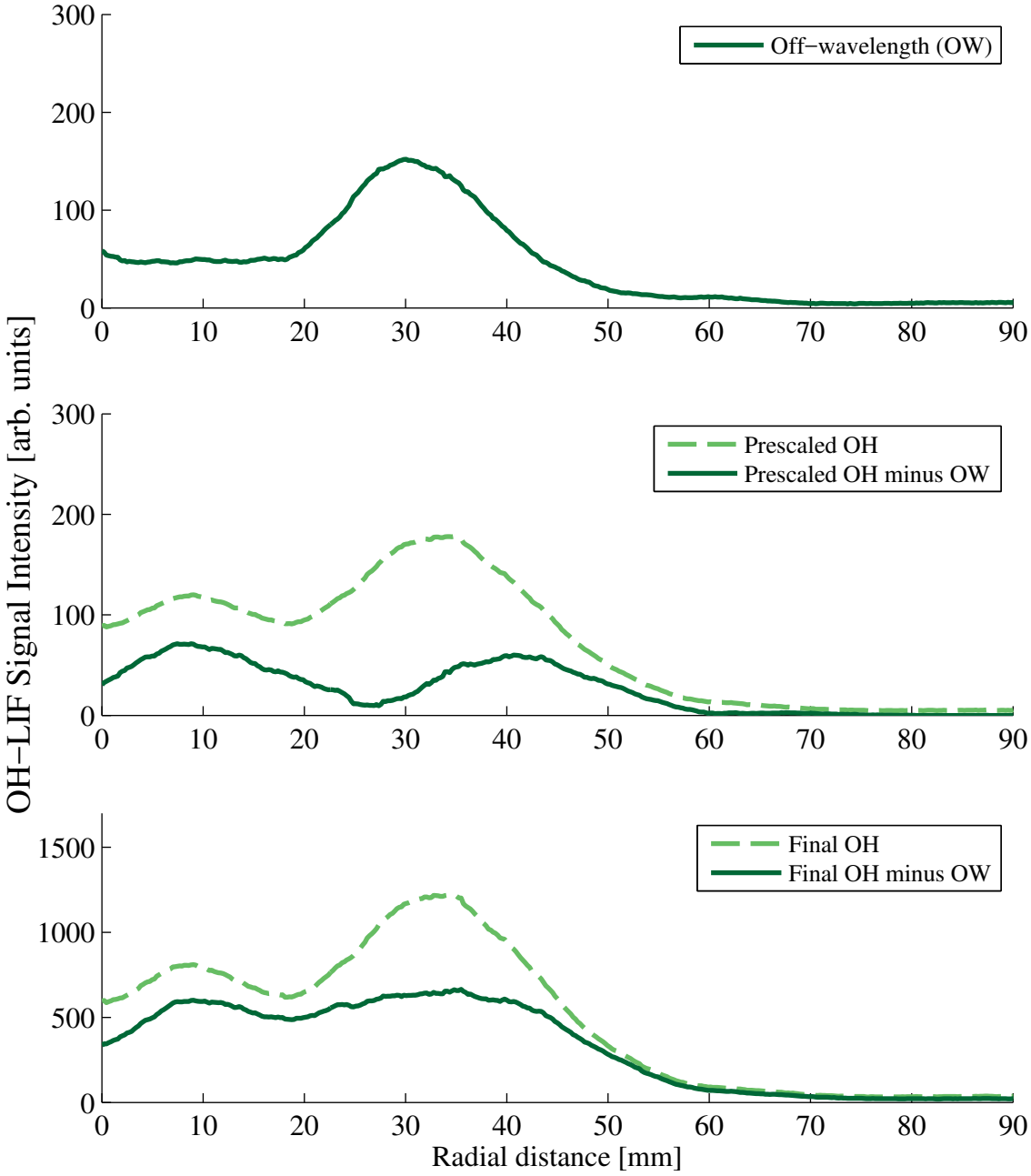

Figure C.23: OH-LIF results for the 30SWL halo at 35.4 L/min measured 25 mm above the burner.

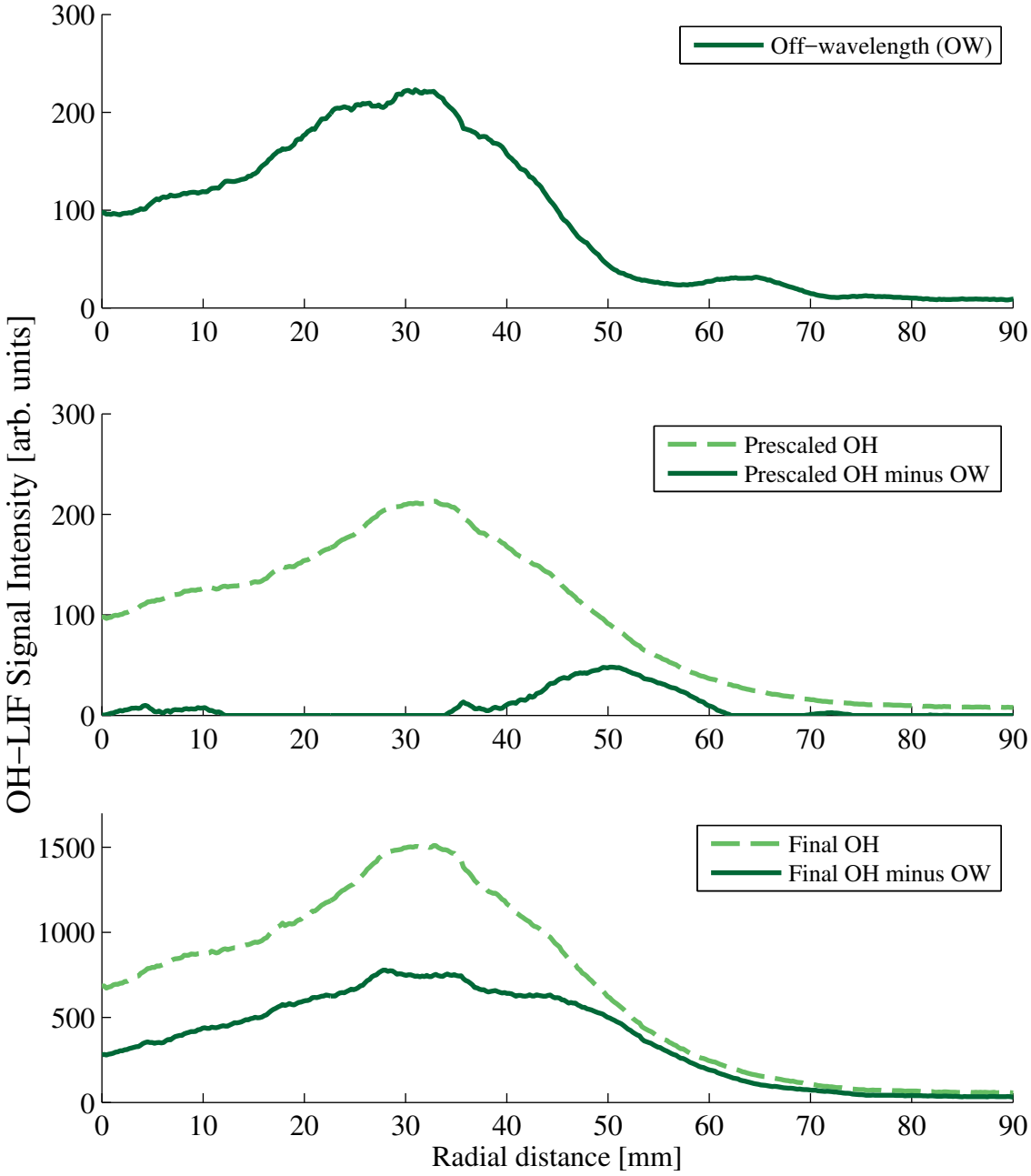

Figure C.24: OH-LIF results for the 30SWL halo at 35.4 L/min measured 40 mm above the burner.

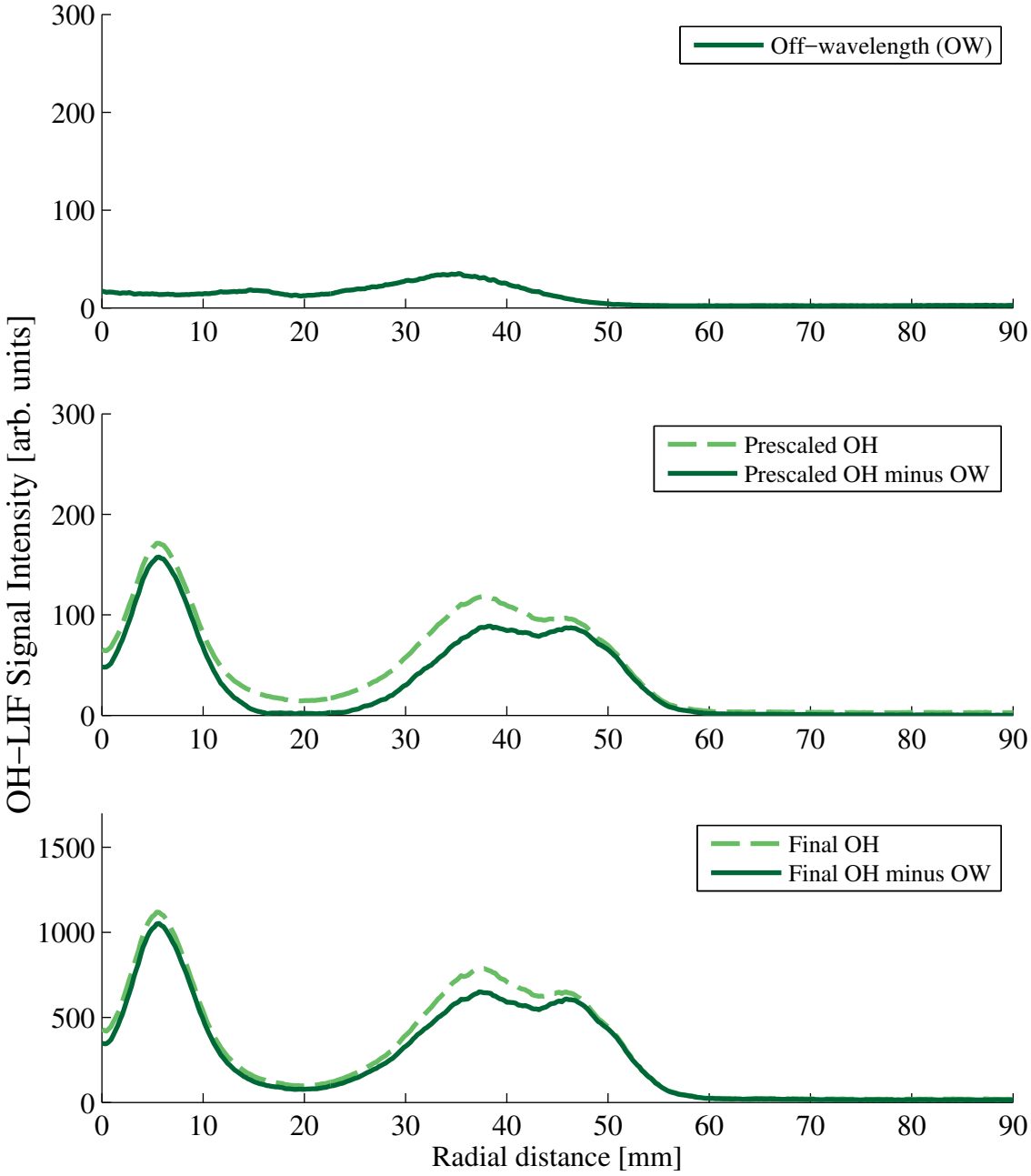

Figure C.25: OH-LIF results for the 30SWL halo at 42.5 L/min measured 10 mm above the burner.

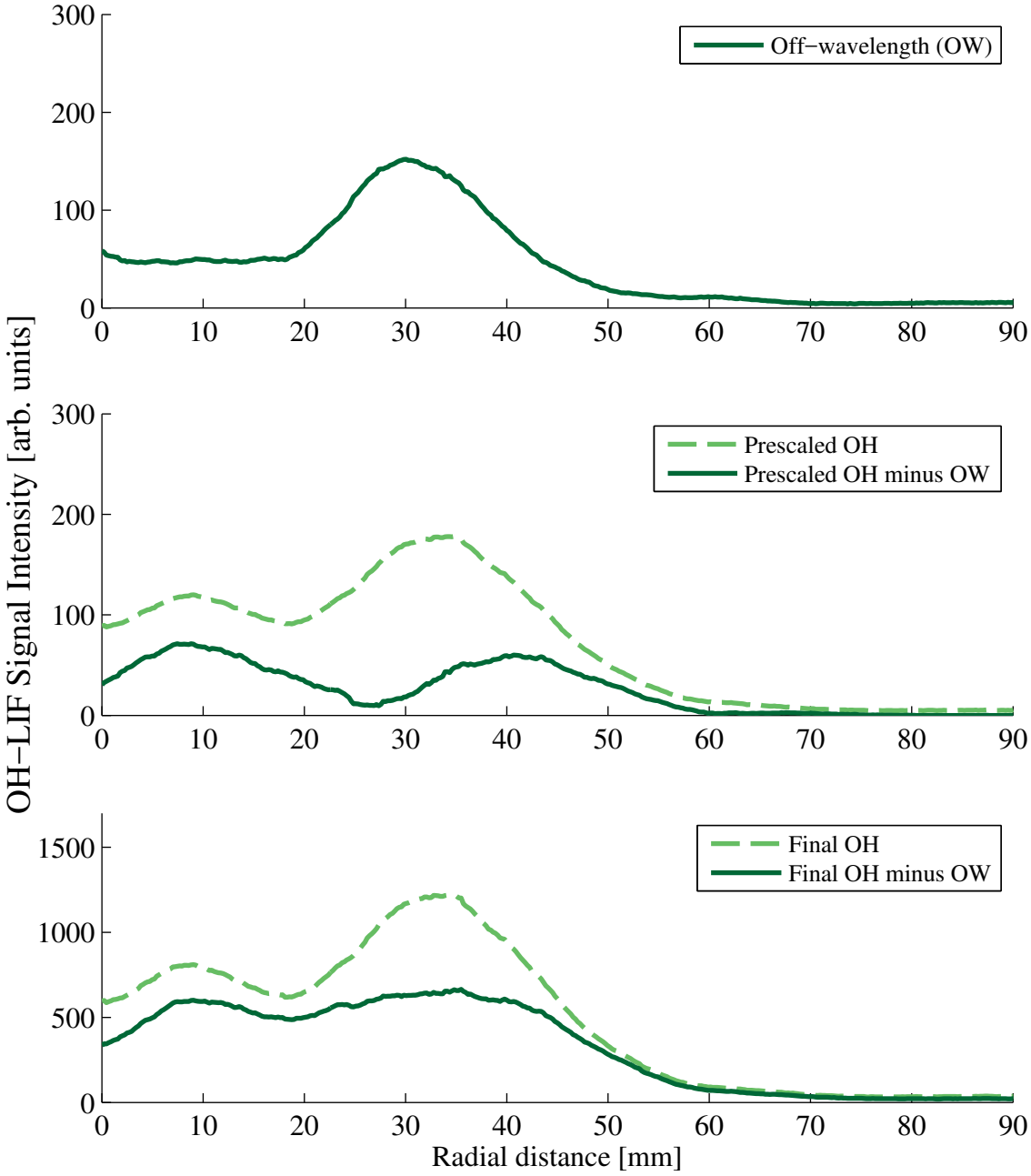

Figure C.26: OH-LIF results for the 30SWL halo at 42.5 L/min measured 25 mm above the burner.

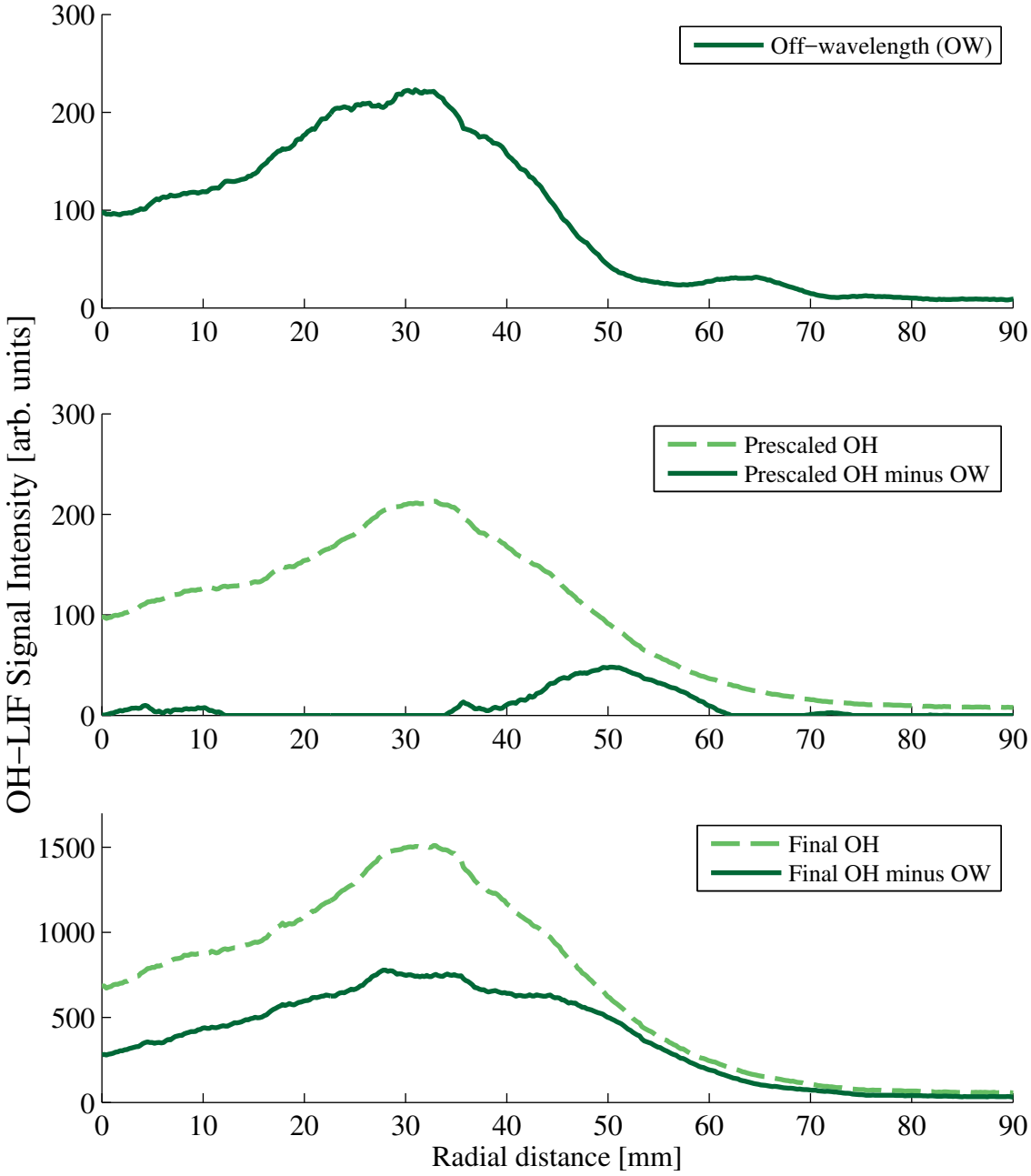

Figure C.27: OH-LIF results for the 30SWL halo at 42.5 L/min measured 40 mm above the burner.

D Peak LII signal: Average and standard deviation

The average and standard deviation of the peak LII signal intensity for all cases, as discussed in the soot intermittency portion of Section 9.3.2. The standard deviation may be used to infer information about the soot intermittency of the flame. The peak signal intensity for each test was found from the top 1000 intensities. The peak intensities from all tests for each case were then averaged, and the averages and standard deviations are reported here.

Table D.1: The averages and standard deviations of the peak LII signal intensities for all cases. Note, HAB = Height above burner; A0 = No air; A1 = 28.3 L/min; A2 = 35.4 L/min; A3 = 42.5 L/min.

Halo	*Air*	*HAB*	*Average Signal [arb. units]*	*Standard Deviation*
Baseline	A0	10 mm	762.2	262.3
		25 mm	1458.8	231.7
		40 mm	1838.8	330.4
90STR	A1	10 mm	779.9	300.4
		25 mm	1210.0	273.5
		40 mm	1487.7	437.4
	A2	10 mm	794.0	256.9
		25 mm	1239.5	263.2
		40 mm	1517.0	480.3
	A3	10 mm	842.7	305.3
		25 mm	1213.2	323.1
		40 mm	1464.9	485.2
30ANG	A1	10 mm	806.5	289.8
		25 mm	1239.5	313.0
		40 mm	1491.4	470.4
	A2	10 mm	788.3	269.4
		25 mm	1179.4	323.7
		40 mm	1459.4	469.1
	A3	10 mm	789.9	294.2
		25 mm	1169.4	326.6
		40 mm	1412.8	493.3
30SWL	A1	10 mm	770.4	301.3
		25 mm	1237.2	312.1
		40 mm	1584.5	474.6
	A2	10 mm	795.5	286.5
		25 mm	1265.8	332.7
		40 mm	1546.2	464.5
	A3	10 mm	820.3	285.9
		25 mm	1257.1	307.9
		40 mm	1512.7	466.6

Bibliography

Laser-Induced Incandescence. *Special Issue of Applied Physics B*, 119(4), 2015.

S. D. Adar, P. A. Filigrana, N. Clements, and J. L. Peel. Ambient Coarse Particulate Matter and Human Health: A Systematic Review and Meta-Analysis. *Current Environmental Health Reports: Air Pollution and Health*, 1:258–274, 2014.

R. J. Adrian. Bibliography of particle image velocimetry using imaging methods: 1917-1995. *TAM Report 817, University of Illinois at Urbana-Champaign*, (UILU-ENG-96-6004), 1996.

R. J. Adrian. Twenty years of particle image velocimetry. *Experiments in Fluids*, 39:159–169, 2005.

P. Alma. *Environmental Concerns*. Cambridge University Press, Cambridge, 1993.

S. Amrose, G. T. Kisch, C. Kirubi, J. Woo, and A. J. Gadgil. Development and Testing of the Berkeley Darfur Stove. Technical report, Lawrence Berkeley National Laboratory, 2008. URL http://cookstoves.lbl.gov/darfur-archives/pdf/dsp2008.pdf.

J. O. Anderson, J. G. Thundiyil, and A. Stolbach. Clearing the Air: A Review of the Effects of Particulate Matter Air Pollution on Human Health. *Journal of Medical Toxicology*, 8: 166–175, 2012.

M. O. Andreae and P. Merlet. Emission of trace gases and aerosols from biomass burning. *Global Biogeochemical Cycles*, 15:955–966, 2001.

R. E. Arku, J. Vallarino, K. L. Dionisio, R. Willis, H. Choi, J. G. Wilson, C. Hemphill, S. Agyei-Mensah, J. D. Spengler, and M. Ezzati. Characterizing air pollution in two low-income neighborhoods in Accra, Ghana. *Science of the Total Environment*, 402:217–231, 2008.

ASHRAE. Thermal Properties of Foods. In *2014 ASHRAE Handbook - Refrigeration (SI Edition)*, chapter 19, page 19.2. American Society of Heating Refrigerating and Air-Conditioning Engineers Inc, 2014.

ASTM International. Standard test methods for direct moisture content measurement of wood and wood-base materials. 2007.

M. Auffan, J. Rose, J.-Y. Bottero, G. V. Lowry, J.-P. Jolivet, and M. R. Wiesner. Towards a definition of inorganic nanoparticles from an environmental, health, and safety perspective. *Nature nanotechnology*, 4:634–41, 2009.

B. Axelsson, R. Collin, and P. E. Bengtsson. Laser-induced incandescence for soot particle size measurements in premixed flat flames. *Applied Optics*, 39(21):3683–3690, 2000.

B. Axelsson, R. Collin, and P. E. Bengtsson. Laser-induced incandescence for soot particle size and volume fraction measurements using on-line extinction calibration. *Applied Physics B*, 72:367–372, 2001.

R. Bailis, M. Ezzati, and D. M. Kammen. Greenhouse gas implications of household energy technology in Kenya. *Environmental Science & Technology*, 37:2051–2059, 2003.

R. Bailis, D. Ogle, N. MacCarty, and D. Still. The Water Boiling Test (WBT). Technical report, Household Energy and Health Programme Shell Foundation, 2007.

M. Bajus. Pyrolysis of Woody Material. *Petroleum & Coal*, 52(3):207–214, 2010.

G. A. Ban-Weiss, L. Cao, G. Bala, and K. Caldeira. Dependence of climate forcing and response on the altitude of black carbon aerosols. *Climate Dynamics*, 38:897–911, 2012.

P. A. Beauchemin and M. Tampier. Emissions from wood-fired combustion equipment. Technical report, British Columbia Ministry of Environment, 2008.

D. Belcher. Carbon Monoxide. In M. Lackner, F. Winter, and A. K. Agarwal, editors, *Handbook of Combustion, Vol. 2: Combustion Diagnostics and Pollutants*, chapter 13, pages 357–374. Wiley-VCH, 2010.

S. Bentson, D. Still, R. Thompson, and K. Grabow. The influence of initial fuel load on fuel to cook for batch loaded charcoal cookstoves. *Energy for Sustainable Development*, 17: 153–157, 2013.

M. H. Bergin, G. R. Cass, J. Xu, C. Fang, L. M. Zeng, T. Yu, L. G. Salmon, C. S. Kiang, X. Y. Tang, Y. H. Zhang, and W. L. Chameides. Aerosol radiative, physical, and chemical properties in Beijing during June 1999. *Journal of Geophysical Research: Atmospheres*, 106(D16):17969–17980, 2001. URL http://onlinelibrary.wiley.com/doi/10.1029/2001JD900073/full{\#}article-nav.

S. C. Bhattacharya, D. O. Albina, and P. Abdul Salam. Emission factors of wood and charcoal-fired cookstoves. *Biomass and Bioenergy*, 23:453–469, 2002a.

S. C. Bhattacharya, D. O. Albina, and A. M. Khaing. Effects of selected parameters on performance and emission of biomass-fired cookstoves. *Biomass and Bioenergy*, 23:387–395, 2002b.

H. Bladh. *On the Use of Laser-Induced Incandescence for Soot Diagnostics: From Theoretical Aspects to Applications in Engines*. Doctoral dissertation, Lund University, 2007.

H. Bockhorn, editor. *Soot Formation in Combustion: Mechanisms and models*. Springer-Verlag, Berlin Heidelberg, 1 edition, 1994.

M. Bolhàr-Nordenkampf. Staged Combustion and Exhaust Gas Recirculation in Fluidized Beds. In M. Lackner, F. Winter, and A. K. Agarwal, editors, *Handbook of Combustion, Vol. 5: New Technologies*, chapter 7, pages 161–179. Wiley-VCH, 2010.

T. C. Bond, D. G. Streets, K. F. Yarber, S. M. Nelson, J.-H. Woo, and Z. Klimont. A technology-based global inventory of black and organic carbon emissions from combustion. *Journal of Geophysical Research*, 109:D14203, 2004a.

T. C. Bond, C. Venkataraman, and O. R. Masera. Global atmospheric impacts of residential fuels. *Energy for Sustainable Development*, 8:20–32, 2004b.

T. C. Bond, S. J. Doherty, D. W. Fahey, P. M. Forster, T. Berntsen, B. J. DeAngelo, M. G. Flanner, S. Ghan, B. Kärcher, D. Koch, S. Kinne, Y. Kondo, P. K. Quinn, M. C. Sarofim, M. G. Schultz, M. Schulz, C. Venkataraman, H. Zhang, S. Zhang, N. Bellouin, S. K. Guttikunda, P. K. Hopke, M. Z. Jacobson, J. W. Kaiser, Z. Klimont, U. Lohmann, J. P. Schwarz, D. Shindell, T. Storelvmo, S. G. Warren, and C. S. Zender. Bounding the role of black carbon in the climate system: A scientific assessment. *Journal of Geophysical Research: Atmospheres*, 118:5380–5552, 2013.

S. Bonjour, H. Adair-Rohani, J. Wolf, N. G. Bruce, S. Mehta, A. Pruss-Ustun, M. Lahiff, E. A. Rehfuess, V. Mishra, and K. R. Smith. Solid fuel use for household cooking: Country and regional estimates for 1980-2010. *Environmental Health Perspectives*, 121(7):784–790, 2013.

K. Booker, R. Cheng, and S. Sadlon. Haiti Trip Report. Technical report, Lawrence Berkeley National Laboratory, 2010.

T. G. Bridgeman, J. M. Jones, and A. Williams. Overview of Solid Fuels, Characteristics and Origin. In M. Lackner, F. Winter, and A. K. Agarwal, editors, *Handbook of Combustion, Vol. 4: Solid Fuels*, chapter 1, pages 1–30. Wiley-VCH, 2010.

R. D. Brook, S. Rajagopalan, C. A. Pope III, J. R. Brook, A. Bhatnagar, A. V. Diez-Roux, F. Holguin, Y. Hong, R. V. Luepker, M. A. Mittleman, A. Peters, D. Siscovick, S. C. Smith, L. Whitsel, and J. D. Kaufman. Particulate Matter Air Pollution and Cardiovascular Disease: An Update to the Scientific Statement From the American Heart Association. *Circulation*, 121:2331–2378, 2010.

M. Bryden, D. Still, P. Scott, G. Hoffa, D. Ogle, R. Bailis, and K. Goyer. Design Principles for Wood Burning Cook Stoves. Technical report, Aprovecho Research Center, Shell Foundation, Partnership for Clean Indoor Air, 2006. URL http://www.pciaonline.org/design-principles.

A. Burluka. Combustion Physics. In M. Lackner, F. Winter, and A. K. Agarwal, editors, *Handbook of Combustion, Vol 1: Fundamentals and Safety*, chapter 3, pages 53–83. Wiley-VCH, 2010.

W. L. Chameides, H. Yu, S. C. Liu, M. Bergin, X. Zhou, L. Mearns, G. Wang, C. S. Kiang, R. D. Saylor, C. Luo, Y. Huang, A. Steiner, and F. Giorgi. Case study of the effects of atmospheric aerosols and regional haze on agriculture: an opportunity to enhance crop yields in China through emission controls? *Proceedings of the National Academy of Sciences of the United States of America*, 96(24):13626–13633, 1999.

D. Champier, J. P. Bedecarrats, M. Rivaletto, and F. Strub. Thermoelectric power generation from biomass cook stoves. *Energy*, 35:935–942, 2010.

D. Champier, J. P. Bédécarrats, T. Kousksou, M. Rivaletto, F. Strub, and P. Pignolet. Study of a TE (thermoelectric) generator incorporated in a multifunction wood stove. *Energy*, 36:1518–1526, 2011.

R. Chen, B. Hu, Y. Liu, J. Xu, G. Yang, D. Xu, and C. Chen. Beyond PM2.5: The role of ultrafine particles on adverse health effects of air pollution. *Biochimica et Biophysica Acta*, 1860:2844–2855, 2016.

Y. Chen and T. C. Bond. Light absorption by organic carbon from wood combustion. *Atmospheric Chemistry and Physics*, 10:1773–1787, 2010.

E. N. Chidumayo and D. J. Gumbo. The environmental impacts of charcoal production in tropical ecosystems of the world: A synthesis. *Energy for Sustainable Development*, 17(2): 86–94, 2013.

M. Y. Choi, G. W. Mulholland, A. Hamins, and T. Kashiwagi. Comparisons of the soot volume fraction using gravimetric and light extinction techniques. *Combustion and Flame*, 102:161–169, 1995.

Z. Chowdhury, L. Thi Le, A. Al Masud, K. C. Chang, M. Alauddin, M. Hossain, A. B. M. Zakaria, and P. K. Hopke. Quantification of indoor air pollution from using cookstoves and estimation of its health effects on adult women in northwest Bangladesh. *Aerosol and Air Quality Research*, 12:463–475, 2012.

S. A. Ciatti. Light Emission from Flames. In M. Lackner, F. Winter, and A. K. Agarwal, editors, *Handbook of Combustion, Vol 1: Fundamentals and Safety*, chapter 11, pages 251–264. Wiley-VCH, 2010.

J. W. Daily. Laser induced fluorescence spectroscopy in flames. *Progress in Energy and Combustion Science*, 23(2):133–199, 1997.

J. S. Daniel and S. Solomon. On the climate forcing of carbon monoxide. *Journal of Geophysical Research*, 103(D11):13249–13260, 1998.

P. Desgroux. Laser-Induced Incandescence. *Special Issue of Applied Physics B*, 112(3), 2013.

C. Di Blasi, G. Signorelli, C. Di Russo, and G. Rea. Product Distribution from Pyrolysis of Wood and Agricultural Residues. *Industrial & Engineering Chemistry Research*, 38: 2216–2224, 1999.

K. Donaldson and W. MacNee. The Mechanism of Lung Injury Caused by PM10. *Environmental Science & Technology*, (10):21–32, 1998.

K. Donaldson, D. Brown, A. Clouter, R. Duffin, W. MacNee, L. Renwick, L. Tran, and V. Stone. The Pulmonary Toxicology of Ultrafine Particles. *Journal of Aerosol Medicine*, 15(2):213–220, 2002.

G. S. Dutt and N. H. Ravindranath. Alternative bioenergy strategies for cooking. In T. B. Johansson, H. Kelly, A. K. N. Reddy, and R. H. Williams, editors, *Renewable energy: sources for fuels and electricity*, pages 653–697. Island Press, Washington, DC, 1993.

N. Englert. Fine particles and human health - A review of epidemiological studies. *Toxicology Letters*, 149:235–242, 2004.

R. J. Evans and T. a. Milne. Molecular characterization of pyrolysis of biomass. 1. Fundamentals. *Energy & Fuels*, 1(2):123–138, 1987.

L. Fagbemi, L. Khezami, and R. Capart. Pyrolysis products from different biomasses: application to the thermal cracking of tar. *Applied Energy*, 69:293–306, 2001.

R. C. Flagan and J. H. Seinfeld. *Fundamentals of Air Pollution Engineering*. Prentice-Hall, Inc, 1988.

C. Galitsky, A. J. Gadgil, M. Jacobs, and Y.-M. Lee. Fuel efficient stoves for Darfur camps of internally displaced persons: Report of field trip to North and South Darfur, Nov. 16 - Dec. 17, 2005. Technical report, Lawrence Berkeley National Laboratory, LBNL-59540, 2006.

H. B. Gao, G. H. Huang, H. J. Li, Z. G. Qu, and Y. J. Zhang. Development of stove-powered thermoelectric generators: A review. *Applied Thermal Engineering*, 96:297–310, 2016.

A. Garo, G. Prado, and J. Lahaye. Chemical Aspects of Soot Particles Oxidation in a Laminar Methane - Air Diffusion Flame. *Combustion and Flame*, 79(3-4):226–233, 1990.

M. Glass and I. M. Kennedy. An improved seeding method for high temperature laser doppler velocimetry. *Combustion and Flame*, 29:333–335, 1977.

S. V. Glinianaia, J. Rankin, R. Bell, T. Pless-Mulloli, and D. Howel. Particulate Air Pollution and Fetal Health: A systematic review of the epidemiologic evidence. *Epidemiology*, 15 (1):36–45, 2004.

Global Alliance for Clean Cookstoves. The Water Boiling Test v4.2.3. Technical report, Global Alliance for Clean Cookstoves, 2013.

Global Alliance for Clean Cookstoves. Gender-Based Violence in Humanitarian Settings: Cookstoves and Fuels. Technical Report August, Global Alliance for Clean Cookstoves, 2016. URL http://cleancookstoves.org/resources/478.html.

J. Gowlett. The discovery of fire by humans: a long and convoluted process. *Philosophical Transactions of the Royal Society of London, Series B*, 371, 2016.

I. Grant, editor. *Selected papers on particle image velocimetry*. SPIE Milestone Series, SPIE Optical Engineering Press, Bellingham, Washington, ms 99 edition, 1994.

Ö. Gustafsson, M. Kruså, Z. Zencak, R. J. Sheesley, L. Granat, E. Engström, P. S. Praveen, P. S. P. Rao, C. Leck, and H. Rodhe. Brown clouds over South Asia: biomass or fossil fuel combustion? *Science*, 323:495–498, 2009.

O. L. Hadley and T. W. Kirchstetter. Black-carbon reduction of snow albedo. *Nature Climate Change*, 2:437–440, 2012.

J. L. Hand and S. M. Kreidenweis. A new method for retrieving particle refractive index and effective density from aerosol size distribution data. *Aerosol Science and Technology*, 36(10):1012–1026, 2002.

A. D. A. Hansen. The Aethalometer. Technical report, McGee Scientific Company, 2005.

A. D. A. Hansen, H. Rosen, and T. Novakov. The Aetholometer - An instrument for the real-time measurement of optical absorption by aerosol particles. *The Science of the Total Environment*, 36:191–196, 1984.

J. Hansen and L. Nazarenko. Soot climate forcing via snow and ice albedos. *Proceedings of the National Academy of Sciences of the United States of America*, 101(2):423–428, 2004.

G. Hartung, J. Hult, and C. F. Kaminski. A flat flame burner for the calibration of laser thermometry techniques. *Measurement Science and Technology*, 17:2485–2493, 2006.

M. D. Hays, P. M. Fine, C. D. Geron, M. J. Kleeman, and B. K. Gullett. Open burning of agricultural biomass: Physical and chemical properties of particle-phase emissions. *Atmospheric Environment*, 39(36):6747–6764, 2005.

E. J. Highwood and R. P. Kinnersley. When smoke gets in our eyes: The multiple impacts of atmospheric black carbon on climate, air quality and health. *Environment International*, 32(4):560–566, 2006.

R. Hosier. Charcoal production and environmental degradation. *Energy Policy*, 21:491–509, 1993.

S. Hosseini, Q. Li, D. Cocker, D. Weise, A. Miller, M. Shrivastava, J. W. Miller, S. Mahalingam, M. Princevac, and H. Jung. Particle size distributions from laboratory-scale biomass fires using fast response instruments. *Atmospheric Chemistry and Physics*, 10(16):8065–8076, 2010.

A. M. Hubbell, F. J. Jareczek, L. Vonnahme, J. M. Hockenberry, and C. Buresh. Smoke exposure among women in Haiti: The case for improved stoves. *Global Public Health*, 8 (7):822–830, 2013.

International Energy Agency. World Energy Outlook 2004. Technical report, International Energy Agency, 2004.

International Energy Agency. World Energy Outlook 2012. Technical report, International Energy Agency, 2012.

International Energy Agency. World Energy Outlook - Special Report: Energy and Air Pollution. Technical report, International Energy Agency, 2016. URL http://www.iea.org/publications/freepublications/publication/WorldEnergyOutlookSpecialReport2016EnergyandAirPollution.pdf.

M. Z. Jacobson. Strong radiative heating due to the mixing state of black carbon in atmospheric aerosols. *Nature*, 409:695–697, 2001.

M. Janbozorgi, K. E. Far, and H. Metghalchi. Combustion Fundamentals. In M. Lackner, F. Winter, and A. K. Agarwal, editors, *Handbook of Combustion, Vol 1: Fundamentals and Safety*, chapter 1, pages 1–26. Wiley-VCH, 2010. ISBN 9783527324491.

J. Jetter and P. Kariher. Solid-fuel household cook stoves: Characterization of performance and emissions. *Biomass and Bioenergy*, 33:294–305, 2009.

J. Jetter, Y. Zhao, K. R. Smith, B. Khan, T. Yelverton, P. Decarlo, and M. D. Hays. Pollutant emissions and energy efficiency under controlled conditions for household biomass cookstoves and implications for metrics useful in setting international test standards. *Environmental Science and Technology*, 46:10827–10834, 2012.

M. Johnson, R. Edwards, C. Alatorre Frenk, and O. R. Masera. In-field greenhouse gas emissions from cookstoves in rural Mexican households. *Atmospheric Environment*, 42: 1206–1222, 2008.

J. M. Jones, A. R. Lea-Langton, L. Ma, M. Pourkashanian, and A. Williams. *Pollutants Generated by the Combustion of Solid Biomass Fuels*. Springer, 2014.

B. Just, S. Rogak, and M. Kandlikar. Characterization of ultrafine particulate matter from traditional and improved biomass cookstoves. *Environmental Science and Technology*, 47: 3506–3512, 2013.

S. P. Kalathoor. Solid particle seeding using cyclone gas flow for optical flow visualization: Design parameters to be considered. *Advances in Aerospace Science and Applications*, 3 (2):57–64, 2013.

A. Kar, I. H. Rehman, J. Burney, S. P. Puppala, R. Suresh, L. Singh, V. K. Singh, T. Ahmed, N. Ramanathan, and V. Ramanathan. Real-time assessment of black carbon pollution in Indian households due to traditional and improved biomass cookstoves. *Environmental Science and Technology*, 46(5):2993–3000, 2012.

E. L. Keating. Solid Fuels. In *Applied Combustion*, chapter 6, pages 203–250. CRC Press, Boca Raton, Florida, 2 edition, 2007.

T. Kirchstetter, C. Preble, O. L. Hadley, and A. J. Gadgil. Quantification of black carbon and other pollutant emissions from a traditional and an improved cookstove. Technical report, Lawrence Berkeley National Laboratory, LBNL-6062E, 2010.

T. W. Kirchstetter and T. Novakov. Controlled generation of black carbon particles from a diffusion flame and applications in evaluating black carbon measurement methods. *Atmospheric Environment*, 41:1874–1888, 2007.

K. Kohse-Höinghaus. Laser techniques for the quantitative detection of reactive intermediates in combustion systems. *Progress in Energy and Combustion Science*, 20 (3):203–279, 1994.

R. Koppmann, K. von Czapiewski, and J. S. Reid. A review of biomass burning emissions, part I: gaseous emissions of carbon monoxide, methane, volatile organic compounds, and nitrogen containing compounds. *Atmospheric Chemistry and Physics Discussions*, 5:10455–10516, 2005.

M. P. Kshirsagar and V. R. Kalamkar. A comprehensive review on biomass cookstoves and a systematic approach for modern cookstove design. *Renewable and Sustainable Energy Reviews*, 30:580–603, 2014.

M. Kumar, S. Kumar, and S. K. Tyagi. Design, development and technological advancement in the biomass cookstoves: A review. *Renewable and Sustainable Energy Reviews*, 26:265–285, 2013.

M. Lackner, A. B. Palotas, and F. Winter. *Combustion: From Basics to Applications*. Wiley-VCH, Weinheim, 2013.

K. Lask and A. Gadgil. Simplified Model for Lighting Cone Design. Technical report, Lawrence Berkeley National Lab, 2015.

A. Leavey, J. Londeree, P. Priyadarshini, J. Puppala, K. B. Schechtman, G. Yadama, and P. Biswas. Real-time particulate and CO concentrations from cookstoves in rural households in Udaipur, India. *Environmental Science & Technology*, 49:7423–7431, 2015.

A. Leipertz and J. Kiefer. Soot and Soot Diagnostics by Laser-Induced Incandescence. In M. Lackner, F. Winter, and A. K. Agarwal, editors, *Handbook of Combustion, Vol. 2: Combustion Diagnostics and Pollutants*, chapter 15, pages 403–423. Wiley-VCH, 2010.

A. Leipertz, F. Ossler, and M. Aldén. Polycyclic Aromatic Hydrocarbons and Soot Diagnostics by Optical Techniques. In K. Kohse-Höinghaus and J. Jeffries, editors, *Applied Combustion Diagnostics*, chapter 13, pages 359–383. Taylor & Francis, New York, 2002.

A. Leipertz, A. Braeuer, J. Kiefer, A. Dreizler, and C. Heeger. Laser-Induced Fluorescence. In M. Lackner, F. Winter, and A. K. Agarwal, editors, *Handbook of Combustion, Vol. 2: Combustion Diagnostics and Pollutants*, chapter 8, pages 219–242. Wiley-VCH, 2010a.

A. Leipertz, S. Pfadler, and R. Schießl. An Overview of Combustion Diagnostics. In M. Lackner, F. Winter, and A. K. Agarwal, editors, *Handbook of Combustion, Vol. 2: Combustion Diagnostics and Pollutants*, chapter 1, pages 1–50. Wiley-VCH, 2010b.

C. Lertsatitthanakorn. Electrical performance analysis and economic evaluation of combined biomass cook stove thermoelectric (BITE) generator. *Bioresource Technology*, 98:1670–1674, 2007.

E. J. T. Levin, G. R. McMeeking, C. M. Carrico, L. E. Mack, S. M. Kreidenweis, C. E. Wold, H. Moosm??ller, W. P. Arnott, W. M. Hao, J. L. Collett, and W. C. Malm. Biomass burning smoke aerosol properties measured during Fire Laboratory at Missoula Experiments (FLAME). *Journal of Geophysical Research Atmospheres*, 115(18):1–15, 2010.

J. J. Lewis and S. K. Pattanayak. Who adopts improved fuels and cookstoves? A systematic review. *Environmental health perspectives*, 120:637–45, 2012.

X. Y. Li, P. S. Gilmour, K. Donaldson, and W. MacNee. Free radical activity and pro-inflammatory effects of particulate air pollution (PM10) in vivo and in vitro. *Thorax*, 51: 1216–1222, 1996.

S. S. Lim, T. Vos, A. D. Flaxman, G. Danaei, K. Shibuya, H. Adair-Rohani, M. A. AlMazroa, and E. al. A comparative risk assessment of burden of disease and injury attributable to 67 risk factors and risk factor clusters in 21 regions, 1990–2010: a systematic analysis for the Global Burden of Disease Study 2010. *The Lancet*, 380:2224–2260, 2012.

C. Liousse, J. E. Penner, C. Chuang, J. J. Walton, H. Eddleman, and H. Cachier. A global three-dimensional model study of carbonaceous aerosols. *Journal of Geophysical Research*, 101(D14):19411–19432, 1996.

J. M. Lobert and J. Warnatz. Emissions from the Combustion Process in Vegetation. In *Fire in the Environment: The Ecological, Atmospheric, and Climatic Importance of Vegetation Fires*, chapter 2, pages 15–37. John Wiley & Sons, Inc., New York, 1993.

N. MacCarty, D. Ogle, D. Still, T. C. Bond, and C. Roden. A laboratory comparison of the global warming impact of five major types of biomass cooking stoves. *Energy for Sustainable Development*, 12:56–65, 2008.

N. MacCarty, D. Still, and D. Ogle. Fuel use and emissions performance of fifty cooking stoves in the laboratory and related benchmarks of performance. *Energy for Sustainable Development*, 14:161–171, 2010.

W. MacNee and K. Donaldson. Mechanism of lung injury caused by PM10 and ultrafine particles with special reference to COPD. *European Respiratory Journal*, 21(Supplement 40):47s–51s, 2003.

R. Mal, R. Prasad, V. K. Vijay, and A. R. Verma. The design, development and performance evaluation of thermoelectric generator (TEG) integrated forced draft biomass cookstove. *Procedia Computer Science*, 52:723–729, 2015.

P. M. Mannucci, S. Harari, I. Martinelli, and M. Franchini. Effects on health of air pollution: a narrative review. *Internal and Emergency Medicine*, 10:657–662, 2015.

M. D. Masekameni, T. Makonese, and H. J. Annegarn. A comparison of emissions and thermal efficiency of three improved liquid fuel stoves. In *2015 International Conference on the Domestic Use of Energy (DUE)*, pages 71–76, Cape Town, 2015. IEEE Xplore.

S. McAllister, J.-Y. Chen, and A. C. Fernandez-Pello. Fuels. In F. F. Ling, editor, *Fundamentals of Combustion Processes*, chapter 1, pages 1–13. Springer, 2011a.

S. McAllister, J.-Y. Chen, and A. C. Fernandez-Pello. Chemical Kinetics. In F. F. Ling, editor, *Fundamentals of Combustion Processes*, chapter 3, pages 49–73. Springer, 2011b.

S. McAllister, J.-Y. Chen, and A. C. Fernandez-Pello. Premixed Flames. In F. F. Ling, editor, *Fundamentals of Combustion Processes*, chapter 6. Springer, 2011c.

S. McAllister, J.-Y. Chen, and A. C. Fernandez-Pello. Non-premixed Flames (Diffusion Flames). In F. F. Ling, editor, *Fundamentals of Combustion Processes*, chapter 7, pages 139–154. Springer, 2011d.

S. McAllister, J.-Y. Chen, and A. C. Fernandez-Pello. Emissions. In F. F. Ling, editor, *Fundamentals of Combustion Processes*, number 2, chapter 9. Springer, 2011e.

G. R. McMeeking, S. M. Kreidenweis, S. Baker, C. M. Carrico, J. C. Chow, J. L. Collett, W. M. Hao, A. S. Holden, T. W. Kirchstetter, W. C. Malm, H. Moosmüller, A. P. Sullivan, and W. Cyle E. Emissions of trace gases and aerosols during the open combustion of biomass in the laboratory. *Journal of Geophysical Research*, 114, 2009.

S. Menon, J. Hansen, L. Nazarenko, and Y. Luo. Climate effects of black carbon aerosols in China and India. *Science*, 297:2250–2253, 2002.

B. Merci, E. Mastorakos, and A. Mura. Modeling of Turbulent Combustion. In M. Lackner, F. Winter, and A. K. Agarwal, editors, *Handbook of Combustion, Vol 1: Fundamentals and Safety*, chapter 8, pages 139–143. Wiley-VCH, 2010.

C. S. Moreau, E. Therssen, X. Mercier, J. F. Pauwels, and P. Desgroux. Two-color laser-induced incandescence and cavity ring-down spectroscopy for sensitive and quantitative imaging of soot and PAHs in flames. *Applied Physics B: Lasers and Optics*, 78(3-4): 485–492, 2004.

A. R. Morr, J. B. Heywood, and A. H. Fitch. Measurements and Predictions of Carbon Monoxide Emissions from an Industrial Gas Turbine. *Combustion Science and Technology*, 11(3-4):97–109, 1975.

G. Myhre, D. Shindell, F.-M. Bréon, W. Collins, J. Fuglestvedt, J. Huang, D. Koch, J.-F. Lamarque, D. Lee, B. Mendoza, T. Nakajima, A. Robock, G. Stephens, T. Takemura, and H. Zhang. Anthropogenic and Natural Radiative Forcing. In T. F. Stocker, D. Qin, G.-K. Plattner, M. Tignor, S. K. Allen, J. Boschung, A. Nauels, Y. Xia, V. Bex, and P. M. Midgley, editors, *Climate Change 2013: The Physical Science Basis. Contribution of Working Group I to the Fifth Assessment Report of the Intergovernmental Panel on Climate Change*, chapter 8, pages 659–740. Cambridge University Press, Cambridge, UK and New York, NY, USA, 2013.

D. Neves, H. Thunman, A. Matos, L. Tarelho, and A. Gómez-Barea. Characterization and prediction of biomass pyrolysis products. *Progress in Energy and Combustion Science*, 37: 611–630, 2011.

Nexant Inc. Assessment of Haiti alternative cooking technologies program. Technical Report November, United States Agency for International Development (USAID), 2010.

T. Nussbaumer. Combustion and Co-combustion of Biomass: Fundamentals, Technologies, and Primary Measures for Emission Reduction. *Energy and Fuels*, 17:1510–1521, 2003.

G. Oberdörster, E. Oberdörster, and J. Oberdörster. Nanotoxicology: An emerging discipline evolving from studies of ultrafine particles. *Environmental Health Perspectives*, 113(7): 823–839, 2005.

I. Obernberger. Decentralized biomass combustion: state of the art and future development. *Biomass and Bioenergy*, 14(1):33–56, 1998.

T. Ohlemiller. Modeling of smoldering combustion propagation. *Progress in Energy and Combustion Science*, 11:277–310, 1985.

T. J. Ohlemiller. Smoldering Combustion. In *SFPE Handbook of Fire Protection Engineering*, chapter 9, pages 2.200–2.210. Springer, 3 edition, 2002.

T. J. Ohlemiller, T. Kashiwagi, and K. Werner. Products of Wood Gasification. Technical report, National Bureau of Standards, 1985.

B. D. Okello, T. G. O'Connor, and T. P. Young. Growth, biomass estimates, and charcoal production of Acacia drepanolobium in Laikipia, Kenya. *Forest Ecology and Management*, 142:143–153, 2001.

S. T. Omaye. Metabolic modulation of carbon monoxide toxicity. *Toxicology*, 180:139–150, 2002.

S. M. O'Shaughnessy, M. J. Deasy, J. V. Doyle, and A. J. Robinson. Performance analysis of a prototype small scale electricity-producing biomass cooking stove. *Applied Energy*, 156:566–576, 2015.

S.-W. Park, C.-H. Jang, K.-R. Baek, and J.-K. Yang. Torrefaction and low-temperature carbonization of woody biomass: Evaluation of fuel characteristics of the products. *Energy*, 45:676–685, 2012.

A. Peters, H. E. Wichmann, T. Tuch, J. Heinrich, and J. Heyder. Respiratory effects are associated with the number of ultrafine particles. *American Journal of Respiratory and Critical Care Medicine*, 155:1376–1383, 1997.

D. P. Pope, V. Mishra, L. Thompson, A. R. Siddiqui, E. A. Rehfuess, M. Weber, and N. G. Bruce. Risk of low birth weight and stillbirth associated with indoor air pollution from solid fuel use in developing countries. *Epidemiologic Reviews*, 32(1):70–81, 2010.

A. K. Prasad. Particle Image Velocimetry. *Current Science*, 79(1):51–60, 2000.

C. V. Preble, O. L. Hadley, A. J. Gadgil, and T. W. Kirchstetter. Emissions and Climate-Relevant Optical Properties of Pollutants Emitted from a Three-Stone Fire and the Berkeley-Darfur Stove Tested under Laboratory Conditions. *Environmental Science and Technology*, 48(11):6484–6491, 2014.

S. Prucker, W. Meier, and W. Stricker. A flat flame burner as calibration source for combustion research: Temperatures and species concentrations of premixed H2/air flames. *Review of Scientific Instruments*, 65:2908, 1994. ISSN 00346748.

M. Raffel, C. Willert, S. Wereley, and J. Kompenhans. *Particle Image Velocimtery: a practical guide*. Springer, 2 edition, 2007.

P. Raman, J. Murali, D. Sakthivadivel, and V. S. Vigneswaran. Performance evaluation of three types of forced draft cook stoves using fuel wood and coconut shell. *Biomass and Bioenergy*, 49:333–340, 2013.

V. Ramanathan and G. Carmichael. Global and regional climate changes due to black carbon. *Nature Geoscience*, 1:221–227, 2008.

V. Ramanathan, P. J. Crutzen, J. T. Kiehl, and D. Rosenfeld. Aerosols, climate, and the hydrological cycle. *Science*, 294:2119–2124, 2001.

V. H. Rapp, J. J. Caubel, D. L. Wilson, and A. J. Gadgil. Reducing Ultrafine Particle Emissions Using Air Injection in Wood-Burning Cookstoves. *Environmental Science & Technology*, 50:8368–8374, 2016.

C. Reboul, J. Thireau, G. Meyer, L. André, P. Obert, O. Cazorla, and S. Richard. Carbon monoxide exposure in the urban environment: An insidious foe for the heart? *Respiratory Physiology & Neurobiology*, 184(2):204–212, 2012.

Regional Wood Energy Development Programme in Asia. Improved solid biomass burning cookstoves: a development manual. Technical Report 44, Food and Agriculture Organization of the United Nations, 1993. URL http://www.fao.org/docrep/006/AD584E/ad584e00.pdf.

G. Rein. Smouldering Combustion Phenomena in Science and Technology. *International Review of Chemical Engineering*, 1:3–18, 2009.

I. Ruiz-Mercado, O. R. Masera, H. Zamora, and K. R. Smith. Adoption and sustained use of improved cookstoves. *Energy Policy*, 39:7557–7566, 2011.

A. D. Sagar and S. Kartha. Bioenergy and Sustainable Development? *Annual Review of Environment and Resources*, 32:131–167, 2007.

R. J. Santoro. Fundamental mechanisms for CO and soot formation. Technical report, NIST, 1994.

R. J. Santoro and C. R. Shaddix. Laser-Induced Incandescence. In K. Kohse-Höinghaus and J. B. Jeffries, editors, *Applied Combustion Diagnostics*, chapter 9, pages 252–286. Taylor & Francis, New York, 2002.

R. Schmidt, H. Ryan, and A. Hoetzel. Carbon Monoxide - Toxicity of Low-Dose Application. *Current Pharmaceutical Biotechnology*, 13(6):837–850, 2012.

C. Schulz, B. F. Kock, M. Hofmann, H. Michelsen, S. Will, B. Bougie, R. Suntz, and G. Smallwood. Laser-induced incandescence: recent trends and current questions. *Applied Physics B*, 83(3):333–354, 2006.

B. D. Shaw. Fundamental Aspects of Combustion. In I. K. Puri, editor, *Environmental Implications of Combustion Processes*, chapter 1, pages 1–32. CRC Press, 1993.

J. W. Shelton. *Solid Fuels Encyclopedia*. Garden Way Publishing, 1983.

D. Shindell, J. C. I. Kuylenstierna, E. Vignati, R. van Dingenen, M. Amann, Z. Klimont, S. C. Anenberg, N. Muller, G. Janssens-Maenhout, F. Raes, J. Schwartz, G. Faluvegi, L. Pozzoli, K. Kupiainen, L. Hoglund-Isaksson, L. Emberson, D. Streets, V. Ramanathan, K. Hicks, N. T. K. Oanh, G. Milly, M. Williams, V. Demkine, and D. Fowler. Simultaneously mitigating near-term climate change and improving human health and food security. *Science*, 335:183–189, 2012.

A. Sinha and R. Toumi. A comparison of climate forcings due to chlorofluorocarbons and carbon monoxide. *Geophysical Research Letters*, 23(1):65–68, 1996.

K. R. Smith, K. Dutta, C. Chengappa, P. P. S. Gusain, O. R. Masera, V. Berrueta, R. Edwards, R. Bailis, and K. N. Shields. Monitoring and evaluation of improved biomass cookstove programs for indoor air quality and stove performance: Conclusions from the Household Energy and Health Project. *Energy for Sustainable Development*, 11:5–18, 2007.

K. R. Smith, N. Bruce, K. Balakrishnan, H. Adair-Rohani, J. Balmes, Z. Chafe, M. Dherani, H. D. Hosgood, S. Mehta, D. Pope, and E. Rehfuess. Millions dead: how do we know and what does it mean? Methods used in the comparative risk assessment of household air pollution. *Annual Review of Public Health*, 35:185–206, 2014.

K. C. Smyth and D. R. Crosley. Detection of Minor Species with Laser Techniques. In K. Kohse-Höinghaus and J. Jeffries, editors, *Applied Combustion Diagnostics*, chapter 2, pages 9–68. Taylor & Francis, New York, 2002.

M. R. Spiegel, S. Lipschutz, and J. Liu. *Mathematical Handbook of Formulas and Tables*. McGraw-Hill, third edition, 2008.

R. J. Šrám, B. Binková, J. Dejmek, and M. Bobak. Ambient air pollution and pregnancy outcomes: A review of the literature. *Environmental Health Perspectives*, 113(4):375–382, 2005.

D. Still, S. Bentson, and H. Li. Results of Laboratory Testing of 15 Cookstove Designs in Accordance with the ISO/IWA Tiers of Performance. *EcoHealth*, 12:12–24, 2015.

A. Suri and M. Horio. Solid Biomass Combustion. In M. Lackner, F. Winter, and A. K. Agarwal, editors, *Handbook of Combustion, Vol. 4: Solid Fuels*, chapter 3. Wiley-VCH, 2010.

K. B. Sutar, S. Kohli, M. Ravi, and A. Ray. Biomass cookstoves: A review of technical aspects. *Renewable and Sustainable Energy Reviews*, 41:1128–1166, 2015. ISSN 13640321.

J. R. Taylor. *An Introduction to Error Analysis: The study of uncertainties in physical measurements*. University Science Books, second edition, 1997.

E. Therssen, Y. Bouvier, C. Schoemaecker-Moreau, X. Mercier, P. Desgroux, M. Ziskind, and C. Focsa. Determination of the ratio of soot refractive index function E(m) at the two wavelengths 532 and 1064 nm by laser induced incandescence. *Applied Physics B: Lasers and Optics*, 89(2-3):417–427, 2007.

C. L. Tien and S. C. Lee. Flame radiation. *Progress in Energy and Combustion Science*, 8: 41–59, 1982.

P. Tikuisis, D. M. Kane, T. M. McLellan, F. Buick, and S. M. Fairburn. Rate of formation of carboxyhemoglobin in exercising humans exposed to carbon monoxide. *Journal of Applied Physiology*, 72(4):1331–1319, 1992.

J. Tryner, B. D. Willson, and A. J. Marchese. The effects of fuel type and stove design on emissions and efficiency of natural-draft semi-gasifier biomass cookstoves. *Energy for Sustainable Development*, 23:99–109, 2014.

UNEP. Integrated assessment of black carbon and tropospheric ozone summary for decision makers. Technical report, United Nations Environment Programme (UNEP), 2011.

United Nations Children's Fund. At a glance: Haiti - statistics, 2012. URL http://www.unicef.org/infobycountry/haiti{_}statistics.html.

S. P. Urbanski. Combustion efficiency and emission factors for wildfire-season fires in mixed conifer forests of the northern Rocky Mountains, US. *Atmospheric Chemistry and Physics*, 13:7241–7262, 2013.

U.S. EPA. Report to Congress on Black Carbon. Technical Report March, United States Environmental Protection Agency, 2012. URL https://www3.epa.gov/blackcarbon/2012report/fullreport.pdf.

USAID. Black carbon emissions in Asia: Sources, impacts and abatement opportunities. Technical Report April, United States Agency for International Development (USAID), 2010.

A. Valavanidis, K. Fiotakis, and T. Vlachogianni. Airborne Particulate Matter and Human Health: Toxicological Assessment and Importance of Size and Composition of Particles for Oxidative Damage and Carcinogenic Mechanisms. *Journal of Environmental Science and Health, Part C*, 26:339–362, 2008.

D. Vamvuka. Overview of Solid Fuels Combustion Technologies. In M. Lackner, F. Winter, and A. K. Agarwal, editors, *Handbook of Combustion, Vol. 4: Solid Fuels*, chapter 2. Wiley-VCH, 2010. ISBN 9783527324491.

R. Van der Plas. Haiti: Strategy to alleviate the pressure of fuel demand on national woodfuel resources. 2007.

R. L. Vander Wal. Laser-induced incandescence: detection issues. *Applied optics*, 35(33): 6548–6559, 1996. ISSN 0003-6935. doi: 10.1364/AO.35.006548.

T. Vos, R. M. Barber, B. Bell, A. Bertozzi-Villa, S. Biryukov, I. Bolliger, F. Charlson, A. Davis, L. Degenhardt, D. Dicker, and E. al. Global, regional, and national incidence, prevalence, and years lived with disability for 301 acute and chronic diseases and injuries in 188 countries, 1990–2013: a systematic analysis for the Global Burden of Disease Study 2013. *Lancet*, 386(9995):743–800, 2015.

J. S. Wallack and V. Ramanathan. The other climate changers: Why black carbon and ozone also matter. *Foreign Affairs*, 88(5):105–113, 2009.

Y. Wang, M. D. Sohn, Y. Wang, K. M. Lask, T. W. Kirchstetter, and A. J. Gadgil. How many replicate tests are needed to test cookstove performance and emissions? — Three is not always adequate. *Energy for Sustainable Development*, 20:21–29, 2014.

D. E. Ward and L. F. Radke. Emissions measurements from vegetation fires: A comparative evaluation of methods and results. In P. J. Crutzen and J. G. Goldammer, editors, *Fire in the Environment: The Ecological, Atmospheric, and Climatic Importance of Vegetation Fires*, chapter 4, pages 53–76. John Wiley & Sons, Inc., 1993.

J. Warnatz, U. Maas, and R. W. Dibble. *Combustion: Physical and chemical fundamentals, modeling and simulation, experiments, pollutant formation.* 2006.

J. Westerweel, G. E. Elsinga, and R. J. Adrian. Particle Image Velocimetry for Complex and Turbulent Flows. *Annual Review of Fluid Mechanics*, 45(1):409–436, 2013. ISSN 0066-4189.

A. Williams, J. M. Jones, L. Ma, and M. Pourkashanian. Pollutants from the combustion of solid biomass fuels. *Progress in Energy and Combustion Science*, 38:113–137, 2012. URL http://linkinghub.elsevier.com/retrieve/pii/S0360128511000530.

T. C. Williams, C. R. Shaddix, K. A. Jensen, and J. M. Suo-Anttila. Measurement of the dimensionless extinction coefficient of soot within laminar diffusion flames. *International Journal of Heat and Mass Transfer*, 50:1616–1630, 2007.

Women's Refugee Commission. Cooking Fuel and the Humanitarian Response in Haiti: Key messages and guidance for action. 2010.

World Health Organization (WHO). Fuel for Life: Household Energy and Health. Technical report, World Health Organization, 2006a. URL http://www.who.int/indoorair/publications/fuelforlife/en/.

World Health Organization (WHO). WHO Air quality guidelines for particulate matter, ozone, nitrogen dioxide and sulfur dioxide: Global update 2005. Technical report, World Health Organization, Geneva, Switzerland, 2006b.

World Health Organization (WHO). WHO Guidelines for Indoor Air Quality: Household Fuel Combustion. Technical report, World Health Organization, 2014. URL http://www.who.int/indoorair/guidelines/hhfc/en/.

World Health Organization (WHO). Ambient air pollution: A global assessment of exposure and burden of disease. Technical report, World Health Organization, Geneva, Switzerland, 2016. URL http://apps.who.int/iris/bitstream/10665/250141/1/9789241511353-eng.pdf.

F. Xu, C. H. Kim, and G. M. Faeth. Soot surface oxidation in hydrocarbon / air diffusion flames at atmospheric pressure. *Combustion and Flame*, 132:43–57, 2003.

R. Yevich and J. A. Logan. An assessment of biofuel use and burning of agricultural waste in the developing world. *Global Biogeochemical Cycles*, 17(4):1095, 2003.

C. Yin, L. A. Rosendahl, and S. K. Kær. Grate-firing of biomass for heat and power production. *Progress in Energy and Combustion Science*, 34:725–754, 2008.

R. J. Yokelson, R. Susott, D. E. Ward, J. Reardon, and D. W. T. Griffith. Emissions from smoldering combustion of biomass measured by open-path Fourier transform infrared spectroscopy. *Journal of Geophysical Research*, 102(D15):18865, 1997.

M. Yonetani. Displacement due to natural hazard-induced disasters - Global Estimates for 2009 and 2010. Technical report, Internal Displacement Monitoring Center; Norwegian Refugee Council, 2011.

J. Zerbs, K. P. Geigle, O. Lammel, J. Hader, R. Stirn, R. Hadef, and W. Meier. The influence of wavelength in extinction measurements and beam steering in laser-induced incandescence measurements in sooting flames. *Applied Physics B: Lasers and Optics*, 96 (4):683–694, 2009.

J. Zhu, M. Y. Choi, G. W. Mulholland, S. L. Manzello, L. A. Gritzo, and J. Suo-Anttila. Measurement of visible and near-IR optical properties of soot produced from laminar flames. *Proceedings of the Combustion Institute*, 29:2367–2374, 2002.

G. Zizak. Laser-Induced Incandescence. *Special Issue of Applied Physics B*, 104(2), 2011.

R. Zlotkowska. Adverse Health Effects of the Exposure to the Spherical Aerosol Particles, including Ultra-Fine Particles. In J. S. Pastuszka, editor, *Synergic Influence of Gaseous, Particulate, and Biological Pollutants on Human Health*, chapter 4, pages 109–122. CRC Press, Boca Raton, Florida, USA, 1 edition, 2016.